MONASH University

Development of Particle-based Numerical Manifold Method (PNMM) for Dynamic Rock Fracturing

Xing Li

A thesis submitted for the degree of Doctor of Philosophy at
Monash University in 2017
Department of Civil Engineering

Copyright notice

Declaration

This thesis contains no material which has been accepted for the award of any other degree or diploma at any university or equivalent institution and that, to the best of my knowledge and belief, this thesis contains no material previously published or written by another person, except where due reference is made in the text of the thesis.

Signature: 

Print Name: Xing Li

Date: 12 December 2017

To my parents, Li Li and Jianru Xu

Abstract

Development of Particle-based Numerical Manifold Method (PNMM) for Dynamic Rock Fracturing

A thesis submitted for the degree of Doctor of Philosophy

Xing Li
Department of Civil Engineering
Monash University
2017

The numerical manifold method (NMM) is a useful tool in rock mechanics to model the continuous and discontinuous behaviors of rock materials and jointed rock masses in a unified framework. One of the main challenges in NMM is the complex geometrical operations between different types of polyhedrons in contact analysis. Attempting to tackle this issue, a particle manifold method (PMM) was developed as an extension by introducing the particle concept into NMM.

The main contribution of this thesis is the development of a particle-based numerical manifold method (PNMM) to simulate the dynamic fracturing of rock materials under different conditions. The proposed method is modified from NMM and PMM. The most distinct characteristic of PNMM is the dual-level discretization. The first level of discretization consists of manifold elements which are constructed by a dual-layer-cover system inherited from NMM. Degrees of freedom and formulae in matrix form are defined and conducted on this level of discretization. Then, particles are introduced within each manifold element as the second level of discretization. On particles, the material properties, body forces, and boundary conditions are defined. A particle integration scheme is proposed to derive the matrices on manifold elements from the parameters on particles. Links and pairs of contact are defined on the level of particles to simulate the initiation and propagation of fractures and the contact between blocks respectively. The enrichment function in XFEM is incorporated around the tip of fracture. Rate-dependent behaviors of rock materials are taken into consideration in PNMM by incorporating the Johnson-Holmquist-Beissel (JHB) model. Last, PNMM is implemented in programming

language C++, aided by several commercial/free software and third-party libraries. The proposed method is calibrated by modelling several fundamental problems. Results of PNMM are verified against analytical solutions and numerical results in literature.

The capabilities of PNMM are further examined and demonstrated in representative cases of dynamic rock fracturing. A numerical study of the rock scratch test has been performed, illustrating how the proposed method can be applied to the analysis of engineering cases involving a rock cutting process. The transition of failure mode from ductile to brittle in the scratch test is successfully simulated, and a corresponding transitional range of cutting depth is obtained. The effect of cutter operational parameters is investigated from the energy point of view. Some advices are given to improve the efficiency of rock cutting in engineering practice. The final part of this thesis is devoted to studying the spalling failure on both experimental and engineering scale. The spalling process and fracturing pattern of rock bars under different loading types and loading rates, as well as a plate impact test are first simulated. Then, a numerical study of the spalling and rockburst in tunnels that are subjected to static in-situ stresses and a far-field dynamic disturbance is performed. Simulation results lead to useful insights concerning the relationship between the in-situ stress, dynamic disturbance, spalling fractures, and rockburst phenomenon. This simulation shows that PNMM is capable of modelling the dynamic failure and estimating the safety of underground openings in two dimensions.

Acknowledgements

This thesis would not have been possible without the collaboration and support of many individuals. First and foremost, I would like to express my deep admiration and gratitude to my supervisor, Professor Jian Zhao, who gave me the amazing opportunity to start the PhD at EPFL in Switzerland and later to transfer to Monash University in Australia with his career change. His support and guidance throughout this dissertation and enthusiasm in performing scientific research have always encouraged me with great optimism. It has been an invaluable experience for me to learn from him not only advanced knowledge of rock mechanics but also the scientific way of thinking.

I owe special acknowledgments to my co-supervisor at Monash, Dr. Qianbing Zhang, in the past two years. He has been a perfect leader and a friend since I was at EPFL, always ready to discuss and to provide invaluable advices on my research. I also wish to thank my co-supervisor at EPFL, Professor Lyesse Laloui, for all his support during the first two years of this dissertation, and especially for his advices during my candidacy exam.

I am grateful to the examiners of this dissertation, Professor Charlie C. Li of Norwegian University of Science and Technology and Professor Shanyong Wang of The University of Newcastle, as well as all panel members of my thesis pre-submission review at Monash, Professor Ranjith Pathegama Gamage, Dr. Ha H. Bui, and Dr. Mohan Yellishetty, for their critical evaluation and valuable comments.

Special thanks go to Dr. Liang Sun and Professor Gaofeng Zhao, whose original idea and earlier work on PMM when they were at EPFL provides the foundation of this research.

I wish to thank Professor Chun'an Tang of Dalian University of Technology for his rich knowledge on the numerical study of rock materials and suggestions for the visualization of PNMM. I would also like to acknowledge his generous help during my stays in Dalian. Also, his colleague, Ms. Hongmei Bai, helped to develop an initial version of the graphical user interface for PNMM code. I also wish to thank Professor Lei He of Southeast

University for his expertise in numerical manifold method and programming, as well as his support and advices when he was at Monash. I would like to thank Professor Yuyong Jiao of China University of Geosciences (Wuhan) for sharing his knowledge and experience in developing a particle-based discontinuous deformation analysis method.

I am grateful to all the current and former members of our research group at Monash University: Yanlong Zheng, Tianshou Ma, Xuhai Tang, Jincheng Fan, Zenghui Liu, Lixiang Xie, Xiaoxuan Kong, Haozhe Xing, Kai Liu, Wei Xiong, Minghe Ju, Fuping Zhang, Pengfei Liu, Xiaofeng Li, Gonglinan Wu, and Tingwen Sun. I especially thank Mrs Jennifer Manson and Ms Min Major for their kind help in the transfer of my PhD candidature.

I am also grateful to my colleagues in the LMR lab at EPFL: Yang Zou, Wei Wu, Lijun Yin, Xin Chen, Erika Paltrinieri, Andrea Delisio, Felipe Orellana, Jean-Paul Dudt, Rosa Ana Turielle, and Barbara Tinguely. The time spent with them in Lausanne will be a memorable experience in my life. I would also like to thank the committee of my candidacy exam in the first year of this dissertation: Prof. Ian F. C. Smith, Prof. Jean-Francois Molinari, and Dr. Jiannong Fang.

I would like to thank my master supervisor Professor Luxian Li at Xi'an Jiaotong University, who encouraged me to pursue my PhD overseas. I also wish to thank Professor Jianchun Li of Southeast University for her strong recommendation during my application to the doctoral program in EPFL.

I acknowledge the financial support provided by the China Scholarship Council (No. 201306280028).

Finally, I would like to express my deepest gratitude to my father, Li Li, my mother, Jianru Xu, and my fiancée, Jinhan Xie, for their love and support over the years.

Xing Li 李星
12 December 2017
Melbourne, Australia

Contents

List of Figures

Appendix

List of Tables

List of Acronyms

3DEC	Three-dimensional Distinct Element Code
AE	Acoustic Emission
BEM	Boundary Element Method
CDM	Continuum Damage Mechanics
CG	Conjugate Gradient method
CGAL	Computational Geometry Algorithms Library
CSM	Crack Smeared Model
CT	Computed Tomography
CZM	Cohesive Zone Model
DDA	Discontinuous Deformation Analysis
DDD	Discontinuous Deformation and Displacement analysis
DEM	Distinct/Discrete Element Method
DLSM	Distinct Lattice Spring Model
DOF	Degree of Freedom
FDM	Finite Difference Method
FDEM	Finite-Discrete Element Method
FEM	Finite Element Method
FLAC	Fast Lagrangian Analysis of Continua
FVM	Finite Volume Method
GEM	Granular Element Method
GFEM	Generalized Finite Element Method
GPD	General Particle Dynamics
JHB	Johnson-Holmquist-Beissel model

LM	Lattice Model
LSM	Lattice Spring Model
MSE	Mechanical Specific Energy
NMM	Numerical Manifold Method
PCG	Preconditioned Conjugate Gradient method
PFC	Particle Flow Code
PMM	Particle Manifold Method
PNMM	Particle-based Numerical Manifold Method
PUM	Partition of Unity Method
RFPA	Realistic/Rock Failure Process Analysis
SHPB	Split Hopkinson Pressure Bar
SPH	Smoothed Particle Hydrodynamics
SRF	Strength Reduction Factor
UDEC	Universal Distinct Element Code
VTK	Visualization Toolkit
XFEM	eXtended Finite Element Method

Chapter 1 Introduction

1.1 Background

Rock mechanics was defined by the US National Committee on Rock Mechanics in 1964 and subsequently modified in 1974: *"Rock mechanics is the theoretical and applied science of the mechanical behavior of rock and rock masses; it is that branch of mechanics concerned with the response of rock and rock masses to the force fields of their physical environment."*

As an important branch of rock mechanics, rock dynamics is the science of the mechanical behavior of rock materials and rock masses under dynamic loading conditions. Typical dynamic loads include earthquake, external impact and explosion-induced wave. Understanding the dynamic responses of both rock materials and rock masses is of significance in dealing with various rock engineering problems, such as rock slope stability analysis, underground excavation, rock blasting and protective construction design. Two important aspects of rock dynamics are dynamic failure and wave propagation.

Studying the dynamic failure of rock involves the topics of crack nucleation, fracture propagation, rock fragmentation and post-failure behavior. Typical rock experiments and engineering issues usually cover one or, in most cases, more topics mentioned above. Results of a series of experimental tests (Masuda et al., 1987, Lajtai et al., 1991) have unveiled that the fracture pattern and mechanical properties of rock materials are affected by the dynamic strain rate. However, the underlying mechanism of the rate dependent behavior is still unclear. Recently, the microstructure of rock material is considered as one of the influence factors leading to this phenomenon. When the mechanical behavior on microscopic scale is concerned, analytical methods turn out to be invalid due to the complex microstructure of rock materials (Figure 1.1a), and experimental approaches will be limited as existing facilities are not sensitive enough to detect the failure process under high loading rates. Under such a circumstance, numerical

methods could be a promising tool to study the mechanism of dynamic effect on rock materials on the microscopic scale.

For wave propagation issues, the prediction of wave attenuation across fractured rock masses is significant in geophysics, seismic wave investigation and rock protective engineering. Theoretical models are generally able to analyze the wave propagation across a single fracture (Zhao and Cai, 2001, Li et al., 2011, Zou, 2016) or a set of parallel fractures (Cai and Zhao, 2000, Zhao et al., 2006). However, the distribution of rock joints can be quite complex in practice as shown in Figure 1.1b, and analytical methods are difficult to be applied for such complex geometry conditions. Again, numerical methods could provide promising solutions for the wave attenuation across highly fractured rock masses.

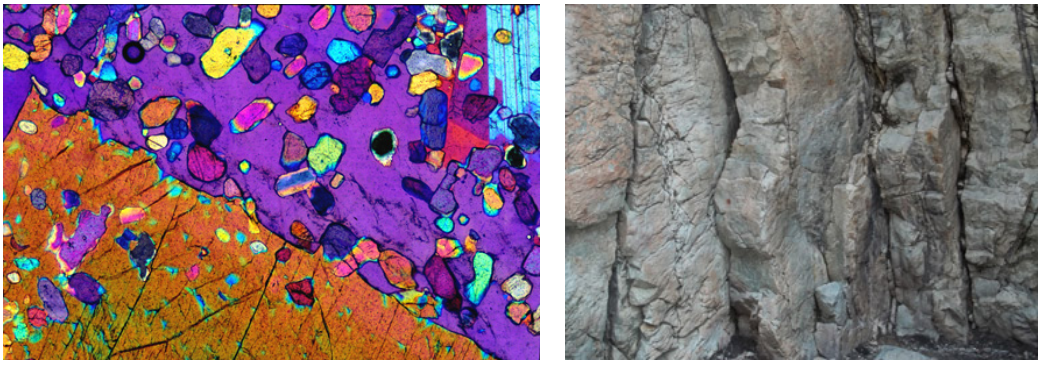

(a) (b)

Figure 1.1 The complex structure of rock at both micro and macro scale: (a) Olivine inclusions in gabbro (5x), courtesy of Prof. Bernardo Cesare, (b) A set of rock joints

Due to the complexity of both rock materials and rock engineering problems, rock is difficult to be modelled by whatever numerical method, comparing with other solid materials. To gain better results, a large number of numerical models have been developed, extended, and applied in this field, including in-house software, commercial software, and open source code. A list of representative PhD thesis within this topic is summarized in Table 1.1.

Table 1.1. A list of representative PhD theses within the topic of numerical simulations of rock dynamics

Year	Author	Model	Title	Institute
2004	H.Y. Liu	RFPA	Numerical modelling of the rock fragmentation process by mechanical tools	Lulea University of Technology
2005	Z.Z. Liang	RFPA	Three dimensional numerical modelling of rock failure process	Dalian university of technology
2009	Y.N. Wang	DEM	Three-dimensional rock-fall analysis with impact fragmentation and fly-rock modeling	The University of Texas at Austin
2010	X.M. An	NMM	Extended Numerical Manifold Method for Engineering Failure Analysis	Nanyang Technological University
2010	H.R. Bao	DDA	Nodal based discontinuous deformation analysis	Nanyang Technological University
2010	S. Levy	FEM	Exploring the physics behind dynamic fragmentation through parallel simulations	Ecole Polytechnique Fédérale de Lausanne
2010	R. Resende	DEM	An investigation of stress wave propagation through rock joints and rock masses	Porto University
2010	G.F. Zhao	DLSM	Development of Micro-Macro Continuum-Discontinuum Coupled Numerical method	Ecole Polytechnique Fédérale de Lausanne
2011	L. He	NMM	Three dimensional numerical manifold method and rock engineering applications	Nanyang Technological University
2011	T. Kazerani	DEM	Micromechanical Study of Rock Fracture and Fragmentation under Dynamic Loads using Discrete Element Method	Ecole Polytechnique Fédérale de Lausanne
2012	O.K. Mahabadi	FDEM	Investigating the influence of micro-scale heterogeneity and microstructure on the failure and mechanical behaviour of geomaterials	University of Toronto
2012	L. Sun	PMM	Particle Manifold Method (PMM) for Multiscale Continuous-Discontinuous Analysis	Ecole Polytechnique Fédérale de Lausanne
2013	C.W. Boon	DEM	Distinct Element Modelling of Jointed Rock Masses: Algorithms and Their Verification	University of Oxford
2013	A. Lisjak	FDEM	Investigating the influence of mechanical anisotropy on the fracturing behaviour of brittle clay shales with application to deep geological repositories	University of Toronto
2013	X.H. Tang	DEM	Impulse-based discrete element modelling of rock impact and fragmentation, with applications to block cave mining	Imperial College London
2013	Z.J. Wu	NMM	Development of numerical manifold method for cracking process in rock	Nanyang Technological University
2013	Y.N. Zhou	FEM	Numerical modeling of rock drilling with finite elements	University of Pittsburgh

Considering the distinct characteristics of rock materials and rock engineering problems, **an ideal numerical method for rock dynamics needs to meet following requirements**:

- Able to simulate the macroscopic behavior of rock masses;
- Able to represent the microstructure of rock materials;
- Able to capture the influence of microstructure on the mechanical properties of rock masses;
- Able to simulate the nucleation and propagation of fractures;
- Able to simulate the complete detachment of intact rock masses;
- Able to simulate the mechanical behaviors of discrete rock masses in post-failure stage;
- Able to simulate the contact behavior among massive discrete rock masses;
- Parameters at both macroscopic and microscopic scale can be experimentally measured or easily determined.

There is no single numerical model that satisfies all of these requirements. Therefore, effort is still needed to further develop existing numerical models.

1.2 Objectives

This thesis aims to develop a novel numerical model targeting at problems in rock dynamics, based on the existing numerical manifold method and recently proposed particle manifold method. Comparing with the well-known numerical manifold method, the proposed method simplifies the contact operation between blocks, improves the flexibility in initiating and determining the propagation path of fractures, and gains the ability to simulate the heterogeneity of rock materials. The proposed model reclarifies and further improves several aspects of the recently proposed particle manifold method, including the adoption of high-order interpolation functions, the development of a particle integration scheme, an enrichment function around fracture tips, the failure of links, the incorporation of a rate-dependent strength model, the expanded applications in rock dynamics, and others. The proposed attempts to meet all the requirements of an ideal numerical method for rock dynamics, as listed in the previous section.

Probably more important than proposing a new numerical model is the validation and application of the proposed model. Another aim of this thesis is to utilize the proposed model to study realistic rock dynamics problems at both laboratory and engineering scale. In this thesis, the failure induced by rock blasting, the spalling of rock materials, the rockburst of tunnels, and the process of rock scratching/cutting are numerically studied using the proposed model. Valuable and inspiring results that help to understand the behavior of rock in engineering practice are obtained. Simulation results are compared with theoretical solution and other numerical results in references to demonstrate the proposed model as a promising tool for modelling rock dynamics problems.

1.3 Structure of the Thesis

This thesis has seven chapters. In **Chapter 1**, a general introduction of the thesis is given, including the complexity of rock materials and rock engineering problems, requirements of an ideal numerical model in this field, and the objectives of this thesis.

Chapter 2 presents a review of existing numerical methods that are widely applied in rock mechanics. The numerical methods are reviewed in three categories: continuous methods, discontinuous methods, and coupled methods. The recent developments and applications of each numerical method are introduced separately, and its advantages and drawbacks are then discussed. Last, the characteristics of four typical numerical methods are compared to find their similarities and differences.

Chapter 3 proposes a novel numerical model for rock dynamics, namely the particle-base numerical manifold method (PNMM). This chapter presents the conception, formulations, basic components, and the implementation of PNMM in detail. First, the dual-layer-cover system and dual-level discretization are introduced respectively to provide the foundation and character of PNMM. Then, necessary mathematical formulae and their numerical implementation are given. The basic components, including particles, links, failure description, and contact accumulation, are introduced. The rate-dependent strength criterion adopted in PNMM is given. Last, the implementation of PNMM is summarized.

This chapter is based on a paper published in the journal *International Journal of Geomechanics*.

Chapter 4 provides several numerical examples for the calibration of PNMM. A cantilever beam bending test is first performed to verify the elastic performance of PNMM. A Brazilian disc test is conducted as a static failure issue. Then, two examples on stress wave propagation are given to validate the ability of PNMM to simulate dynamic issues. Last, the rate-dependent failure under rock blasting is simulated, as a representative issue in rock dynamics. This chapter is based on a paper published in the journal *International Journal of Geomechanics* and a conference paper presented at the *2nd International Conference on Rock Dynamics and Applications* (RocDyn-2).

Chapter 5 presents a numerical study of rock scratching/cutting using PNMM. The scratching processes under different cutting depths are first simulated, where the failure pattern and cutting force are discussed. Then, the effect of cutter operational parameters on the cutting force and the energy consumed by the cutter is studied. Three operation parameters of the cutter are considered, including the cutting depth, cutting speed, and cutter rake angle. Accordingly, advices are given to improve the efficiency of rock cutting in engineering practice. This chapter is based on a paper accepted by the journal *Tunnelling and Underground Space Technology*.

Chapter 6 presents a numerical study of spalling and spalling-induced rockburst under dynamic disturbance using PNMM. The spalling of rock bars is first simulated. The spalling process and fracturing pattern under different loading types and loading rates are investigated respectively. Then, the spalling in plate impact tests are studied. Two types of impactor with various impact speed are adopted. Last, simulations of the rockburst of a rock tunnel under static in-situ stresses and a dynamic disturbance are carried out to investigate the relationship between the in-situ stresses, dynamic disturbance, spalling fractures, and rockburst phenomena. This chapter is based on a paper submitted to the journal *Tunnelling and Underground Space Technology*.

Chapter 7 gives a brief overview of the contributions and findings of this thesis, as well as some recommendations for future work.

Appendix A presents an algorithm used in PNMM for the generation of links.

Appendix B gives an overview of the code developed for PNMM.

Appendix C presents the source code of an algorithm used in PNMM for the generation of blocks and new manifold elements.

Appendix D is for the implementation of matrices and block matrices in PNMM. The source code is given in detail.

Appendix E gives the methods and source code of two solvers to the system of linear equations.

Appendix F provides an example of the *vtk* file for the post-process of PNMM.

Chapter 2 A Review of Numerical Methods for Rock Dynamics

This chapter presents a review of several existing numerical methods that are widely applied in rock mechanics. The numerical methods are classified into three categories: continuous methods, discontinuous methods, and coupled methods. Continuous methods are suitable for those problems whose system is a continuum with infinite degree of freedoms. The behavior of such system is dominated by the governing differential equation of the problem and the continuity conditions at the interfaces between adjacent elements. This type of method is mostly used for rock masses with no fractures. It can also be used for the rock mass with a few or many fractures, the behavior of which being established through equivalent properties. Discrete methods are for those problems whose system is a combination of a finite number of well-defined components. Usually there is no need to discretize such a system, as it has been automatically done. The behavior of such system is dominated by the well-defined inter-relations between adjacent components. This type of method is most suitable for moderately fractured rock masses where the number of fractures is too large for continuous methods, and/or where large displacements of individual blocks are possible. A coupled method, in most cases, is a combination of one continuous method and one discrete method implicitly or explicitly, aiming to combine the characteristics of both methods. The development and application of the numerical methods belonging to each category is first introduced separately. Then the characteristics of several typical numerical methods are compared to find their advantages and disadvantages.

2.1 Continuous Methods

2.1.1 Finite Element Method

The term finite element method (FEM) was first used by Clough (1960) for plane stress problem, henceforth the FEM has become the mainstream numerical tool in engineering

science. Unfortunately, the FEM has not been vastly adopted in rock mechanics and rock engineering, as in many other fields. The major hindrance to its application on rock mechanics is the simulation of fracturing process. There are mainly three techniques dealing with the fracturing problem in FEM: the element degradation approach, the boundary breaking approach, and the element breaking approach.

The element degradation approach

The element degradation approach treats the rock fracturing process as a sequence of element failures. The most representative method adopting this approach is the continuum damage mechanics (CDM). The CDM is firstly used for brittle fracturing analysis (Bonora, 1997). Further, the Weibull distribution is introduced into CDM to represent the heterogeneity and statistic failure criteria, and then the damage evolution and crack propagation in concrete and rock are simulated (Prisco and Mazars, 1996, Kuna-Ciskal and Skrzypek, 2004). Another degradation technique, namely the crack smeared model (CSM), is realized by modelling the cracks and joints on equivalent continuum concepts of elastic degradation and/or softening plasticity. Due to its computational convenience, the CSM is commonly used in concrete fracturing under high strain rates and failure of ceramic refectory materials (Ali, 1996, Andreev and Harmuth, 2003, Tang and Tang, 2015). The element degradation approach has been adopted in many commercial FEM codes. In ABAQUS (2017), the elements whose failure criterion is locally reached are removed and visualized as a crack. In ANSYS (2017), the CSM is used to simulate the fracture process of concrete-like material. The advantage of the element degradation approach is that remeshing is not required in its calculation process. However, this method fails to give an explicit description of the fracture surface, and its simulation result depends on its mesh size and orientation.

The realistic failure process analysis (RFPA) is a representative model and software package that uses the CDM technique. RFPA was originally proposed by Tang (1997). It is a development of FEM especially for rock mechanics and engineering, based on damage mechanics and statistical theory. RFPA is able to simulate the whole fracturing process, including the initiation, propagation and coalescence of cracks, without any assumption

about where and how fractures should occur. In RFPA, uniform elements with the same shape and size are adopted in both 2D and 3D conditions, and there is no geometric priority in any orientation (Tang and Kaiser, 1998). The elemental mechanical properties, including the uniaxial impressive strength, the elastic modulus, the density and Poisson's ratio, are assumed to follow a Weibull distribution (Figure 2.1a). Such a statistical variability enables the model to simulate the non-linear deformation of a quasi-brittle behavior with an ideal brittle constitutive law at the locale scale. In addition, the approach of damage mechanics is employed to model the mechanical behavior of meso-scale elements. For each element, the material is assumed to be linear elastic, isotropic and damage-free before loading. The Mohr-Coulomb criterion with tension cut-off and the maximum tensile stress criterion are adopted to judge whether damage or failure occurs in the element (Zhu et al., 2006). When the element meets the damage criterion, damage occurs in the element. For damaged elements, the stiffness is reduced monotonically according to the elastic damage model (Tang et al., 2007, Wang et al., 2011a). Every damage in the element is regarded as the source of an acoustic event as the failed element must release its elastic energy store during the deformation. By recording the number of damaged elements and the energy they released, RFPA is able to simulate the acoustic emission (AE) activities, including the AE event rate, magnitude and location (Figure 2.1).

Since 2009, RFPA has been a commercial software package provided by Mechsoft (RFPA, 2017). The application of RFPA includes the failure process of underground excavations (Zhu et al., 2010, Wang et al., 2013, Jia and Zhu, 2015), tunnels (Wang et al., 2012), the Brazilian disc specimens (Zhu and Tang, 2006, Wang et al., 2014b, Dai et al., 2015, Zhu et al., 2015), boreholes (Tang et al., 2017a), the temperature-induced cracking (Yu et al., 2015), fracturing of layered materials due to surface cooling (Tang et al., 2017b) and many other cases (Wang et al., 2011a, Wang et al., 2011b, Wang et al., 2014a).

Modelling results in these papers have shown the outstanding ability of RFPA to simulate the failure process of rock masses. However, in order to naturally simulate the heterogeneity of rock masses through a statistical distribution, elements in RFPA need to be very small in size and the distribution coefficient needs to be carefully decided.

Moreover, as an extension of FEM, RFPA is still based on small deformation analysis. Therefore, it is only able to simulate the initiation and propagation process of the fractures in rock masses, but unable to simulate the large displacement of fractured rock blocks. To overcome this shortcoming, a coupled method of the RFPA and the discontinuous deformation analysis has been proposed as the discontinuous deformation and displacement (DDD) method (Gong and Tang, 2017) recently.

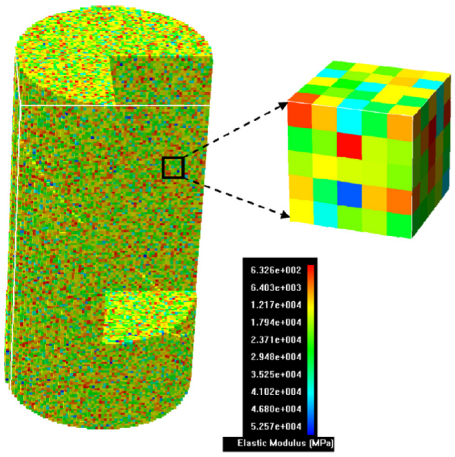

(a)

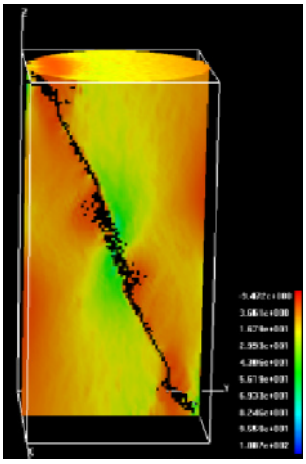

(b)

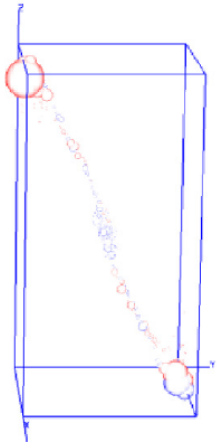

(c)

Figure 2.1 RFPA results of fractures in a cylindrical specimen with two pre-existing flaws: (a) 3D inhomogeneous model; (b) fractures evolution; (c) AE distribution (Wang et al., 2014a)

The boundary breaking approach

The boundary breaking approach represents the fracture process through separating adjacent elements and inserting interface elements along their element boundaries. The most successful development of this approach is the cohesive zone model (CZM) (Hillerborg et al., 1976, Belytschko et al., 1976), which has been successfully implemented to simulate the fracture and fragmentation in brittle materials, multiple discrete crack propagation, and dynamic crack growth (Figure 2.2) in ceramic materials (Camacho and Ortiz, 1996, Yang and Chen, 2005, Zhou and Molinari, 2004, Zhou et al., 2005, Molinari et al., 2007, Levy et al., 2010, Yao et al., 2015, Vocialta et al., 2017). The advantage of the boundary breaking approach is that the fracture can be explicitly described. However, a remeshing technique is required to eliminate the element dependence and stress singularity, which could be difficult in implementation, increase the computation cost, and accumulate calculation errors.

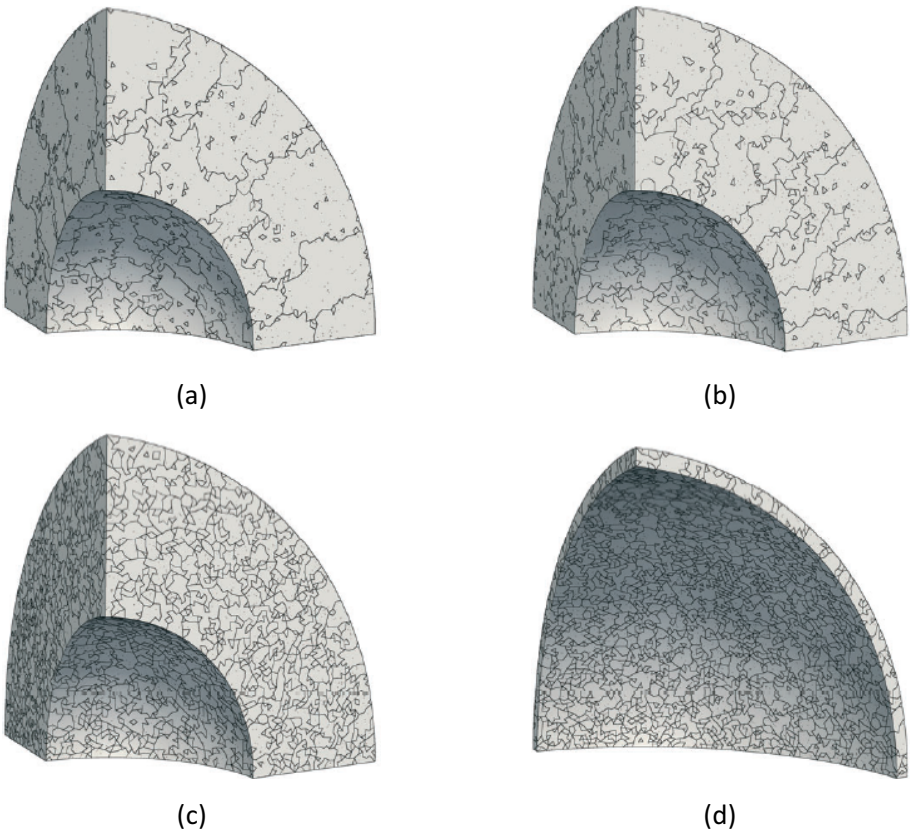

Figure 2.2 Borders of the fragments under different strain rates simulated by FEM with cohesive elements: (a) 6 × 10^3 s^{-1}; (b) 1 × 10^4 s^{-1}; (c) 4 × 10^4 s^{-1}; (d) 4 × 10^4 s^{-1} (thin plate) (Vocialta et al., 2017)

The element breaking approach

The element breaking approach was born with the development of the generalized or extended finite element methods (GFEM/XFEM). Both GFEM and XFEM are based on the partition of unity method (PUM) (Babuška and Melenk, 1997), which allows for addition of a priori knowledge about the solution into the approximation space of the numerical solution. In fact, GFEM and XFEM use exactly the same method, while the former targets solving problems with complex geometry with less error and computer resources (Strouboulis et al., 2003, Strouboulis et al., 2007) and the latter targets treating crack propagation problems (Moës et al., 1999, Moës and Belytschko, 2002). They have been regarded as an alias to each other in some literature (Garzon et al., 2014, Gupta and Duarte, 2014). In this thesis, the acronyms GFEM and XFEM will be used interchangeably.

XFEM can be seen as a development to the standard FEM. In FEM, shape functions are pre-defined, depending on the type of elements only and not related to the specific problem. However, in XFEM, shape function spaces are locally enriched using the functions suitable to represent a priori known properties of the modelled problem. Specifically, in crack propagation problems, the Heaviside function and the near tip asymptotic functions are adopted to represent the jump of displacement across crack surface and the singularity around the crack tip respectively. The XFEM elements are allowed to contain one or more cracks, therefore the mesh generation can be quite simple and any remeshing is unnecessary in XFEM. XFEM with higher orders have been developed and applied to crack propagation problems (Stazi et al., 2003, Laborde et al., 2005, Lan et al., 2013, Song et al., 2015). The development history of XFEM/GFEM can be found in (Belytschko et al., 2009). XFEM has become a standard module of ABAQUS since its version 6.9 in 2009. Unfortunately, the application of XFEM in rock mechanics is very limited. XFEM/GFEM has the advantage of mesh independency in dealing with weak and strong discontinuities. Nevertheless, this method also suffers from its disadvantages. For example, the global stiffness matrix can become singular if the crack truncates a very small part of a finite element (Peters and Hackl, 2005). XFEM also encounters ill-condition problems when using higher order cover functions (Strouboulis et al., 2007).

In summary, FEM is very convenient and flexible to treat material heterogeneity, non-linear deformability, complex boundary conditions, in situ stresses and gravity. However, the continuum assumption in FEM makes it unsuitable to deal with the complete detachment and large-scale fracture opening problems (Jing and Hudson, 2002, Jing, 2003), which are the most concerned issues in rock mechanics.

2.1.2 Finite Difference Method and Finite Volume Method

The finite difference method (FDM) (Narasimhan and Witherspoon, 1976) is one of the oldest numerical techniques for the solution of sets of partial differential equations. Its basic concept is to replace the partial derivatives of the objective function by differences defined over certain spatial intervals, which yields a system of algebraic simultaneous equations of the objective functions at a grid (mesh) of nodes over the domain of interest. The implementation of FDM is quite simple in both two- and three-dimensional cases, as no local trial functions are employed to approximate the PDEs in the neighborhoods of the sampling points, and no global system of equations in matrix form needs to be formed and solved. However, the conventional FDM with regular grid systems suffers from its inflexibility in dealing with fractures, complex boundary conditions and material inhomogeneity.

To overcome these shortcomings, the finite volume method (FVM) is developed as a branch of FDM. FVM is also a direct approximation of the partial differential equations as FDM, but in an integral sense. A FVM model can be easily constructed from a standard FEM mesh (Bailey and Cross, 1995), and FVM is as flexible as FEM in handling material inhomogeneity and mesh generation. Therefore, FVM is also regarded as a bridge between FDM and FEM (Selmin, 1993). The continual improvement of FDM and FVM ensures that they are still one of the most popular numerical methods in rock mechanics.

The most well-known computer software using the FDM/FVM approach is the FLAC, short for Fast Lagrangian Analysis of Continua, code group (FLAC, 2017). FLAC2D and FLAC3D are both widely used for the stress analysis of non-linear rock engineering problems in recent years (Shabanimashcool and Li, 2012, Shabanimashcool and Li, 2013, Wang et al.,

2013, Hasanpour et al., 2014, Kang et al., 2014, Li et al., 2014d, Nemcik et al., 2014, Resende et al., 2014, Chemenda, 2015, Lin et al., 2015, Zhang and Goh, 2015, Zhang et al., 2015a, Zhao et al., 2015). An example of the progressive failure of jointed rock slopes with different strength reduction factor (SRF) is presented in Figure 2.3.

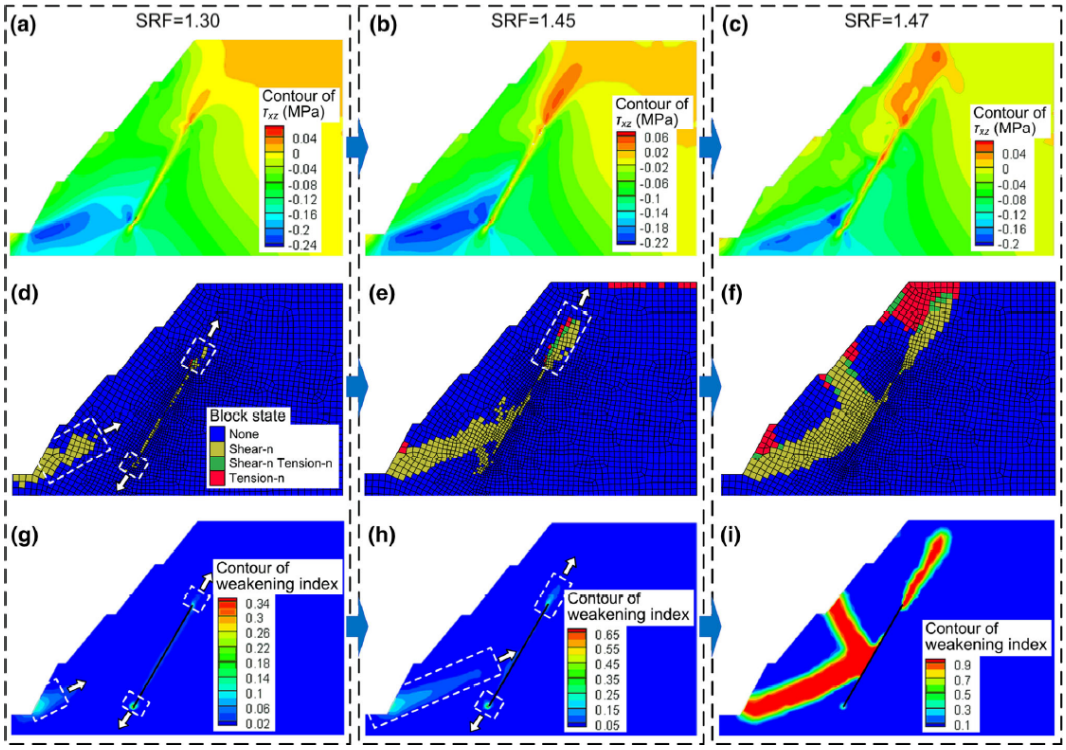

Figure 2.3 A study of the progressive failure of jointed rock slopes using FLAC3D: (a) τ_{xz} at SRF = 1.30; (b) τ_{xz} at SRF = 1.45; (c) τ_{xz} at SRF = 1.47; (d) failure zone at SRF = 1.30; (e) failure zone at SRF = 1.45; (f) failure zone at SRF = 1.47; (g) weakening index at SRF = 1.30; (h) weakening index at SRF = 1.45; (i) weakening index at SRF = 1.47 (Zhang et al., 2015a)

The primary shortcoming of FDM and FVM is that the explicit representation of fractures is not easy, because the finite difference schemes in FDM and interpolations in FVM both require the continuity of the functions between neighboring grid points. Although a special fracture element has been established for FVM (Caillabet et al., 2000, Granet et al., 2001), it is still not a straightforward and easy-to-implement approach.

2.1.3 Boundary Element Method

Different from FEM, the boundary element method (BEM) initially seeks a weak solution at the global level through an integral statement. Specifically, BEM uses given boundary conditions to fit boundary values into the integral equation, rather than values throughout the space defined by a partial differential equation.

Notable examples of BEM application in the field of rock mechanics include the stress and deformation analysis of underground excavations (Beer and Poulsen, 1994, Beer and Poulsen, 1995, Cerrolaza and Garcia, 1997, Pan et al., 1998, Shou, 2000, Griffith et al., 2014, Wu et al., 2015) and borehole tests for permeability measurements (Lafhaj and Shahrour, 2000). A representative BEM code is FROCK, developed by the rock mechanics group at MIT. This code is used to simulate the crack propagation resulting from quasi-static loading as a quasi-static process, i.e., dynamic effects are not taken into consideration. A recent improvement of FROCK can be found in (Da Silva and Einstein, 2013).

It is an advantage that BEM reduces the model dimension with a simpler mesh over the model surface. However, BEM is not as efficient as volume-discretization methods in dealing with material heterogeneity, non-linear material behaviors and damage evolution process. In general, the BEM is more suitable for solving problems of fracturing in homogeneous and linearly elastic bodies.

2.1.4 Meshless Methods

Meshfree methods are a large family of numerical methods. Their key idea is to provide accurate and stable numerical solutions for integral equations or partial differential equations with all kinds of possible boundary conditions using a set of arbitrarily distributed nodes or particles without mesh constraints.

Major advantages of meshfree methods, when being compared with mesh-base methods, include: (1) accuracy can be controlled more easily, since nodes or particles can be locally

inserted with ease (h-adaptivity) if needed; (2) problems with moving discontinuities, such as crack propagation, shear bands and phase transformation, can be easily treated; (3) large deformations can be easily handled; (4) higher order shape functions; (5) non-local interpolation character; and (6) no mesh alignment sensitivity. However, disadvantages occur at the same time in meshfree methods. Shape functions in meshfree methods are rational functions, thus a high-order integration scheme is required to ensure the accuracy. Besides, the treatment of essential boundary conditions is not straightforward since the shape functions are not interpolants. And coming with the simplicity in no mesh generation, more computational effort is needed when generating the shape functions over the selected node or particle clusters. In general, the computational cost of meshfree methods is believed to be higher than that of FEM (Nguyen et al., 2008). Some good reviews for meshfree methods can be found in (Belytschko et al., 1996, Li and Liu, 2002, Idelsohn and Onate, 2006, Nguyen et al., 2008).

The smoothed particle hydrodynamics (SPH) method (Lucy, 1977, Gingold and Monaghan, 1977) is one of the oldest and most popular meshfree methods. SPH was originally proposed for astrophysics in three-dimensional open space, and shortly later its applications were extended to fluid and solid mechanics due to its simplicity and Lagrangian nature. In SPH, the domain is discretized by particles that interact with each other through a kernel basis. The contact between two particles is automatically established when one particle comes within the influence domain of the other. Such an influence domain is defined by the support size of the kernel function.

SPH has the advantage of robustly computing material point history even at severely deformed configuration and still avoiding large computational cost of remeshing in Lagrangian framework or of calculating conventions in Eulerian framework. In the standard SPH, the kernel function is chosen irrespective of the material properties and therefore interactions between particles remain unaffected despite material damage, causing difficulties in modelling localized crack path and/or clustered fragments formation after multiple crack-interactions. Many enriched and analytical kernel functions have been proposed to overcome this shortcoming (Li and Liu, 2002). Latest

applications of SPH covers soil mechanics (Wang and Chan, 2014), impact dynamics (Islam, 2011, Chakraborty and Shaw, 2013, Bresciani et al., 2016), rock failure (Deb and Pramanik, 2013) and rock blasting (Fakhimi and Lanari, 2014). Recently, a novel general particle dynamics (GPD) method is proposed by incorporating the Mohr-Coulomb criterion and the Weibull statistical approach into SPH to simulate the progressive failure process of rock slopes (Zhou et al., 2015). Some reviews of SPH can be found in (Liu and Liu, 2010, Monaghan, 2012). An example of the simulated projectile impaction is given in Figure 2.4.

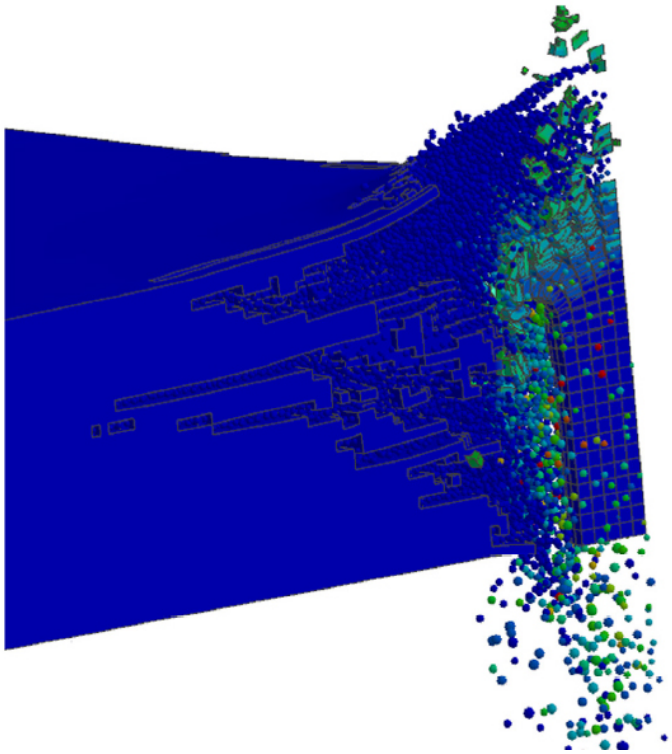

Figure 2.4 A study of projectile impaction using SPH (Bresciani et al., 2016)

2.2 Discontinuous Methods

The term discontinuous method here indicates the discrete element methods and other discontinuous methods. The discrete element methods are a large family of numerical methods. The distinct element method (DEM) is a class of discrete element methods that use an explicit time-domain integration scheme to solve the equations of motion for rigid or deformable discrete bodies with deformable contacts. Since DEM is almost the most

well-known explicit discrete element methods, researchers tend to use the term DEM and discrete element method interchangeably. On the other hand, the discontinuous deformation analysis (DDA) method is the most famous implicit discrete element method.

2.2.1 Discrete Element Method

DEM treats the simulated material as an assembly of separate particles or blocks.

Particle-base DEM

The particle-based DEM is mainly adopted to simulate the granular micro-structure of the material through particles with varying diameters. Adjacent particles can contact each other through bonds. The contact is typically assigned with a normal and shear stiffness as well as a friction coefficient. Crack nucleation is simulated by breaking of bonds while fracture propagation is obtained by coalescence of continuous bond breakages. Blocks of arbitrary shapes can be formed as a result of the simulated fracturing process and can subsequently interact with each other.

Two types of bonds are typically used in the particle-base DEM: the contact bond and the parallel bond. In the contact bond model, an elastic spring with a constant normal and shear stiffness functions between the bonded particles, allowing only normal and shear forces to be transmitted. In the parallel bond model, the moment induced by particle rotation is resisted by a set of elastic springs uniformly distributed over a finite-sized section lying on the contact plane between the bonded particles. One of the major drawbacks of the bonded-particle model is that the straightforward adoption of circular/spherical particles cannot fully capture the behavior of complex-shaped and highly interlocked grain structures, which is common in hard rocks. To overcome this limitation, a clustered particle model (Potyondy and Cundall, 2004) (Figure 2.5a) and later a clumped particle model (Cho et al., 2007) (Figure 2.5b) is proposed respectively. In clumped particle model, a group of particles are glued together to behave as a single rigid body. Clumped particles can act like a single particle that has an irregular shape but moves as a deformable and non-breakable body.

Apart from sphere, particles in other shapes have also been developed to improve the geometry description of this method, including ellipsoids (Vu-Quoc et al., 2000, Yan et al., 2010, Zheng et al., 2013), superquadrics (Wellmann and Wriggers, 2012), polyhedral (Feng et al., 2012, Smeets et al., 2015) (Figure 2.5c), and the combination of simple shape primitives, e.g., spheres (Lu and McDowell, 2007, Ferellec and McDowell, 2010, Fang et al., 2015) and ellipsoids (John et al., 2009). Furthermore, Mollon and Zhao (2014) generated three-dimensional particles with realistically complex shapes. A recent review of the particle-based DEM can be found in (Carmona et al., 2014).

The granular element method (GEM) is a newborn development of DEM (Andrade et al., 2012). This method provides geometrical enhancements of grain shapes through the flexibility of non-uniform rational basis-splines. Grain geometrical information is directly obtained from advanced experiments using visualization tools such as X-ray computed tomography (CT). The implementation of GEM is straightforward, with all other standard DEM procedure remaining intact, only minimal changes are required to existing DEM codes. Later, GEM is extended to three-dimensional cases (Lim and Andrade, 2014), and a contact dynamics approach is integrated into GEM to simulate the granular systems, comprising of rigid or highly stiff angular particles, subjected to quasi-static or intense dynamic flow conditions (Lim et al., 2014). These improvements prove GEM as a promising branch of DEM.

Besides, Tarokh and Fakhimi (2014) investigated the effect of particle size on the size of fracture process zone. Wiącek and Molenda (2014) investigated the effect of particle size distribution on rock behavior. Ding et al. (2014) investigated the effect of model scale and particle size distribution on rock behavior. Lee and Hashash (2015) proposed an impulse-based DEM (iDEM) on features of the impulse-based dynamic simulation to reduce the computation cost. Galouei and Fakhimi (2015) investigated the effect of specimen size and material ductility on the size of fracture process zone.

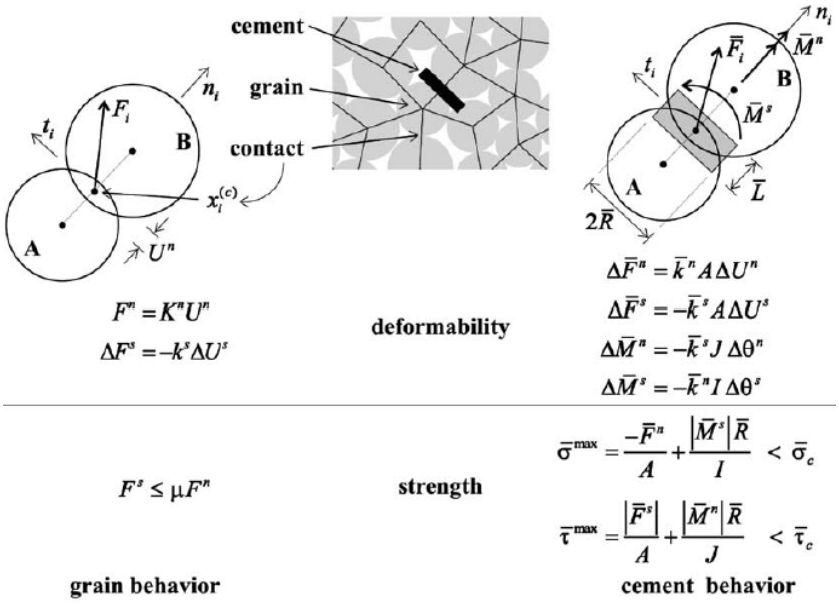

(a)

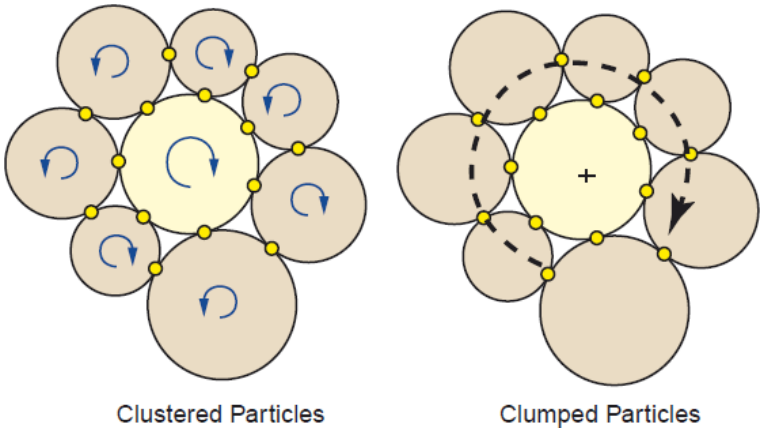

(b)

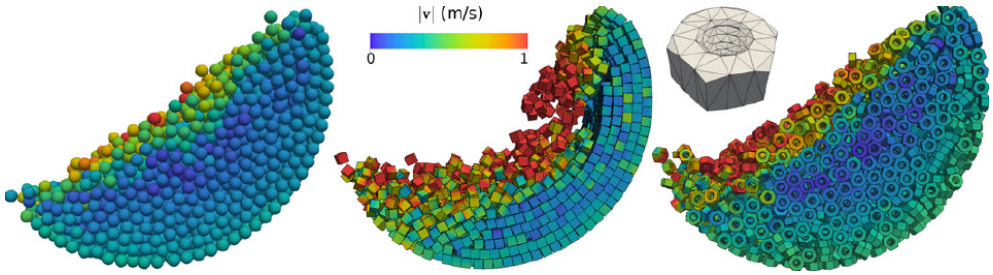

(c)

Figure 2.5 Different particle models: (a) bonded-particle model (Potyondy and Cundall, 2004); (b) clumped particle model (Cho et al., 2007); (c) arbitrary polyhedral model (Smeets et al., 2015)

The particle flow code (PFC) is the most widely used commercial particle-based DEM software, its most recent application covers the simulation of rock failure (Whittles et al., 2006, Sarfarazi et al., 2014, Sima et al., 2014, Yang et al., 2014c, Fan et al., 2015, Khazaei et al., 2015), rock blasting (Fakhimi and Lanari, 2014), rock slope (Wang et al., 2003, Lu et al., 2014), underground excavation (Li et al., 2014b), the split Hopkinson pressure bar (SHPB) test (Li et al., 2014c), rock cutting (Wyk et al., 2014, He and Xu, 2015), falling rock (Bock and Prusek, 2015), geogrid stabilized ballast (Ngo et al., 2014), rock compaction process (Dattola et al., 2014), the shear behavior of rock joints (Bahaaddini et al., 2015), transversely isotropic rock (Park and Min, 2015), and other engineering situations (Liu et al., 2014a). Zhang and Wong (2014) reviewed the methods of choosing an appropriate loading rate and give recommended loading rates for uniaxial compressive tests and Brazilian disk tests in PFC.

Yade is another well-known software for particle-based DEM. It is an open source code with an active community. An increasing number of researchers are using this code to study both rock mechanics (Smilauer, 2010) and engineering (Thoeni et al., 2014, Boon et al., 2015).

Block-based DEM

The block-based DEM discretizes the computational domain into blocks using a finite number of intersecting discontinuities. Each block is internally subdivided using a finite difference (or volume) scheme for calculation of displacement, strain and stress. Model deformability is captured by an explicit large strain Lagrangian formulation. The mechanical interaction between blocks is characterized by compliant contacts using a finite stiffness together with a tensile strength criterion in the normal direction and a tangential stiffness together with a shear strength in the tangential direction. A primary disadvantage of the standard block-based DEM is that rock failure can only be captured either in terms of plastic yielding (e.g., Mohr-Coulomb criterion with tension cut-off) or displacements of pre-existing discontinuities. Therefore, new discontinuities could not be driven within the continuum portion of the model, so that discrete fracturing through intact rock could not be simulated (Lisjak and Grasselli, 2014).

The universal distinct element code (UDEC) and the three-dimensional distinct element code (3DEC) are the most representative commercial code of block-based DEM for two-dimensional and three-dimensional problems respectively. They have been widely used to simulate the wave propagation (Chen and Zhao, 1998, Cai and Zhao, 2000, Fan et al., 2004, Zhao et al., 2006, Lei et al., 2006, Zhao et al., 2008a, Zhao et al., 2008b, Deng et al., 2012, Zhu et al., 2013), rock failure (Kazerani and Zhao, 2010, Gu and Ozbay, 2014) (Figure 2.6), rock fragmentation (Gong et al., 2005, Gong et al., 2006a), stability of rock slope (Liu et al., 2014b, Francioni et al., 2014, Gischig et al., 2015), underground oil storage facility (Li et al., 2014a), and underground explosion (Deng et al., 2015). In addition to the public DEM codes mentioned above, some researchers also developed in-house codes for specific problems (Wang, 2009, Wang and Tonon, 2011, Tang, 2013, Jiang et al., 2014b, Deng et al., 2014).

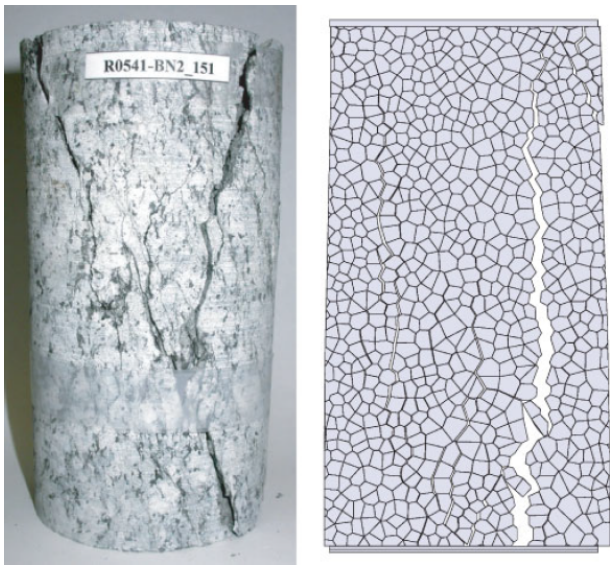

Figure 2.6 A granite failure in uniaxial compression test simulated by UDEC (Kazerani and Zhao, 2010)

In summary, a general difficulty in DEM simulation is the validation of micro-scale parameters. These parameters cannot be measured directly, but can only be determined through extensive calibrations based on experimentally measured macro-scale properties (usually the uniaxial compressive test simulation and Brazilian disk test simulation are adopted). This trial and error procedure can be complicated and tricky. In order to obtain

a more robust micro-scale contact model, many improvements to the model (Jiao et al., 2004, Kazerani et al., 2012, Kazerani, 2013, Kazerani and Zhao, 2014, Psakhie et al., 2014) and the calibration procedure (Fakhimi and Villegas, 2007, Ding et al., 2014) has been proposed.

2.2.2 Discontinuous Deformation Analysis

The discontinuous deformation analysis (DDA) method is an implicit discrete element method developed for the modelling of the static and dynamic behaviors of discrete block systems, originally proposed by Dr. Genhua Shi (Shi and Goodman, 1985, Shi and Goodman, 1989). DDA has been an open source project written by Dr. Shi since it was born.

The blocks in DDA is deformable and can be arbitrarily shaped. The kinematic constraints of no tension and no penetration between blocks can be imposed by a number of methods, including the penalty method, the Lagrange multiplier method and the augmented Lagrangian method. The frictional behavior along block interfaces is modelled by a Mohr-Coulomb criterion. Similar to FEM, the governing equations in DDA are represented by a global system of linear equations obtained by minimizing the total potential energy of the system. A global system of equations in matrix form needs to be formed and solved. Displacements and strains are taken as variables and the stiffness matrix of the model is assembled by differentiating several energy contributions, including block strain energies, contacts between blocks, displacement constraints and external loads. In standard DDA, each block is simply deformable with constant strain and stress fields. Improved models are achieved by introducing higher order strain fields or by subdividing each block into a set of simply deformable sub-blocks (Lin et al., 1996).

DDA has been widely used in the simulation of rock sliding (Hatzor et al., 2004, Wu et al., 2009, Wu, 2010, Ning and Zhao, 2013, Yang et al., 2014a, Jiao et al., 2014, Zhang et al., 2015b), rock fracturing (Kong and Liu, 2002, Bao and Zhao, 2013, Chen et al., 2013, Tian et al., 2014), rock blasting (Mortazavi and Katsabanis, 2001, Ning et al., 2011a, Ning et al., 2011b), rock fall (Sasaki et al., 2004, Wu et al., 2005), wave propagation in rock masses

(Jiao et al., 2007, Gu and Zhao, 2009), jointed rock masses (Lin et al., 1996, Tsesarsky and Talesnick, 2007, He and Zhang, 2015) (Figure 2.7), temperature-induced cracking process (Jiao et al., 2015b), masonry structures (Kamai and Hatzor, 2008, Jiang et al., 2014a), and the response of rockbolt (Nie et al., 2014).

Recent developments of DDA include a viscous boundary in DDA (Jiao et al., 2007), non-reflecting boundaries (Fu et al., 2015), the implementation of augmented Lagrangian method (Bao et al., 2014), a rock bolt element in DDA (Nie et al., 2014), a contact constitutive model for rock fragmentation (Jiao et al., 2012), a vertex-vertex contact algorithm (Fan and He, 2015), an edge-edge contact algorithm (Zhang et al., 2014b), the coupled NMM-DDA method (Miki et al., 2010), the DDD model based on DDA and RFPA (Gong and Tang, 2017), the nodal-based DDA (Bao and Zhao, 2013, Tian et al., 2014), a linear complementarity DDA procedure that avoids artificial parameters (Zheng and Li, 2015), a failure version of DDA that can simulate the whole process of rock failure (Zhu et al., 2014a, Jiao et al., 2015a), and a coupled hydro-mechanical model using DDA (Chen et al., 2013).

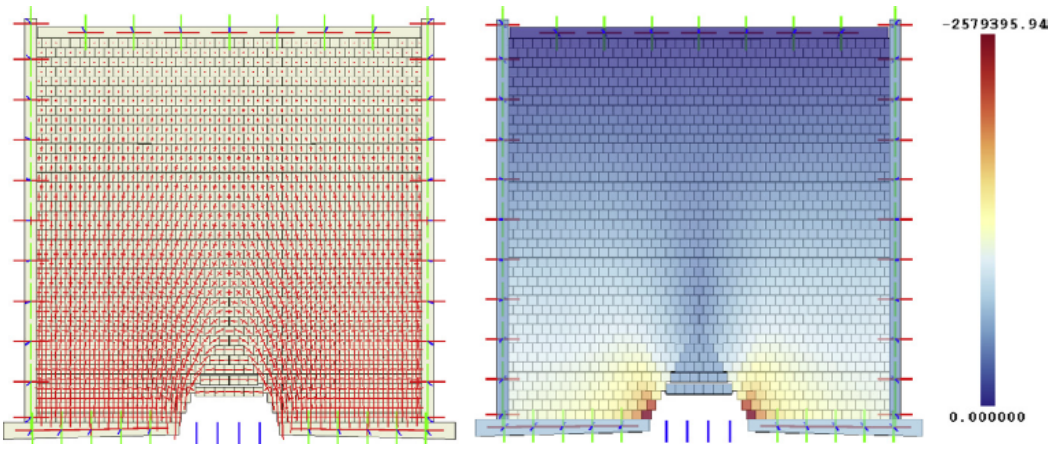

Figure 2.7 A study of arching mechanism to underground excavation in jointed rock mass using DDA: (a) principal stress vector after excavation; (b) contour of minor principle stress (He and Zhang, 2015)

In DDA, the equilibrium condition can be automatically satisfied for quasi-static problems, without using excessive iteration cycles which is necessary in DEM. Benefited from its implicit formulations, large time step can be adopted in DDA without inducing numerical instability. Besides, closed-form integrations for the block stiffness matrices can be performed without the need of numerical integration techniques. These advantages distinguished DDA from continuous methods and DEM. Therefore, DDA has emerged as an attractive model for rock dynamics. However, three drawbacks are still restricting the development of DDA. First, as a block-based method, the contact detection between a large number of arbitrarily shaped blocks can be complicated, especially in three-dimensional cases. Second, the condition of no tension and no penetration between blocks needs to be examined at every time step, after calculating the displacements of blocks. If the condition is found to be failed, contacts between blocks need to be modified and the displacements of blocks needs to be re-calculated until the condition is satisfied. This is the so-called "open-close iteration" procedure. As this procedure can be time-consuming or even endless in some situations, one needs to change the determined time step to get a better performance according to his experience. Last, in standard DDA, fractures cannot be driven into blocks so that discrete fracturing through intact rock cannot be simulated, which is the same as block-based DEMs.

2.2.3 Lattice Model

The lattice models (LMs) are also a family of numerical methods. Their common concept is based on the atomic lattice models originated from condensed matter physics. In these models, material is represented by a system of discrete units interacting via connecting elements. These discrete units are much coarser than atomic ones in practice and may represent larger volumes of heterogeneities such as clusters of grains. LMs simulate fractures by either simply removing connecting elements that exceed the strength limit or successively degrading their mechanical properties according to cohesive laws.

The most representative method in this family is the lattice spring model (LSM). It was originally developed by Hrennikoff (1941) to solve continuum elasticity problems. The classical LSM can only solve the problems with a fixed Poisson's ratio, namely 1/3 in two-

dimensional plane-stress cases and 1/4 in three-dimensional cases. Due to this limitation, LSM had stayed underdeveloped for a long time. Recently, due to its suitability for fracturing simulations of solids, many researchers have renewed their interest in this method (Darve and Nicot, 2005, Holeček and Moravec, 2006, Wang et al., 2009, Hahn et al., 2010, Cui et al., 2011, Zhao and Zhao, 2012).

The distinct lattice spring model (DLSM) (Zhao, 2010) is a newly developed branch of LSM. In DLSM, the restriction on the Poisson's ratio is successfully removed through a technique to evaluate spring deformations using the local strain rather than the particle displacements. DLSM has been applied to simulate the stress wave propagation in rock masses (Zhu et al., 2011, Zhao, 2014b), rock fracturing (Jiang et al., 2017) (Figure 2.8), rock behaviors under different loading rates (Gong and Zhao, 2014, Zhao et al., 2014a), response of impaction (Zhao et al., 2013b), and jointed rock masses (Zhao, 2015). Recent developments of DLSM include coupling with NMM to simulate the dynamic failure of rock masses (Zhao et al., 2012), large deformation analysis (Zhao, 2014a), parallelization (Zhao and Khalili, 2012, Zhao et al., 2013a), and a four-dimensional LSM (Zhao, 2017).

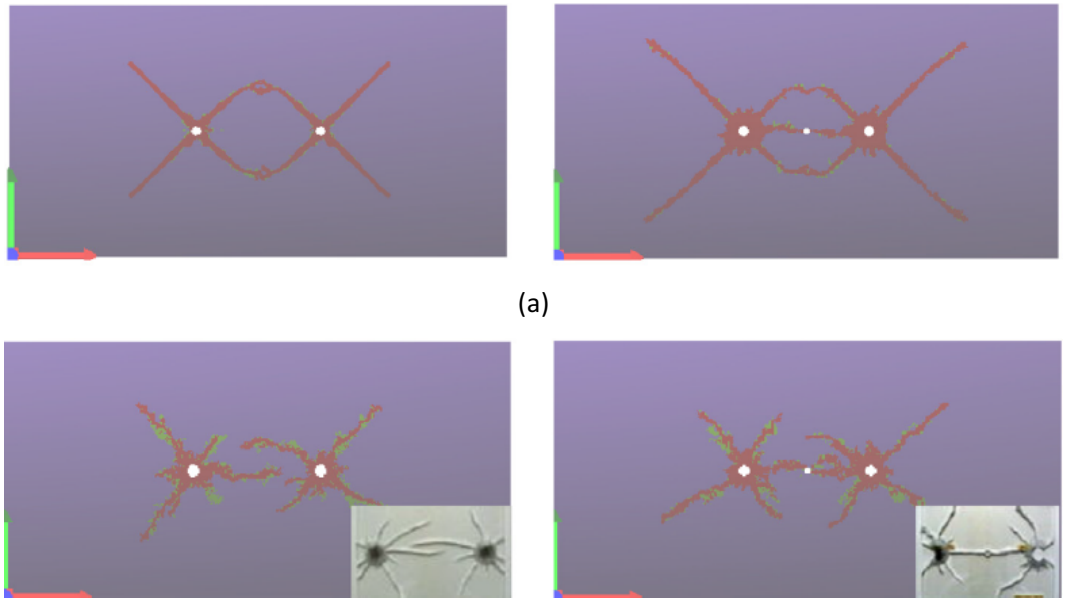

(a)

(b)

Figure 2.8 Crack propagation on PMMA plates simulated by DLSM: (a) homogeneous plates; (b) inhomogeneous plates

2.3 Coupled Methods

The characteristics of a specific scientific or engineering issue should be taken into consideration when choosing from continuous and discontinuous methods. In general, continuous methods are good at the stress analysis in pre-failure stage, whereas discontinuous methods are good at the motion analysis in post-failure stage. Some work has also been done to avoid the disadvantages of each type by combining continuous and discontinuous methods. This type of method is called the coupled (or hybrid) method. There are two ways to combine the continuous and discontinuous method. A straightforward way is to explicitly adopt two different numerical methods, one continuous method and one discontinuous method in most cases, for the simulation. Each numerical method is applied on its own domain, and a consistent condition is imposed on the common domain to connect two methods. Another way is to implicitly combine the continuous and discontinuous method, developing a new method that presents the characteristics of both methods.

2.3.1 Numerical Manifold Method

The numerical manifold method (NMM) is originally proposed by Dr. Genhua Shi through a series of conference papers (Shi, 1991, Shi, 1992, Shi, 1995, Shi, 1997). NMM provides a framework to unify continuous and discrete methods by implicitly combining FEM and DDA. Two cover systems are adopted in NMM, namely the mathematical cover and the physical cover. NMM is derived based on the finite cover approximation theory and is named after the mathematical notion of manifolds. NMM uses truncated discontinuous shape functions to simulate the fractures and treat the continuum bodies, fractured bodies, and assemblage of discrete blocks in a unified form. NMM allows arbitrary boundaries and internal physical features in the physical domain without meshes conforming to them. Therefore, the meshing task in NMM is greatly simplified and fracturing process can be modelled without remeshing. NMM simulates fractures simply by splitting physical covers that are completely separated by the fractures into several separate covers and assigning each cover an independent local function. Complex cracks with arbitrary number of branches are modelled in an exactly way as the modelling of a single crack. NMM implements a novel simplex integration method proposed by Dr. Shi

for both NMM and DDA (Shi, 1996). This integration method is able to conveniently evaluate the weak form integration over elements intersected by internal discontinuities and/or external boundaries, without the need of element partitioning like what XFEM does. Another distinct feature of NMM is that the frictional contact condition between the two sides of a crack or two discrete blocks can be accurately satisfied, due to the contact logic in NMM.

Ma et al. (2010) prove that FEM is a special case of NMM when following conditions are satisfied: (1) mathematical covers in NMM are generated from a finite element mesh; (2) weight functions defined on mathematical covers are finite element shape functions; (3) cover functions defined on physical covers are constants, and (4) physical features including internal discontinuities (e.g., cracks and material interfaces) and external boundaries do not intersect manifold elements. Meanwhile, as NMM is developed based on DDA, it preserves all the characteristics of discrete element modelling, such as the kinematics constraints and contact detection and modelling. The number of degrees of freedom (DOFs) in NMM is usually much higher than that of DDA as there are more than one manifold elements in each block in most cases. The benefit at this cost is that NMM provides a more accurate displacement and stress field in blocks than DAA. It can be concluded that if every discrete block is a single manifold element with linear displacement field, NMM will degenerate into DAA exactly.

In the original version of NMM developed by Dr. Shi, the simplest triangular manifold element with constant cover function is adopted for two dimensional issues, lacking the criteria for crack initiation and propagation. Since then, various developments as well as applications have been made in the past decades. Shyu and Salami (1995) implemented quadrilateral isoparametric elements in NMM. Chiou et al. (2002) studied the mixed mode fracture propagation by combining NMM with the virtual crack extension method. Cheng et al. (2002) incorporated Wilson elements into NMM to increase the accuracy of quadrilateral covers. Chen et al. (1998) proposed NMM with high-order cover functions, and later Su et al. (2003) developed a subroutine in the commercial software Mathematica to derive expressions for high-order NMM automatically. Lin et al. (2005)

developed the formulations of three dimensional NMM with high-order cover functions and proposed a fast simplex integration method based on special matrix operations, without considering the linear dependence problem. He and Ma (2010) proposed a three-dimensional NMM based on tetrahedron elements. Terada et al. (2003) introduced the finite cover method as an alias of NMM. Su and Xie (2005) proposed an Eulerian NMM for large deformation. Zhang et al. (2009) compared the accuracy of rectangular and triangular mathematical elements under different circumstances. An et al. (2011) investigated the linear dependence problem of NMM approximation space using finite element covers and polynomial local functions at both elemental and global level. For the sake of fracture simulation, Li and Cheng (2005) developed an enriched meshless manifold method for two dimensional crack modelling. Ma et al. (2009), Zhang et al. (2010), and An (2010) incorporated the enriched functions of XFEM/GFEM into standard NMM to simulate complex cracks.

Recently, NMM has been greatly improved and widely applied. He et al. (2014) customized a hierarchical contact algorithm for NMM in three-dimension. Cai et al. (2013) proposed a generalized and efficient covers generation procedure, which is applicable for dealing with interfaces, inclusions, and discontinuities with complex geometry. Zheng and Xu (2014) proposed strategies for several specific issues that NMM may encounter in the simulation of crack propagation, including the rank deficiency induced by high-order cover functions, the integrals with singularity of 1/r, and kinked cracks. Yang et al. (2014b) refined the mathematical covers near crack tips. Qu et al. (2014) proposed an explicit time integration algorithm for NMM. Zhao et al. (2014b) improved the performance of NMM in the simulation of stress wave propagation in rock masses by incorporating the Newmark system equations, edge-to-edge contact scheme, and non-reflection boundary condition. Wu and Fan (2014) developed a time-dependent absorbing boundary condition for wave propagation problems. Wong and Wu implemented NMM and studied the process of rock fracturing in many different circumstances (Wu et al., 2013, Wu and Wong, 2013a, Wu and Wong, 2013b, Wong and Wu, 2014, Wu and Wong, 2014) (Figure 2.9). Ning et al. (2011c), Zheng et al. (2014), and An et al. (2014) analyzed the stability of rock slopes with two-dimensional NMM, while He et al. (2013) extended the analysis to three-dimension (Figure 2.10). Zhao et al. (2012) coupled NMM with DLSM to simulate the

dynamic failure of rock masses. Zhang et al. (2014a) study the thermo-mechanical behavior of fractures in planar solids. Chen and Li (2015) improved the generation of manifold elements to bypass the overlapping procedure of irregular and complicated physical covers.

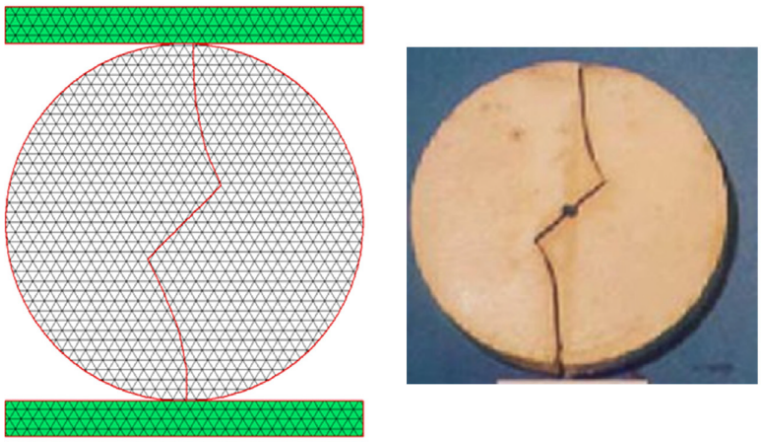

Figure 2.9 Failure of Brazilian tensile disc test in pre-fractured specimen simulated by 2D NMM (Wong and Wu, 2014)

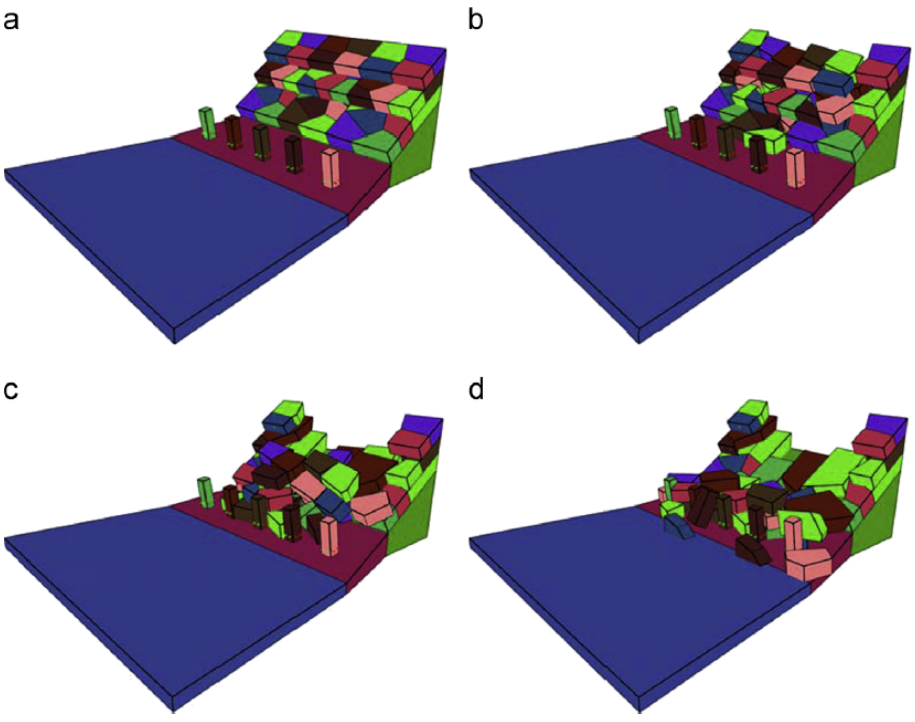

Figure 2.10 Road protection from rock slope failure simulated by 3D NMM (He et al., 2013)

NMM has been a promising numerical method for rock mechanics in recent years, due to its great advantages in theory for continua-discontinua analysis. However, as a block-based model, its geometrical and topological operations, as well as the contact detection and operation, could be quite complicated, especially in three-dimensional cases. Furthermore, NMM is generally suitable for the analysis at macroscopic scale, but not at microscopic scale.

2.3.2 Finite-Discrete Element Method

The finite-discrete element method (FDEM), also known as the coupled finite discrete element method, is another continua-discontinua method for rock mechanics, originally proposed by Munjiza (2004). FDEM blends FEM with DEM, but it should not be confused with the explicitly coupled FEM/DEM method, which represents the far-field and near-field through FEM and DEM respectively. Two representative code of FDEM are ELFEN (Klerck, 2000) and Y-Geo (Mahabadi et al., 2012a).

FDEM discretize the simulation domain into blocks as a DEM first. Then, every block is treated as a FEM domain and is further discretized using a finite element mesh. In calculation, the DEM concept is used to detect contacts and to deal with interactions between blocks, while FEM techniques are adopted for the computation of internal forces and the initiation of new fractures.

FDEM allows new fractures to be initiated within and to completely cut through blocks. The insertion of a new fracture can be accomplished using two algorithms, namely the intra-element method and the inter-element method. The intra-element insertion drives a new fracture along its direction of propagation by simply splitting the finite elements. In this case, a local adaptive remeshing may be necessary to achieve an element topology and avoid highly-skewed sliver elements that could decrease the numerical stability. In the inter-element method, a new fracture is turned to the existing element boundary most favorably oriented with respect to the direction of propagation.

Recent applications of FDEM in rock mechanics include underground excavation (Lisjak et al., 2015) (Figure 2.11), the acoustic emission in brittle rocks (Lisjak et al., 2013), the simulation of the split Hopkinson pressure bar (Rougier et al., 2014), the failure of Brazilian disks (Mahabadi et al., 2010, Mahabadi et al., 2012b, Cai, 2013), naturally fractured pillars (Elmo and Stead, 2010), open pit slopes (Vyazmensky et al., 2010), and underground excavations (Lisjak et al., 2014).

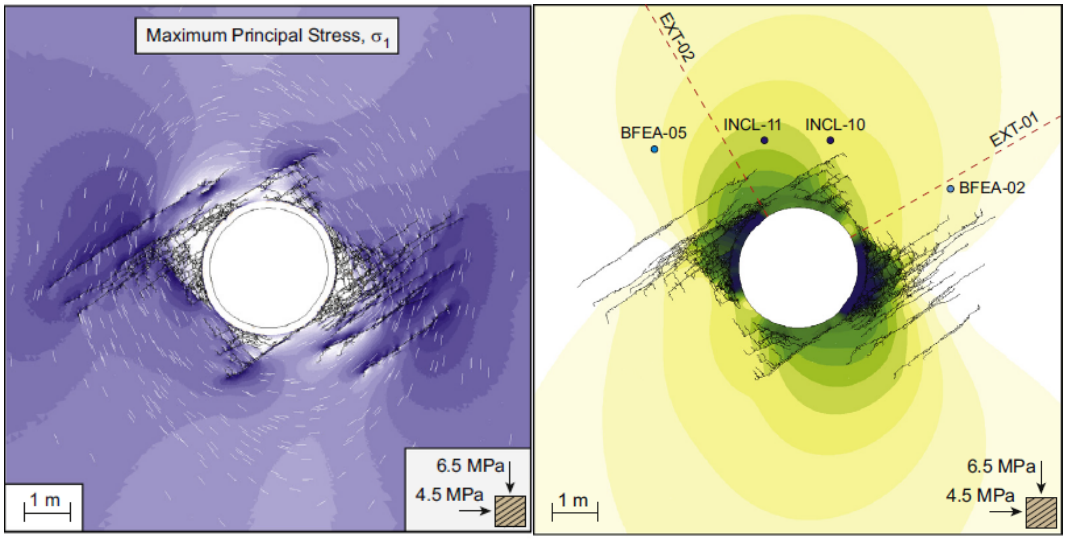

(a) (b)

Figure 2.11 Fractures around a circular tunnel simulated by FDEM: (a) contour of maximum principal stress; (b) contour of displacement (Lisjak et al., 2015)

A major drawback of FDEM is that it is as inflexible as FEM in dealing with cracks. As it is usually impossible to predict the position of initiated fractures and their propagation directions prior to the simulation, all blocks in FDEM need to be decently discretized. This fact leads to a grand number of finite elements in most cases. Therefore, FDEM is always computationally expensive, especially in the simulation of rock engineering issues. Besides, a group of micro parameters need to be determined in FDEM for each simulation, most of which cannot be directly measured via laboratory tests and therefore must be estimated via calibration procedures (Tatone and Grasselli, 2015).

2.4 Comparisons and Challenges

The FEM, DEM and NMM are chosen as three typical numerical methods in the field of rock mechanics in this section, due to their wide application. Together with the XFEM, these four models are compared in Table 2.1.

Table 2.1 A comparison of FEM, XFEM, DEM and NMM for their performance in rock dynamics

	FEM	**XFEM**	**DEM**	**NMM**
Fundamental theory	Principle of minimum potential energy	• Principle of minimum potential energy • Partition of unity • Fracture mechanics	• Newton's second law (on particles) • Force-displacement law (at contacts)	• Principle of minimum potential energy • Partition of Unity • Mathematical manifold
Basic component	Finite element	Finite element	Particle/Block	Manifold Element
Interpolating function	Element shape function	• FEM shape function • Heaviside function • Asymptotic near-tip functions	None	• Cover function • Weight function • Asymptotic near-tip functions (optional)
Numerical integration	Gaussian quadrature	• Gaussian quadrature • Generation of subdomains along cracks	None	• Simplex integration • Gaussian quadrature in the subdomains along cracks
Fracture representation	Element separation (assisted by cohesive element insertion) or Element degradation (implicit representation)	Natural and explicit representation	Bonds breakage and particles/blocks separation	Natural and explicit representation
Fracture propagation path	Along the edge of finite elements (assisted by cohesive element) or along the finite elements (element degradation)	Across the finite elements	Along the edge of adjacent particles/blocks	Across the manifold elements
Complete detachment simulation	Not easy	Not easy	Natural	Natural

Contact pair	Polygon-Polygon	Polygon-Polygon	Particle-Particle / Polygon-Polygon	Polygon-Polygon
Contact position	On contact surface	On contact surface	On contact surface and within continua	On contact surface
Contact implementation	• Contact mechanics • Numerical constraint technique (e.g., penalty method, Lagrange multiplier method, augmented Lagrange method)	• Contact mechanics • Numerical constraint technique (e.g., penalty method, Lagrange multiplier method, augmented Lagrange method)	• Two parts of contact forces: 1) Grain-based portion (particle overlap, including normal force, shear force and friction); 2) Cement-based portion (parallel bond, including normal force, shear force and moment) • Microscopic parameters must be determined through a series of validation procedure to reproduce typical macroscopic behavior	• Normal and shear forces • Normal contact stiffness is related to the Young's modulus of blocks; Shear contact stiffness is related to the normal stiffness • Open-close iteration (a trial-and-error procedure to ensure the non-penetration condition)
Trial-and-error procedure	Unnecessary	Unnecessary	Essential (to determine micro parameters)	Essential (to prevent block penetration)
Typical code	• Abaqus • ANSYS	• Abaqus • Code by Dr. Philip Moseley	• PFC • UDEC • 3DEC	• open-source project by Dr. Genhua Shi

Generally, FEM and XFEM are not flexible enough in dealing with rock masses complete detachment and the post-failure behavior, which greatly limits their application in rock dynamics. DEM properly simulates the microstructure of rock materials but is somewhat inefficient to simulate the macroscopic behaviors of massive rock masses, while the NMM has an opposite character. As for contact, DEM and NMM encounter quite different difficulties. Contact is the dominating force in DEM, which is defined on each pair of neighboring elements (particle or block). For large scale analysis, the number of contact pairs could be very large. In NMM, the contact is only defined between discrete bodies, instead of it basic computational components. Therefore, the number of contact pairs in NMM could be rapidly reduced when comparing to DEM. However, since NMM is a block-

based method, the contact detection and operation is conducted on polygons, which could be complicated and time consuming, especially in three-dimensional cases.

In conclusion, NMM, as a promising numerical method for rock dynamics, meets following challenges:

- Inefficient to simulate the microstructure of rock materials;
- Difficult to study the heterogeneity of rock materials;
- Inefficient to capture mechanical responses at microscopic scale;
- Contact operation could be simplified.

The work in this thesis is inspired by limitations of existing numerical methods in simulating rock materials and rock engineering problems, especially the challenges of NMM listed above. The aim of this research is to propose a novel numerical method for rock dynamics based on NMM by overcoming its essential disadvantages. The outcome of this thesis is to provide a potentially ideal numerical tool for rock dynamics. The proposed method is supposed to meet the unique requirements raised by the complexity of rock materials and rock engineering problems.

Chapter 3 Particle-based Numerical Manifold Method (PNMM)

PNMM is developed from the Particle Manifold Method (Sun et al., 2013) and Numerical Manifold Method (Shi, 1991, Ma et al., 2010). It is proposed by introducing the particle concept into NMM. The purpose of this development is primarily to simplify the geometrical Boolean operation and contact operation in NMM. Same as NMM, PNMM is inherently a continuum-discontinuum numerical model, providing a unified analysis framework for both pre- and post-failure behaviors. PNMM is flexible in considering the heterogeneity of rock materials and simulating the initiation and propagation of fractures, which separates it from NMM. PNMM inherits the most distinct characteristics of NMM, i.e., the mathematical covers and physical covers, but also utilizes a group of particles to form an extra level of discretization.

This chapter presents the conception, formulations, basic components, and the implementation of PNMM in detail. First, the dual-layer-cover system and dual-level discretization are introduced respectively to provide the foundation and character of PNMM. Then, the necessary mathematical formulae and their numerical implementation are given. The basic components, including particles, links, failure description, and contact accumulation, are introduced. The failure criterion adopted in PNMM is given. Last, the implementation of PNMM is summarized.

This chapter is based on a paper published in the journal International Journal of Geomechanics:

Li, X., Zhang, Q. B., He, L., Zhao, J., 2017. Particle-Based Numerical Manifold Method to Model Dynamic Fracture Process in Rock Blasting. *International Journal of Geomechanics*. 17 (5), E4016014.

3.1 The Dual-layer-cover System

The most distinct characteristics of NMM is its cover system. PNMM adopts a same dual-cover system as NMM, namely the mathematical cover system and the physical cover system.

The first layer is the mathematical cover system. It is independent of the shape of modelling domains but has to cover all the space the modelling domain may occupy. The mathematical cover system is usually generated from a uniform triangular or quadrangular FEM mesh, from which the finite elements that share a same node form a mathematical cover. It is common to find mathematical covers overlapped. The mathematical cover systems with different geometric patterns can be generated from several kinds of typical FEM mesh, as illustrated in Figure 3.1. The pattern of mathematical cover system is supposed to have a slight influence on simulation results (Zhang et al., 2009).

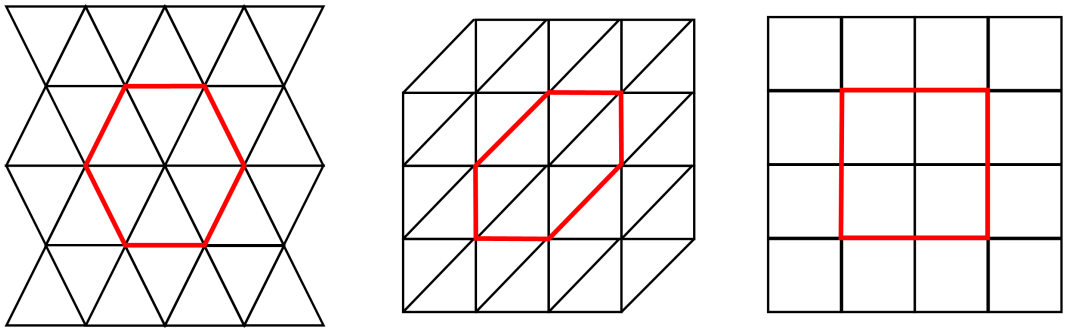

Figure 3.1 Typical patterns of the mathematical cover

The second layer is the physical cover system. A physical cover is the intersection of a mathematical cover and the modeling domain. The physical cover system is to connect the uniform mathematical cover system with the arbitrary modeling domain. The overlap of neighboring physical covers is called a manifold element. A manifold element is the basic computation unit in both NMM and PNMM.

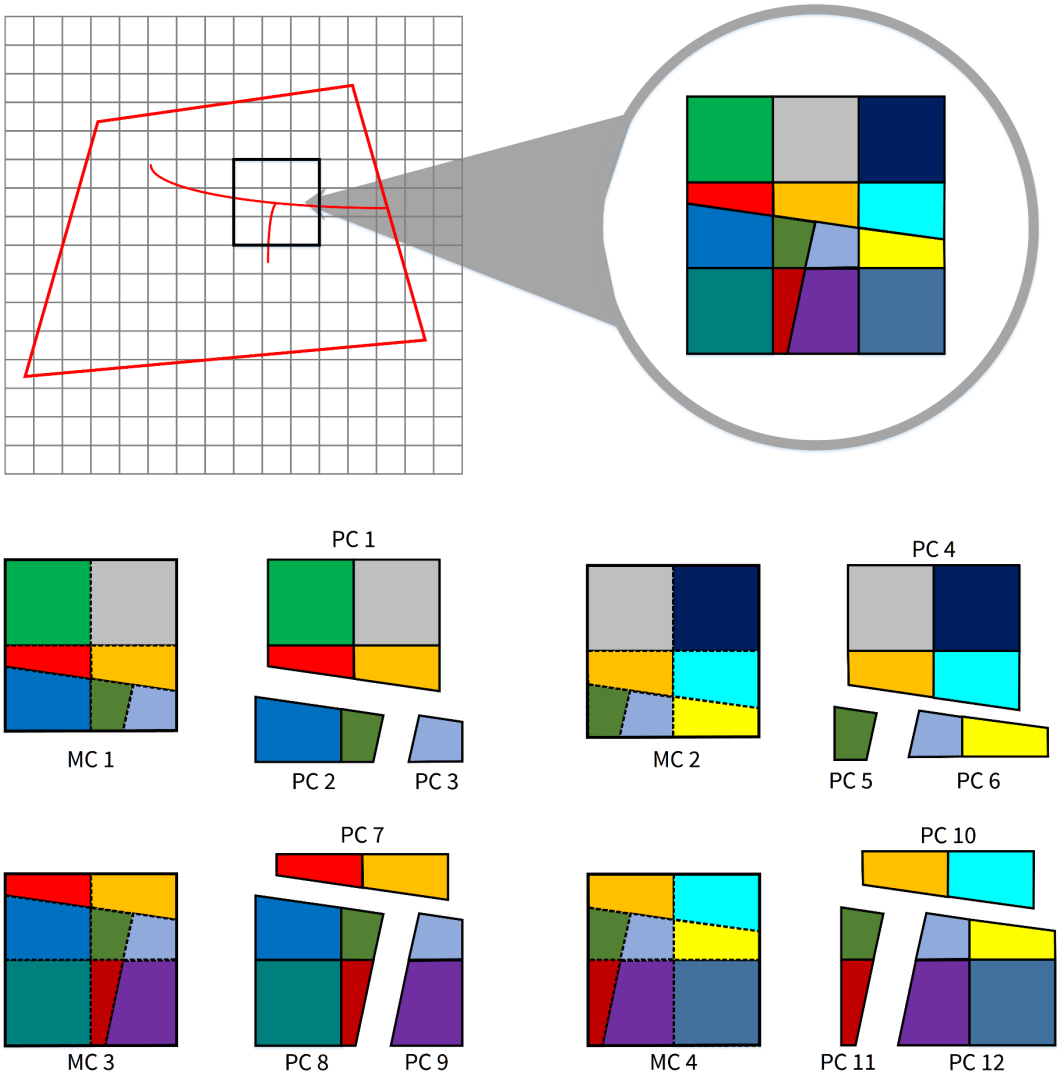

Figure 3.2 The mathematical cover (MC) and physical cover (PC) around a branched crack

An apparent advantage of the dual-layer-cover system is that multiple cracks and the crack with complex geometry can be flexibly handled. Discontinuities (e.g., cracks, joints, material interfaces, holes) within the modelling domain will interact with mathematical covers to form extra physical covers. A modelling domain that contains a branched crack is taken as an example in Figure 3.2. Around the intersection of two branches of the crack, 4 mathematical covers are separated into 12 physical covers. The common domain of these 12 physical covers will generate 14 manifold elements in total. In the case where the branched crack does not exist, only 9 manifold elements will be generated in the same domain. Obviously, more cracks will generate more physical covers and therefore more

manifold elements. By increasing the number of manifold elements, on which the DOFs are defined, PNMM naturally simulates internal discontinuities in a similar way to NMM.

3.2 The Dual-level Discretization

The basic idea of PNMM is to represent the microstructure of rock materials with a group of particles and to simulate the macroscopic behavior of rock masses through polygonal elements. In a representative example shown in Figure 3.3, a block of rock (modeling domain) is discretized into manifold elements in the first discretization. Then, in the second discretization, each manifold element is further discretized into a group of internal particles.

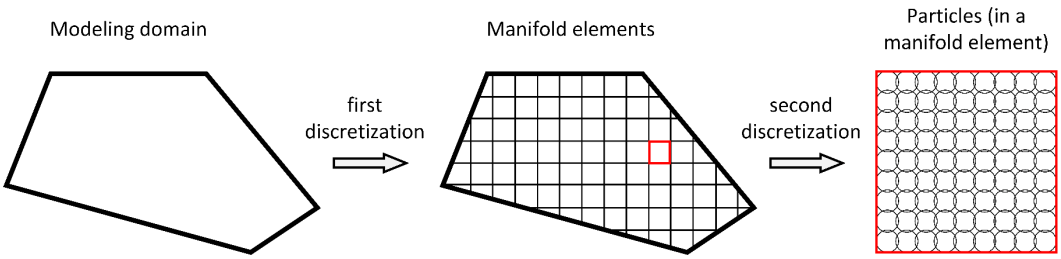

Figure 3.3 The dual-level discretization in PNMM

The first discretization is the result of the dual-layer-cover system. Manifold elements are generated in this process. This discretization reduces the infinite DOF of a continuum to finite DOFs of manifold elements. However, the second discretization does not further affect the number of DOF of the model. That is to say, the DOFs of the model are defined on manifold elements rather than internal particles. In calculation, mechanical responses of manifold elements are solved prior to particles. Then, the behavior of each internal particle is simply derived from the mechanical fields of its governing element. In such a way, the dual-level discretization enables PNMM to simulate the microstructure of rock materials without rapidly increasing the DOF of the model.

The generation of particles is conducted in each polygonal element. For regular-shaped elements (e.g., squares, rectangles, equilateral triangles, and isosceles triangle), particles can be distributed evenly. The number of particles is determined by the accuracy requirement, represented by a setting parameter given by the user. In such circumstance, the area of each particle is the same and the sum of their areas equals the area of the element.

For general-shaped elements, an inner mesh needs to be generated in the second discretization. This procedure is efficiently conducted by incorporating the computational geometry algorithms library (CGAL). CGAL is a software project that provides easy access to efficient and reliable geometric algorithms in the form of a C++ library. It is used in various areas needing geometric computation, such as geographic information systems, computer aided design, molecular biology, medical imaging, computer graphics, and robotics. The 2D Triangulation function in this library is executed by PNMM. The adopted function divides a polygonal element into inner triangular elements, without the need of any seed point. Then, one particle is generated in each inner element. The center of the particle is the centroid of the inner element. The area of the particle is equal to the area of the inner element. In such a way, the sum of particle areas remains equal to the area of the polygonal element.

In both schemes for the generation of particles, it always need to calculate the area and centroid of a polygon in variety of shapes. This is conducted by a subroutine in PNMM, as follow

$$A = \frac{1}{2}\left|\sum_{i=0}^{n-1}(x_i y_{i+1} - x_{i+1} y_i)\right|, \quad \text{with } (x_n, y_n) = (x_0, y_0) \tag{1}$$

$$\begin{cases} C_x = \dfrac{1}{6A}\displaystyle\sum_{i=0}^{n-1}(x_i + x_{i+1})(x_i y_{i+1} - x_{i+1} y_i) \\ C_y = \dfrac{1}{6A}\displaystyle\sum_{i=0}^{n-1}(y_i + y_{i+1})(x_i y_{i+1} - x_{i+1} y_i) \end{cases} \tag{2}$$

where A is the area of the polygon, n is the number of vertices, x_i and y_i are the coordinates of the ith vertex, C_x and C_y are the coordinates of the centroid.

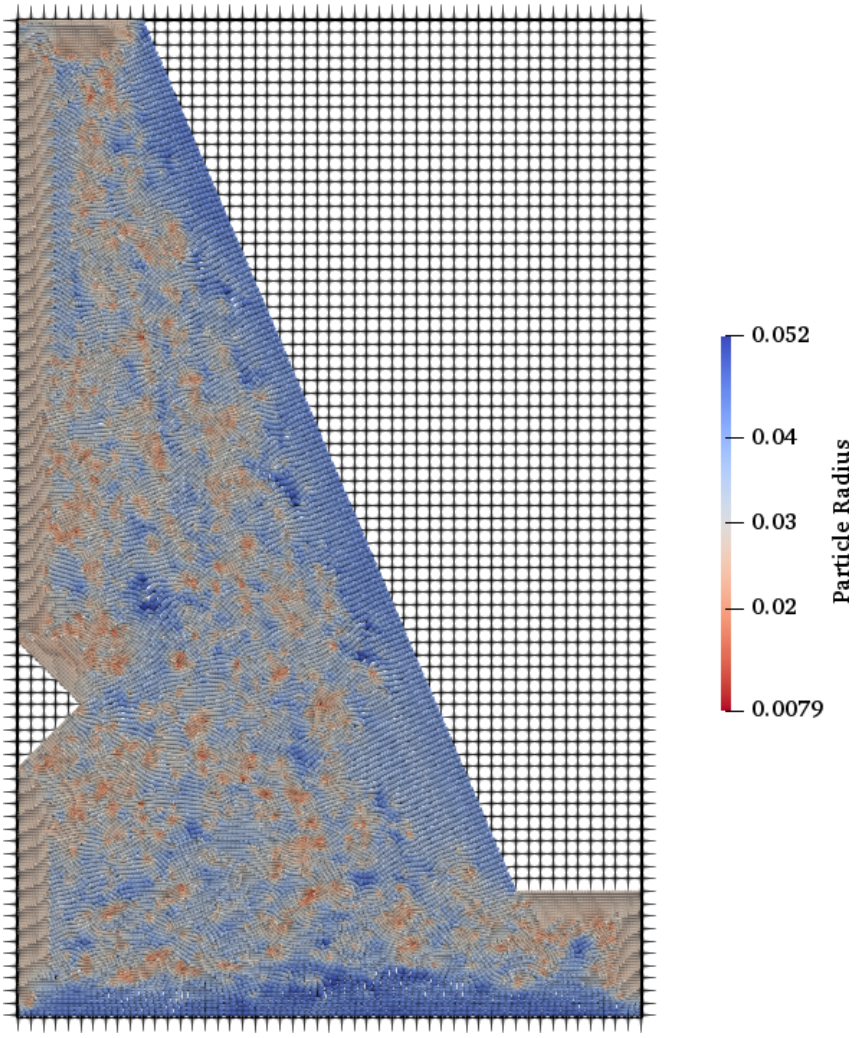

(a)

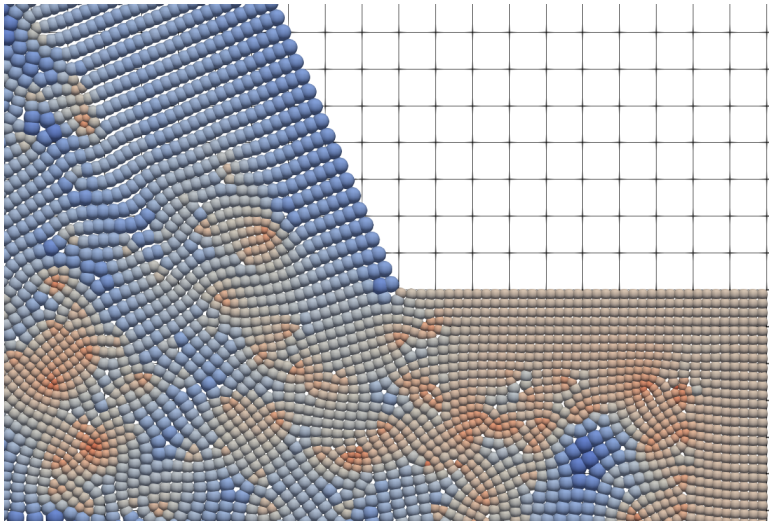

(b)

Figure 3.4 An example of the particles in PNMM: (a) a slope; (b) an enlarged view

In practice, the second scheme is adopted in most cases. Therefore, particles in PNMM are usually assigned with varying diameters. Due to the limitation of geometry, particles naturally overlap each other to ensure the conservation of mass, as they are carrying a realistic density.

A practical example of the dual-level discretization is shown in Figure 3.4. The mathematical cover in quadrangular pattern and particles discretization of a rock slope is presented. The height of the slope is 16 m, the width of slope is 10 m. The radius of particles varies from 0.0079 to 0.052 m.

3.3 Formulation Inherited from NMM

PNMM inherits most basic formulae from NMM.

3.3.1 Local Approximation

On each mathematical cover M_i, a cover function is independently defined, representing the local approximation, as

$$\mathbf{u}_i = \sum_{j=1}^{n} \mathbf{T}_{ij}(x)\mathbf{d}_{ij} = \mathbf{T}\mathbf{d}_i \tag{3}$$

where $\mathbf{u}_i$ is the cover function on the ith mathematical cover, n is the number of DOFs, $\mathbf{T}$ is the basis of the cover function, and $\mathbf{d}_i$ is the vector of DOFs. Although a constant cover function is usually adopted in the standard NMM, considering the fact that there are usually 10^1~10^3 particles within a mathematical cover in PNMM, the linear or quadric cover function should be adopted. In two-dimensional cases, they can be expressed in matrix form respectively as

$$\mathbf{u}_i = \begin{bmatrix} 1 & x & y \\ & 1 & x & y \end{bmatrix} [d_1 \quad \dots \quad d_6]^T \tag{4}$$

$$\mathbf{u}_i = \begin{bmatrix} 1 & x & y & x^2 & y^2 & xy \\ & 1 & x & y & x^2 & y^2 & xy \end{bmatrix} [d_1 \quad \dots \quad d_{12}]^T \tag{5}$$

The primary issue when using higher degree polynomials as the cover function is the rank deficiency of the stiffness matrix. To tackle this issue, Lin (2003) has suggested to exclude some monomials from the complete higher degree cover functions. Recently, An et al. (2011) proposed an approach to predict the rank deficiency and found that the rank deficiency is unrelated to the nullity of the stiffness matrix. Fan et al. (2017) proposed a novel NMM with derivative DOFs to eliminate the linear dependence. Some other effort on this topic can also be found in (Ghasemzadeh et al., 2014, Zheng and Xu, 2014).

Cover functions of different physical covers then are combined together to form the local approximation for a manifold element. This combination is conducted by the weight function φ_i, which satisfies

$$\sum_i \varphi_i(\mathbf{x}) = 1 \quad \text{and} \quad \begin{cases} \varphi_i(\mathbf{x}) \geq 0, & \forall \mathbf{x} \in P_i \\ \varphi_i(\mathbf{x}) = 0, & \forall \mathbf{x} \notin P_i \end{cases} \tag{6}$$

where P_i is the ith physical cover. The term weight function is originally used by Shi (1992). However, Lin (2003) reported that the term has been used ambiguously since then, and demonstrated that NMM is similar to meshless methods by clarifying the weight function from the partition of unity's perspective. After that, this function is also called a PU function in some literature (Ma et al., 2010).

A convenient way for constructing the weight function is to use the element shape functions in FEM. Specifically, for the mathematical cover in type A and type B, three weight functions on a triangular physical cover is the FEM shape functions in a triangular element, which can be expressed as

$$\begin{bmatrix} \varphi_1 \\ \varphi_2 \\ \varphi_3 \end{bmatrix} = \frac{1}{det(\Delta)} \begin{bmatrix} A_{11} & -A_{12} & A_{13} \\ -A_{21} & A_{22} & -A_{23} \\ A_{31} & -A_{32} & A_{33} \end{bmatrix} \begin{bmatrix} 1 \\ x \\ y \end{bmatrix} \tag{7}$$

with

$$\Delta = \begin{bmatrix} 1 & x_1 & y_1 \\ 1 & x_2 & y_2 \\ 1 & x_3 & y_3 \end{bmatrix} \tag{8}$$

where x_i and y_i are the coordinates of the triangular physical cover, and $\boldsymbol{A}_{ij}$ is the minor of matrix Δ. Hence, we have

$$\begin{cases} \varphi_1 = \dfrac{1}{det(\Delta)}(A_{11} - A_{12}x + A_{13}y) \\ \varphi_2 = \dfrac{1}{det(\Delta)}(-A_{21} + A_{22}x - A_{23}y) \\ \varphi_3 = \dfrac{1}{det(\Delta)}(A_{31} - A_{32}x + A_{33}y) \end{cases} \tag{9}$$

and

$$\begin{cases} \dfrac{\partial \varphi_1}{\partial x} = -\dfrac{A_{12}}{det(\Delta)} \\ \dfrac{\partial \varphi_1}{\partial y} = \dfrac{A_{13}}{det(\Delta)} \end{cases}, \begin{cases} \dfrac{\partial \varphi_2}{\partial x} = \dfrac{A_{22}}{det(\Delta)} \\ \dfrac{\partial \varphi_2}{\partial y} = -\dfrac{A_{23}}{det(\Delta)} \end{cases}, \begin{cases} \dfrac{\partial \varphi_3}{\partial x} = -\dfrac{A_{32}}{det(\Delta)} \\ \dfrac{\partial \varphi_3}{\partial y} = \dfrac{A_{33}}{det(\Delta)} \end{cases} \tag{10}$$

For the type C mathematical cover, four weight functions on a quadrangular physical cover is the FEM shape functions in a quadrangular element, which can be expressed as

$$\begin{cases} \varphi_1 = \dfrac{x - x_2}{x_1 - x_2} \cdot \dfrac{y - y_4}{y_1 - y_4} \\ \varphi_2 = \dfrac{x - x_1}{x_2 - x_1} \cdot \dfrac{y - y_3}{y_2 - y_3} \\ \varphi_3 = \dfrac{x - x_4}{x_3 - x_4} \cdot \dfrac{y - y_2}{y_3 - y_2} \\ \varphi_4 = \dfrac{x - x_3}{x_4 - x_3} \cdot \dfrac{y - y_1}{y_4 - y_1} \end{cases} \tag{11}$$

In this case, we have

$$\begin{cases} \dfrac{\partial \varphi_1}{\partial x} = \dfrac{1}{x_1 - x_2} \cdot \dfrac{y - y_4}{y_1 - y_4} \\ \dfrac{\partial \varphi_1}{\partial y} = \dfrac{x - x_2}{x_1 - x_2} \cdot \dfrac{1}{y_1 - y_4} \end{cases}, \begin{cases} \dfrac{\partial \varphi_2}{\partial x} = \dfrac{1}{x_2 - x_1} \cdot \dfrac{y - y_3}{y_2 - y_3} \\ \dfrac{\partial \varphi_2}{\partial y} = \dfrac{x - x_1}{x_2 - x_1} \cdot \dfrac{1}{y_2 - y_3} \end{cases}$$
$$\begin{cases} \dfrac{\partial \varphi_3}{\partial x} = \dfrac{1}{x_3 - x_4} \cdot \dfrac{y - y_2}{y_3 - y_2} \\ \dfrac{\partial \varphi_3}{\partial y} = \dfrac{x - x_4}{x_3 - x_4} \cdot \dfrac{1}{y_3 - y_2} \end{cases}, \begin{cases} \dfrac{\partial \varphi_4}{\partial x} = \dfrac{1}{x_4 - x_3} \cdot \dfrac{y - y_1}{y_4 - y_1} \\ \dfrac{\partial \varphi_4}{\partial y} = \dfrac{x - x_3}{x_4 - x_3} \cdot \dfrac{1}{y_4 - y_1} \end{cases} \tag{12}$$

Using the weight function to combine the cover functions of related physical covers, the displacement field of a manifold element is finally taken as,

$$\mathbf{u}_e(\mathbf{x}) = \sum_{i=1}^{m} \varphi_i(\mathbf{x})\mathbf{u}_i(\mathbf{x}) = \sum_{i=1}^{m} \mathbf{N}_i(\mathbf{x})\mathbf{d}_i = \mathbf{N}_e\mathbf{d}_e \tag{13}$$

where *m* indicates the number of physical covers.

3.3.2 Equations in Matrix Form

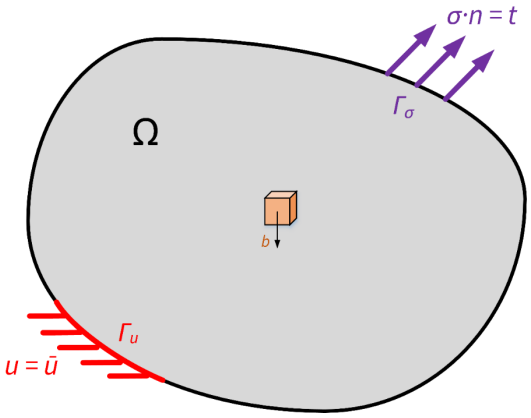

Figure 3.5 A typical continuum problem, subjected to Neumann and Dirichlet boundaries

The governing equation for the displacement field of the continuum illustrated in Figure 3.5 is,

$$\begin{cases} \nabla\sigma + b = \rho\ddot{u} \\ u = \bar{u} \quad \text{on } \Gamma_u \\ \sigma \cdot n = t \quad \text{on } \Gamma_\sigma \end{cases} \tag{14}$$

where σ is the Cauchy stress tensor, b is the body force per unit volume, ρ is the density, and $\ddot{u}$ is the acceleration tensor.

PNMM has the same theoretical foundation as NMM. The linear elastic constitutive model is adopted for general cases. Coupling the governing equation with constitutive equations, strain-displacement equations and the space discretization, the potential energy of the continuum can be obtained. By minimizing the potential energy, the global equation in matrix form can be obtained as

$$\mathbf{Kd} + \mathbf{M}\ddot{\boldsymbol{d}} = \boldsymbol{F} \tag{15}$$

where **K** is the global stiffness matrix, **d** the global vector of unknowns, **M** the global mass matrix, and **F** the global vector of equivalent loads. These global matrices are formed by assembling element matrices.

The stiffness matrix for manifold element *e* is

$$\mathbf{K}_e = \int_A \mathbf{B}_e^T \mathbf{E} \mathbf{B}_e dA \tag{16}$$

The elasticity matrix **E** can be further expressed as

$$\mathbf{E} = \frac{E_0}{1-\nu_0^2}\begin{bmatrix} 1 & \nu_0 & 0 \\ \nu_0 & 1 & 0 \\ 0 & 0 & (1-\nu_0)/2 \end{bmatrix} \tag{17}$$

where $E_0 = E, \nu_0 = \nu$ and $E_0 = E/(1-\nu^2), \nu_0 = \nu/(1-\nu)$ for plane stress and plane strain case respectively, where *E* is the Young's modulus and *v* is the Poisson's ratio. The manifold element strain matrix $\mathbf{B}_e$ is assembled from the physical cover strain matrix $\mathbf{B}_i$ as follow

$$\mathbf{B}_e = [\mathbf{B}_1 \quad \dots \quad \mathbf{B}_n] \tag{18}$$

where *n* is the number of physical covers, and

$$\mathbf{B}_i = \mathbf{L}\mathbf{N}_i = \mathbf{L}(\varphi_i \mathbf{T}) \tag{19}$$

where **L** is the differential operator, taking the following form

$$\mathrm{L}(\cdot) = \begin{bmatrix} \dfrac{\partial(\cdot)}{\partial x} & \\ & \dfrac{\partial(\cdot)}{\partial y} \\ \dfrac{\partial(\cdot)}{\partial y} & \dfrac{\partial(\cdot)}{\partial x} \end{bmatrix} \tag{20}$$

The mass matrix for manifold element *e* is

$$\mathbf{M}_e = \int_A \rho \mathbf{N}_e^T \mathbf{N}_e dA \tag{21}$$

where

$$\mathbf{N}_e = [\mathbf{N}_1 \quad \dots \quad \mathbf{N}_n] \tag{22}$$

The element vector of equivalent loads is obtained from the Neumann boundary condition and body force,

$$\mathbf{F}_e = \mathbf{N}_e^T \mathbf{t} + \int_A \mathbf{N}_e^T \mathbf{b} dA \tag{23}$$

where **t** and **b** are external force and body force in vector form respectively.

Considering that the unknowns in PNMM are usually not displacements, and the union of mathematical covers is not identical to the modeling domain, the Dirichlet boundary condition can only be superimposed in a weak form, using the penalty method

$$\mathbf{K}_e += \delta \int_{\Gamma_u} \mathbf{N}_e^T \mathbf{N}_e d\Gamma, \quad \mathbf{F}_e += \delta \int_{\Gamma_u} \mathbf{N}_e^T \overline{\mathbf{u}} d\Gamma \tag{24}$$

where δ is the penalty number.

After solving the global equation Eq.15, one can obtain the displacement field of each manifold element through Eq.13. Then, the strain and stress field of each manifold element can be obtained as

$$\boldsymbol{\varepsilon}_e = \mathbf{L}\mathbf{u}_e = \mathbf{B}_e \mathbf{d}_e \tag{25}$$

and

$$\boldsymbol{\delta}_e = \mathbf{E}\boldsymbol{\varepsilon}_e \tag{26}$$

The mechanical behavior of a particle is determined by the manifold element it locates in. According to the mechanical fields of the manifold element *e*, the displacement, strain and stress of an internal particle can be directly obtained as

$$\mathbf{u}_i = \mathbf{u}_e(\mathbf{x}_i^c),\ \ \boldsymbol{\varepsilon}_i = \boldsymbol{\varepsilon}_e(\mathbf{x}_i^c),\ \ \boldsymbol{\sigma}_i = \boldsymbol{\sigma}_e(\mathbf{x}_i^c) \tag{27}$$

where $\mathbf{x}^c$ indicates the coordinates of the centroid of the particle. In PNMM, the mechanical field on each particle is assumed to be constant.

Although most equations in PNMM are the same with those in NMM, they are quite different in calculation. In NMM, there is only one discretization, making the manifold element as the only computation unit. The cover functions, weight function, DOFs, boundary conditions, body force, and material properties are all implemented on manifold elements. However, in PNMM, particles form a second level of discretization. The cover functions, weight function, and DOFs are still defined on manifold elements, whereas material properties, body force, and boundary conditions are defined on particles. Particles in a same manifold element may have different properties and carry different conditions. Parameters defined on all the particles in a manifold element will be assembled into the element matrices for calculation.

3.3.3 Dynamics Scheme

In PNMM, the dynamic analysis is performed by the Newmark-*β* method, which gives a recurrence relation of displacements, velocities and accelerations between time step *t* and *t+Δt*,

$$u_{t+\Delta t} = u_t + \dot{u}_t \Delta t + \left(\frac{1}{2} - \alpha\right)\Delta t^2 \ddot{u}_t + \alpha \Delta t^2 \ddot{u}_{t+\Delta t} \tag{28}$$

$$\dot{u}_{t+\Delta t} = \dot{u}_t + (1-\beta)\Delta t \ddot{u}_t + \beta \Delta t \ddot{u}_{t+\Delta t} \tag{29}$$

where u_t, $\dot{u}_t$ and $\ddot{u}_t$ is the displacement, velocity and acceleration at time *t* respectively, *Δt* is the time step, and *α* and *β* are parameters determined by the requirement of stability and accuracy. The acceleration at time *t+Δt* can be solved as

$$\ddot{u}_{t+\Delta t} = \frac{1}{\alpha \Delta t^2}(u_{t+\Delta t} - u_t) - \frac{1}{\alpha \Delta t}\dot{u}_t - \left(\frac{1}{2\alpha} - 1\right)\ddot{u}_t \tag{30}$$

Taking the relationship between system unknowns and dynamical variables into consideration,

$$\mathbf{d} = \mathbf{N}^{-1}\mathbf{u}, \dot{\mathbf{d}} = \mathbf{N}^{-1}\dot{\mathbf{u}}, \ddot{\mathbf{d}} = \mathbf{N}^{-1}\ddot{\mathbf{u}}$$

the equation of motion can be expressed in a recurrence form,

$$\begin{aligned}\left(\mathbf{K}_{t+\Delta t} + \frac{1}{\alpha \Delta t^2}\mathbf{M}_{t+\Delta t}\right)\mathbf{d}_{t+\Delta t} \\ = \mathbf{F}_{t+\Delta t} + \mathbf{M}_{t+\Delta t}\left[\frac{1}{\alpha \Delta t^2}\mathbf{d}_t + \frac{1}{\alpha \Delta t}\dot{\mathbf{d}}_t + \left(\frac{1}{2\alpha} - 1\right)\ddot{\mathbf{d}}_t\right]\end{aligned} \tag{31}$$

Combining different values of α and β, different time-domain integration formats can be obtained. In this research, the average acceleration scenario will be adopted by setting α=0.25 and β=0.5.

3.4 Particle Integration Scheme

Although the mathematical covers in PNMM are formed by a uniform triangular or rectangular FEM mesh, manifold elements may have a general shape due to the intersection with physical features, e.g., discontinuities and boundaries. Therefore, an integration scheme over elements like that in FEM is inapplicable, and it will be inconvenient to subdivide each manifold element for the purpose of integration. A simplex integration scheme is developed in NMM, but it is limited to the cases of polynomial integrands. Moreover, mechanical properties, body forces, and boundary conditions in PNMM are all defined on particles rather than polygonal elements. Hence, the quadrature in PNMM has to be conducted on particles.

Considering that the manifold element contains a collection of internal particles whose total area is the same as the element, these particles can be seen as a natural

discretization of the element. Assuming that the integrand is constant within each particle, which is consistent with the assumption of constant mechanical field on each particle, a particle integration scheme is proposed as

$$\int_A f(\mathbf{x})dA = \sum_{i=1}^{p}[f(\mathbf{x}_i^c)\cdot A_i] = \pi\sum_{i=1}^{p}[f(\mathbf{x}_i^c)\cdot r_i^2] \tag{32}$$

where p is the number of particles, the coordinates of the centroid of the ith particle, A_i the area of the ith particle and r_i the radius of the ith particle.

The particle integration scheme is graphically illustrated in Figure 3.6. For integration, particles can be simply regarded as the collocation of a group of numerical integration points. The weight of each point is taken as the area of the particle, which just makes sense as particles in an element have a same area in total as the element and parameters are defined as scalars on each particle. The overlap between particles has no physical meaning and will not affect the accuracy of the integration. It should be noted that the particle integration scheme is a numerical integration technique, while the simplex integration scheme is an analytical one.

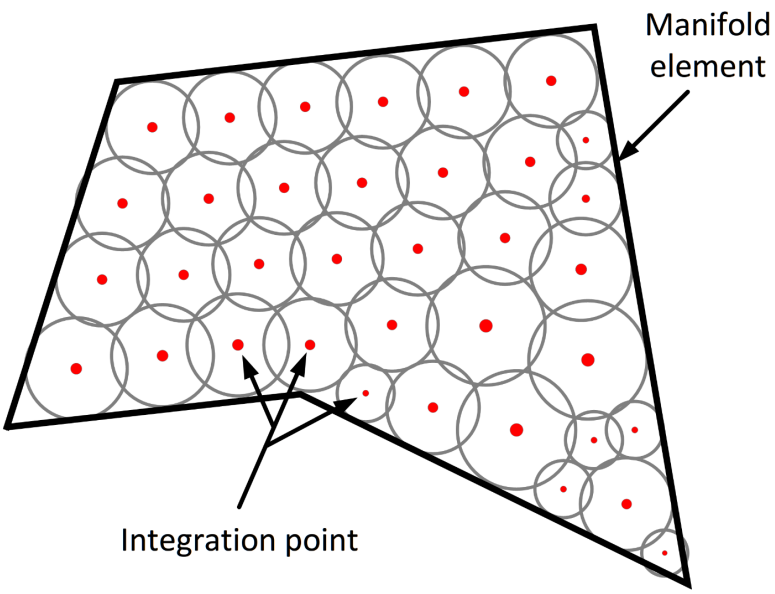

Figure 3.6 The particle integration scheme

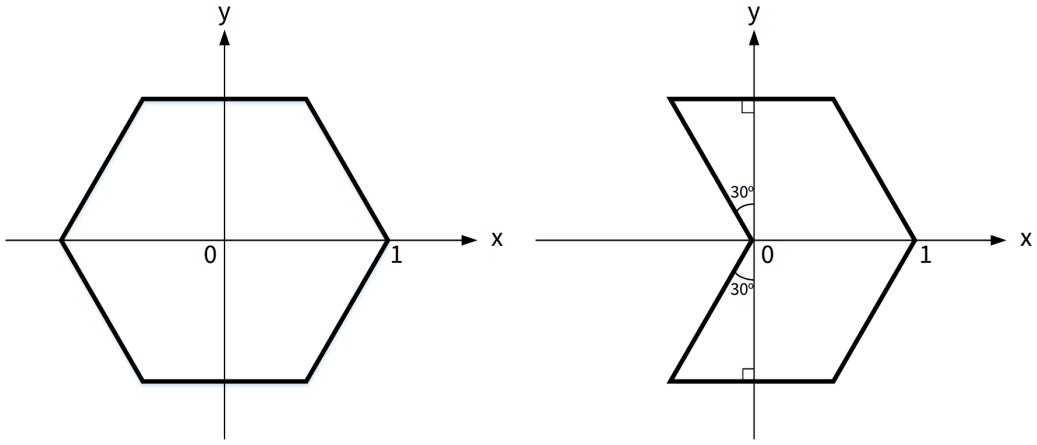

Figure 3.7 The integration domain to verify the accuracy of particle integration scheme: (a) a hexagonal domain; (b) a subdomain of the hexagon

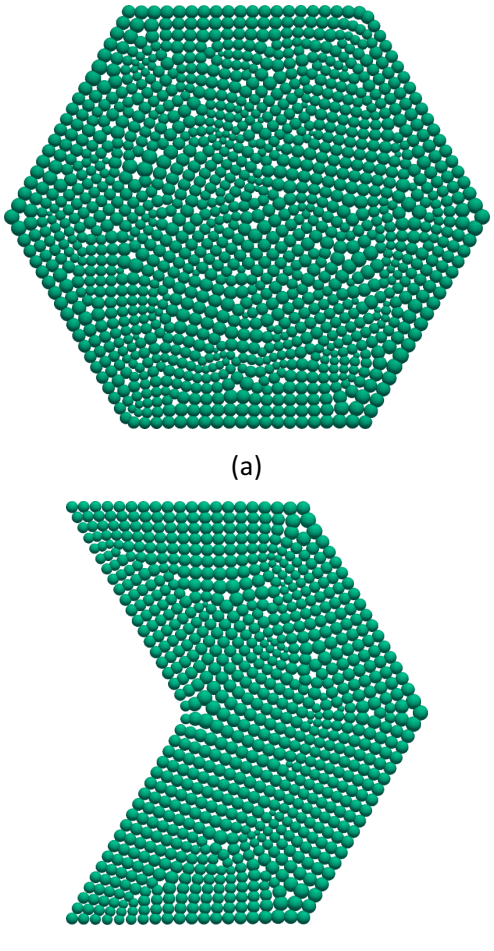

Figure 3.8 Particles in the integration domain: (a) 1,291 particles in the hexagonal domain; (b) 843 particles in the subdomain

To examine the accuracy of the particle integration scheme, two numerical examples have been conducted. The first example is to calculate the integration over a hexagonal domain, while the second one is over a subdomain of the hexagon, as shown in Figure 3.7. For the particle integration scheme, two integration domains are approximated by a group of constant particles, as shown in Figure 3.8. Particles here only represent integration points and weights. They are generated in the way as described previously. Different numbers of particles are generated for the integration to compare its influence on the accuracy.

A third-degree polynomial $f(x,y)$ and a trigonometric function $g(r,\theta)$ in polar coordinate system are chosen as the integrand,

$$f(x,y) = x^3 + y^3 + x^2y + xy^2 + x^2 + y^2 + xy + x + y + 1 \tag{33}$$

$$g(r,\theta) = \sqrt{r}\cos\frac{\theta}{2} \tag{34}$$

From the results listed in Table 3.1 and the error analysis shown in Figure 3.9, one is able to conclude that good integration results can be obtained when there are enough internal particles (the number in this example should be 50~100), and increasing the number of particles will improve the accuracy of the quadrature scheme.

An attractive advantage of the particle integration scheme is that the integration domain can be either convex or concave polygons. Besides, it is theoretically suitable for any integrand, including polynomial, exponential, and trigonometric functions. However, it is believed that the accuracy will be affected by the size distribution as well as the position of particles, especially when the number of particles is relatively small.

The calculation process of PNMM, as illustrated in Figure 3.10, can be summarized as follow:

- *Step 1*: Using the material properties, the body force, and the boundary conditions (both kinematics and loads) defined on particles, together with the

cover functions, weight functions, and DOFs on manifold elements, element matrices are generated on each manifold element. This step is carried out by the particle integration scheme.

- *Step 2*: Element matrices are assembled, and the global matrices are generated.
- *Step 3*: The global equation in matrix form is solved, and the vector of unknowns on each manifold element is obtained.
- *Step 4*: According to the displacement, stress, and strain fields of each manifold element, mechanical behaviors of particles are derived.

Table 3.1 Integration results using the particle integration scheme

Hexagonal domain		
Particle number	$f(x,y)$	$g(r,\theta)$
9	3.54248	1.23440
46	3.65263	1.25359
156	3.67222	1.26023
331	3.67689	1.26088
1291	3.67965	1.26161
Analytical result	3.68061	1.26188
Subdomain of the hexagon		
Particle number	$f(x,y)$	$g(r,\theta)$
9	3.00075	1.08677
33	3.07521	1.09146
100	3.09447	1.09244
209	3.09924	1.09259
843	3.10231	1.09278
Analytical result	3.10326	1.09282

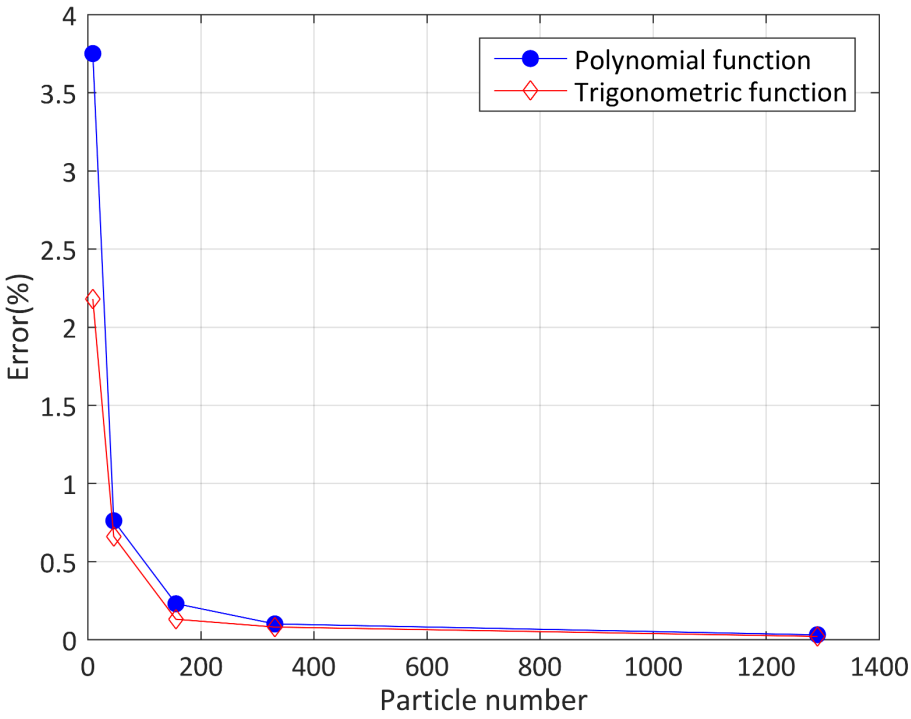

(a)

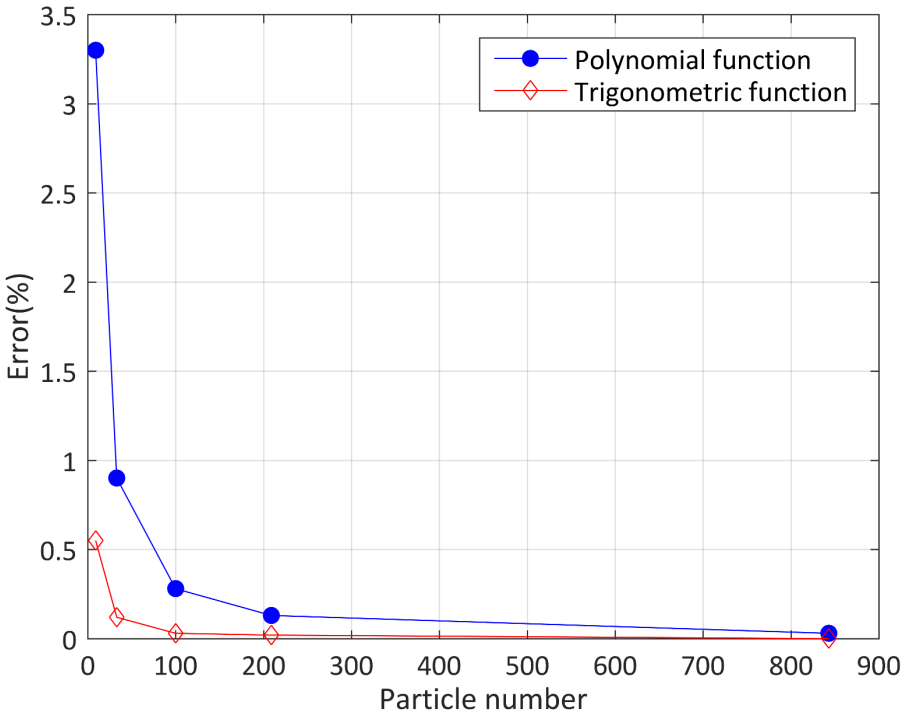

(b)

Figure 3.9 Integration errors using the particle integration scheme: (a) on the hexagonal domain; (b) on the subdomain

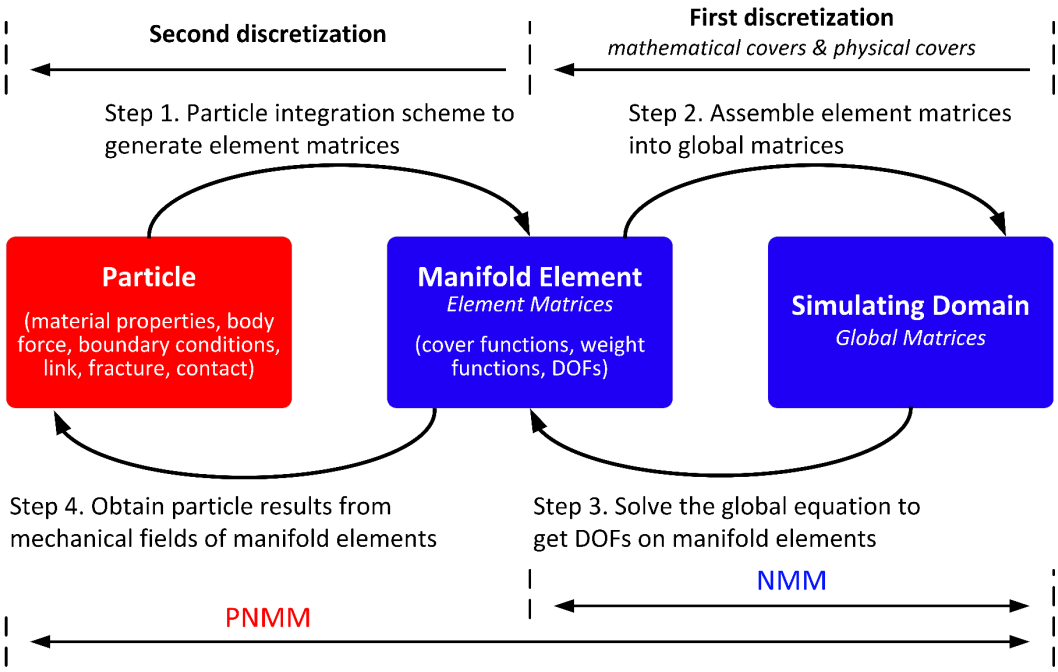

Figure 3.10 The calculation process of PNMM

3.5 Links and Fractures

Another basic component in PNMM is the link. A link represents the continuous status between particles. Links are also used to represent the initiation and propagation of fractures.

3.5.1 Generation of Links

A link is generated between two particles that satisfy following three conditions at the same time:

- Two particles are next to each other geometrically;
- Two particles belong to the same block/object;
- There are no micro/macro fractures between two particles.

The Munjiza-NBS contact detection algorithm (Munjiza and Andrews, 1998) is implemented in PNMM for the generation of links. The algorithm is fast in performance

and low in CPU use. For a two-dimensional space shown in Figure 3.11, a rectangle space defined by [x_{min}, y_{min}, x_{max}, y_{max}] is first found to cover all the particles. Then, the rectangle space is divided into identical cells with a size of h, the total number of cells in the x and y direction is calculated as

$$m = \frac{x_{max} - x_{min}}{h} - 1 \tag{35}$$

and

$$n = \frac{y_{max} - y_{min}}{h} - 1 \tag{36}$$

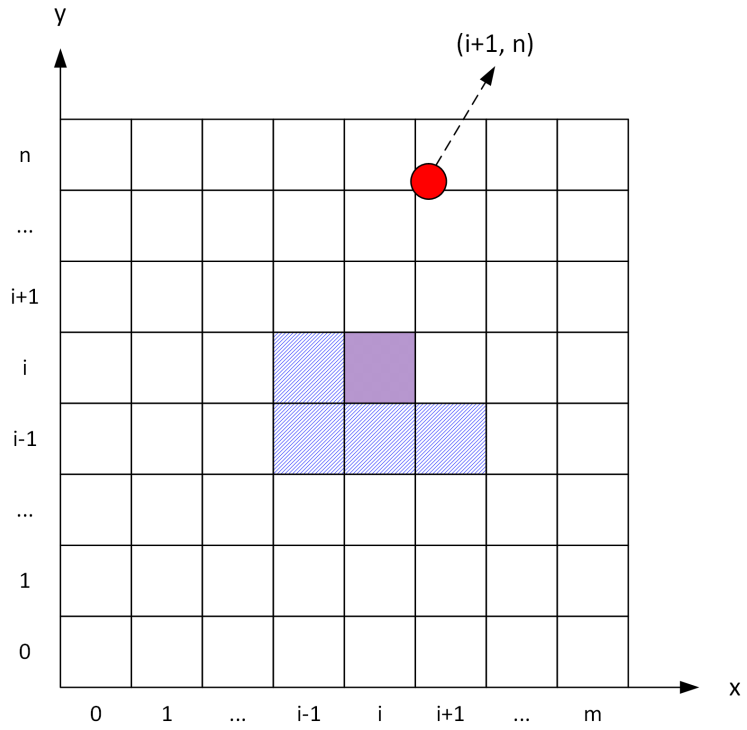

Figure 3.11 The NBS contact detection algorithm in two-dimensional space

The cells in x and y direction is indexed from 0 ~ m and 0 ~ n respectively. A pair of indices in the x and y direction will locate a specific cell. Then, each particle is orientated in a cell with the index of (i_x, i_y), where

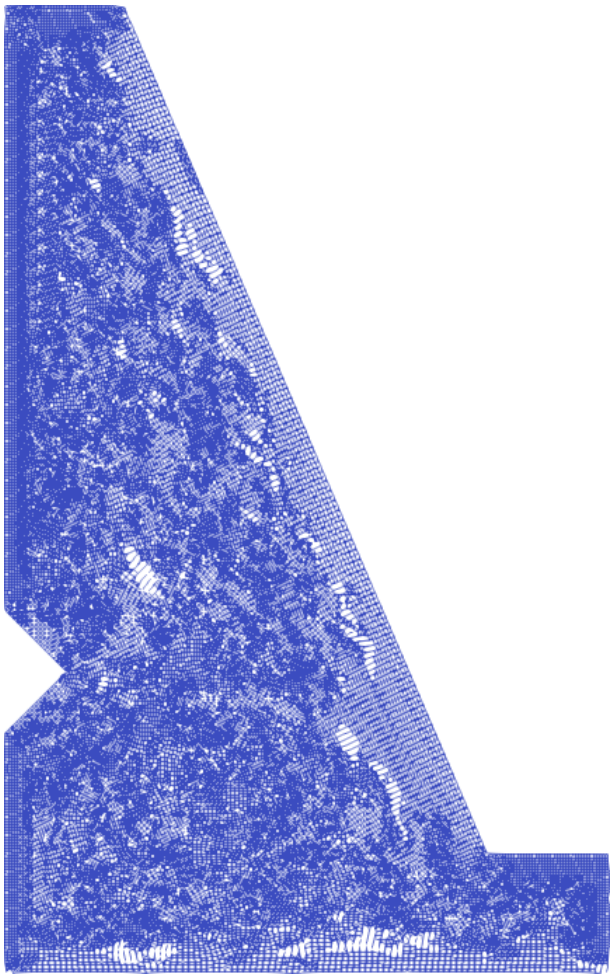

(a)

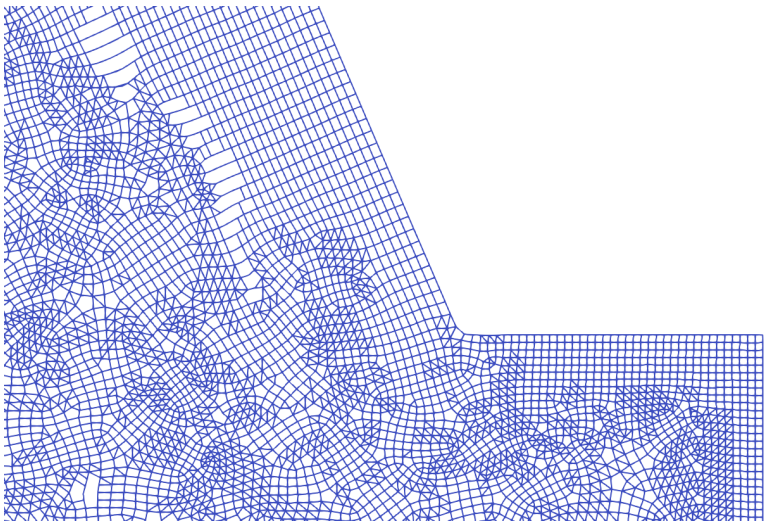

(b)

Figure 3.12 An example of the link network in PNMM: (a) a slope; (b) an enlarged view

$$i_x = floor\left(\frac{x - x_{min}}{h}\right) \tag{37}$$

$$i_y = floor\left(\frac{y - y_{min}}{h}\right) \tag{38}$$

where the operator $floor(\cdot)$ is to calculate the largest integral value that is not greater than a number.

For a particle in cell (*i, i*), PNMM checks if it is close enough to another particle locating in the cell (*i-1, i-1*), (*i, i-1*), (*i+1, i-1*), (*i-1, i*), and (*i, i*), if there is any in the cell. If the distance of two particles is equal to the sum of their radii, a link will be generated between them. The algorithm for the generation of links in PNMM is summarized in Appendix A.

The link network generated for the same example in Figure 3.4 is illustrated in Figure 3.12. Particles are not plotted in the figure for the sake of clarity. Each line segment represents a link.

It should be noted that links are different from contacts between particles, which will be presented later. Since the motion of particles is determined by the displacement field of manifold elements they belong to, there is no additional force defined on the link. Specifically, the occurrence of links only represents the continuous status between particles without containing any other physical meaning.

3.5.2 Failure Description

The failure description is crucial in dealing with the nucleation, propagation, and coalescence of cracks as well as the fragmentation of intact rock masses. Particles in PNMM are supposed to be unbreakable, which means cracks cannot be driven into particles and, hence, there is no need to define any fracture parameter on particles.

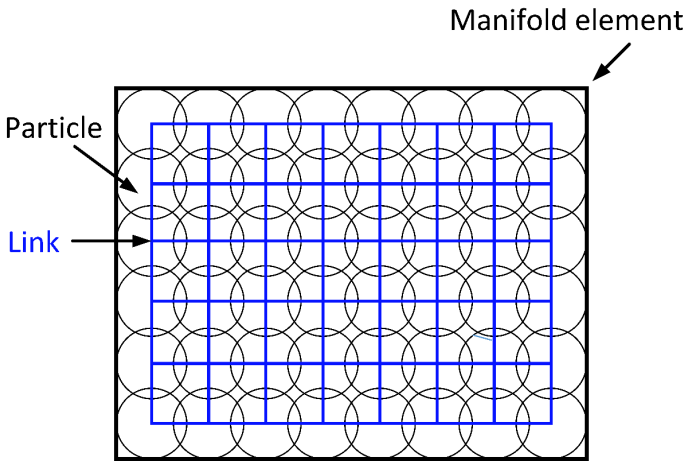

(a)

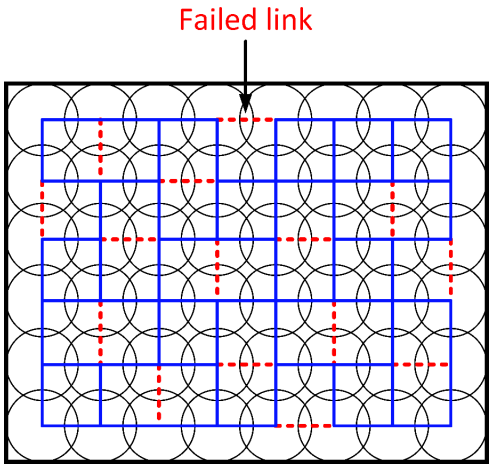

(b)

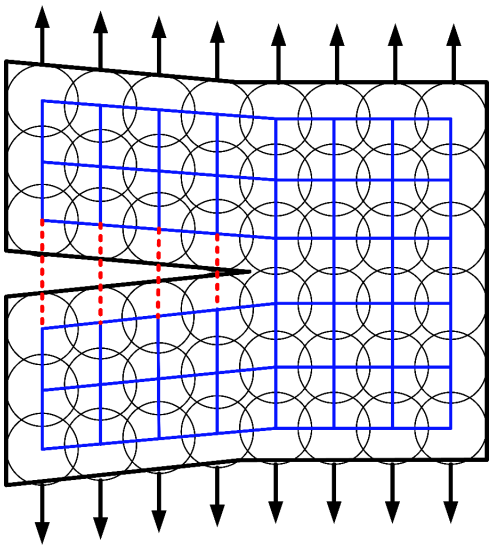

(c)

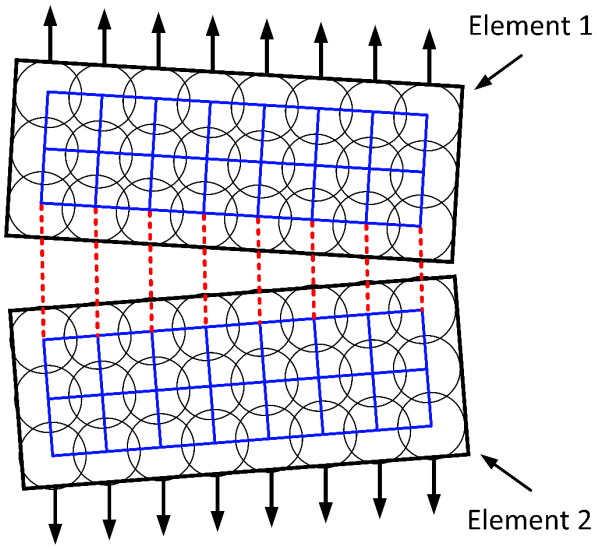

(d)

Figure 3.13 Failure description in PNMM: (a) Links between continuous particles; (b) Failed links simulate micro cracks; (c) Consecutive failed links simulate macro fractures; (d) Failed links separate a manifold element and its internal particles

A link is the basic failure unit in PNMM. In the continuum illustrated in Figure 3.13a, each pair of adjacent particles in a continuum is connected by a link to represent the continuity status. The failure of links simulates the micro-crack within the rock (Figure 3.13b), while consecutive failed links simulate the initiation and propagation of fractures on macroscopic level as illustrated in Figure 3.13c. Adjacent particles without a link are regarded as a pair of disconnected particles. After breaking one or more links in a manifold element, the topological relation between particles will be re-detected. And once disconnected particles separate internal particles into two or more groups, the manifold element will be accordingly subdivided, representing that the macro fracture has propagated across the manifold element (Figure 3.13d). Separate manifold elements continue to perform as common elements respectively in following calculation steps.

As particles in PNMM are currently supposed to be undeformable, in order to ensure the deformability of the rock mass, adjacent particles are allowed to further penetrate into or detach from each other without breaking their links. Instead, the failure of a link is based on the average stress and/or strain of the two particles it connects,

$$\sigma_l = \frac{\sigma_1 + \sigma_2}{2} \tag{39}$$

$$\varepsilon_l = \frac{\varepsilon_1 + \varepsilon_2}{2} \tag{40}$$

where σ_l and ε_l are the average normal/shear stress and strain respectively, σ_1 and ε_1 are the stress and strain tensor of the first particle respectively, and σ_2 and ε_2 are the stress and strain tensor of the second particle respectively. For simplicity, we hereafter term σ_l and ε_l the link stress and link strain respectively.

The failure criterion is applied on links, rather than on particles or manifold elements. Once the failure criterion is met on a link, the link is supposed to be broken/failed. Different failure criteria could be adopted in PNMM. Once a proper failure criterion is chosen (e.g., the Mohr-Coulomb criterion), the tensile and shear cracks could be easily identified on links. As PNMM is primarily developed for rock dynamics in this research, a rate-dependent failure model, namely the Johnson-Holmquist-Beissel model is adopted, whose details will be provided later.

As can be seen from Figure 3.13c, particles in the manifold element containing a crack tip still constitute only one manifold element. Such a manifold element has no more DOFs than a normal one. Though polynomial cover functions are able to approximate smooth functions well, they are unsuitable to capture the high gradient solutions for singular problems around the crack tip. Hence, a cover function enrichment scheme is adopted to improve the computational accuracy. Inspired by XFEM (Moës et al., 1999) and NMM (Ma et al., 2009, Wu and Wong, 2013b), the enrichment based on the following four basic functions is adopted in PNMM,

$$\{\Psi_1 \quad \Psi_2 \quad \Psi_3 \quad \Psi_4\} = \left\{\sqrt{r}\sin\frac{\theta}{2} \quad \sqrt{r}\cos\frac{\theta}{2} \quad \sqrt{r}\sin \quad \sin\frac{\theta}{2} \quad \sqrt{r}\sin\theta\cos\frac{\theta}{2}\right\} \tag{41}$$

The enriched cover function is

$$\tilde{\mathbf{u}}_i = [\mathbf{T} \quad \boldsymbol{\Psi}]\begin{bmatrix}\mathbf{d}_i \\ \mathbf{d}_\Psi\end{bmatrix} = \tilde{\mathbf{T}}\tilde{\mathbf{d}}_i \tag{42}$$

The enriched element displacement field is

$$\tilde{\mathbf{u}}_e(\mathbf{x}) = \sum_{i=1}^{m} \varphi_i(\mathbf{x})\tilde{\mathbf{u}}_i(\mathbf{x}) = \sum_{i=1}^{m} \tilde{\mathbf{N}}_i(\mathbf{x})\tilde{\mathbf{d}}_i = \tilde{\mathbf{N}}_e\tilde{\mathbf{d}}_e \tag{43}$$

Since PNMM naturally simulates the surface of fractures by separating manifold elements as shown in Figure 3.13d. There is no need to adopt the Heaviside enrichment of XFEM in the manifold elements along the surface of fractures. Therefore, only the manifold element containing a fracture tip is enriched, as illustrated in Figure 3.14.

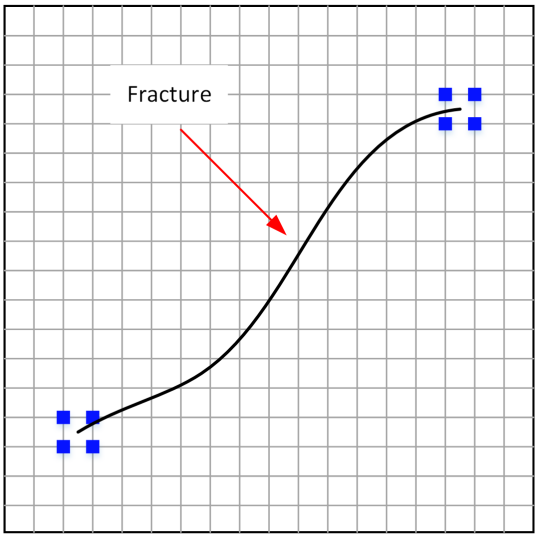

Figure 3.14 Enrichment around fracture tips

3.6 Particle Contact

The detection and operation of contact is concise in PNMM. Two types of contact are defined: the particle-particle contact and particle-plane contact, as shown in Figure 3.15. Particles on the surface of different blocks may form a pair of particle-particle contact when they are adjacent to each other. The particle-plane contact is to simulate the interaction between deformable bodies and rigid static/moving walls or infinite planes.

The detection criterion for the particle-particle and particle-plane contact can be respectively expressed as

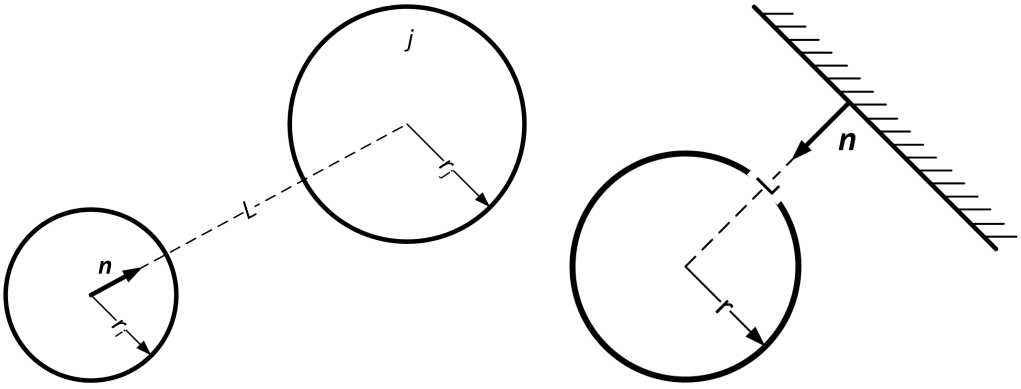

Figure 3.15 Particle contact in PNMM: (a) Particle-Particle contact; (b) Particle-Plane contact

$$L - \left(r_i + r_j\right) \leq \Delta \tag{44}$$

and

$$L - r \leq \Delta \tag{45}$$

where *Δ* is the contact threshold.

The difference between a pair of contact and a link is that there is no force defined on the link whereas the contact force is applied. The operation of contact force is proposed by Sun (2012). For the particle-particle contact, following components in matrix form is added to the global matrices using penalty method

$$\begin{cases} \mathbf{K}_{ii}^{e} \mathrel{+}= p\mathbf{C}_i^T\mathbf{C}_i \\ \mathbf{K}_{jj}^{e} \mathrel{+}= p\mathbf{C}_j^T\mathbf{C}_j \end{cases}, \quad \begin{cases} \mathbf{K}_{ij}^{e} \mathrel{-}= p\mathbf{C}_i^T\mathbf{C}_j \\ \mathbf{K}_{ji}^{e} \mathrel{-}= p\mathbf{C}_j^T\mathbf{C}_i \end{cases}, \quad \begin{cases} \mathbf{F}_{i}^{e} \mathrel{+}= p\left(L - R_i - R_j\right)\mathbf{C}_i^T \\ \mathbf{F}_{j}^{e} \mathrel{-}= p\left(L - R_i - R_j\right)\mathbf{C}_j^T \end{cases} \tag{46}$$

where *p* is the contact stiffness, and

$$\mathbf{C}_i = \boldsymbol{n}[\mathbf{N}(c) + R_i\mathbf{B}^{nor}(c)] \tag{47}$$

where ***n*** is the vector of contact direction, the operator *·(c)* is the value at the particle centroid, and $\mathbf{B}^{nor}$ is the normal components (first two rows) of the element strain matrix. For the particle-plane contact, following components in matrix form should be added

$$\mathbf{K}_{ii}^{e} \mathrel{+}= p\mathbf{W}_i^T\mathbf{W}_i, \quad \mathbf{F}_i^{e} \mathrel{-}= p(L - r)\mathbf{W}_i \tag{48}$$

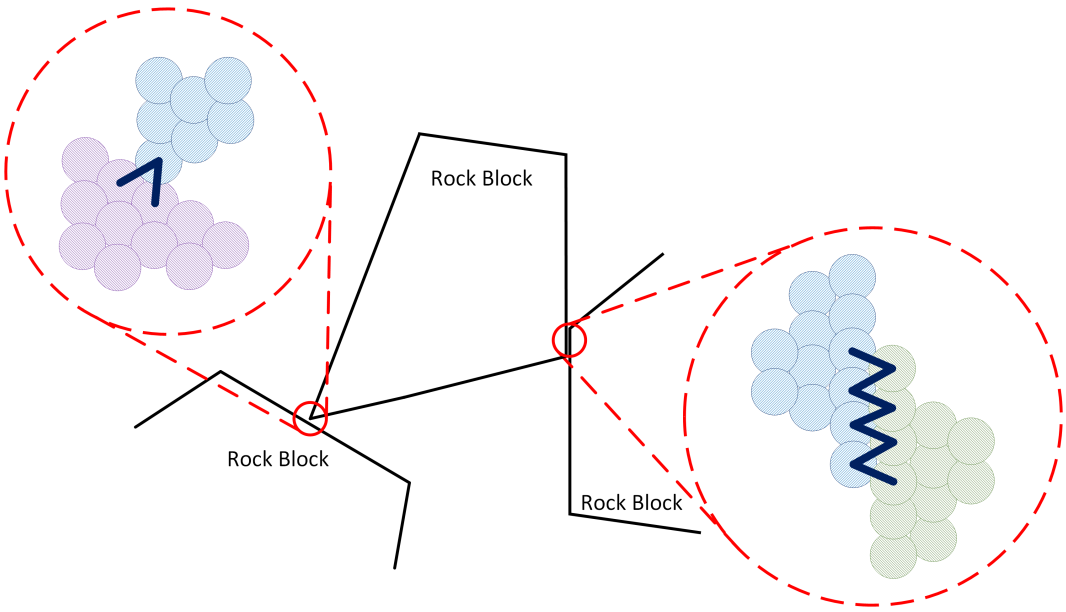

Figure 3.16 From particle-particle contact to block-block contact

with

$$\mathbf{W}_i = \boldsymbol{n}[\mathbf{N}(c) - R_i \mathbf{B}^{nor}(c)] \tag{49}$$

Comparing with the block-block contact in NMM, contacts in PNMM are greatly simplified in both detection and operation. Although the direction of a pair of contact is randomly determined by the position of two particles at particle scale. PNMM accumulates the contact to simulate the complex block-block contact at macro-scale, as illustrated in Figure 3.16. The contact force between blocks is the sum of contact forces between particles. Therefore, the effect of randomly distributed particles could be somewhat eliminated.

3.7 Particles in PNMM

The primary difference between PNMM and NMM is the introduction of particles. However, particles in PNMM are based on a quite different concept when compared to other particle-based methods, e.g., the bonded-particle model (Potyondy and Cundall, 2004), the smoothed particle hydrodynamics (Liu and Liu, 2010), and the reproducing

kernel particle method (Liu et al., 1995). Therefore, for clarity, a summary of the particle aspect of PNMM is provided in this section.

First, particles carry parameters and assist to simulate the heterogeneity of rock materials. In PNMM, particles are assigned individual parameters, including material properties, body forces, and boundary conditions. Considering that the DOFs are defined on manifold elements instead of particles, the dimension of global matrices is independent of the number of particles. However, on the other hand, numeric values of global matrices are obtained as a result of the particle integration scheme, which is conducted on particles. When different material properties are given to particles in a single element, the element still behave in a homogeneous way as that in NMM, which is for sure as it has the same DOFs and local approximation. The material properties of the element, implicitly obtained from integration, is a weighted average of the values defined on the particles. Conducting such a weighted average as described previously on each element, the model will therefore behave as an inhomogeneous material on the element level. From this perspective, PNMM have similarities with RFPA (Tang, 1997). Parameters on particles, in this way, influence the global matrices. However, the heterogeneity of rock is not in the scope of this thesis, which could be an important application of PNMM in the future.

Second, the movement of a particle is governed by the element it locates in, namely by the covers. Particles in a single element are not solved separately. Instead, the DOFs of an element are solved from the global equation, whereafter the movement of all internal particles are naturally determined by the displacement field. Particles belonging to the same element are in this way glued together as a deformable body, whose material properties are defined in an equivalent way as just mentioned.

Third, fractures are simulated on the particle level. In PNMM, the continuous status between adjacent particles is defined as a link. A micro-crack is supposed to be generated as long as the failure criterion is met on the link. The initiation and propagation of macro-cracks is carried out by consecutive micro-cracks. Therefore, based on particles and their links, cracks can be initiated, and the fracturing path is easier to be determined in the

proposed model. These capabilities are both absent in the conventional NMM (Ma et al., 2010).

Last, one important benefit coming with the introduction of particles is to simplify the block-block contact in NMM to the particle-particle contact. In PNMM, a pair of contact can be defined on neighboring particles without a link. The contact detection and contact operation between particles is believed to be easier and more straightforward than that between polygonal blocks.

3.8 Rate-dependent Behaviors of Rock in PNMM

Recalling the importance of studying the rate-dependent behaviors of rock materials mentioned in Chapter 1, PNMM has been primarily developed for rock dynamics. To accurately simulate the dynamic behavior of rock materials and rock masses over a wide range of strain rates, reliable constitutive models should be incorporated.

For brittle materials subjected to large strains, high strain rates and high pressures, Johnson and Holmquist (1992) developed the JH-1 model. In JH-1 model, the material strength is expressed as a function of the pressure, strain rate and damage. The pressure is related to the volumetric strain and the effect of permanent crushing. The damage is determined by the accumulation of the plastic volumetric strain, equivalent plastic strain and pressure. However, JH-1 model fails to consider the progressive damage with the increase of deformation. The JH-2 model (Johnson and Holmquist, 1994) softens the strength and increases the bulking pressure gradually as the damage accumulates. As a result, in JH-2 model, the material strength is dependent on the intact strength, fractured strength, strain, strain rate, pressure, and damage. Later, Johnson, Holmquist, and Beissel proposed the Johnson-Holmquist-Beissel (JHB) model (Johnson et al., 2003, Holmquist and Johnson, 2005, Holmquist and Johnson, 2011). Apart from including a phase change, JHB model is distinguished from JH-1 model by incorporating an analytic description for both intact and failed strengths and the failure strain. The JH models have been applied to various brittle materials, including concrete (Holmquist et al., 1993), ceramic (Johnson

et al., 2003, Holmquist and Johnson, 2005), glass (Holmquist and Johnson, 2011), and rock (Ma and An, 2008).

In this research, the JHB model is adopted as the rate-dependent failure criterion and has been incorporated into PNMM as a subroutine. For dynamic problems, where the rate-dependent behaviors of rock need to be considered, the incorporated JHB model will be executed to calculate the dynamic strength at a specific strain rate.

The JHB model consists of (1) an analytic description for intact and failed strength, (2) a damage variable, and (3) a pressure portion, which is graphically illustrated in Figure 3.17.

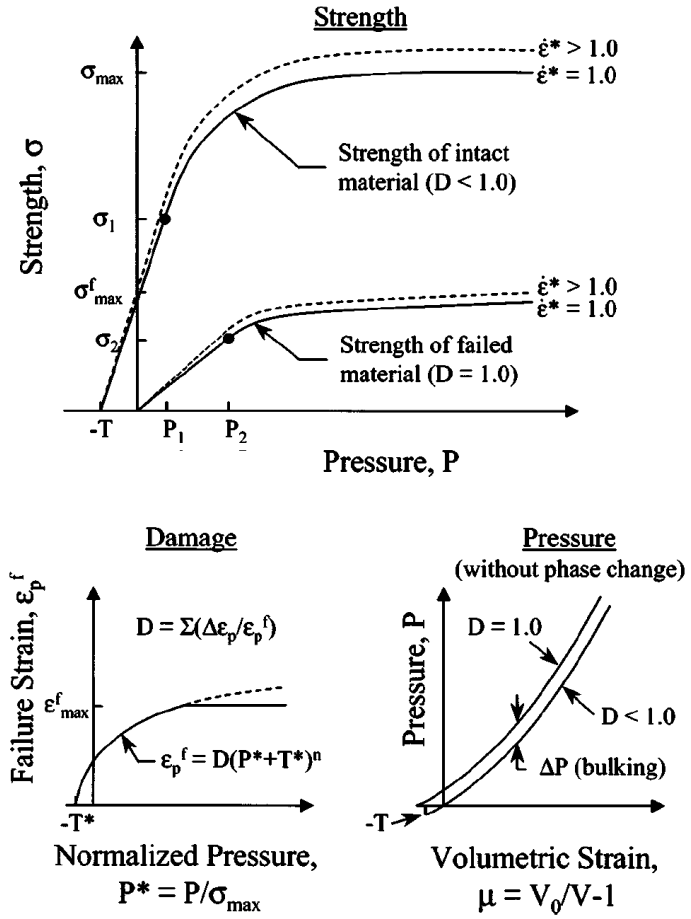

Figure 3.17 The JHB model (Johnson et al., 2003)

First, in JHB model, the dynamic strength σ_c is dependent on the damage D, the pressure P, and the dimensionless strain rate $\dot{\varepsilon}^*$. The strength at the strain rate of $\dot{\varepsilon}^*$ is

$$\sigma_c = \sigma_0(1.0 + C \ln \dot{\varepsilon}^*) \tag{50}$$

where σ_0 is the strength at $\dot{\varepsilon}^* = 1.0$ and C is the dimensionless strain rate constant. For intact material, i.e. $D < 1.0$, the strength σ_0 can be expressed as

$$\sigma_0 = \begin{cases} \sigma_i(P+T)/(P_i+T) & P \le P_i \\ \sigma_i + (\sigma_{max} - \sigma_i)\{1 - exp[-\sigma_i(P-P_i)/((\sigma_{max}-\sigma_i)(P_i+T))]\} & P > P_i \end{cases} \tag{51}$$

where σ_i is the strength at pressure P_i, T is the static tensile strength, σ_{max} is the maximum strength (for rock materials, is the compression strength).

Second, in PNMM, the damage variable D for each manifold element is simply re-defined as the ratio between the number of damaged links and the total number of links, expressed as

$$D = N_l^b / N_l \tag{52}$$

where N_l^b and N_l are the number of broken links and total links respectively.

Third and last, the hydrostatic pressure without a phase change P is

$$P = \begin{cases} K_1\mu + K_2\mu^2 + K_3\mu^3 + \Delta P & \text{compressive pressure} \\ K_1\mu & \text{tensile pressure} \end{cases} \tag{53}$$

where K_1 is the bulk modulus, K_2 and K_3 are material constants, μ is the compression variable due to the volume change defined as $\mu = V_0/V - 1$, V_0 and V and are initial and current volume respectively, and ΔP is the pressure increment for the dilatation effect after compression failure.

The implemented JHB model is executed at every time step in PNMM and applied on every link. Once the stress of a link reaches the dynamic strength obtained from the JHB

model, the link is supposed to break. To be specific, the failure criterion for the link is $\sigma_l = \sigma_c$.

A group of constants need to be determined before applying the JHB model. In this research, the JHB parameters for granite are adopted. The dimensionless strain rate constant *C* is 0.00965, taken from a semi-empirical rate-dependent strength equation for concrete (Tedesco and Ross, 1998). This value is very close to the measured value for silicon carbide (Holmquist and Johnson, 2005), which is also a brittle material. The strength constants σ_i and P_i are calculated to be 59 MPa and 17 MPa respectively by applying the curve fitting technique to the Hoek-Brown criterion (Li et al., 2017b). The pressure constants K_2 and K_3 are assumed to be -23 GPa and 2980 GPa respectively with reference to (Ai and Ahrens, 2006).

3.9 Implementation

The code of PNMM is developed according to the concept, components, and formulation presented in previous sections. The flowchart of the implemented PNMM is illustrated in Figure 3.18, and each step in the figure is explained in detail as follows:

Step 1. *Input the model and Generate mathematical covers*. The model is created in other software and read by PNMM from text files. The text file imported into PNMM includes the geometry information of the model, material properties, and some other setting variables. Three types of mathematical covers are adopted in PNMM (Figure 3.1).

Step 2. *Generate manifold elements*. The generation of manifold elements is based on the topological operation between the imported model and mathematical covers (Section 3.1).

Step 3. *Generate particles*. Details of this task are given in Section 3.2.

Step 4. *Generate links*. Details of this task are given in Section 3.5.1 and Appendix A.

Step 5. *Generate blocks*. This step is to detect how many blocks are involved in the model. A block is constituted of a group of particles, where each two particles are found to be connected through arbitrary numbers of links. A so-called

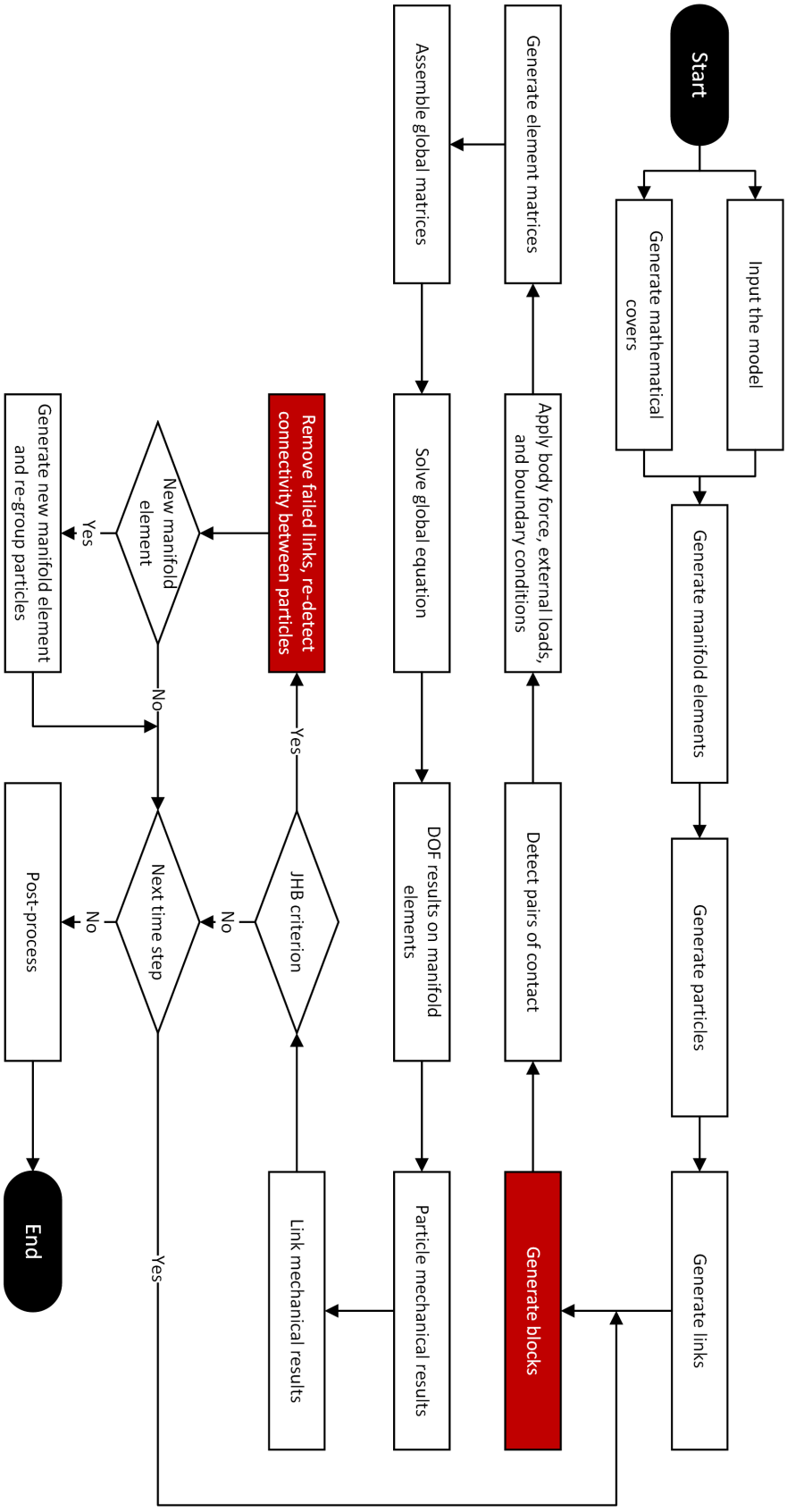

Figure 3.18 The flowchart of PNMM

seed filling method is adopted to accomplish this task. Details of this method can be found in (Sun, 2012). The source code of the seed filling method implemented in PNMM is given in Appendix C.

Step 6. *Detect pairs of contact*. A pair of contact is detected according to Eq.44 or Eq.45.

Step 7. *Apply body force, external loads, and boundary conditions*. These parameters are defined on particles and applied to the element matrices via Eq.23 and Eq.24.

Step 8. *Generate element matrices*. The element matrices are generated using the proposed particle integration scheme. Details have been given in Section 3.3.2 and Section 3.4. A class template `Matrix` is implemented in the code of PNMM to abstract the frequent operations on element matrices. A brief introduction of `Matrix` is given in Appendix D.

Step 9. *Assemble global matrices*. A class template `BlockMatrix` is implemented in the code of PNMM to construct the global matrices. A brief introduction of `BlockMatrix` is given in Appendix D.

Step 10. *Solve global equation*. This step is to solve the Eq.15 or Eq.31. Details of this task will be given later.

Step 11. *DOF results on manifold elements*. Results on manifold elements are derived from the global vector of unknowns, which is solved in the previous step.

Step 12. *Particle mechanical results*. Mechanical results on particles are derived from the mechanical fields of a manifold element using the Eq.27.

Step 13. *Link mechanical results*. Mechanical results on a link are obtained from the two particles it connects using the Eq.39 and Eq.40.

Step 14. *JHB criterion*. The JHB model is implemented in PNMM and applied on each link at every time step. Once the JHB criterion is met, the status of the link will be set to failed. Details of the JHB model are presented in Section 3.8.

Step 15. *Remove failed links, re-detect connectivity between particles*. This task is accomplished by the seed filling method as well (see Step 5 for details).

Step 16. *Generate new manifold element and re-group particles*. Additional manifold elements need to be generated when fractures have propagated through an element, as stated in Section 3.1.

Step 17. *Post-process*. PNMM writes the simulation result into an external text file, which will be later processed by other post-process software.

PNMM is implemented in the programming language C++. Based on the PMM project, which is developed by Dr. Liang Sun at École Polytechnique Fédérale de Lausanne (EPFL), Switzerland (Sun, 2012), an in-house code of PNMM is written by the author. An overview of the PNMM code is given in Appendix B.

PNMM is a command-line program. It reads the model, including the geometry information of the model, boundary conditions, material properties, and calculation settings, from text files. After the calculation completes, PNMM writes the results, including the position and mechanical results of particles and the status of links, into text files for visualization. Many software and code packages are used by or incorporated into PNMM to carry out a complete simulation. They are concluded as follows:

- The commercial FEM software *ANSYS* and the free meshing software *Gmsh* (Geuzaine and Remacle, 2009) are used in the pre-process to generate the model. Interfaces to PNMM are written as a subroutine.
- The C++ library *CGAL* is incorporated to conduct the 2D discretization.
- The C++ library *Eigen* is incorporated to solve the global equation in matrix form. *Eigen* provides a fast conjugate gradient solver for sparse matrices. Details on the algorithm of the equation solver are provided in Appendix E.
- *Git* is used for version control.
- *Doxygen* is used to automatically generate the documentation of PNMM. A screenshot of the generated documentation is shown in Figure 3.19. The documentation of PNMM is available at *https://www.particlenmm.org*
- *ParaView* is used for the post-process of PNMM (Figure 3.20). A brief introduction to the post-process of PNMM is available in Appendix F.

PNMM

Main Page | Classes | Files | Search

Class List

Here are the classes, structs, unions and interfaces with brief descriptions:

Block	The rock block that consists of a group of particles
BlockMatrix	A block matrix class based on the matrix class
Calculator	Linear equations solver
FEMElement_2D	The FEM element in 2D
FEMNode_2D	The FEM nodes in 2D
Kinematics	Kinematics variables and operations
Line	A basic geometry component - line
Link_DiskToDisk	The link between two 2D disk particles
Loadings	Loadings variables and operations
ManifoldElement_2D	The manifold element in 2D
ManifoldNode_2D	The manifold node in 2D
MaterialProperties	Material properties
Matrix	A matrix class based on vectors
Mechanics	Mechanics variables and operations
Mesh	FEM mesh
Node	A basic geometry component - node
Particle_Disk	2D disk particle
ParticleModel	Particle model
Polygon	A basic geometry component - polygon
StarCover	The star cover in 2D

Generated by doxygen 1.8.13

Figure 3.19 The documentation of PNMM

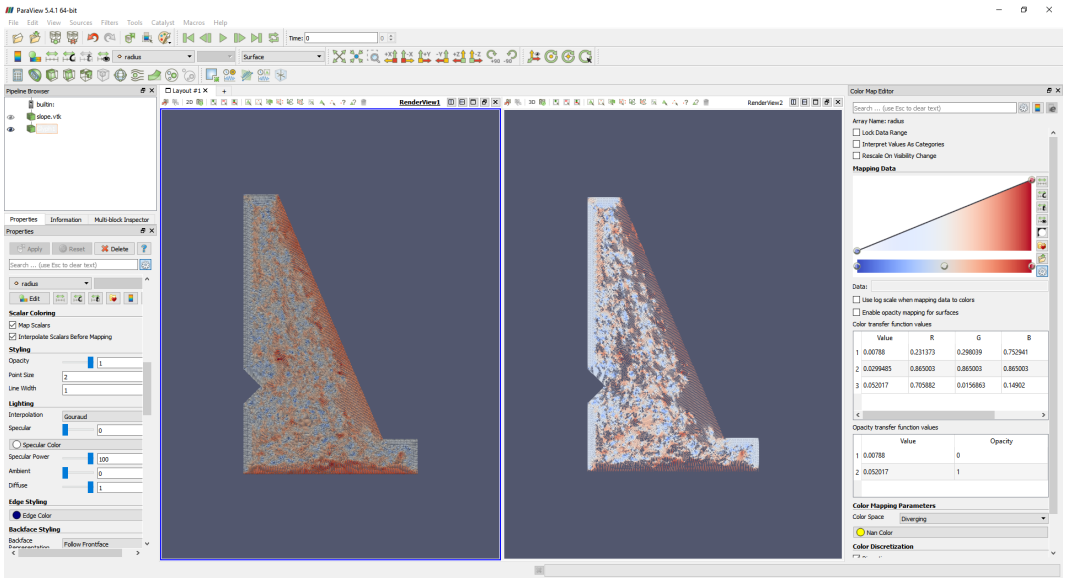

Figure 3.20 ParaView for post-process

3.10 Summary

A particle-based numerical manifold method is proposed in this chapter. The fundamental conception, formulations, and the implementation of PNMM are given in detail. The dual-layer-cover system inherited from NMM is first briefly discussed in Section 3.1, which constructs the first level of discretization in PNMM. Particles are introduced into PNMM in Section 3.2 as the second level of discretization. The dual-level discretization is the most distinct characteristic of PNMM. Formulation of PNMM is given in matrix form in Section 3.3. Matrices in the formulae and DOFs in PNMM are all defined and conducted on the first level of discretization, namely on the manifold elements. Meanwhile, material properties, body forces, and boundary conditions are defined on particles the second level of discretization. The bridge between the parameters on particles and the matrices on manifold elements is the particle integration scheme, which is presented in Section 3.4. The particle integration scheme is easy to implement and is theoretically suitable for any integrand and integration domain. The initiation/propagation of fractures and contact between objects in PNMM are performed on the second level of discretization as described in Section 3.5 and Section 3.6. The enrichment function in XFEM around the tip of fracture is adopted in PNMM to improve the accuracy. The particle aspect of PNMM is summarized in Section 3.7 for clarity. Its roles in PNMM and difference with other particle-based models are discussed. The JHB model is introduced and incorporated into PNMM to simulate the dynamic response of rock materials in Section 3.8. Parameters of JHB model adopted in this thesis are then given. Last, PNMM is implemented in programming language C++, aided by several commercial/free software and third-party libraries. Details are given in Section 3.9.

The proposed PNMM is suitable for simulations of rock dynamics, since it could be easily applied to study the heterogeneity of rock materials, the initiation and propagation of fractures, the detachment and post-failure behavior of fragments, the contact between blocks, and the rate-dependent behavior of rock, as will be validated in following chapters.

Chapter 4 PNMM Modelling of Some Fundamental Problems

In this chapter, several numerical examples are provided for the calibration of the proposed model. A cantilever beam bending test is first performed to verify the elastic performance of PNMM. Second, the Brazilian disc test is conducted as a static failure issue. Then, two examples on stress wave propagation are given to validate the ability of PNMM to simulate dynamic issues. Last, the rate-dependent failure under rock blasting is successfully simulated by PNMM, as a representative issue in rock dynamics.

This chapter is based on a paper published in the journal International Journal of Geomechanics:

Li, X., Zhang, Q. B., He, L., Zhao, J., 2017. Particle-Based Numerical Manifold Method to Model Dynamic Fracture Process in Rock Blasting. *International Journal of Geomechanics*. 17 (5), E4016014.

and a conference paper presented at the 2nd International Conference on Rock Dynamics and Applications (RocDyn-2) held on 18-19 May 2016 in Suzhou, China:

Li, X., Zhang, Q. B., He, L., Zhao, J., 2016. Validation study of the Particle-based Numerical Manifold Method (PNMM) on stress wave propagation, *Rock Dynamics: From Research to Engineering*. CRC Press, Suzhou, 335-340.

4.1 Cantilever Beam

An elastic-static analysis is first conducted to calibrate the proposed PNMM model. Through this test, the effects of particle resolution and the number of manifold element on calculation accuracy are discussed.

Considering the cantilever beam with a length of 40 mm and a height of 10 mm, as shown in Figure 4.1. The elastic constitutive model is adopted in this example. The model is supposed to be homogeneous. The Young's modulus of the beam is assumed to be 10 GPa. The Poisson's ratio of the beam is 0.3. A downward pressure is uniformly imposed on the right end of the beam. The value of the pressure is 1 MPa. The left end of the beam is fixed. The constant cover function is adopted in this simulation.

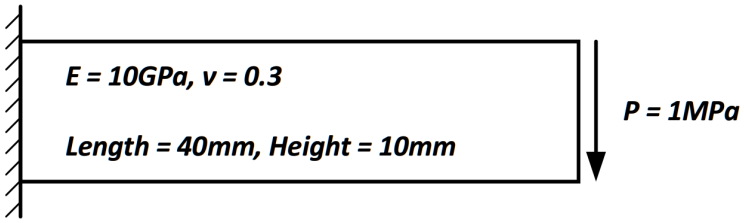

Figure 4.1 A cantilever beam

Analytical solution to the deflection of the cantilever beam is given by

$$w(x) = \frac{Fx^2}{6EI}(3L - x) = \frac{2Px^2}{EH^2}(3L - x) \tag{54}$$

where *F* is the load applied on the free end of the beam, *I* is the area moment of inertia of the beam's cross section, *L* is the length of the beam, and *H* is the height of the beam.

First, two models with the same mathematical cover, and therefore the same number of manifold elements, but different numbers of particles are established. There are 32 manifold elements and 400 evenly distributed particles (Figure 4.2a) in the Model I, while the Model II has 32 manifold elements and 10,000 evenly distributed particles (Figure 4.2b). The particle resolutions, defined as the ratio of the number of particles to the number of manifold elements, of these two models are 12.5 and 312.5 respectively. In simulations, the displacement in the direction of y-axis along the central line of the beam is taken as the deflection. Numerical results and the analytical prediction of the cantilever beam deflection are shown in Figure 4.3. Results in the figure demonstrate that a model with higher particle resolution leads to a more accurate result, which is as expected. However, the difference between the results of two models is in fact quite small and

negligible. This difference is mainly due to the effect of the number of particle on the accuracy of particle integration scheme, as has proved in the previous chapter.

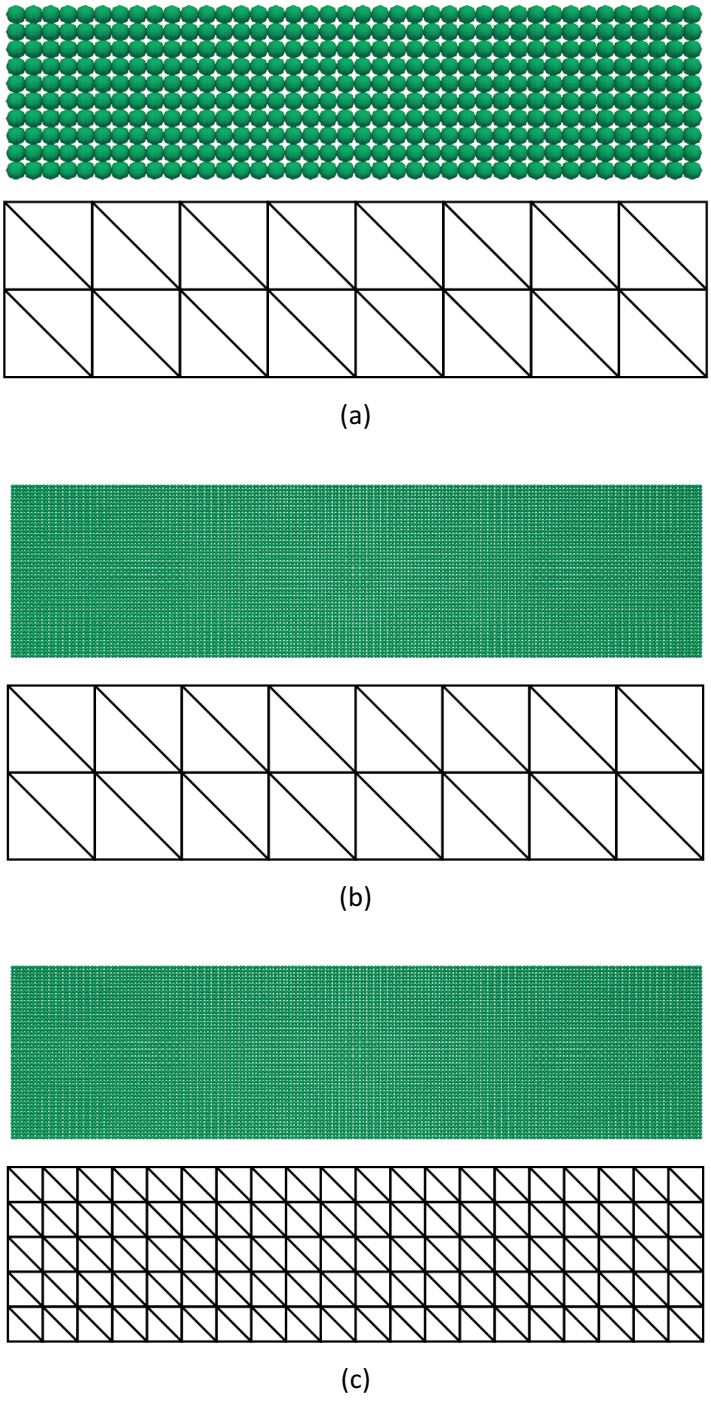

Figure 4.2 PNMM models for the cantilever beam: (a) Model I with 32 manifold elements and 400 particles; (b) Model II with 32 manifold elements and 10,000 particles; (c) 200 manifold elements and 10,000 particles

From the figure, we can also conclude that both of Model I and Model II give poor results for the beam deflection. The reason is that they both do not have enough manifold elements for bending problems. Recalling that the DOFs in PNMM are defined on manifold elements, rather than particles. Although Model II has much more particles that Model I, the number of manifold element of them are the same. Therefore, the number of DOFs in these two models are the same as well.

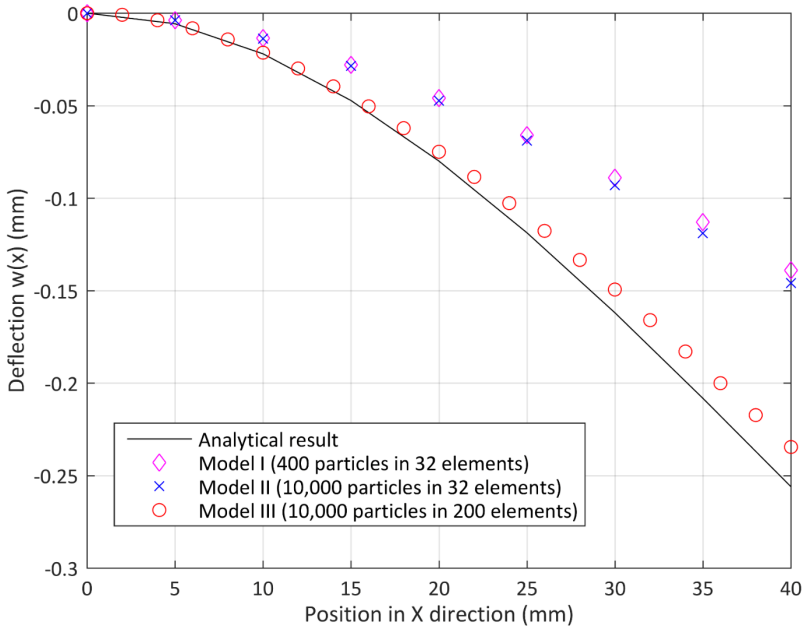

Figure 4.3 The deflection of the cantilever beam

A third model is introduced for this simulation. Model III (Figure 4.2c) has the same number of particles as Model II. But the number of manifold elements is increased to 200, by reducing the size of mathematical covers. As a result, the particle resolution of this model is equal to 50, which will be efficient for the particle integration scheme. The simulation result of Model III agrees well with the analytical result, as shown in Figure 4.3. It can be concluded that, in spite of a lower particle resolution, Model III still provides a much better result than Model II, as it has a larger number of manifold elements and, consequently, DOFs.

As can be seen from this example, the effect of particle resolution on the accuracy of PNMM is limited. For homogeneous models, the accuracy of PNMM is mainly controlled by the number of manifold elements.

4.2 Brazilian Disc Test

Brazilian disc test is an indirect experiment to measure the quasi-static tensile strength of rock. Considering a Brazilian disc test with the setup as shown in Figure 4.4. The radius of the rock disc is 25 mm. The rock material is assumed to be homogenous. The material properties are 20 GPa for Young's modulus and 0.2 for Poisson's ratio. The tensile strength of the material is set to be 2 MPa.

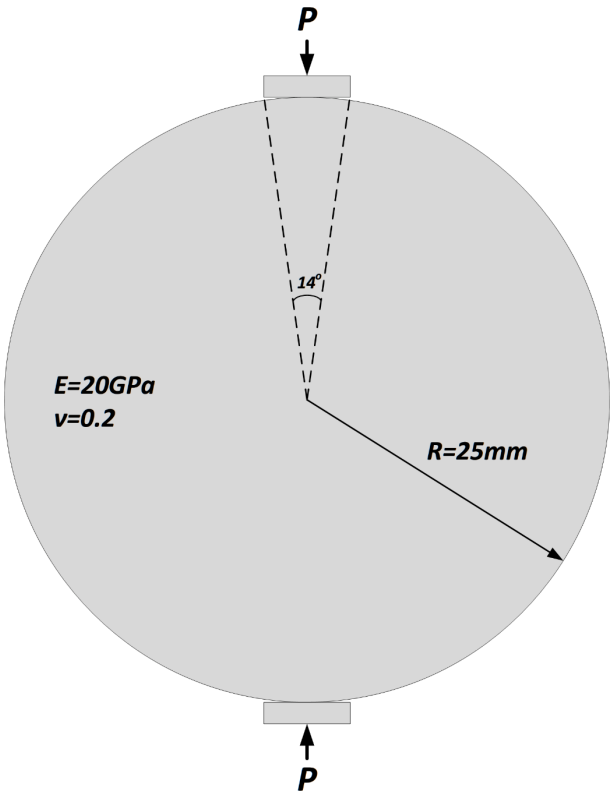

Figure 4.4 The Brazilian disc test model

The adopted PNMM model consists of 15,256 manifold elements and 65,122 particles. At the beginning of simulation, the load *P* at two ends of the disc is equal to zero. The load *P*

increases quasi-statically during the simulation with an increment of 1 kN per step. The mechanical response of the disc is calculated at every increment of the load until fails. Before the peak load P_{max} is reached, the model deforms elastically. At this stage, stresses are distributed in a representative way as shown in Figure 4.5.

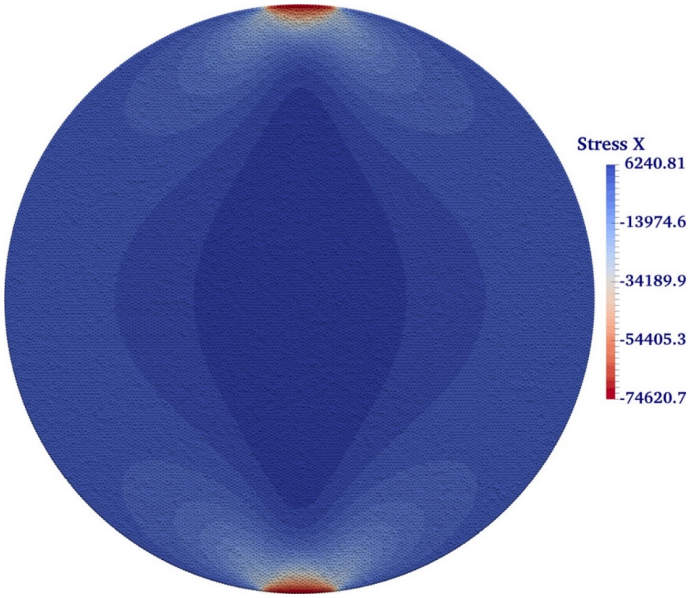

(a)

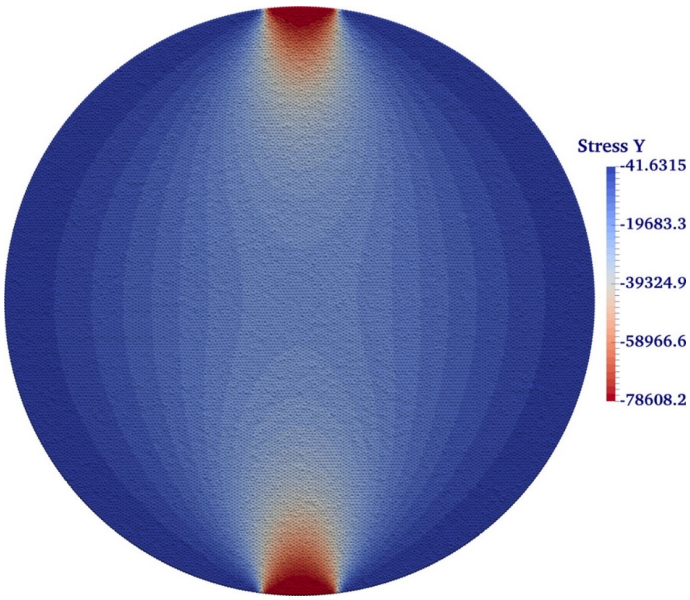

(b)

Figure 4.5 Stress distribution in the Brazilian disc: (a) sigma-x; (b) sigma-y

The peak load P_{max} in this simulation is 167 kN. When the applied load reaches this value, fractures appear in the center of the model and then propagates quickly towards the upper and lower bounds. The failure process is illustrated in Figure 4.6, in which the failed links are plotted as red straight lines. The simulated fracture pattern agrees well with experimental result in Figure 4.6d.

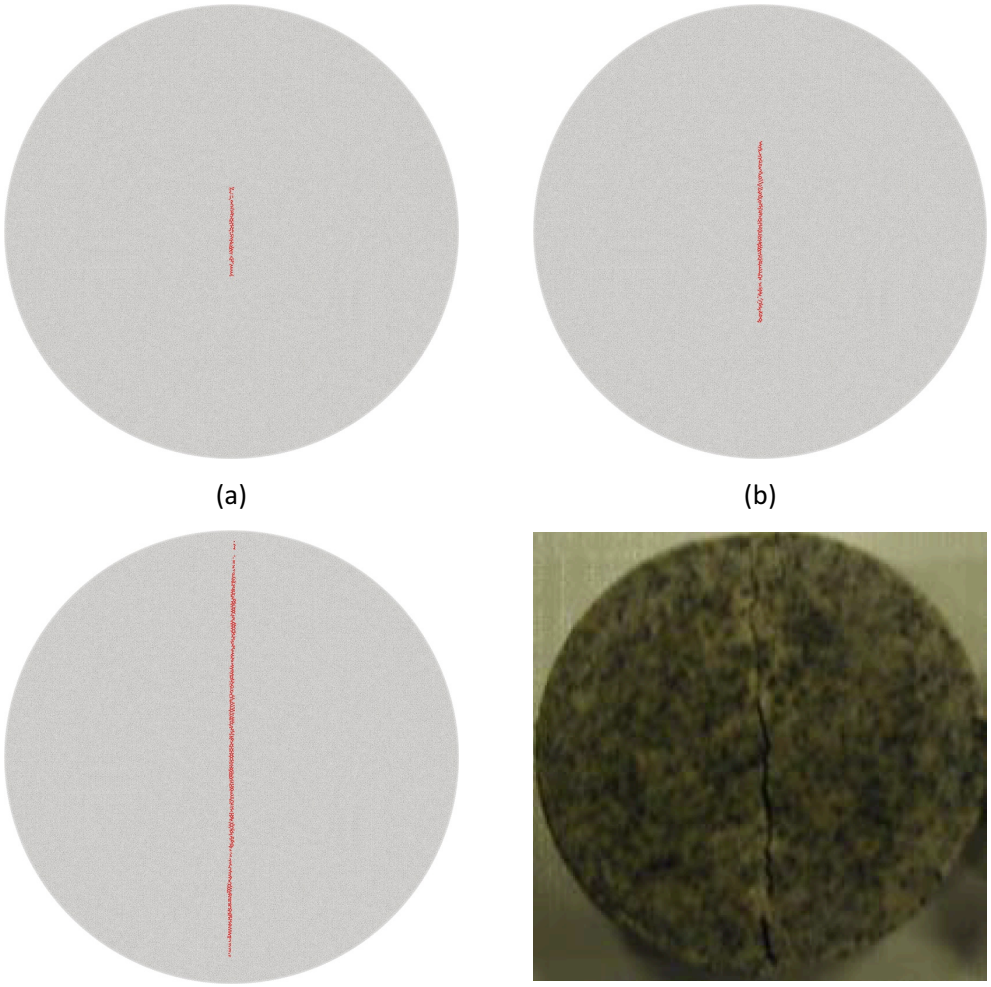

Figure 4.6 The process of fracture propagation in Brazilian disc test: fracture with a length of (a) 10 mm, (b) 20 mm, (c) 48 mm; and (d) experimental result (Liu, 2004)

In experiments, the tensile strength of the specimen is estimated as (Zhang and Zhao, 2014)

$$\sigma_t = \frac{P_{max}}{\pi t R} \tag{55}$$

where t is the thickness of the disc and R is the radius of the disc. Substituting the simulation result P_{max} = 167 kN into this equation, the indirectly measured peak strength is 2.126 MPa, which is close to the tensile strength adopted in the numerical simulation. Therefore, the accuracy of PNMM is confirmed.

4.3 Stress Wave Propagation

Stress wave propagation is an important issue in studying the dynamic fracturing of rock. Two numerical examples with elastic stress wave will be performed for validation.

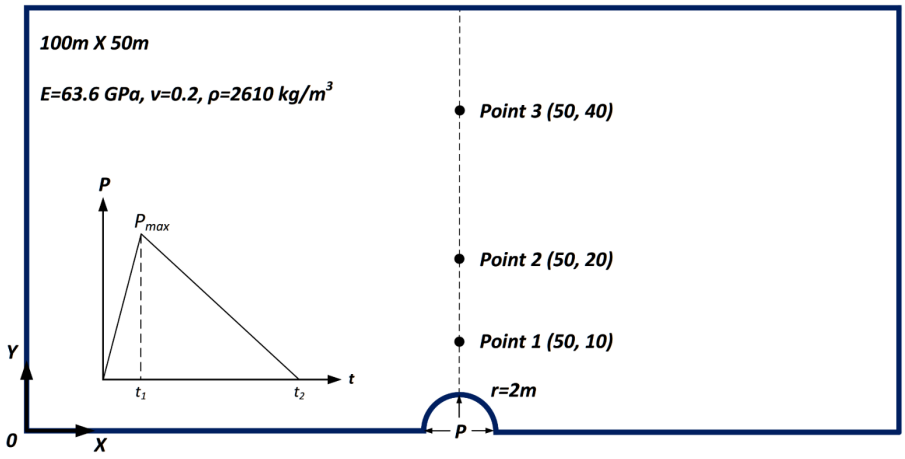

Figure 4.7 The stress wave propagation in a rock cavern

The first example illustrates the wave propagation in a rock cavern as shown in Figure 4.7. The rock cavern is semi-circle in shape. The radius of the cavern is 2 m. The modelling domain has a dimension of 100 m × 50 m. The rock material is assumed to be homogenous. The material properties are 63.6 GPa for Young's modulus, 0.2 for Poisson's ratio, and 2,610 kg/m^3 for density. The propagated wave is induced by an explosion load P uniformly applied on the surface of the rock cavern. The peak value of the load P_{max} is 30 MPa. The durations of the rising stage t_1 and the descending stage t_2-t_1 are 0.1 ms and 0.4 ms respectively. The theoretical velocity of P-wave is calculated as follow

$$v_P = \sqrt{\frac{E(1-\nu)}{\rho(1+\nu)(1-2\nu)}} \tag{56}$$

Substituting material parameters into the equation above, the velocity of P-wave in this example is calculated to be 5,203 m/s.

The adopted PNMM model consists of 10,298 manifold elements and 41,145 particles. Figure 4.8 shows the process of wave propagation in the rock cavern predicted by PNMM. The wave arrives at the upper bound of the model at the time of 9.72 ms, being in good agreement with the theoretical result 9.61 ms which can be easily derived from the theoretical wave velocity.

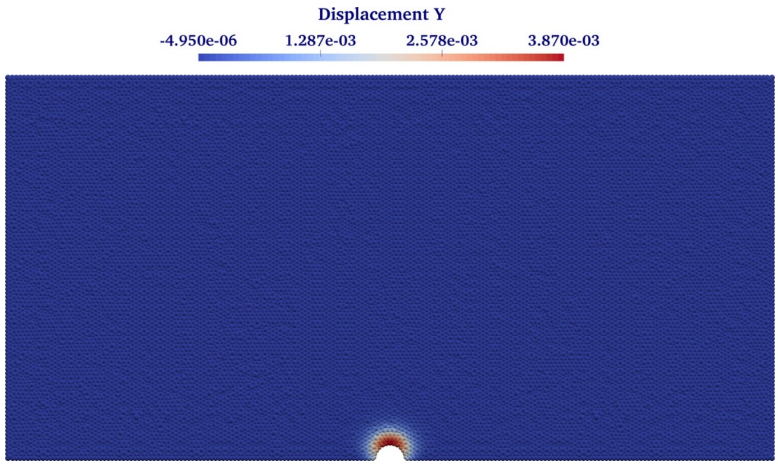

(a)

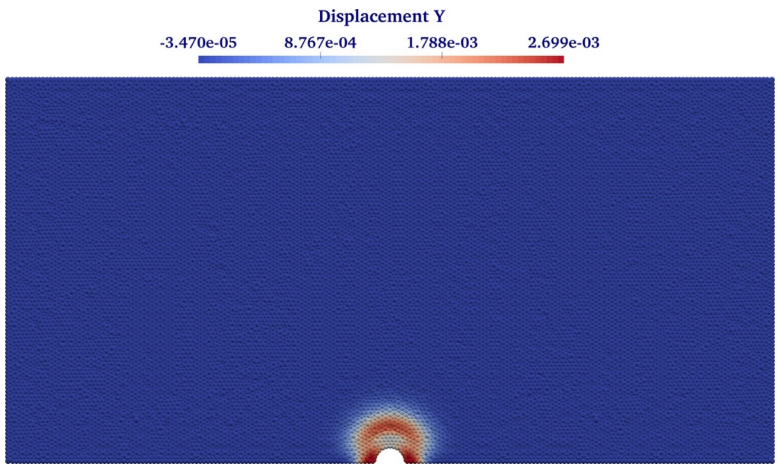

(b)

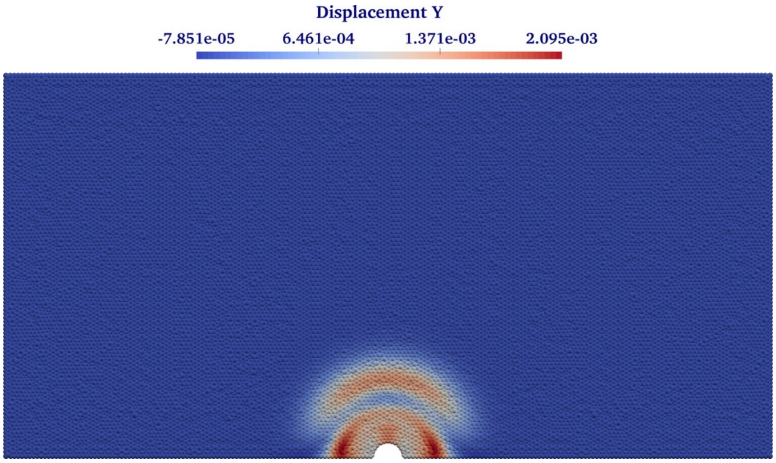
Displacement Y
-7.851e-05
6.461e-04
1.371e-03
2.095e-03

(c)

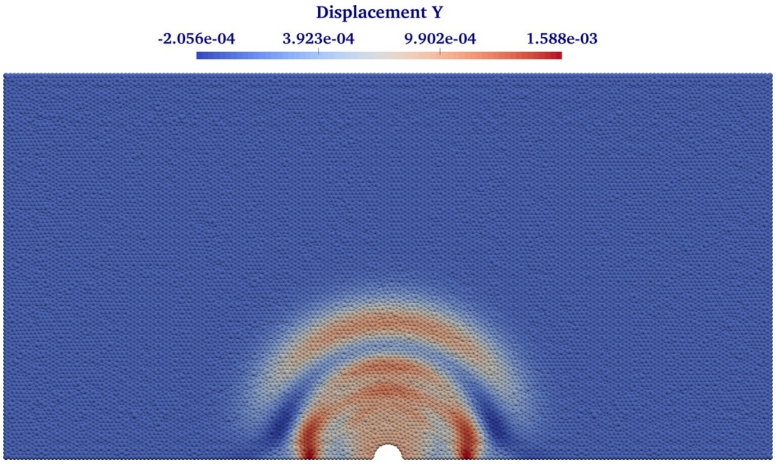
Displacement Y
-2.056e-04
3.923e-04
9.902e-04
1.588e-03

(d)

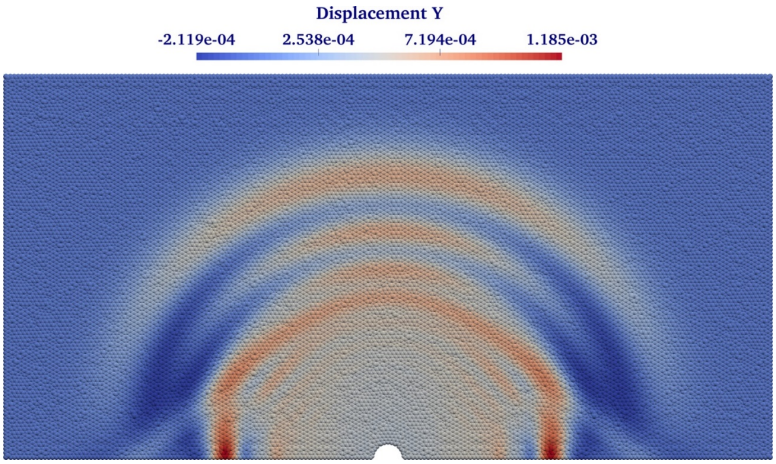
Displacement Y
-2.119e-04
2.538e-04
7.194e-04
1.185e-03

(e)

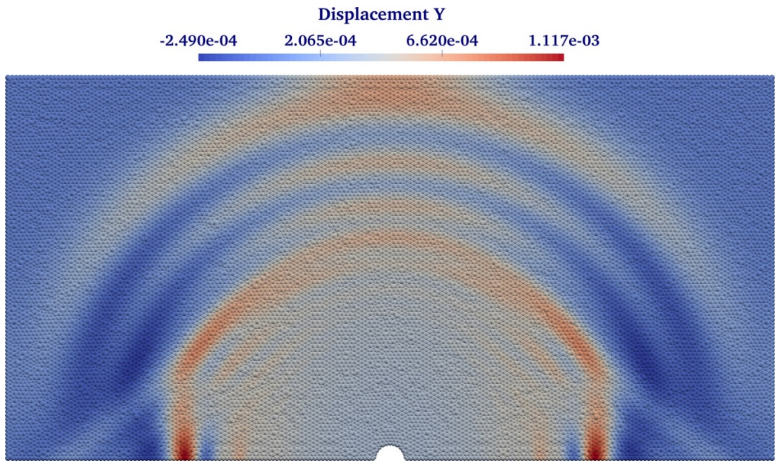

(f)

Figure 4.8 The stress wave propagation in a rock cavern: (a) t = 0.6 ms; (b) t = 1.2 ms; (c) t = 2.4 ms; (d) t = 4.0 ms; (e) t = 8.0 ms; (f) t = 10.0 ms

Three monitoring points have been set in the model as illustrated in Figure 4.7. The time-displacement results of three monitoring points obtained by PNMM agree well with those simulated by Abaqus, which is plotted in Figure 4.9. Therefore, the ability of PNMM in modelling wave propagation in homogeneous elastic materials is verified.

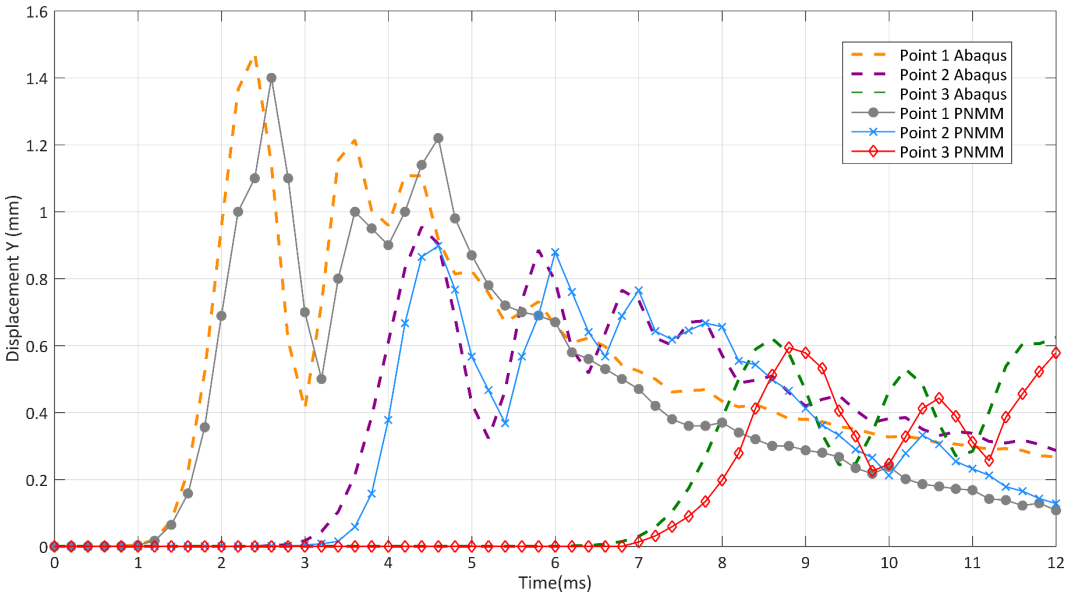

Figure 4.9 The stress wave propagation in a rock cavern: displacement histories at monitoring points

The second example is the stress wave propagation across a material interface. As shown in Figure 4.10, the lower half of the model is a rock cavern the same as the first part, while the upper half of the model is a rectangle domain with a dimension of 100 m × 50 m. The material properties of the rock part are 10 GPa for Young's modulus, 0.2 for Poisson's ratio, and 2,610 kg/m^3 for density. Material properties of steel are assigned to the upper part: 200 GPa for Young's modulus, 0.3 for Poisson's ratio, and 7,600 kg/m^3 for density.

The propagated stress wave is induced by an explosion load *P* uniformly applied on the surface of the rock cavern and transmitted to the steel part. The applied explosion load *P* is the same as that in the first example. Four monitoring points as illustrated in the figure are set to examine the incident wave, transmitted wave, and reflected wave.

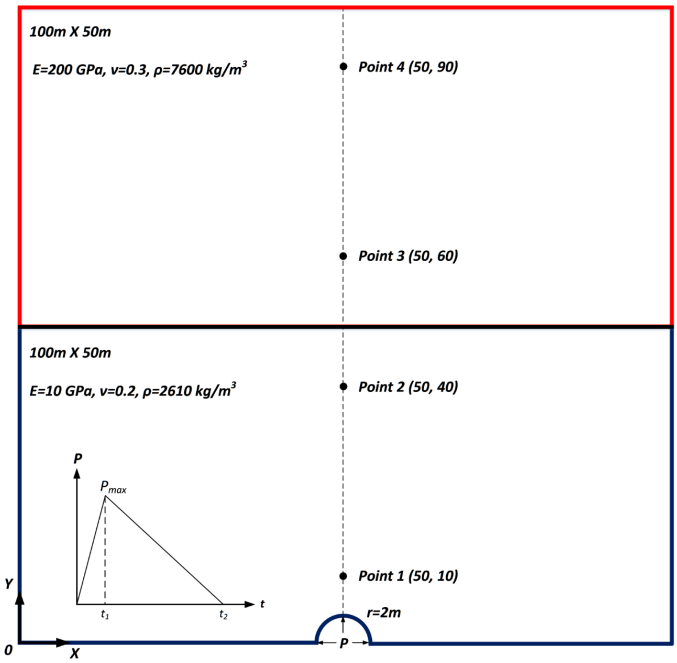

Figure 4.10 The stress wave propagation across a material interface

The adopted PNMM model consists of 22,452 manifold elements and 89,726 particles. Figure 4.11 shows the process of the stress wave propagation across material interface predicted by PNMM. The incident wave arrives the material interface at 24 ms (Figure 4.11b). This result agrees well with the theoretical wave velocity, which is calculated to

be 2,063.3 m/s. The transmitted wave and reflected wave are generated at the material interface (Figure 4.11). The transmitted wave arrives at the upper bound of the steel plate at about 30 ms (Figure 4.11d).

The time-velocity results at monitoring points obtained by PNMM are shown in Figure 4.12. From the result of Point 2, one can conclude that the reflected wave passes through at about 30 ms, as the velocity downwards in this period has a greater maximum value than the last period.

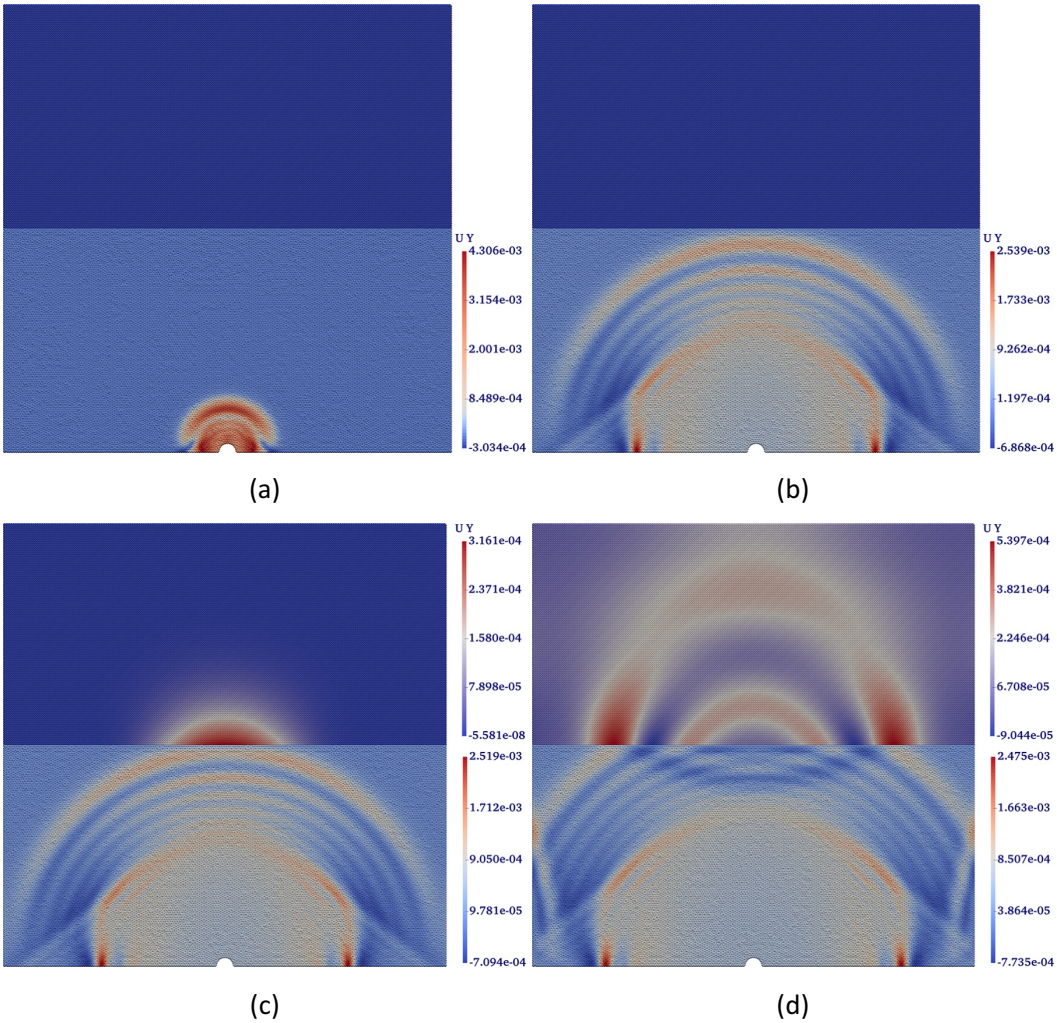

Figure 4.11 The stress wave propagation across a material interface: (a) t = 5 ms; (b) t = 24 ms; (c) t = 25 ms; (d) t = 30 ms

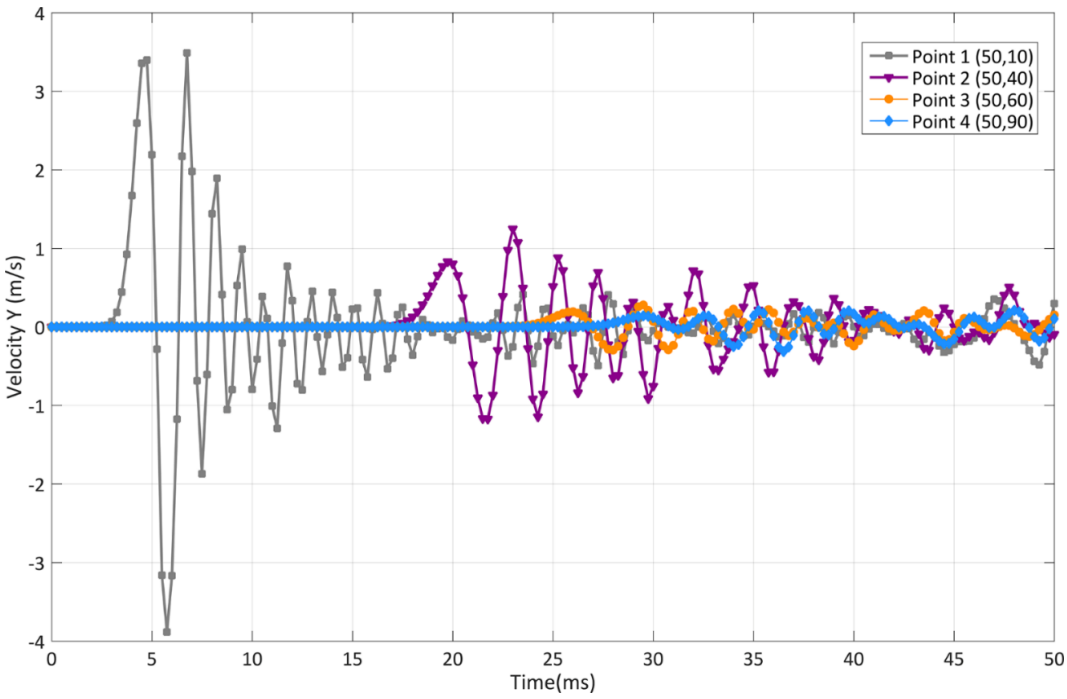

Figure 4.12 The stress wave propagation across a material interface: velocity histories at monitoring points

4.4 Rock Blasting under Different Loading Rates

In this section, PNMM is coupled with the JHB model to simulate rock fracturing subjected to dynamic loadings. Considering a borehole blasting issue as illustrated in Figure 4.13. The simulating domain is a square with the side to be 6 m in length. The domain has four non-reflecting boundaries in order to represent a large enough plane. The borehole locates at the center of the domain and has a diameter of 0.12 m.

Properties for the granite with good quality are used to simulate the rock material: 70 GPa for Young's modulus, 0.2 for Poisson's ratio, and 2,650 kg/m^3 for density. The bulk modulus K_1 is calculated to be 39 GPa by using the relationship

$$K_1 = \frac{E}{3(1-2\nu)} \tag{57}$$

where *E* is the Young's modulus and *v* is the Poisson's ratio. The static tensile of the rock material is 14 MPa. The compressive strength is 157 MPa. Other constants in the JHB model can be found in Section 3.8.

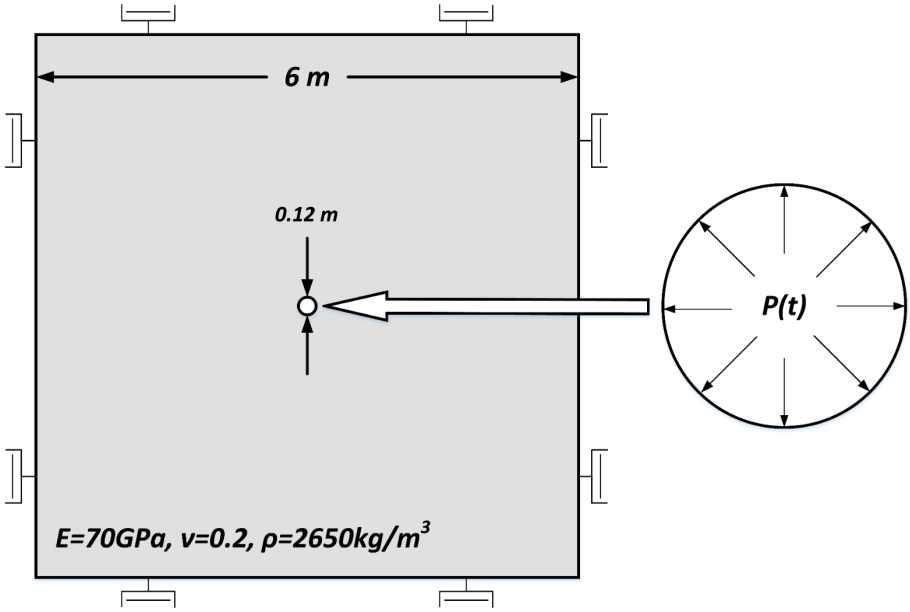

Figure 4.13 A borehole blasting

A radial pressure wave is applied uniformly on the borehole surface. The pressure is expressed in the general form of an impulse function as follow (Cho and Kaneko, 2004),

$$P(t) = P_0 \xi \left(e^{-\alpha t} - e^{-\beta t} \right) \tag{58}$$

with

$$\xi = \frac{1}{e^{-\alpha t_0} - e^{-\beta t_0}}, \quad t_0 = \frac{1}{\beta - \alpha} \ln \frac{\beta}{\alpha} \tag{59}$$

where P_0 is the peak pressure, α and β are two constants. In this example, the peak pressure P_0 is set to be 200 MPa and the ratio β/α is kept as a constant of 1.5. By setting the rising time t_0 to 10 μs, 20 μs, and 200 μs, three different cases can be obtained with the loading rate calculated to be 20, 10, and 1.0 MPa/μs respectively. The applied impulse pressures of three cases are graphically illustrated in Figure 4.14.

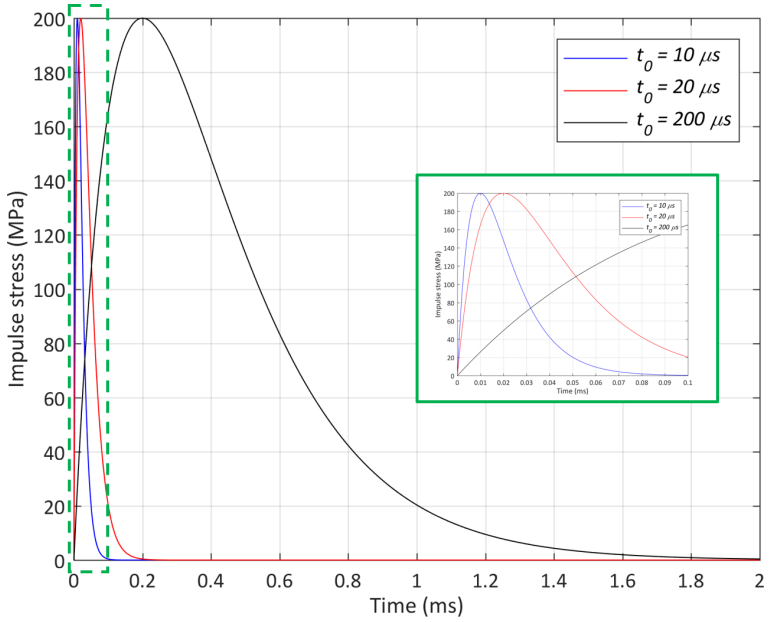

Figure 4.14 The applied impulse pressure in borehole blasting

The adopted PNMM model consists of 18,976 manifold elements and 81,632 particles. Simulation results for different loading rates are shown in Figure 4.15. Red lines in the figure indicate the fractures (i.e., failed links) within the rock. It is obvious that different loading rates produce distinct failure patterns. When the loading rate of the borehole pressure is high, a crushed zone is created around the borehole. It is believed that the crushed zone forms on condition that the explosion peak pressure exceeds the dynamic compressive strength of the rock material. The blast energy is greatly dissipated in creating the crushed zone and there is nearly no radial fracture occurred. The radius of crushing zone is about 0.25 m, which is 4.2 times the radius of the borehole. This is within the range observed in laboratory experiments which is from 1 to 10 (Hagan, 1979). The duration of the generation of crushing zone is 12 μs. When the loading rate is intermediate, the crushed zone appears slightly farther to the borehole with a radius of 0.31 m. Meanwhile, the alleviated crushed zone is followed by several short fractures in radial direction. The longest radial fracture has a length of 0.57 m. When the loading rate further decreases, the crushed zone shrinks to about 0.16 m. However, massive long radial fractures occur and therefore leads to a bigger fracture area. The longest radial fracture is 1.73 m in length.

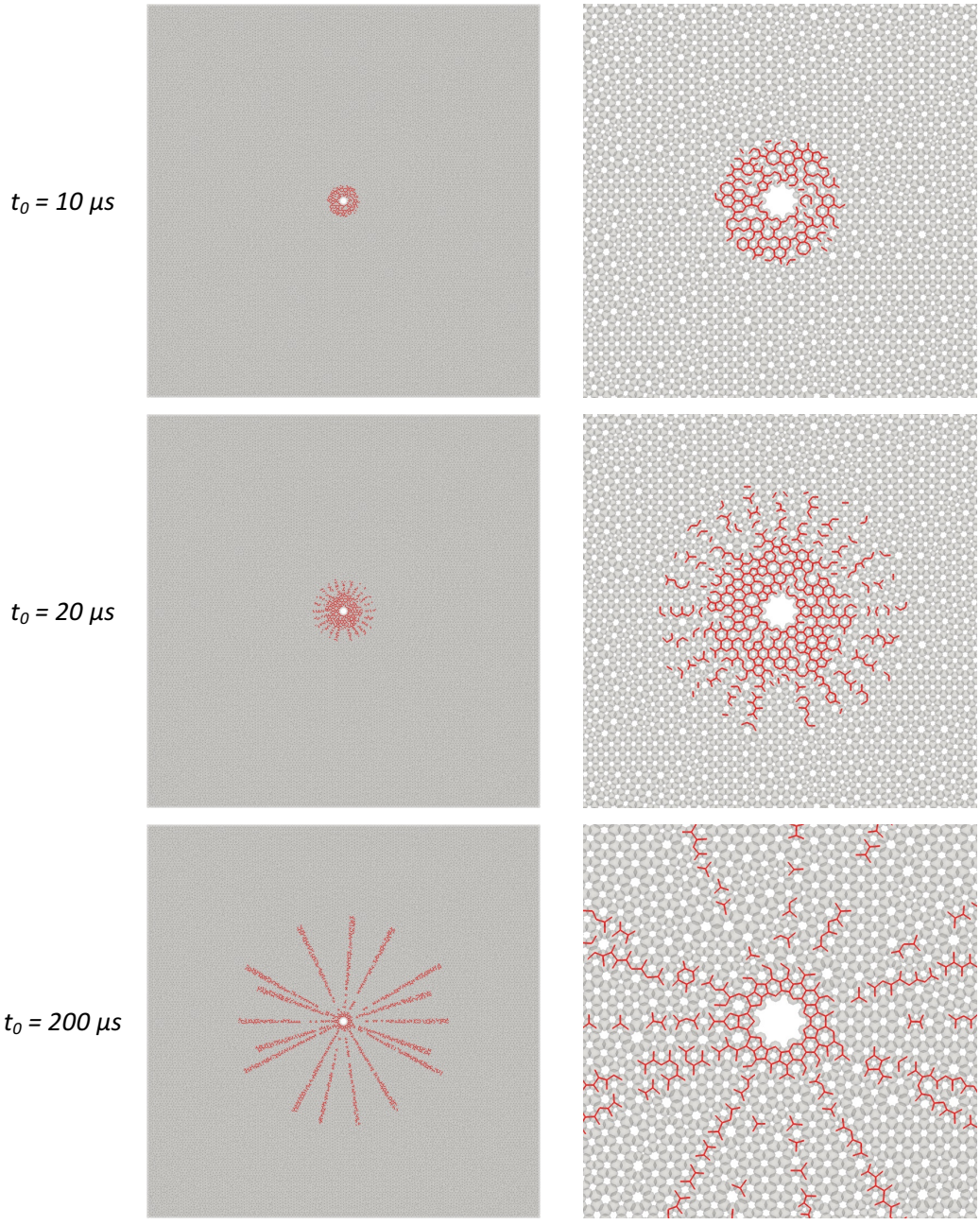

Figure 4.15 The borehole blasting under different loading rates: (a) global view; (b) enlarged view around the borehole

The fracturing process with the lowest loading rate is shown in Figure 4.16. As can be seen, a crushing zone is first created. At the outer bound of the crushing zone, localized fractures are then generated and finally grow radially without preferential directions. In practice, long radial fractures with a minimal crushed zone is usually regarded as an

efficient blasting operation. Therefore, simulation results here indicate that the loading rate should be controlled as low as possible to improve the efficiency, which is also beneficial to the damage control.

The results in this section agree well with the findings reported in (Donzé et al., 1997, Cho et al., 2003) and the numerical simulation results in (Munjiza et al., 2000, Ma and An, 2008).

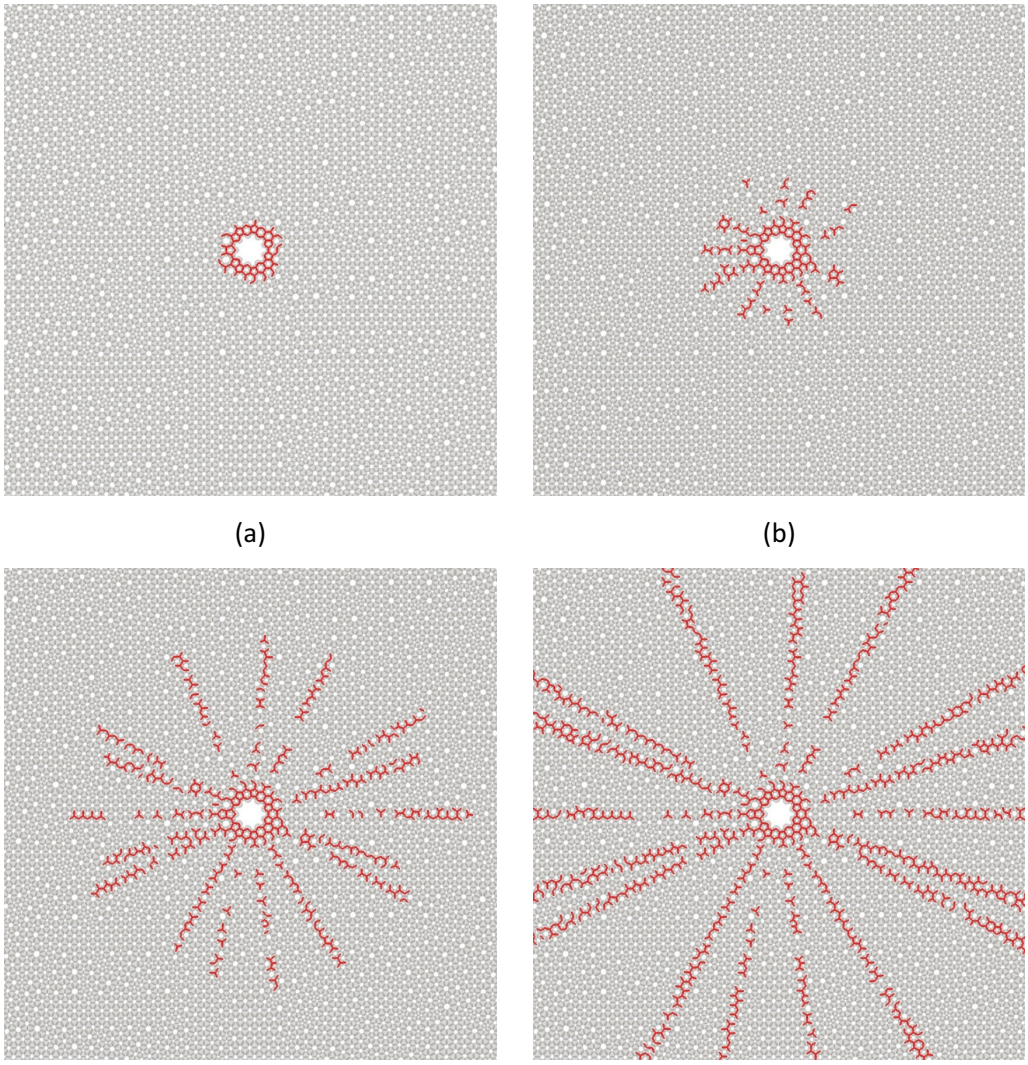

Figure 4.16 The fracturing process of borehole blasting with t_0 = 200 μs: (a) t = 50 μs; (b) t = 120 μs; (c) t = 250 μs; (d) t = 500 μs

4.5 Summary

This chapter presents several calibration examples of the proposed PNMM model. A cantilever beam is studied to validate PNMM for static issues. The Brazilian disc test is conducted to validate PNMM for fracturing issues under quasi-static conditions. Two examples of stress wave propagation demonstrate the applicability of PNMM for dynamic issues. The incorporated JHB failure model is examined by a borehole blasting simulation. The fracturing pattern under different loading rates agree well with the findings and simulations in literature. Simulation results also indicate that the accuracy of PNMM is primarily determined by the number of manifold elements. However, the number of particles should still be carefully chosen to ensure the accuracy of the particle integration scheme, as well as the path of fracture propagation.

Chapter 5 Rock Scratch Test and Its Fragmentation Process

This chapter presents a numerical study of rock scratching using PNMM. The scratching processes with different cutting depths are first simulated, where the failure pattern and cutting force are discussed. Then, a parametric study is performed by a series of numerical simulations. The effect of cutter operational parameters on the cutting force and energy consumed by the cutter are studied. Three operation parameters of the cutter are considered in this chapter, including the cutting depth, cutting speed, and cutter rake angle. Advices are given to improve the efficiency of rock cutting in engineering practice.

This chapter is based on a paper accepted by the journal *Tunnelling and Underground Space Technology*: Li, X., Zhang, Q. B., and Zhao, J. A numerical study of rock scratch tests using the particle-based numerical manifold method.

5.1 Introduction

The interaction between rock and a cutting tool has been at the core of many rock engineering applications, including exploration drilling, mining, tunnelling, sawing, and grinding. With a noticeable trend to mine and drill for reserves at greater depth in recent years, the demand for the continual cutting of rock at high in-situ stress and high temperature conditions is rapidly increasing in civil engineering industries. Low cutting efficiency and high cutter consumption due to poor cutting conditions has been regarded as one of the main problems encountered in deep ground projects (Gong et al., 2016). A better understanding of the rock-tool interaction is necessary to overcome this problem.

The rock cutting process involves penetrating a cutting tool into the rock and removing a fraction of rock material by moving the cutting tool. There are typically two types of rock

cutting in practice: cutting with a cutter and normal indentation with a wedge (Huang et al., 2013). The difference between these two processes is the moving direction of the cutting tool. In the *indentation* process, the cutting tool, usually a wedge indenter, penetrates into and induces a fragmentation of rock. The direction of the motion of the cutting tool is normal to the surface of rock. Research on this type of rock cutting process can be found in (Liu et al., 2002, Gong et al., 2005, Gong et al., 2006a, Gong et al., 2006b, Ma et al., 2011, Wang et al., 2011b, Li et al., 2016, Tkalich et al., 2016, Xiao et al., 2017). In the other cutting process, the direction of the motion of the cutting tool is parallel to the surface of rock at a certain penetration depth. This type of rock cutting process is also termed as *scratching*.

The scratch test is probably one of the oldest techniques in the characterization of mechanical material properties, since the Mohs' hardness scale was introduced to quantify the scratch resistance of minerals in 1824 (Akono et al., 2011). Following the effort initiated by Detournay and Defourny (1992), the scratch test has emerged as a promising alternative to determine the strength of various materials ranging from soft to hard, including polymers, metals, ceramics, and rocks (Akono and Ulm, 2011, Rodriguez et al., 2017). Attractively, extensive experiment results have clearly showed a relationship between the energy consumed in a scratch test and the uniaxial compressive strength of rocks, on condition that the cutting depth is shallow (Schei et al., 2000, Richard et al., 2012, Che et al., 2016). Theoretical analysis and experimental observations also indicated a ductile-brittle failure transition of rock when the cutting depth goes from shallow to deep (Richard, 1999, Huang and Detournay, 2008).

However, the mechanism of scratch tests remains a challenging problem due to its complexity. In the process of a scratch test, problems of the tool-rock interaction, fracture initiation and propagation in rocks, and the separation of rock fragments are involved. Besides, the setup of a scratch test is also found to influence the testing result (He et al., 2017).

Considering the limited applicability of analytical solutions, numerical simulations have been widely performed on this topic. Kou et al. (1999) utilized RFPA to simulate the scratch test of inhomogeneous rocks and successfully predicted the damage under and ahead of the cutter and variously shaped chips ahead of the cutter. However, due to the limitation of their model, they failed to simulate the complete process of scratch tests but could only predict the initiation of fractures due to the contact between the cutter and rock. Huang and Detournay (2008) showed an intrinsic length scale of rock material could influence its behaviour in scratch tests using DEM. The effect of the intrinsic length scale on the critical depth of the ductile–brittle failure mode transition is further studied in (Huang et al., 2013). However, their simulation results were found to considerably overestimate the effect of the length scale when comparing to experimental results, due to the sensitivity of particle distributions and micro parameters in DEM. He and Xu (2015) attempted to overcome this sensitivity and obtain a more realistic ratio between compressive and tensile strength by proposing a cluster DEM. Zhou and Lin (2014) revisited this length scale in FEM. Similarly, Jaime et al. (2015) utilized an explicit FEM to simulate the fragmentation of rock and the force applied on the cutter during a complete scratch test. However, due to the limitation of FEM, failed elements were immediately eliminated from the model, leading to a so-called zero cutting force phenomenon and a considerable low energy consumed by the cutter in their simulation. A fine enough mesh must be adopted in FEM to overcome this shortcoming.

In fact, the characters of PNMM are especially suitable for the simulation of a scratch test. Considering that PNMM is an inherently continuum-discontinuum model, it is capable of simulating the interaction between the cutter and rock, the initiation and propagation of fractures, the separation and post-failure motion of fragments, and the rate-dependent behaviour of rock materials. Therefore, in this chapter, PNMM is applied to the study of rock scratch tests. The complete scratching process of rock is first simulated. Then, the transition of ductile and brittle failure is presented. Last, parametric studies are performed to investigate the effect of cutting setup on the energy consumed by the cutter.

5.2 Numerical Model

The setup for the scratch test in this research is shown in Figure 5.1a. The rectangular rock sample has a length of 38.4 mm and a height of 8.0 mm. The rock sample is supposed to be homogenous. Material properties of the South Africa gabbro (Zhang, 2014) are assigned to the rock sample: 2,900 kg/m^3 for density, 61.0 GPa for Young's modulus, 0.13 for Poisson's ratio, 11.55 MPa for static tensile strength, and 227.2 MPa for compressive strength. The JHB parameters of the rock can be found in the Section 3.8 of this thesis.

An inclined thin cutter in the shape of a rectangle is adopted in the simulation, representing a perfectly sharp cutter in scratch tests (Adachi et al., 1996). For a sharp cutter, the only force between the rock sample and cutter is applied on the inclined surface of the cutter. The cutting force has two components: one is the pressure in the direction normal to the cutter surface, the other one is the friction in the direction parallel to the cutter surface. The cutter moves rightward at a constant cutting speed. The cutting direction is parallel to the surface of the rock sample. In this simulation, the cutter is supposed to be rigid. The contact force applied on the cutter surface is recorded during scratching. Three operational parameters of the cutter are taken into consideration, including the cutting depth d, rake angle ϑ, and cutting speed v, as illustrated in Figure 5.1b. The effect of operational parameters will be studied in this research. The PNMM model for this simulation consists of 62,370 manifold elements and 374,220 particles.

It is important to measure the efficiency of rock cutting from the energy point of view. In scratch tests, the mechanical specific energy (MSE) is defined as the energy consumed by the cutter to remove a unit volume of rock (Detournay and Defourny, 1992). In a special case, where the cutter is moving at a constant cutting speed v with a constant cutting depth d, MSE could be simply defined as (Jaime et al., 2015)

$$MSE = \frac{Work\ by\ cutter}{Volume\ of\ removal} = \frac{F_H x}{Volume\ of\ removal} \tag{60}$$

where F_H is the average cutting force parallel to the horizontal direction, x is the travel distance of the cutter, and the *volume of removal* in PNMM simulations is the size of

particles (rock fragments and dust) that are removed from the model (rock sample). The unit of MSE can be expressed as MJ/m^3 or MPa.

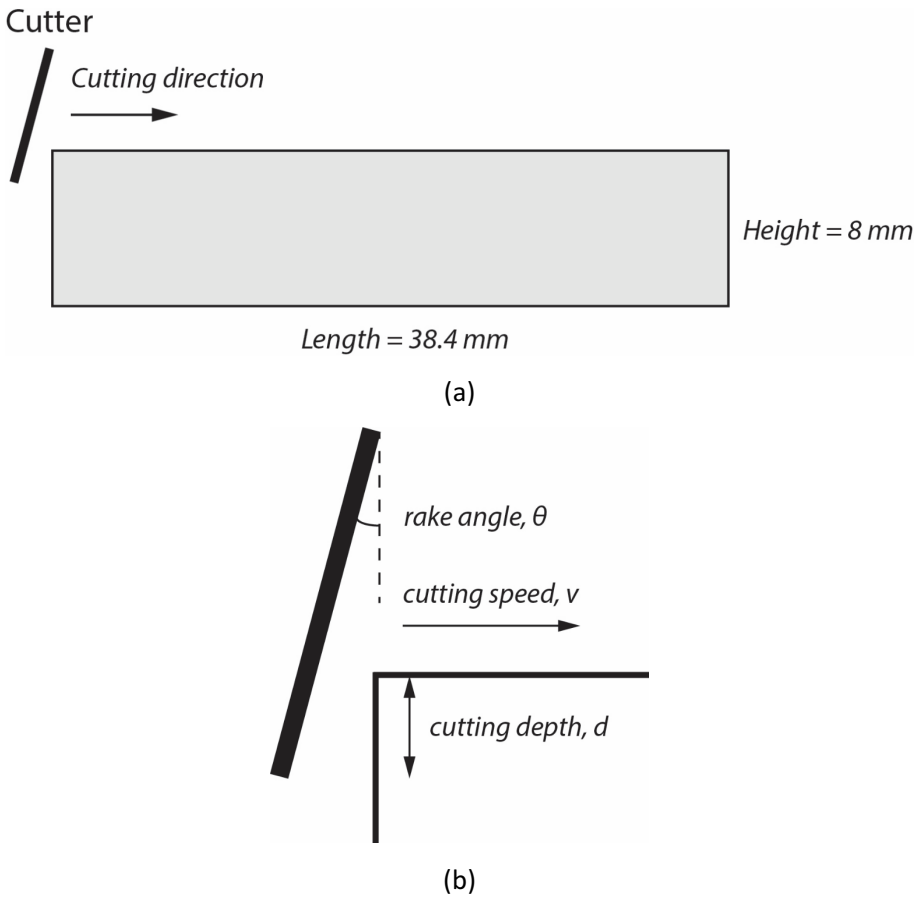

Figure 5.1 The rock scratch test: (a) geometry conditions; (b) cutter

5.3 Brittle and Ductile Failure

It has been well known that there is a critical cutting depth in scratch tests, at which the failure mode of rock will be changed. When the actual cutting depth is smaller than the critical depth, i.e. in a shallow cutting, the rock failure displays the characteristics of a ductile failure mode and cutting energy is primarily dissipated within the failed material, as illustrated in Figure 5.2a; When the actual cutting depth is larger than the critical depth, i.e. in a deep cutting, the failure mode of rock becomes brittle and cutting energy is mainly dissipated in creating fractures ahead of the cutter and the kinetic energy of rock fragments, as shown in Figure 5.2b.

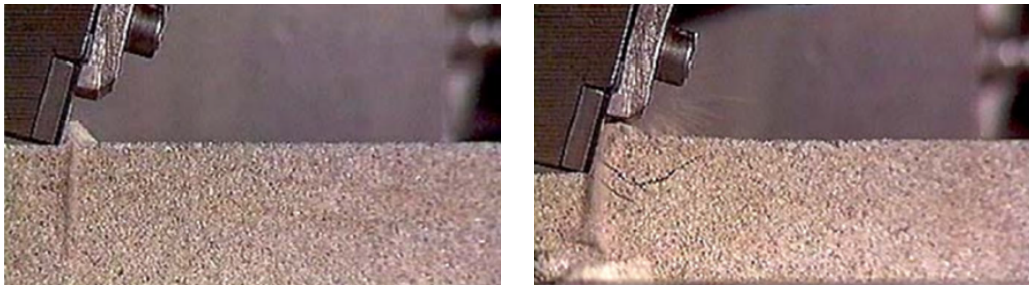

(a) (b)

Figure 5.2 Failure modes in experimental scratch tests: (a) ductile failure in shallow cuts; (b) brittle failure at deep cuts (Richard, 1999).

For rock cutting process, such as drilling and tunnelling, a ductile failure mode is often preferable to a brittle mode, as it is in a gentle way and safe to workers and equipment. However, since the efficiency of a ductile cutting is lower than that in a brittle mode, a deeper cutting is preferable in practice. Besides, researchers have shown that the critical depth of rock is closely related to and, hence, can be used to measure its uniaxial compressive strength. Therefore, estimating the critical depth of a rock has been an important question in scratch tests (He and Xu, 2016, He et al., 2017, Zhou and Lin, 2013).

The phenomenon of the transition from ductile to brittle failure with an increasing cutting depth will be examined in this section to validate the simulation results of PNMM. For this purpose, three cases with a same rake angle of 15° and a constant cutting speed of 4 m/s are performed. The cutting depths are 0.2 mm, 0.5 mm, and 1.0 mm in three cases respectively. It should be noted that the cutting speed in this simulation is much higher than that in an experimental test, which is usually on the order of mm/s. The reason for this high cutting speed is to shorten the scratching process and to reduce the computation time to a practical level (3 days for each case). The cutting speed we adopted is the same as that in the FEM analysis performed by Jaime et al. (2015).

For the case with a cutting depth of 0.2 mm, the simulated scratching process is presented in Figure 5.3. Red dots in Figure 5.3a indicate the particles with failed links (i.e., fractures). The cutter is not plotted in the figure for the sake of clarity. Simulation results show that

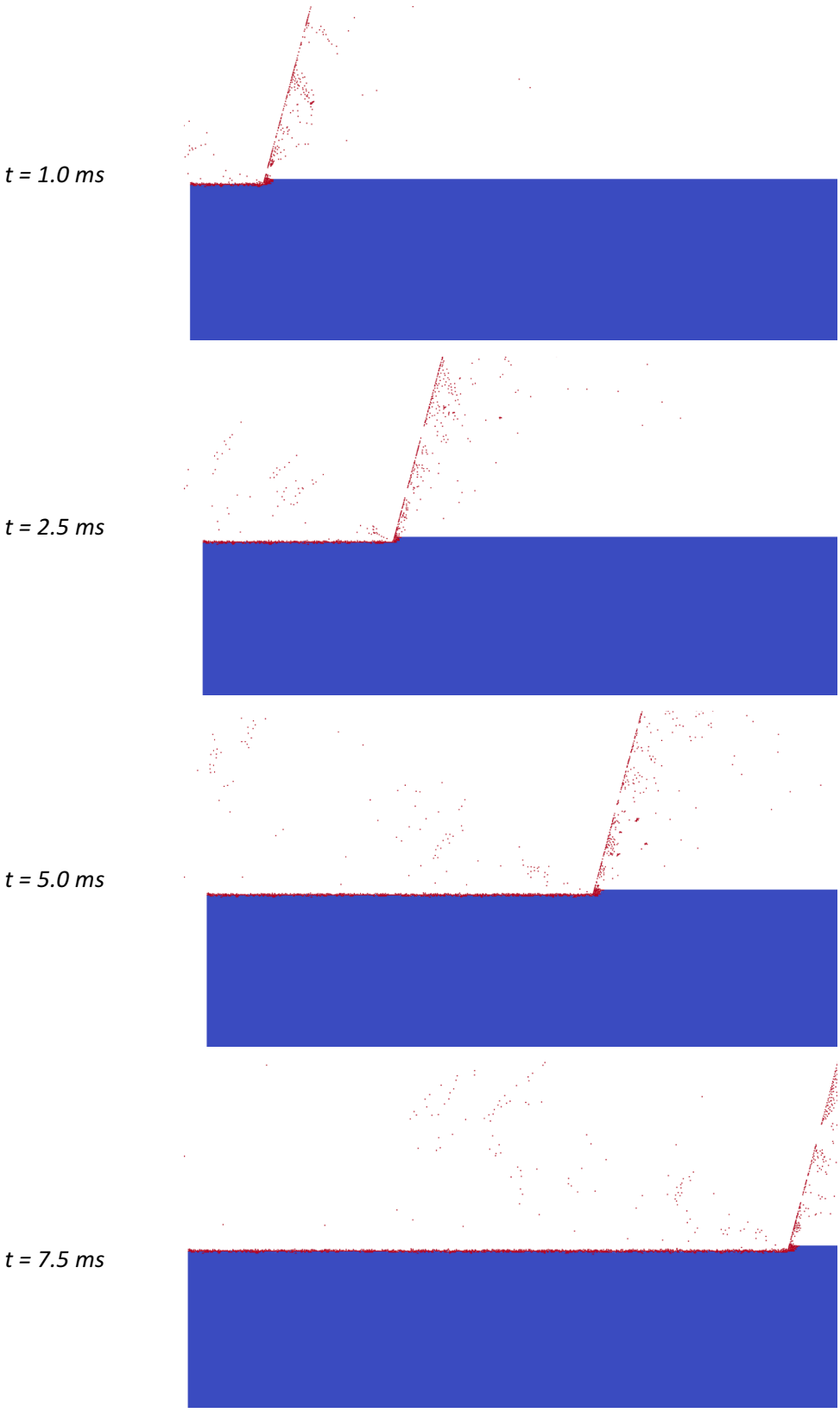

(a)

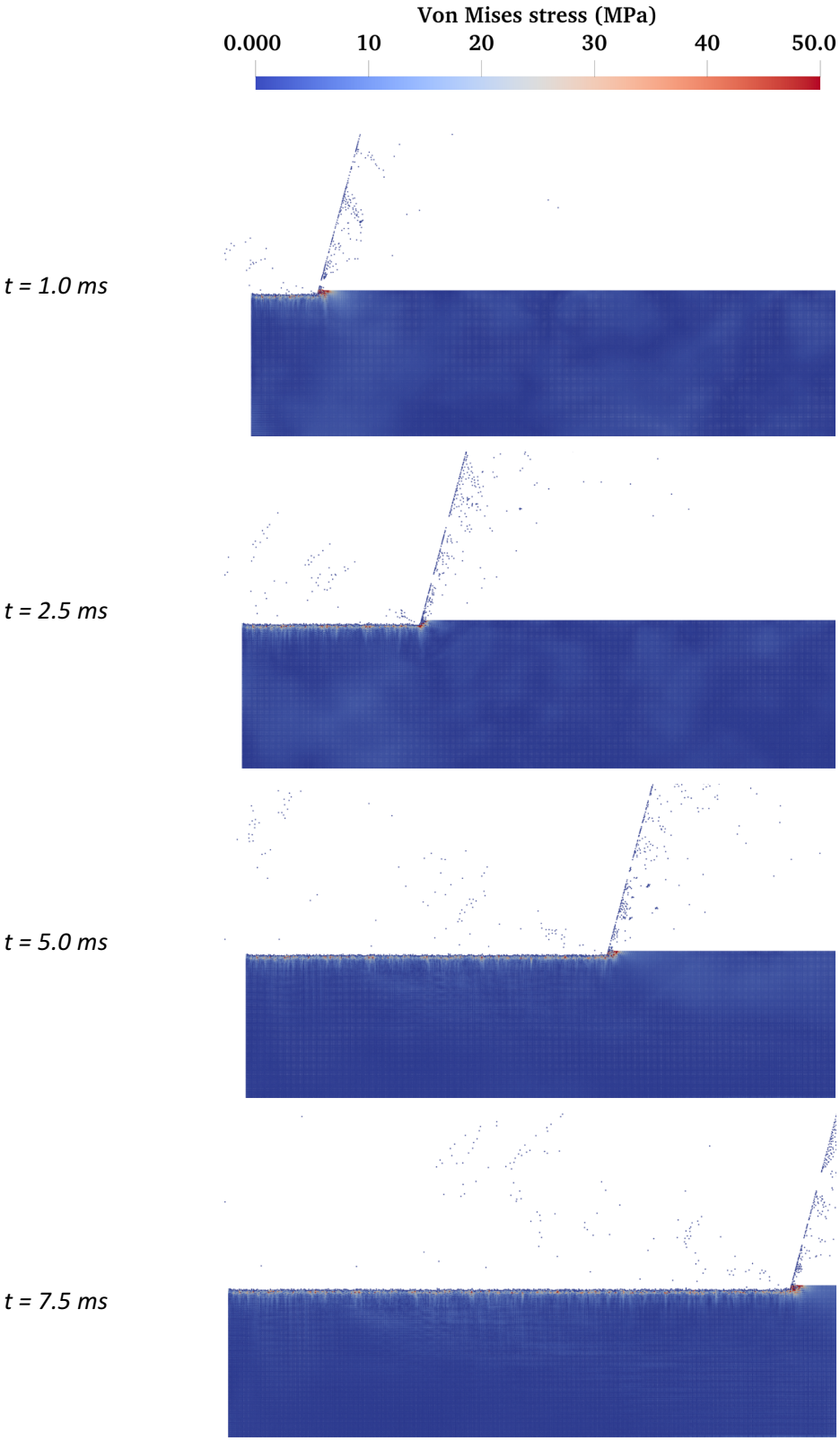

(b)

Figure 5.3 The scratching process of a shallow cut: (a) distribution of fractures (red dots indicate failed materials); (b) distribution of von Mises stress

the stress concentration occurs in a small region around the tip of the cutter. The propagation of material failure is almost consistent with the moving of the cutter. All particles along the path of the cutter are fractured from the rock sample. No fragment is generated in this case. Instead, rock dust (represented by individual particles) pile up along the surface of the cutter. Rock dust in front of the cutter has a high velocity to move upward rather than remain on the surface of the rock sample, due to the high cutting speed we adopted. There is some rock dust left behind the cutter, due to the shape of the cutter we used. After the scratching process is completed, a thin layer of dust is left on the surface of rock sample, and the rock sample has a smooth surface.

For the case with a cutting depth of 0.5 mm, simulation results are shown in Figure 5.4. The scratching process of this case is similar to the case of 0.2 mm. The ductile mode of failure still dominates. However, there are a small number of rock fragments generated in the test, e.g., at the tip of the cutter when t = 5.0 ms (Figure 5.4c). The generated rock fragments usually do not pile up along the surface of the cutter, but have a higher velocity than the cutter to fly forward. After the scratching process is completed, a layer of dust is left on the surface of rock sample as well, whereas the rock sample has a less smooth surface than the previous case. It could be concluded that when the cutting depth is intermediate, the dominating model of failure is in the transition from ductile to brittle. This result validates the experimental observation in (Dagrain et al., 2004)

Simulation results of the case with a cutting depth of 1.0 mm are presented in Figure 5.5. The brittle mode of failure dominates in this case. Although there is still rock dust generated by scratching, the number and size of rock fragments are both considerably increased. The ratio of the size of rock fragments to the size of rock dust is approximately 60:40. The fragment is typically initialed by the fracture from the tip of the cutter to the rock surface in front of the cutter (Figure 5.5a). Once a fragment is generated in this way, rock materials in the small area in front of the cutter tip have a great chance to be crashed into rock dust by the cutter (Figure 5.5c). Velocities of rock fragments are usually greater than the cutter in the forward direction. It is also common to see the rotation of rock fragments. The surface of the rock sample is quite rough after the scratching process is completed in this case.

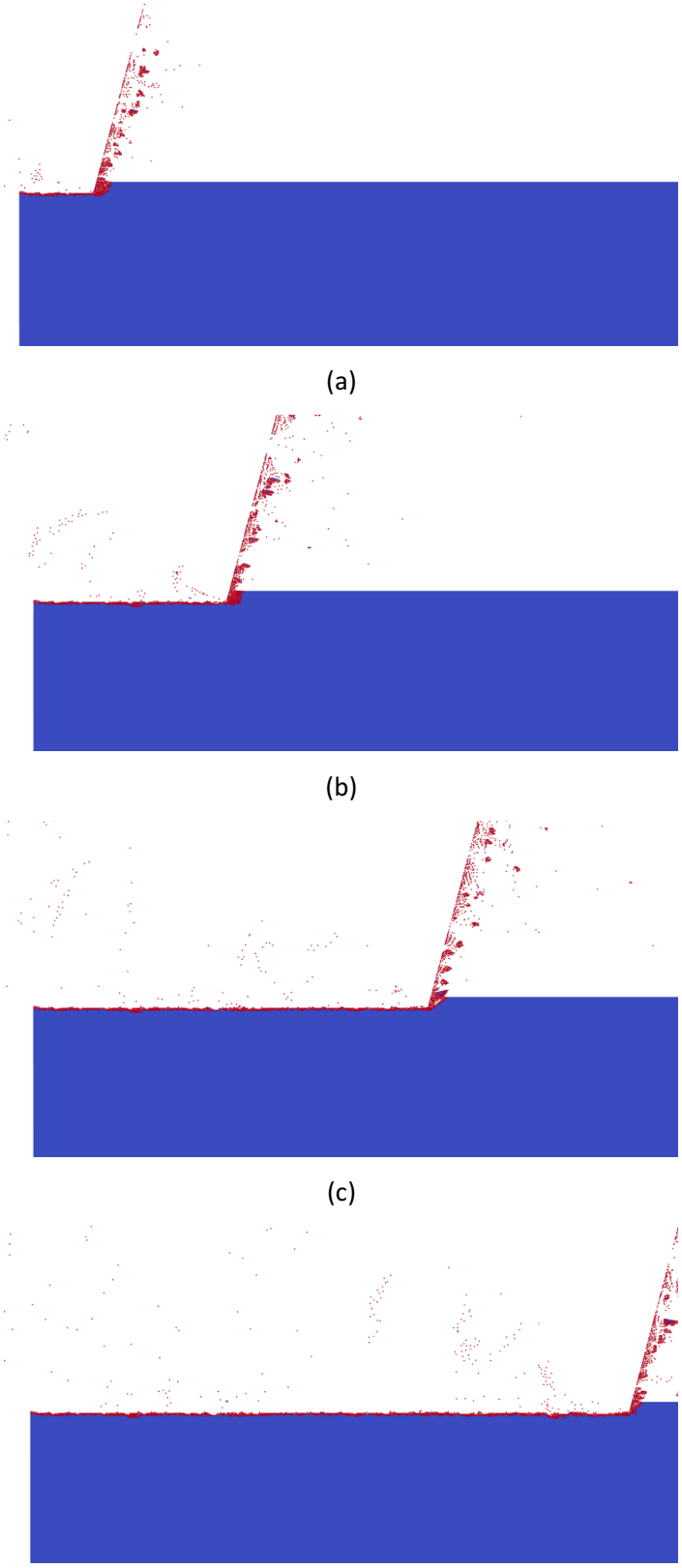

(a)

(b)

(c)

(d)

Figure 5.4 The scratching process of an intermediate cut: (a) t = 1.0 ms; (b) t = 2.5 ms; (c) t = 5.0 ms; (d) t = 7.5 ms (red dots indicate failed materials)

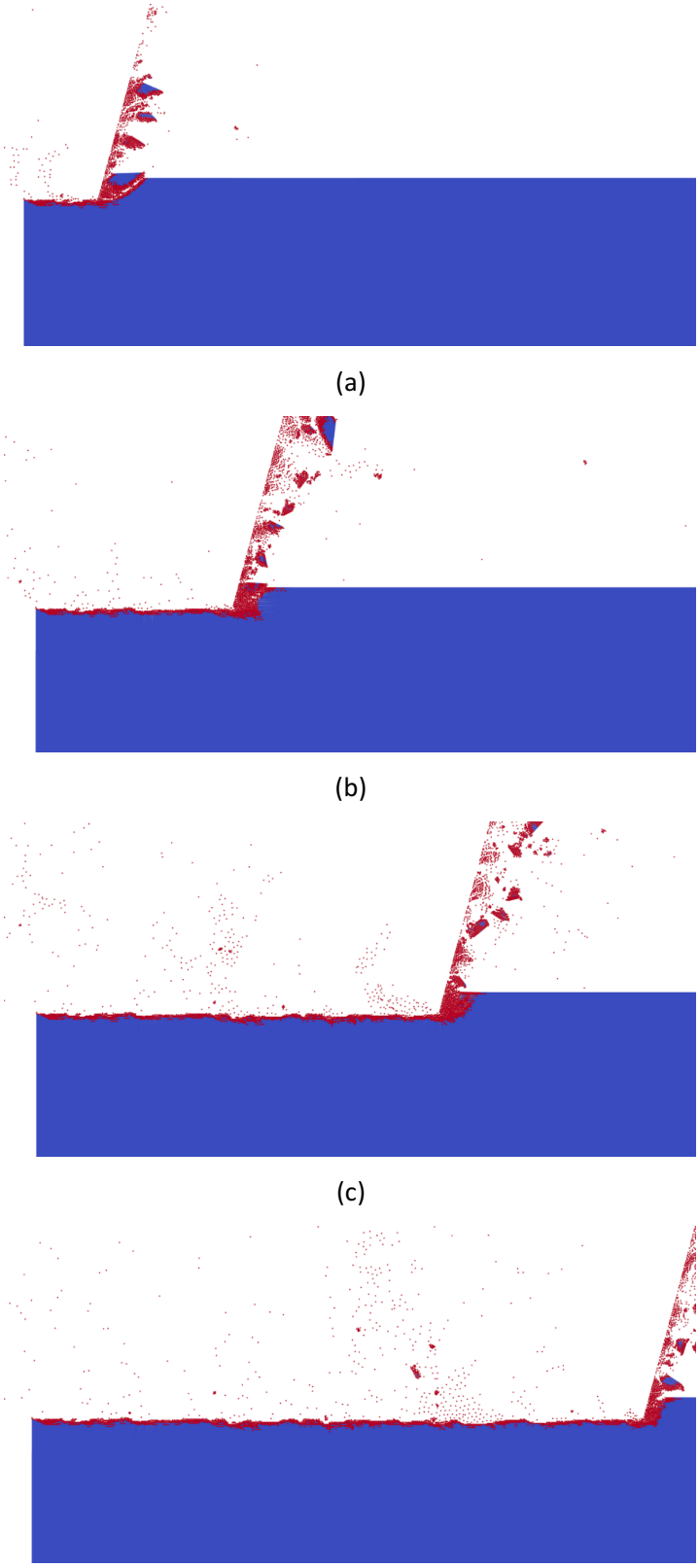

(a)

(b)

(c)

(d)

Figure 5.5 The scratching process of a deep cut: (a) t = 1.0 ms; (b) t = 2.5 ms; (c) t = 5.0 ms; (d) t = 7.5 ms (red dots indicate failed materials)

The cutting force applied normal to the cutter surface in the process of scratching are recorded in three cases and summarized in Figure 5.6.

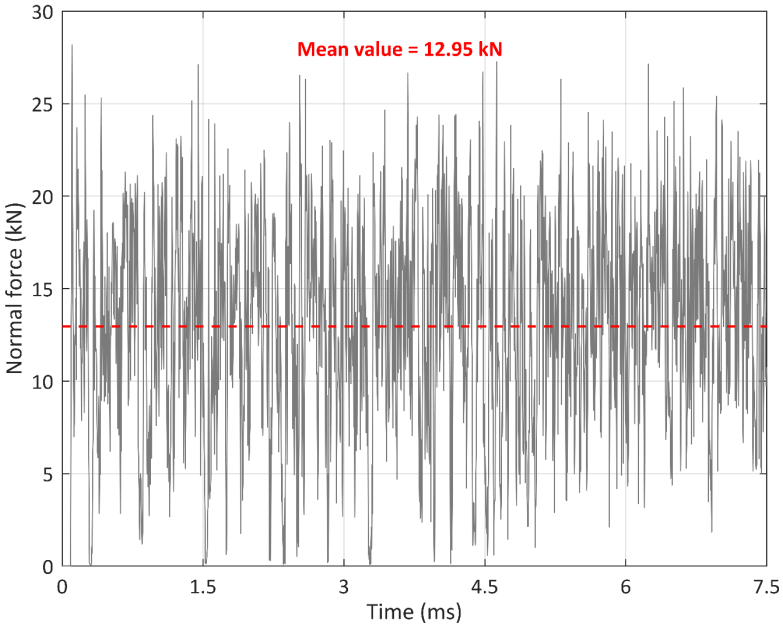

(a)

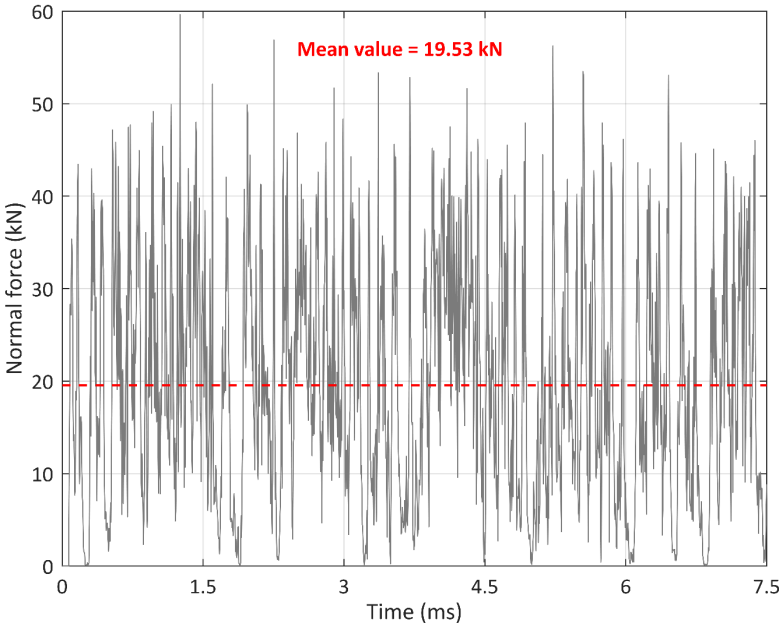

(b)

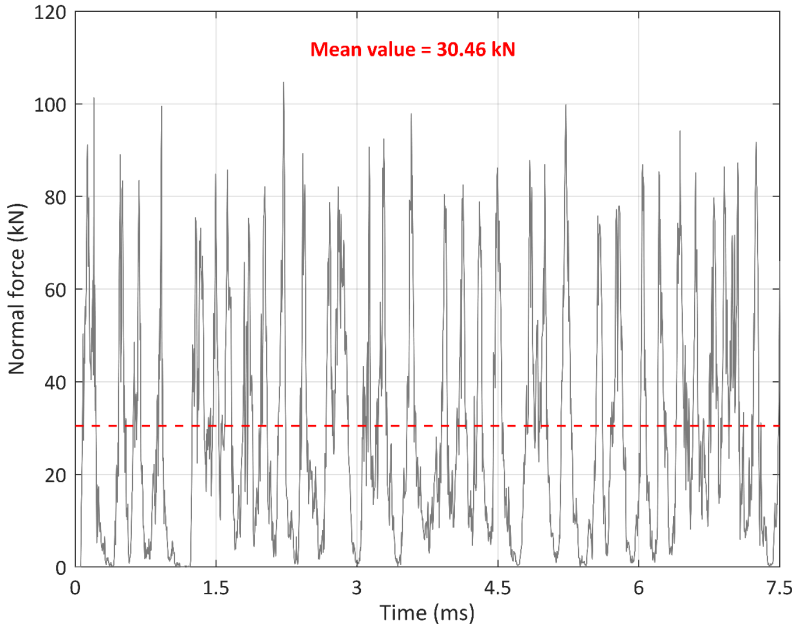

(c)

Figure 5.6 Variation of cutting forces applied normal to the cutter surface: (a) ductile failure in the shallow cut d = 0.2 mm; (b) ductile-brittle failure in the intermediate cut d = 0.5 mm; (c) brittle failure in the deep cut d = 1.0 mm

Mean values of normal cutting force in the shallow, intermediate, and deep cut are 12.95 kN, 19.53 kN, and 30.46 kN respectively. It is clearly shown that the cutting force increases with the increase of cutting depth as expected. Simulation results demonstrated that, in the shallow cut, the cutting force fluctuates about the mean value throughout the process of scratching. The cutting force in any period is approximately the same. The difference between the maximum and minimum cutting force is small. However, in the deep cut, the cutting force usually increases to a peak value and then drops rapidly. This result is identical to the failure pattern of deep cuts. The increase of the cutting force is to initiate the fracture in front of the cutter, before a rock fragment is generated. The rapid drop of the cutting force is due to the release a rock fragment and the generation of rock dust. The length of the period that has a considerably low cutting force is related to the size of the rock fragment which is generated before this period. The different between the maximum and minimum cutting force in this case is larger than that in the shallow cut as well. As for the intermediate cut, the cutting force in this case has both the characteristics of the shallow cut and deep cut in different periods. This result shows again that there is

a transitional rage of cutting depth where the failure of rock is in a combination of the ductile and brittle mode.

5.4 Effect of Cutter Operational Parameters

A group of numerical simulations are conducted in this section to study the effect of operational parameters of the cutter on the scratch test. As shown in Figure 5.1, three operational parameters of the cutter are taken into consideration, including the cutting depth d, rake angle ϑ, and cutting speed v. The cutting force is recorded in each simulation. And then, the mean value of normal cutting force and MSE (see Eq.60) are calculated and compared.

Effect of cutting depth

To study the effect of cutting depth, thirteen simulations with a same rake angle ϑ = 15° and a same cutting velocity v = 4.0 m/s are performed. The cutting depths of thirteen simulations are 0.15, 0.2, 0.3, 0.4, 0.5, 0.6, 0.7, 0.8, 0.9, 1.0, 1.2, 2.4, and 3.6 mm respectively. Simulation results are presented in Figure 5.7.

Results of MSE explicitly show the effect of cutting depth in three phases: When the cutting depth is smaller than 0.5 mm, where the ductile mode of failure dominates as has been discussed, the MSE decreases rapidly from 276.8 MPa to 138.6 MPa with the cutting depth increases from 0.15 mm to 0.4 mm; When the cutting depth is in the range between 0.4 mm and 0.8 mm, the MSE continues to decrease with a much lower rate and in a nonlinear manner, from 138.6 MPa to 95.5 MPa; When the cutting depth further increases, where the failure mode has been transferred to brittle, the MSE decreases very slowly and almost remains constant. In the case where the cutting depth in increased to 3.6 mm, the MSE is equal to 77.8 MPa. Therefore, a conclusion could be made that MSE decreases rapidly in ductile failure, remains approximately constant in brittle failure, and decreases at an intermediate rate in the transition from ductile to brittle failure. The transition from ductile to brittle mode of failure could be estimated from the result of MSE as in the range of cutting depth from 0.4 to 0.8 mm.

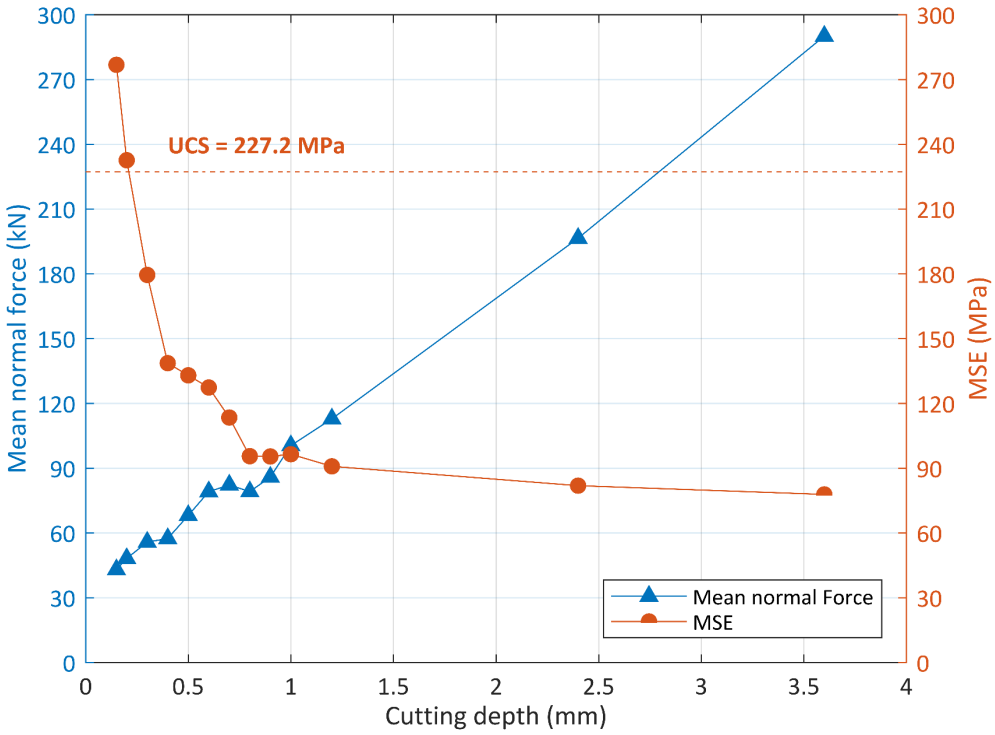

Figure 5.7 Effect of cutting depth on the mean normal cutting force and MSE in scratch test, with a cutting velocity of 4 m/s and a rake angle of 15 degree

The critical failure mode transition cutting depth is always associated with the uniaxial compressive strength of the rock material by researchers. Based on a numerical study, Zhou and Lin (2013) proposed that the critical transition depth d_c is proportional to a fractional power of the uniaxial compressive strength σ_c as follows:

$$d_c = 5.6\sigma_c^{-0.43} \tag{61}$$

where the units of d_c and σ_c are mm and MPa respectively. Substituting the value of compressive strength in this simulation, namely 227.2 MPa, into this equation, the critical transition depth d_c given by their model is 0.54 mm, which falls into the transition range estimated by PNMM simulations.

Since the MSE decreases with the increase of cutting depth, it is energy- and cost-efficient to adopt a high cutting depth in engineering practice. However, in deep cuts, the force applied on the cutter increases linearly whereas the decrease of MSE is negligible. An

extreme high cutting force could damage the cutter and lead to an extra cost. Consequently, for a rock cutting process in mining, drilling, and tunneling, it could be advised from the energy point of view that a cutting depth slightly greater than the critical transition depth should be chosen so that the failure of rock is in brittle mode and the cutting force required is small.

Effect of cutting speed

Twelve cases with a constant cutting depth of 1.2 mm and a constant rake angle of 15° have been performed in total to study the effect of cutting speed. The cutting speed varies from 0.4 to 50 m/s in these cases. Simulation results are summarized in Figure 5.8. It should be noted that all of twelve cases are deep cuts and in brittle failure mode.

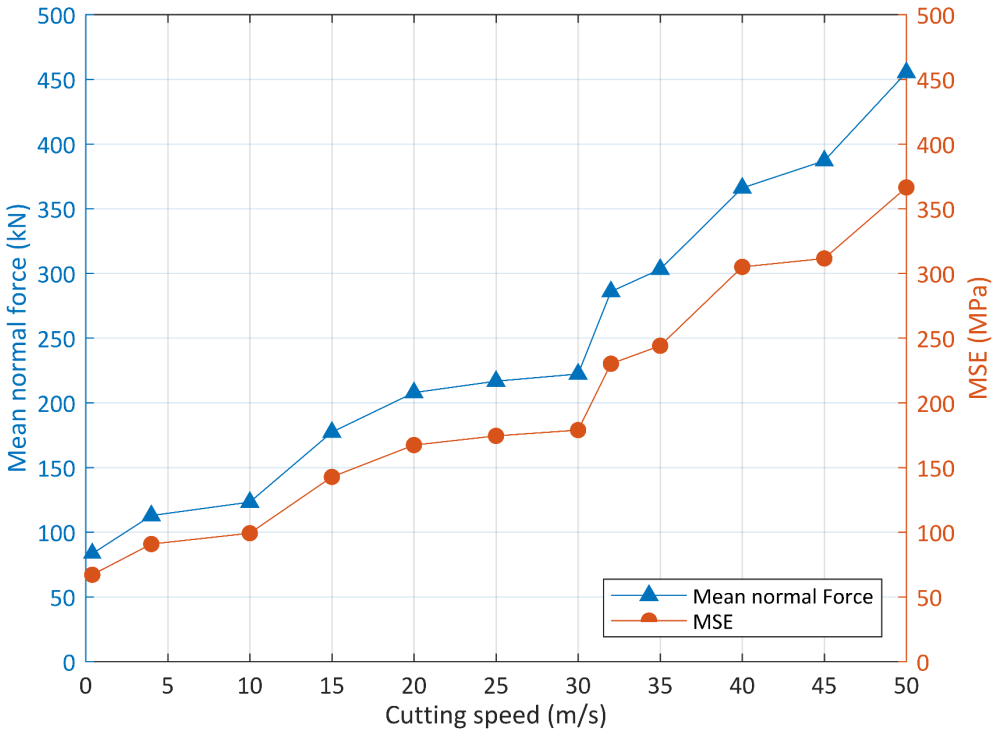

Figure 5.8 Effect of cutting speed on the mean normal cutting force and MSE in scratch test, with a cutting depth of 1.2 mm and a rake angle of 15 degree

Although He and Xu (2016) observed in experimental tests that the effect of cutting speed can be regarded as negligible for low cutting speed, which is on the order of mm/s. Simulation results show that when the cutting speed is high, its effect on scratching could be significant, due to the rate-dependent behavior of rock materials. Specifically, both of the cutting force and MSE increase with the increase of cutting speed. Such an increase of the cutting force has also been reported in a FEM simulation in (Menezes et al., 2014). The increased energy consumption at high cutting speeds, in this study, is mainly dissipated as the increased kinetic energy of rock fragments and rock dust, as well as in the crash of rock fragments.

The figure also indicates that there is a critical cutting speed in scratch test, above which the increase of cutting force and MSE is accelerated. In this example, the critical cutting speed is equal to 30 m/s. The values of MSE at the cutting speed of 0.4, 30, and 50 m/s are equal to 67.1, 178.9, and 366.4 MPa respectively. Therefore, the values of average MSE increasing rate in the range of 0.4 ~ 30 m/s and 30 ~ 50 m/s are 3.78 and 9.38 respectively. The accelerated increasing rate of both cutting force and MSE in scratch test is supposed to be related to the relationship between the strain rate and compressive strength of rock materials, which is in a similar manner as summarized by Zhang and Zhao (2014).

Effect of rake angle

Thirteen cases with a constant cutting depth of 1.2 mm and a constant cutting velocity of 4.0 m/s are performed to study the effect of cutter rake angle. A sequence of rake angles ranging from 0° to 60° is adopted in the cases. Results of the mean value of normal cutting force and MSE are summarized in Figure 5.9.

As shown in the figure, the increase of cutting force with the increase of cutter rake angle is significant, especially when the rake angle is greater than 30°. In cases the rake angle ranges from 20° to 30°, the normal cutting force approximately has a constant value around 150 kN. The cutting force has the most rapid variation when the rake angle is between 30° and 45°, increasing from 155.3 kN to 387.3 kN. The cutting force reaches a

maximum value of 469.3 kN when the rake angle is 60°. Comparing to cutting force, the value of MSE has a much moderate variation with the increase of cutter rake angle. In all cases, the value of MSE falls into the range of 50 MPa and 140 MPa. Specifically, the value of MSE monotonically increases from 50.9 MPa to its maximum value 136.5 MPa, accompanying with the increase of rake angle from 0° to 45°. Then, the value of MSE slightly decreases, though the cutting force continues to increase.

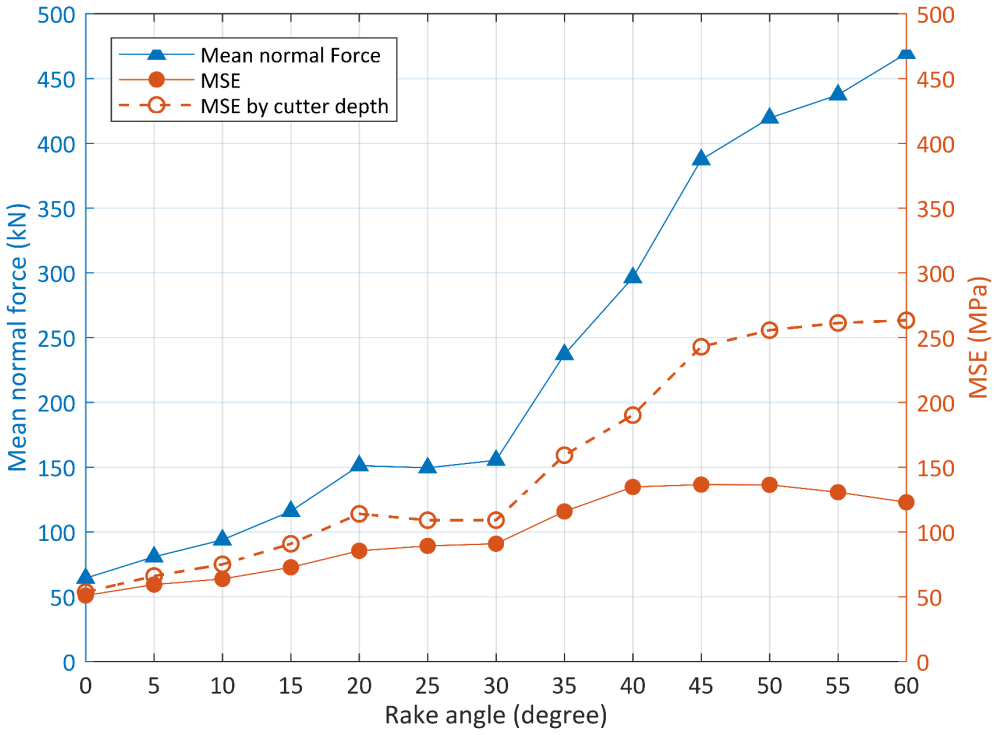

Figure 5.9 Effect of rake angle on the mean normal cutting force and MSE in scratch test, with a cutting depth of 1.2 mm and a cutting speed of 4 m/s

Simulation results indicate that when the cutter rake angle is small, both the cutting force and MSE increase at a relatively moderate rate. However, when the cutter rake angle becomes great, say greater than 30° in this study, the cutting force rapidly increases whereas the MSE slightly increases and then decreases. The difference between cutting force and MSE at great cutter rake angle is due to the increase of actual cutting depth. The term *actual cutting depth* is defined as the realistic depth of removed rock in a scratch test. In PNMM simulations, the actual cutting depth is calculated as the ratio of the

volume of removal (see Eq.60) to the travel distance of cutter. As shown in Figure 5.5, when the rake angle is small, the actual cutting depth of rock along the path of cutting is almost the same as the depth of cutter. However, when the rake angle becomes great, the difference between the actual cutting depth and the depth of cutter becomes significant. A snapshot of the case with a rake angle of 30° is presented in Figure 5.10. The surface of rock sample is rough after scratching in this case. And, as can be seen from the figure, the actual cutting depth of this case is noticeably greater than the depth of cutter, which is approximately equal to the actual cutting depth at the left boundary of rock. In fact, the simulation result demonstrates that, with a constant cutting depth of cutter, the actual cutting depth of rock increases with the increase of cutter rake angle. In the most severe case, i.e. the rake angle is equal to 60°, the actual cutting depth is more than twice as great as the cutter depth. If the volume of removal in Eq.60 is calculated by the depth of cutter rather than the actual cutting depth, the value of MSE would be greatly overestimated, as plotted in Figure 5.9.

In conclusion, due to the increase of both cutting force and MSE at great rake angles, a small rake angle of cutter is recommended in practice. Besides, it is interesting to notice that cutting force and MSE remains almost constant in a narrow range of rake angle, which is 20° to 30° in this study.

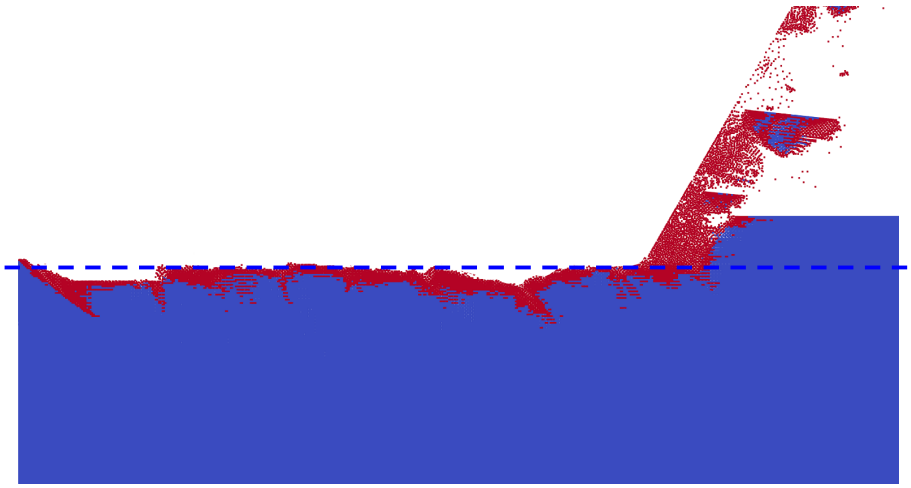

Figure 5.10 The actual cutting depth of the scratch test with a rake angle of 30 degree, a cutting depth of 1.2 mm, and a cutting speed of 4 m/s, at the time of 5 ms (red dots indicate failed materials; dash line indicates the depth of cutter)

5.5 Summary

The process of rock cutting has been a significant issue in many rock engineering applications. In this chapter, PNMM is applied to study the scratching of rock material by considering its dynamic behaviour. The failure patterns of ductile and brittle scratching are first simulated. It is validated that at an intermediate cutting depth the mode of rock scratching is in the transition from ductile to brittle, and the failure pattern is in a combination of ductile and brittle mode. The cutting forces in the ductile, brittle, and mixed mode of scratching are studied and compared. Then, a parametric study is performed by a series of PNMM simulations to study the effect of operational parameters of the cutter. Following conclusions can be drawn from the simulation results:

1) The effect of cutting depth is divided into three phases. The value of MSE decreases rapidly when the mode of failure is ductile, remains approximately constant when the mode of failure is brittle, and decreases nonlinearly at an intermediate rate when the mode of failure is in the transition from ductile to brittle. The range of the transitional cutting depth could be estimated from the result of MSE. In the practice of rock cutting, a cutting depth slightly greater than the transition depth is advised since it provides the failure of rock in brittle mode and the cutting force required is small.
2) The effect of high cutting speed is significant. The cutting force and MSE both increase with the increase of cutting speed. A critical cutting speed exists, above which the increase of cutting force and MSE are accelerated. The value of the critical cutting speed is believed to be related to the relationship between the dynamic compressive strength of rock and strain rates.
3) The effect of cutter rake angle is significant on the cutting force but moderate on MSE. The actual cutting depth is defined in this study, which is found to be increased with the increase of cutter rake angle. In cases where the cutter rake angle is large, the actual cutting depth could be noticeably greater than the cutting depth of cutter, leading to a significant difference between the cutting force and MSE. The cutting force and MSE are found to be both constant in a narrow range of cutter rake angle, whose mechanism though is still unclear and needs to be studied in future work.

Chapter 6 Rock Spalling and Related Rockburst Triggered by Far-field Dynamic Disturbance

This chapter presents a numerical study of spalling and spalling-induced rockburst under dynamic disturbance using PNMM. The spalling of rock bars under 1D stress condition is first simulated. The spalling process and fracturing pattern of the long bar under different loading types, including decreasing, increasing, and symmetrical triangular waves, and loading rates are investigated respectively. Then, the spalling in plate impact tests are numerically studied. Two types of impactor with various impact speed are used in this simulation. Last, a simulation of the spalling and rockburst of rock tunnels subjected to static in-situ stresses and dynamic disturbance is carried out to investigate the relationship between the in-situ stress, dynamic disturbance, spalling fractures, and rockburst phenomenon.

This chapter is based on a paper submitted to the journal *Tunnelling and Underground Space Technology*: Li, X., Zhang, Q. B., and Zhao, J. A numerical study of spalling and related rockburst under dynamic disturbance using a particle-based numerical manifold method (PNMM).

6.1 Introduction

There has been a noticeable trend to mine and construct underground caverns at greater depth in recent years. As in-situ stresses increase with depth, stress-induced rock fracturing, especially the sudden and violent failure of rock, will be a great threat to the construction, equipment, and the safety of mining worker. *Rockburst* is defined as a sudden rupture and explosion of rock on the surface of rock wall and is associated with a seismic event (Kaiser, 1996). Cai et al. (2012) classified rockbursts into three types,

including *strain burst*, *pillar burst* and *fault-slip burst*. *Strain bursting*, as the most common rockburst type in many mines, is a phenomenon that a certain volume rock wall violently destroys under high stresses (Gong et al., 2012). Strain bursts can be either mining-induced by energy release or dynamically-induced by remote seismic events. The strain energies stored in the failing rock and surrounding masses are released in a strain bursting, such that the failure is in a violent manner. Research shows that strain bursting is closely related to the spalling failure of rock. The term *spalling* here represents the development of visible tensile fractures under compressive loading, induced by either the stress concentration of a stress flow around underground openings or remote seismic event (Kaiser and McCreath, 1994). Ortlepp (2001) described a strain bursting as a superficial spalling with violent ejection of fragments. Diederichs (2007) stated that the spalling failure could happen before the actual strain bursting, and strain bursting is induced by the energy release of parallel and thin spall slabs. He et al. (2012) clearly showed the transfer of dominating failure type from spalling to strain bursting with the increase of in-situ stress in experimental tests. In this thesis, the term *spalling* is used to describe the tensile failure process due to the reflection of a compression wave at free surface or material interfaces (Weerheijm and Van Doormaal, 2007). The spalling in this definition is induced by a remote compressive stress wave. This phenomenon has been widely used to determine the dynamic tensile strength of a variety of brittle materials (e.g., rock, concrete, and ceramics) under shock wave loading in experiments, as these materials have a much lower tensile strength comparing to their compression strengths.

The spalling method falls into the category of indirect tension testing methods. The most common type of spalling tests is to utilize long bars under 1D stress wave condition (Díaz-Rubio et al., 2002). Schuler et al. (2006) measured the tensile strength and determined the specific fracture energy at strain rates between 10^1 and 10^2 s^{-1}. Forquin and Erzar (2010) measured the tensile strength of both dry and wet concrete under strain rates between 30 and 180 s^{-1}. Lu and Li (2011) determined the tensile strength of dry concrete under strain rates between 10^{-4} and 10^2 s^{-1}. Millon et al. (2016) conducted tests under strain rates varying from 1 to 520 s^{-1} on two sedimentary rocks, namely sandstone and limestone. Li et al. (2017a) adopted a modified split Hopkinson pressure bar (SHPB) to measure the spall strength of granite with a static confining load up to 30 MPa. Another

application of spalling phenomenon is the normal plate-impact experiment under 1D strain wave propagation condition, by which the spall strength as well as the Hugoniot properties of brittle materials are measured (Yuan and Prakash, 2013, Zhang et al., 2017). Efforts have also been made to numerically study the spalling phenomenon of rocks and rock-like materials. Cho et al. (2003) adopted a Finite Element Method (FEM) code to simulate the spalling of rock bars. Erzar and Forquin (2011) numerically studied the spalling of concrete using a mesoscopic method. Zhu and Tang (2006) applied the RFPA model to the simulation of spalling in rock bars, and studied the effect of the rock heterogeneity on dynamic tensile strength (Zhu, 2008). Then, Xu et al. (2016) extended the model and studied the spalling of fiber-reinforced concrete in the manner of both long bars and plate impact.

Some researchers have also numerically studied the spalling and spalling-induced rockburst in tunnels. Zhu et al. (2014b) adopted the AUTODYN code to study the spalling and zonal disintegration around a tunnel induced by stress wave. Mitelman and Elmo (2016) simulated the blast-induced spalling of tunnels using ELFEN, a hybrid FDEM code. However, no in-situ stress is considered in both of their research. Zhu et al. (2010) pointed out that rockbursts may occur when the rock mass is first supposed to be under high static in-situ stresses and then triggered by a far-field dynamic disturbance. Therefore, they adopted RFPA as the numerical method and studied tunnel rockbursts with varying in-situ stresses and dynamic disturbances. Similarly, Weng et al. (2017) utilized ANSYS/LS-DYNA to simulate the tunnel rockburst in three-dimensional cases. The rockburst in their simulation was triggered by a blast loading at the advancing surface of the tunnel. However, as the numerical models they adopted are both based on FEM, they are not able to simulate the post-failure stage of rock (Jing, 2003), including the behavior of fragmented rocks and the effect of spall slabs on rockburst. Besides, their work did not utilize a rate-dependent constitutive model to capture the tensile strength under dynamic loading.

In this chapter, PNMM is applied to numerically study the spalling of rock and the spalling-induced rockburst of rock tunnels. In following sections, the application of PNMM is first

extended to the spalling of long rock bars for further validation. Then, the simulation of spalling induced by plate impact will be conducted as a contact issue to confirm the model. At last, inspired by the work in (Zhu et al., 2010), tunnel rockbursts induced by dynamic disturbance will be numerically studied.

6.2 Spalling of Long Bars

The spalling of long rock bars is studied as a plane stress problem in this section. The purpose is to validate the proposed method by comparing with theoretical analysis.

6.2.1 Numerical Model

The long bar in this simulation, as shown in Figure 6.1a, has a length of 1.0 m and a width of 0.04 m. A triangular compression wave is uniformly applied on the left end of the bar. The peak value and decreasing time of the triangle wave is 50 MPa and 100 μs respectively, as illustrated in Figure 6.1b. The right end of the bar is set to be free. The model is supposed to be homogenous. The material properties are 2,650 kg/m^3 for density, 70.0 GPa for Young's modulus, 0.2 for Poisson's ratio, and 14 MPa for static tensile strength. The PNMM model consists of 2,500 manifold elements and 10,521 particles.

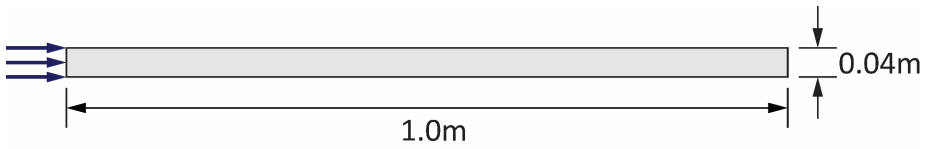

(a)

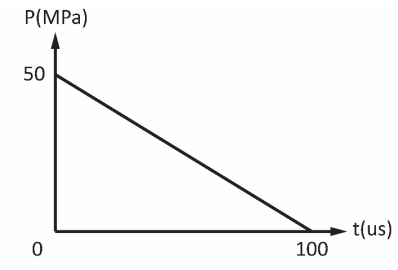

(b)

Figure 6.1 The long bar subjected to a triangular compression wave with a free end: (a) geometry and boundary conditions; (b) the applied triangular compression wave

The dynamic tensile strength of the rock bar and the thickness of the first spall will be examined in this simulation. Analytical equations for the spalling of long bars are based on the 1D wave theory. Specifically, the dynamic tensile strength of materials in spalling tests can be estimated from the velocity history of the free end using the pull-back velocity method (Schuler et al., 2006), as follows

$$\sigma_t^d = \rho v_p (v_1 - v_2)/2 \tag{62}$$

where σ_t^d is the dynamic tensile strength, v_p is the stress wave velocity, and v_1 and v_2 are the first local maximum and local minimum value of the free surface velocity respectively. v_1 - v_2 is the so-called pull-back velocity. The dynamic tensile strength in spalling tests is also named the spall strength. The analytical solution to the thickness of the first spalling piece h is (Wang et al., 2007)

$$h = \frac{\lambda}{2} \cdot \frac{\sigma_t^d}{\sigma_p} \tag{63}$$

where λ is the wave length of the compression stress, and σ_p is the peak value of the compression stress.

6.2.2 Spalling Process

The simulated spalling process is illustrated in Figure 6.2. The applied compression stress wave travels from the left end to the right end of the bar. The P-wave velocity in the bar can be calculated to be 5,140 m/s, making the compression wave to reach the free (right) end at the time of about 195 μs ideally. Then, the compression wave is reflected as a tensile wave, and a tensile stress zone is formed. As the tensile stress zone propagates back toward the left end of the bar, the amplitude of the tensile stress wave increases as well.

At the time of 248 μs, the amplitude of tensile stress reaches 23.0 MPa, and the first spall fracture is generated. Therefore, the dynamic tensile strength at this loading rate is simulated to be 23.0 MPa, which is calculated by the JHB model. The distance from the first spall fracture to the free end is 121.5 mm.

The spall fracture forms a new free end for stress waves. The compression wave on the left surface of the spall fracture is reflected as a tensile wave propagating toward the left end of the bar, while the tensile wave on the right surface of the spall fracture is reflected as a compression wave propagating toward the right end of the bar. At the time of 254 μs and 260 μs, the second and third spall fractures are generated to the left of the first spall fracture in sequence. The distance from the first spall fracture to the second and third one is 32.9 mm and 68.4 mm respectively.

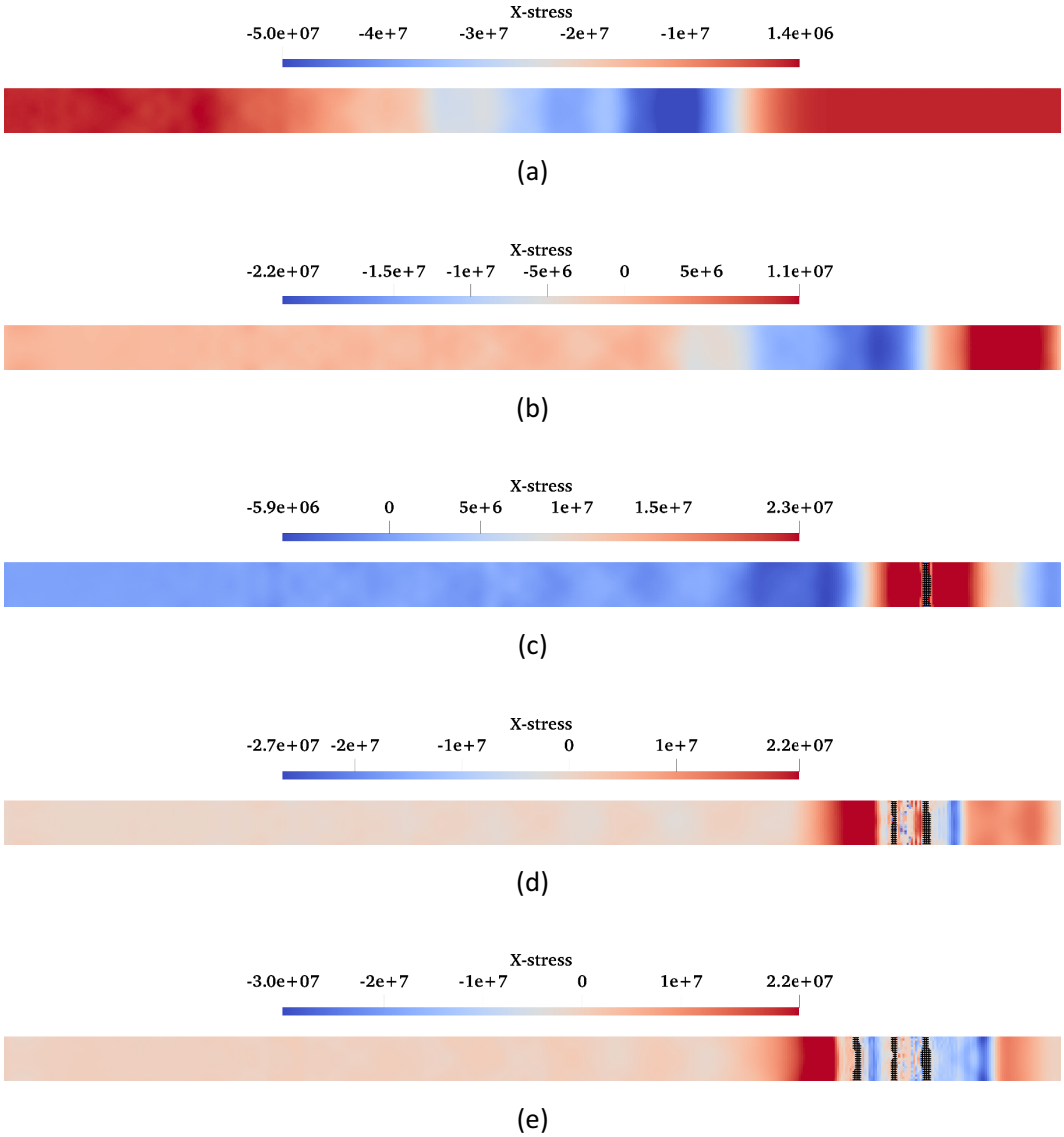

Figure 6.2 The spalling process of long bar subjected to decreasing triangular compression wave: (a) t = 150 μs; (b) t = 235 μs; (c) t = 248 μs; (d) t = 254 μs; (e) t = 260 μs

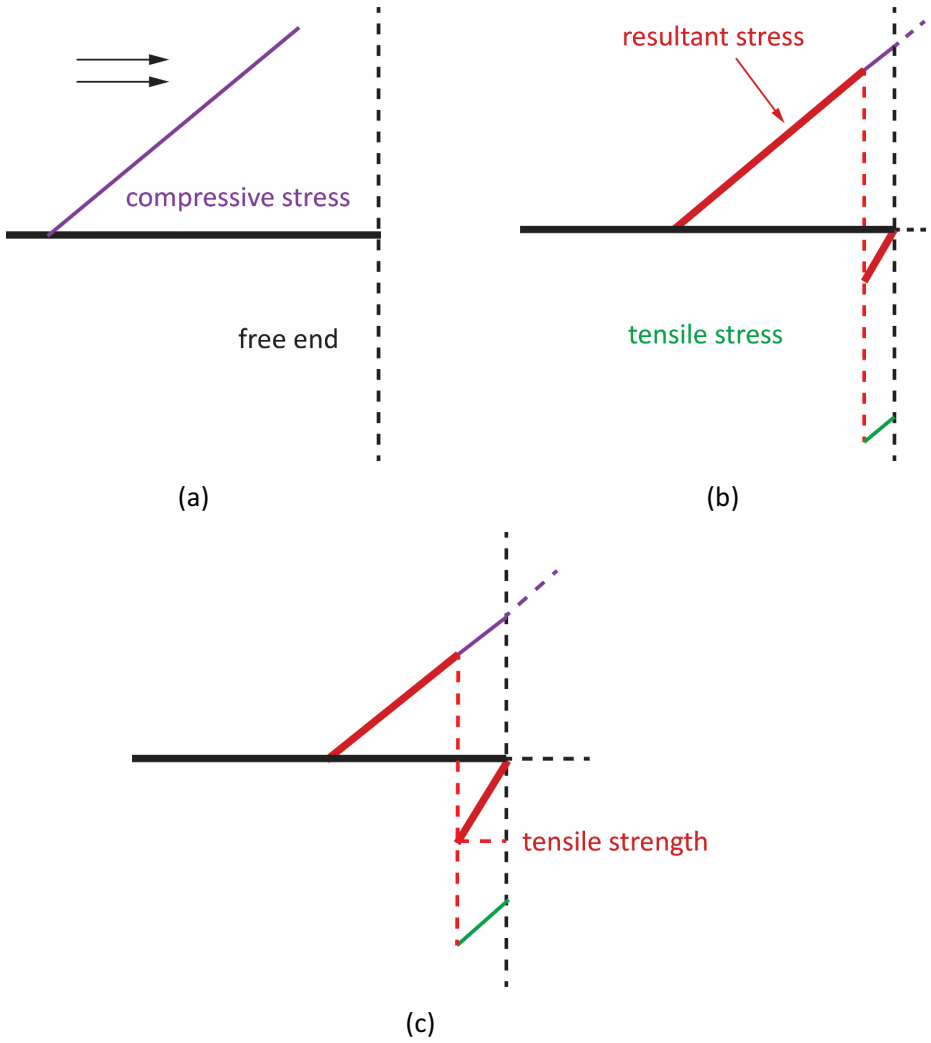

Figure 6.3 1D wave analysis for the spalling under decreasing triangular compression wave: (a) the incident compressive stress wave; (b) the reflected tensile stress forms a tension area; (c) the tensile strength is reached

The spalling process induced by the decreasing triangular compression wave can be explained by the 1D wave analysis in Figure 6.3. The compressive stress is plotted above the 1D bar, while the tensile stress is plotted below. The resultant stress is the realistic stress suffered by the rock during spalling. There is only compressive stress before the compression wave reaches the free end and reflects (Figure 6.3a). After the reflection, the resultant stress is still compression to the left of reflected tensile stress, as there is only compressive stress in this portion. However, in the part where tensile stress exists, the resultant stress is changed to tension, as the reflected tensile stress is always higher than the compressive stress at a specific point (Figure 6.3b). With the further propagation of

waves, the resultant stress is gradually transferred from compression to tension. Meanwhile, the peak value of the tension part of the resultant stress is gradually increased. The first spalling happens when the peak value increases to the tensile strength, as shown in Figure 6.3c. After the first spalling takes place, the compressive stress to the left of the spalling fracture takes the fracture as a new free surface and reflects to tensile stress. On condition that the peak value of this part of compressive stress is still higher than the tensile strength, it will be able to create more spalling fractures after the reflection, with the same process of the first fracture. At the same time, the tensile stress to the right of the first fracture takes the fracture as a free surface as well and reflects to a compressive stress. Considering that the reflected compressive stress is higher than the remaining tensile stress, the resultant stress in this portion will be changed to compression, making it hard to generate more spalling fractures. However, because the peak value of the reflected tensile stress itself is higher than the tensile strength, it is still possible to form spalling fractures in this portion of the bar after several reflections.

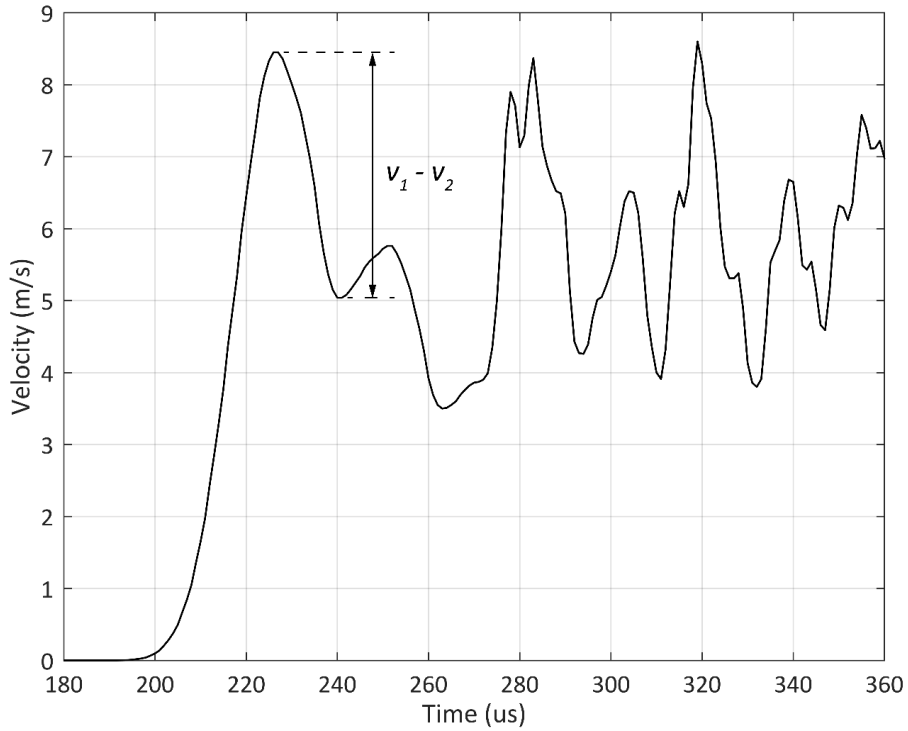

Figure 6.4 The free surface velocity of long bar subjected to decreasing triangular compression wave

The particle velocity of the free end is recorded and illustrated in Figure 6.4. The figure shows that the compression wave reaches the free end at the time of 194 μs, which agrees well with the theoretical result previously mentioned. The pull-back velocity can be obtained from the figure as 3.45 m/s (v_1 and v_2 are 8.49 m/s and 5.04 m/s respectively). According to Eq.62, the spall strength is calculated to be 23.5 MPa. Substituting the spall strength into Eq.63, we have the theoretical solution to the thickness of the first spall as 120.8 mm. Both theoretical results agree well with the simulation.

6.2.3 Effect of Loading Rate

Two more simulations are conducted to study the effect of loading rate on the spall strength. The peak value of the decreasing triangular compression wave is kept as 50 MPa, whereas the decreasing time is changed to 50 μs and 200 μs respectively.

The spalling process of these two simulations is similar as described previously, despite a different thickness of the first spall. Although, in simulations, the dynamic tensile strength is inherently determined by the JHB model. We can still use the pull-back velocity method to theoretically estimate the spall strength, being consistent with experimental tests. And we have proved that PNMM simulations agree well with the results of the pull-back velocity method.

The particle velocities of the free end with different loading rates are plotted in Figure 6.5. Substituting the pull-back velocities from simulations into Eq.62, spall strengths at different loading rates can be estimated, as summarized in Table 6.1. The term *dynamic ratio* is defined as the ratio of the spall strength to the static tensile strength. Results indicate that under the loading rates ranging from 250 to 1,000 GPa/s, the dynamic ratio increases from 1.38 to 2.53. This result is reasonable when comparing to experimental tension test (Zhang and Zhao, 2014).

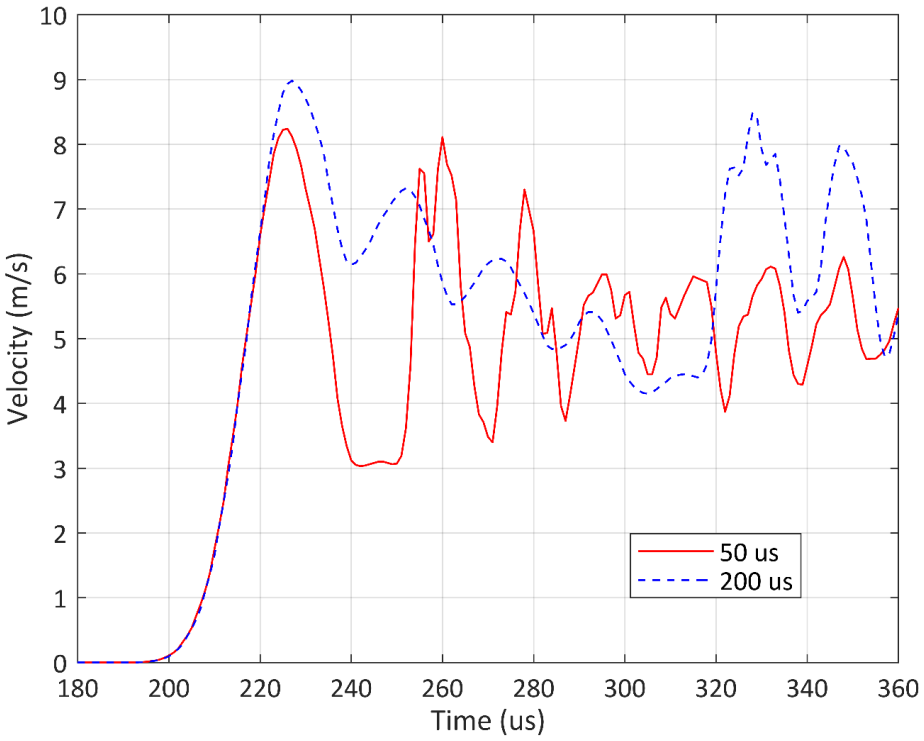

Figure 6.5 The free surface velocities under different loading rates

Table 6.1. Spall strengths at different loading rates estimated by the pull-back velocity method

Decreasing time (μs)	Loading rate (GPa/s)	v_1 (m/s)	v_2 (m/s)	Pull-back velocity (m/s)	Spall strength (MPa)	Dynamic ratio
50	1,000	8.24	3.03	5.21	35.48	2.53
100	500	8.49	5.04	3.45	23.50	1.68
200	250	8.98	6.14	2.84	19.34	1.38

6.2.4 Effect of Loading Type

The effect of loading types on the spalling fracture pattern is studied by imposing an increasing and a symmetrical triangular compression wave, as illustrated in Figure 6.6, on the bar respectively. Both loadings have a peak value of 50 MPa and a total duration of 100 μs.

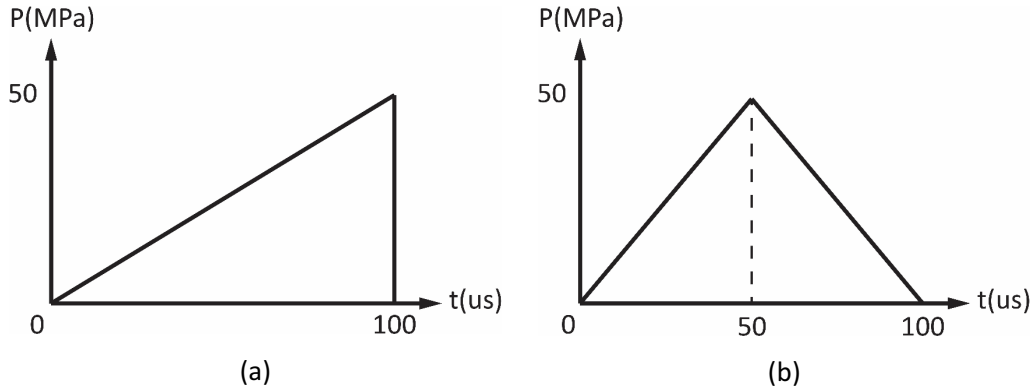

Figure 6.6 Compression loads applied on the long bar to study the effect of loading types: (a) the increasing triangular wave; (b) the symmetrical triangular wave

Increasing triangular wave

The spalling process under the increasing triangular wave is presented in Figure 6.7. The first spalling occurs at the time of 444 μs. The thickness of the first spall is 148.3 mm. Different from the case of decreasing triangular wave, following spall fractures are generated to the right of the first one. At the time of 450 and 454 μs, the second and third spalling take place at 37.9 and 63.1 mm to the first one respectively.

The difference in spalling fracture pattern can be explained by the 1D wave analysis shown in Figure 6.8. For the increasing triangular compression wave, the reflected tensile stress is lower than the incident compressive stress. Therefore, the resultant stress is still compression along the whole bar (Figure 6.8b). Only after the reflected tensile stress has passed the tail of the incident compressive stress, a tension area could be created on the bar (Figure 6.8c). The first spalling happens at the tail of the incident compressive stress, when the resultant tensile stress is increased to the tensile strength (Figure 6.8d).

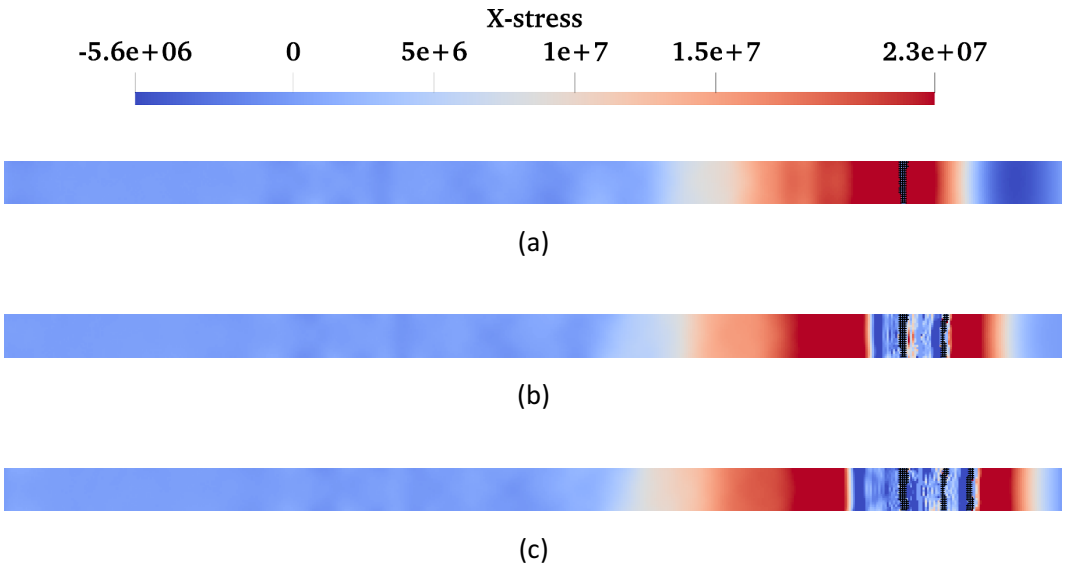

Figure 6.7 The spalling process of long bar subjected to increasing triangular compression wave: (a) t = 444 μs; (b) t = 450 μs; (c) t = 454 μs

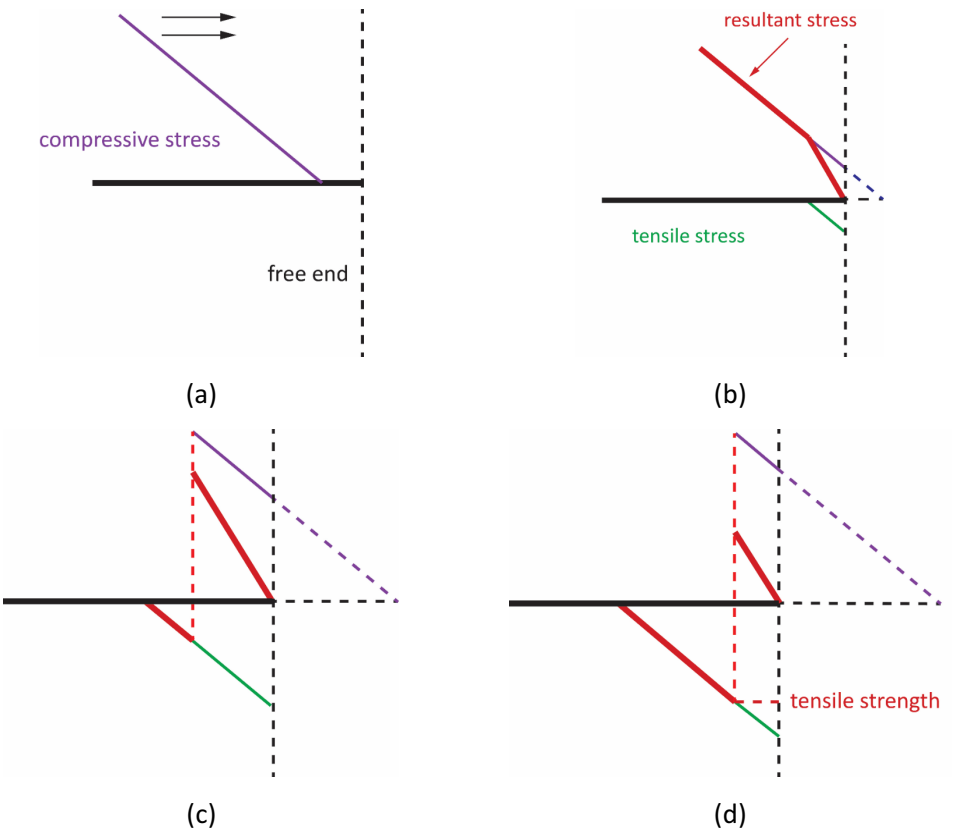

Figure 6.8 1D wave analysis for the spalling under increasing triangular compression wave: (a) the incident compressive stress; (b) the reflected tensile stress is not high enough to form a tension area; (c) the reflected tensile stress passes the incident compressive stress and forms a tension area; (d) the tensile strength is reached

After the occurrence of the first spalling, the tensile stress to the left of the spalling fracture continues propagating toward the left end of the bar and no compressive stress is reflected at this side. As the peak value of the tensile stress wave is lower than the spall strength, no spalling is possible to happen to the left of the first one. At the same time, the tensile stress to the right of the first spalling fracture takes the fracture surface as a free surface and reflects as a compressive stress. However, as the value of the reflected compressive stress is lower than the tensile stress that propagates toward the first spalling fracture, a tensile stress zone is form near the spall fracture. Therefore, following spalling fractures have the potential to be generated in this area.

Symmetrical triangular wave

The spalling pattern under the symmetrical triangular wave is quite unique. The spalling process of this case is presented in Figure 6.9. As shown in the figure, instead of a single spalling fracture, a spalling zone is generated at the time of 426 μs. The spalling zone has an initial width of 41.5 mm, and is further expanded to 99.7 mm at 436 μs. The 1D wave analysis for the generation of spalling zone is given in Figure 6.10. Due to the equal increasing and decreasing slopes of the symmetrical triangular wave, the resultant stress along a considerable zone is constant and reaches the spall strength simultaneously. This simulation result validates the experiment test and analysis by Díaz-Rubio et al. (2002). They suggested that symmetrical waves should be avoided in spalling tests that attempt to measure the dynamic tensile strength of materials.

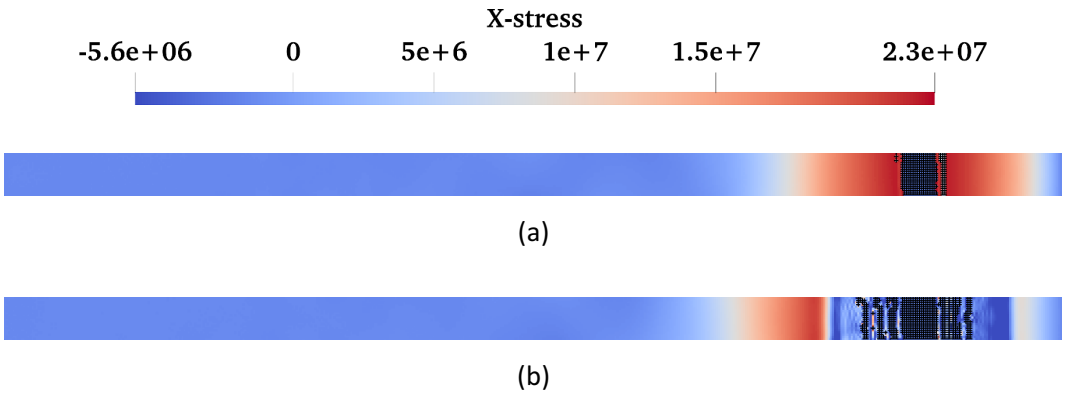

Figure 6.9 The spalling process of long bar subjected to symmetrical triangular compression wave: (a) t = 426 μs; (b) t = 436 μs

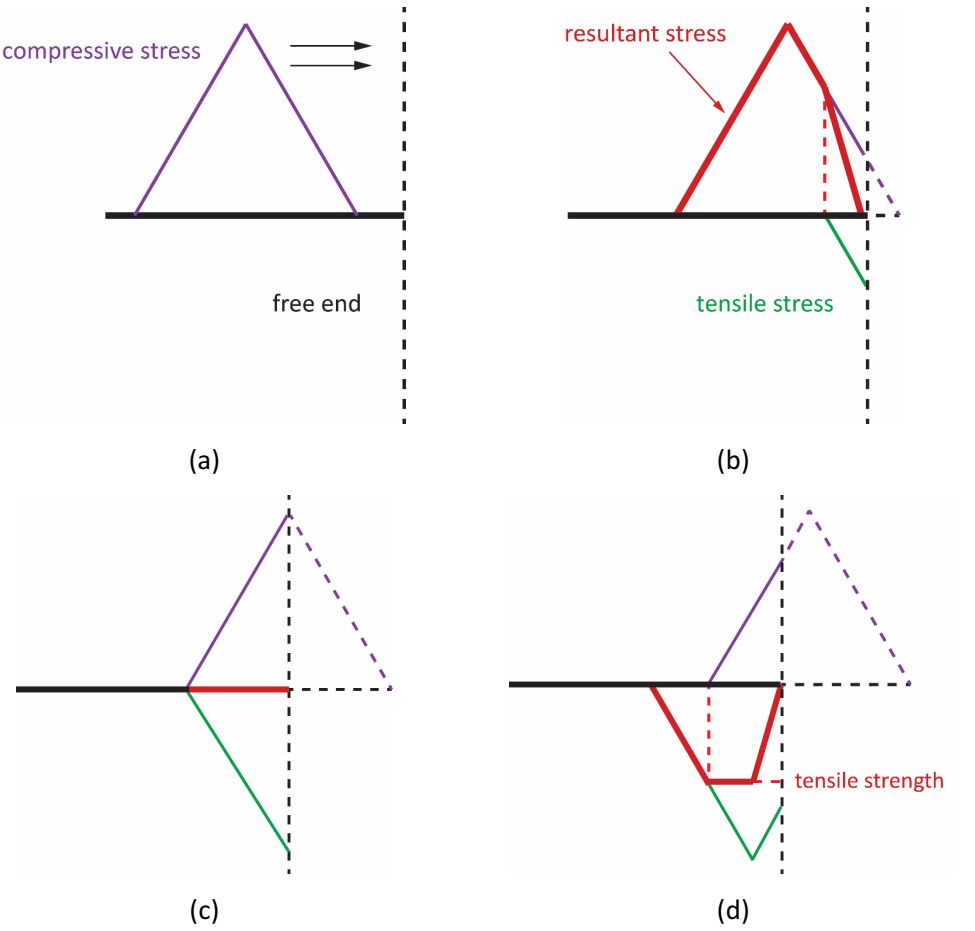

Figure 6.10 1D wave analysis for the spalling under symmetrical triangular compression wave: (a) the incident compressive stress; (b) the reflected tensile stress is not high enough to form a tension area; (c) the reflected tensile stress is equal to the incident compressive stress; (d) the tensile strength is reached along a zone

6.3 Spalling of Rock Plates under Impact Loading

A plate impact test will be studied in this section to extend the spalling simulation to 2D cases. The setup for the impact simulation is graphically illustrated in Figure 6.11. Two flyers are adopted in the test: a long flyer with the same length as the target and a short flyer with half the length of the target. Two flyers are both 3 mm in width. In both tests, the target has a length of 50 mm and a width of 5 mm. The flyer is parallel to the target. The flyer is supposed to be made of aluminum, with a density of 2,703 kg/m^3, a Young's modulus of 70.87 GPa, and a Poisson's ratio of 0.345. The material properties of the target are 2,650 kg/m3 for density, 70.0 GPa for Young's modulus, 0.2 for Poisson's ratio, and 14

MPa for static tensile strength. The flyer impacts the target at two speeds: 10 m/s for a low-speed impact, and 200 m/s for a high-speed impact.

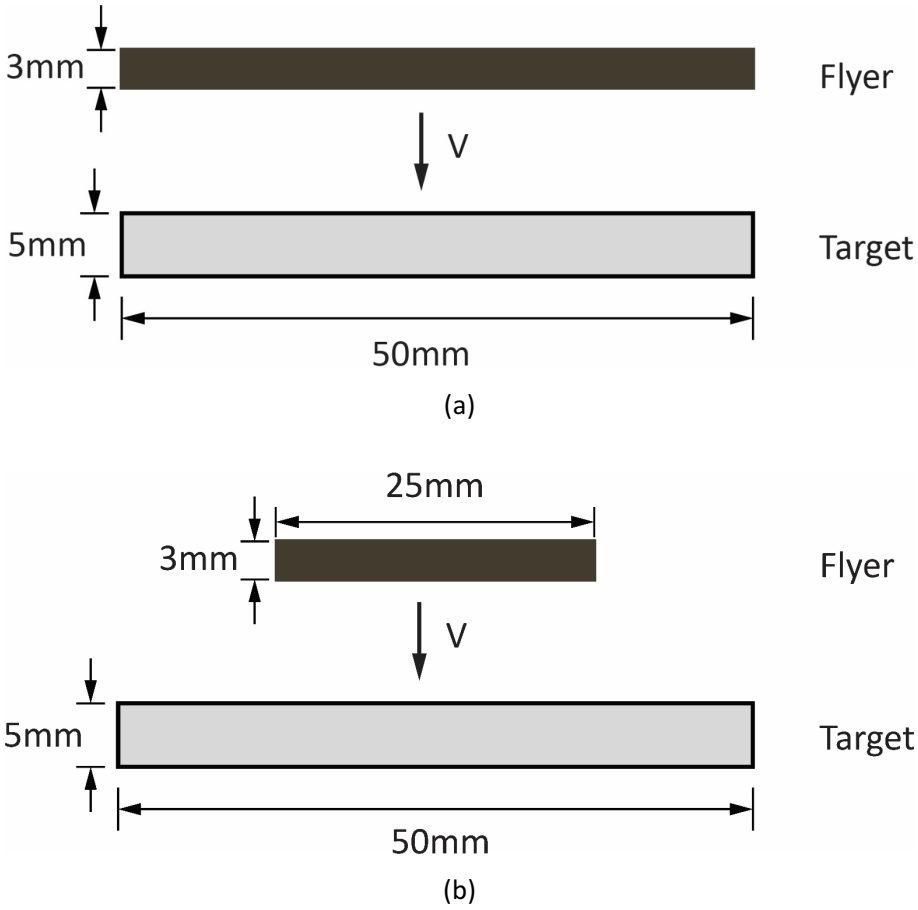

Figure 6.11 The plate impact test: (a) long flyer; (b) short flyer

Long flyer

The PNMM model for the long flyer test consists of 41,024 manifold elements and 328,192 particles. The spalling process of the low-speed impact is presented in Figure 6.12. The spalling process of this case is similar to that of rock bars. The stress wave is generated in the target due to the impact contact between the flyer and target. The impact wave arrives at the lower bound of the target at 1.6 μs and reflected. Spalling fractures are generated by the reflected stress in a narrow area near the center of the target at 2.2 μs. The length of the fractured area is almost the same as the length of the target. Then, spalling fractures are extended to the left and right boundaries of the target, and the

target is consequently separated into two parts. At the time of 43.5 μs, an obvious difference between the flying speeds of two parts exists. The lower half has an average velocity of 7.76 m/s, while the upper half has an average velocity of 4.72 m/s.

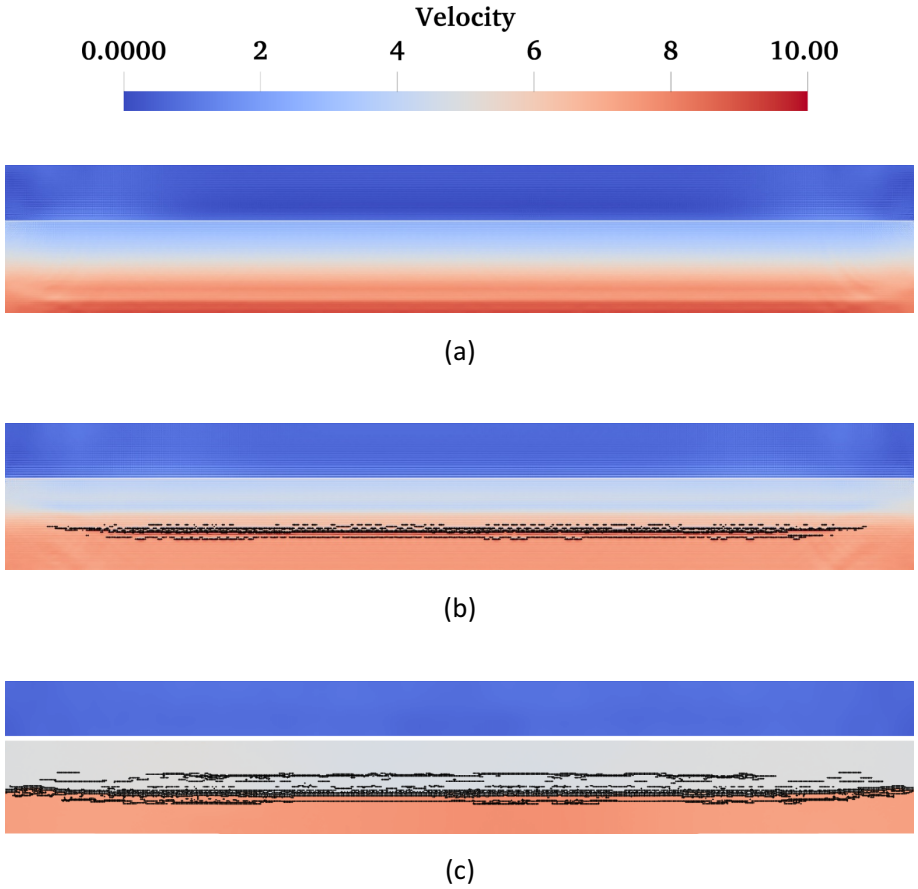

Figure 6.12 The spalling process of the long flyer impact at low speed: (a) t = 1.6 μs; (b) t = 2.2 μs; (c) t = 43.5 μs

Simulation results of the high-speed impact is presented in Figure 6.13. The target is heavily damaged in this case. Fractures are not explicitly plotted in the figure for the sake of clarity. Comparing to the low speed test, more spalling fractures are generated and the target is fractured into more layers in this case. However, the spalling fractures are found to be still parallel to the flyer and target, except when it is close to the left and right boundaries of the target, due to the boundary effect.

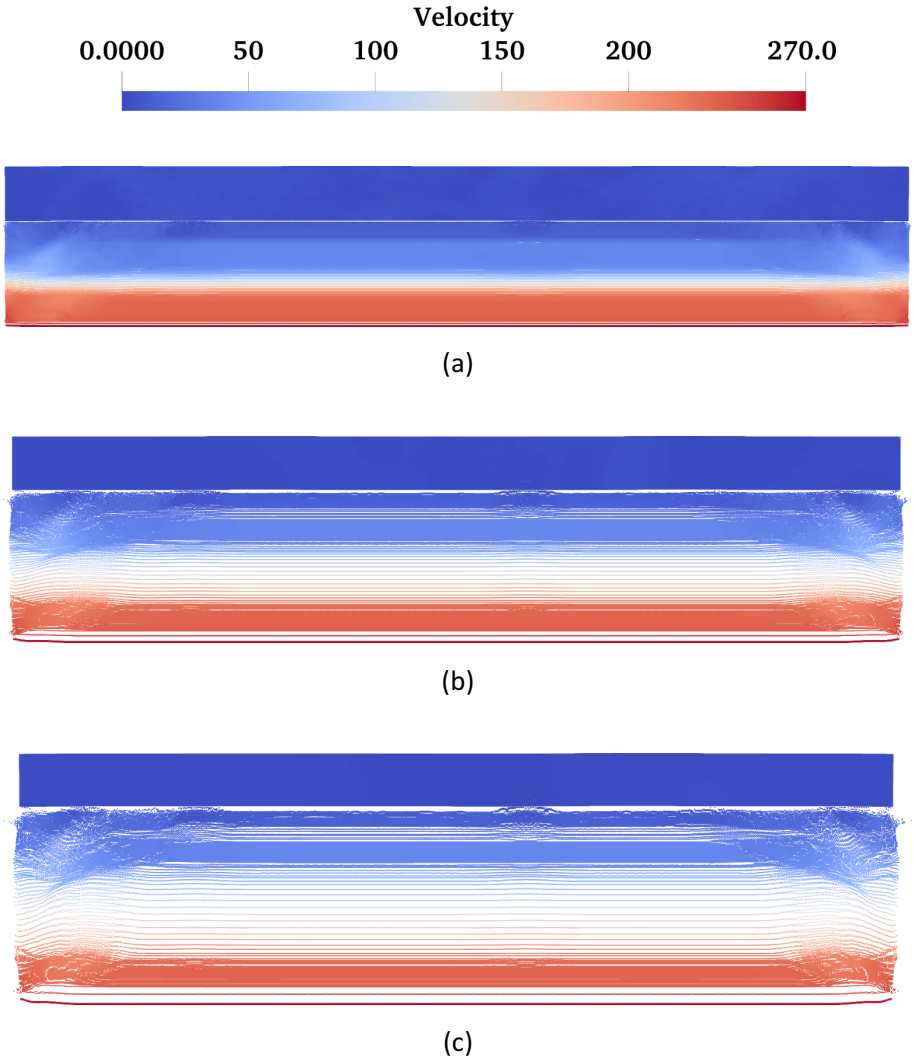

Figure 6.13 The spalling process of the long flyer impact at high speed: (a) t = 5 μs; (b) t = 15 μs; (c) t = 25 μs

Short flyer

The PNMM model for the short flyer test consists of 33,332 manifold elements and 266,656 particles.

The spalling process of the low-speed impact is presented in Figure 6.14. The impact wave arrives at the lower bound of the target at 1.6 μs and reflected. Spalling fractures are generated by the reflected stress in a narrow area near the center of the target at 2.2 μs. The fracturing zone is shorter than the flyer. Then, some longitudinal fractures are

generated from the spalling zone to the lower bound of the target, creating several spalling pieces from the target. The speed of these spalling pieces is non-uniform at their creation (namely 5.4 μs), but becomes uniform with the increase of the simulation time (e.g., at 43.5 μs). The final speed of spalling pieces is between 6 and 8 m/s. We can imagine that if the simulation time is further increased, theses spalling pieces will be extracted from the target and fly away. There are also some fractures originating from the upper bound of the target, due to the mismatch between the length of the flyer and target.

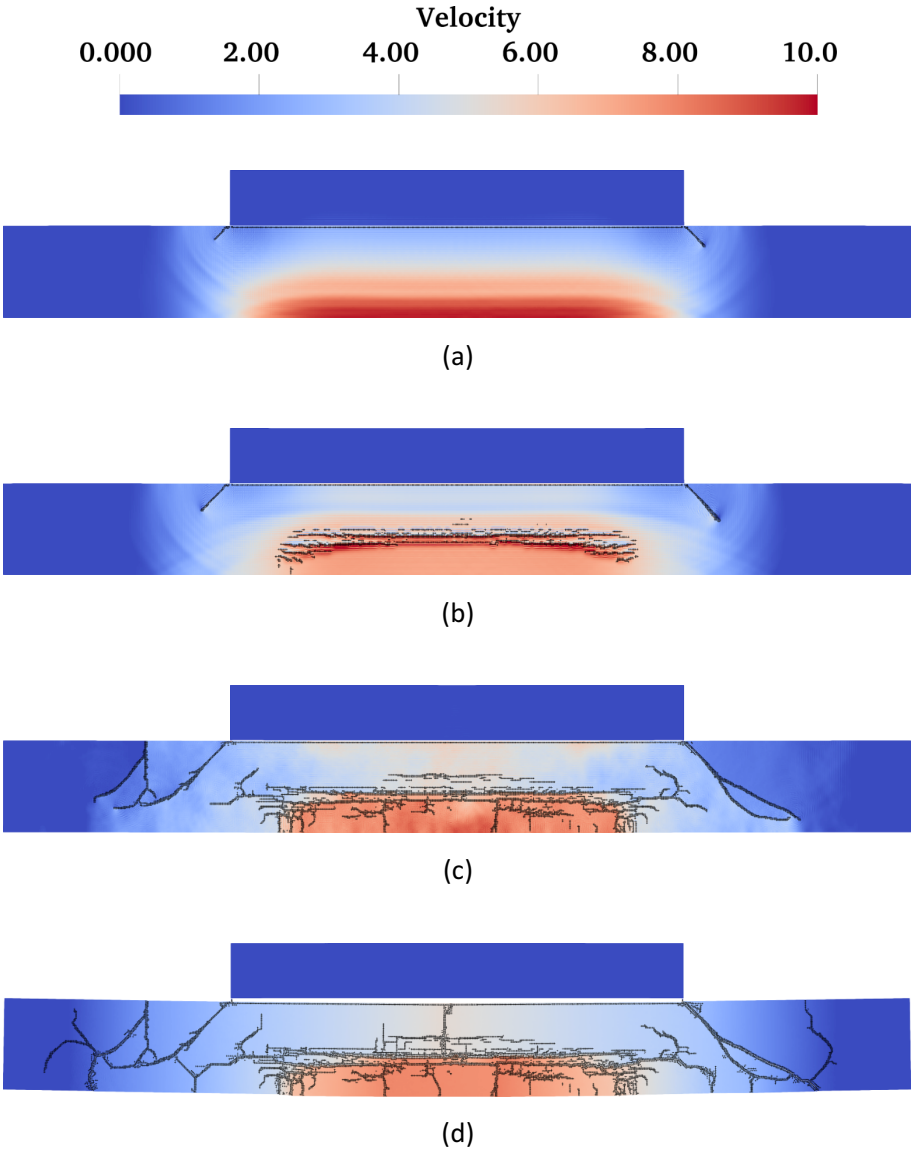

Figure 6.14 The spalling process of the short flyer impact at low speed: (a) t = 1.6 μs; (b) t = 2.2 μs; (c) t = 5.4 μs; (d) t = 43.5 μs

The rock plate is almost completely damaged when the impact speed increases to 200 m/s. The simulation results at this speed is presented in Figure 6.15. Again, fractures are not explicitly plotted in the figure for the sake of clarity. A spalling fracture can be clearly identified near the lower bound of the target. Moreover, due to the high impact stress, the spalling piece and the rock plate are both severely fractured afterward. The spalling process and fracture pattern is similar to that simulated by Zhang et al. (2015c).

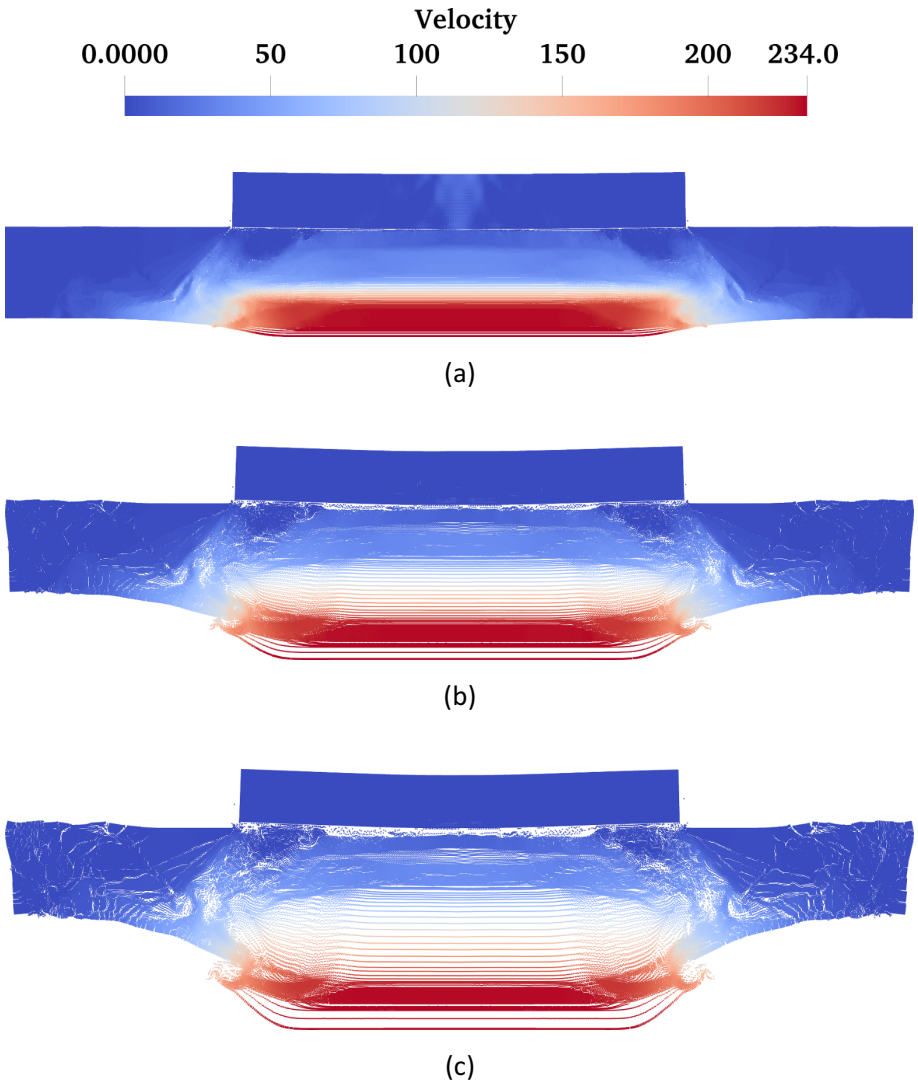

Figure 6.15 The spalling process of the short flyer impact at high speed: (a) t = 5 μs; (b) t = 15 μs; (c) t = 25 μs

6.4 Rockburst Induced by Dynamic Disturbance

6.4.1 Numerical Model

The spalling and rockburst of a tunnel triggered by the dynamic disturbance will be studied in this section. As depicted in Figure 6.16, a square domain with the size of 20 m × 20 m is taken into consideration with a tunnel located at the center of the domain. The tunnel is 1 m in height and has a semicircular roof with a radius of 1 m. The model is supposed to be homogeneous. Material properties of the model are 2,650 kg/m^3 for density, 70.0 GPa for Young's modulus, 0.2 for Poisson's ratio, and 14 MPa for static tensile strength. The PNMM model for this example consists of 59,562 manifold elements and 502,002 particles.

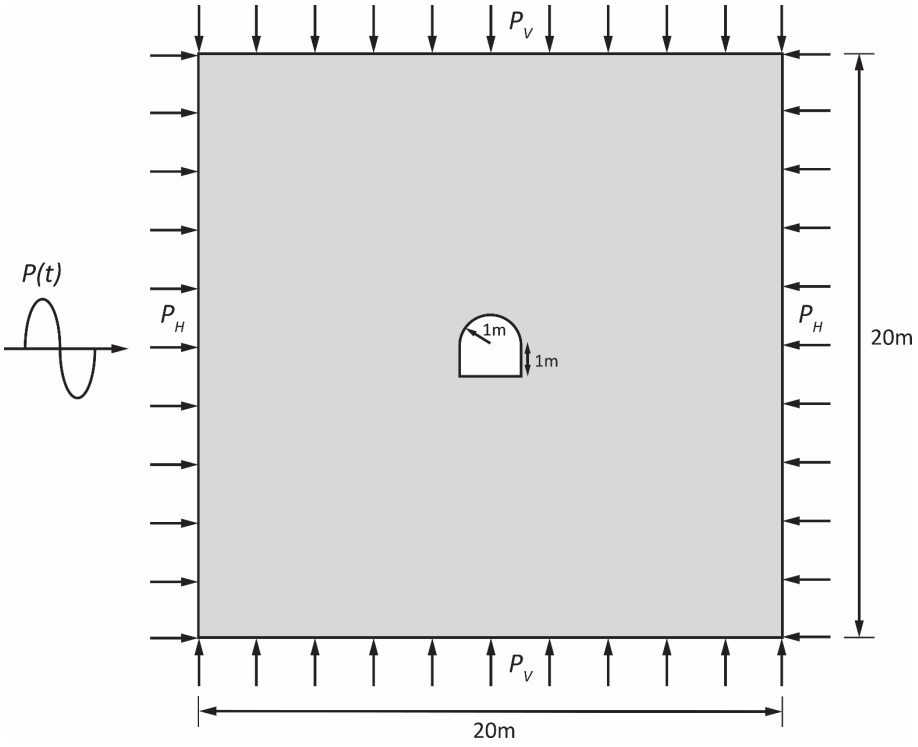

Figure 6.16 The tunnel subjected to in-situ stresses and a dynamic disturbance

The simulation is divided into two stages. In the first stage, static in-situ stresses are imposed on the model to obtain the initial stress state. Specifically, the horizontal stress P_H is applied on the left and right boundaries of the model, and the vertical stress P_V is

applied on the top and bottom boundaries simultaneously. Various groups of in-situ stresses will be applied in the following simulations to study its effect on the rockburst. Then, in the second stage, a dynamic disturbance *P(t)* is uniformly imposed on the left boundary to trigger the spalling and rockburst. The applied dynamic disturbance is in the form of an impulse function, given by Eq.58. In this example, the peak value P_0 is set as 50 MPa, the rising time t_0 is set as 2 ms, and the ratio β/α is kept as a constant of 1.5.

6.4.2 Spalling and Rockburst in Tunnel

The mechanism of the spalling and rockburst phenomenon in tunnels triggered by dynamic disturbance is studied first. The horizontal and vertical in-situ stress are both set to 10 MPa. Simulation results, including distributions of the maximum principal stress and minimum principal stress, and particle velocity at different time steps are presented in Figure 6.17 and Figure 6.18 respectively. An enlarged view around the tunnel is adopted in figures. Fractures are explicitly indicated as solid black lines.

From the results of maximum and minimum principal stress (Figure 6.17) at t = 0, we can conclude that the roof, floor, and left and right surfaces of the tunnel are all under the state of compression before the dynamic disturbance is applied. The distribution of compressive stresses around the tunnel is jointly determined by the shape of the tunnel and the combination of horizontal and vertical in-situ stresses. After the dynamic disturbance is applied, a compressive stress wave propagates from the left boundary of the model toward the tunnel, and reaches the left surface of the tunnel at t = 1.74 ms. The incident stress wave takes the left surface, as well as the left half of the roof, of the tunnel as a free surface and reflects as a tensile wave. Therefore, the superposition of the reflected tensile stress, the incident compressive stress and the initial compressive stress induced by the in-situ stress arises in this area. A domain under the state of tension is consequently formed on condition that the reflected tensile stress is greater than the sum of the compressive stresses.

At t = 2.14 ms, a spalling fracture is generated since the resultant tensile stress reaches the tensile strength of the rock. The distance from the spalling fracture to the surface of

the tunnel is 0.57 m. Wave propagations in the rock become complicated due to the creation and propagation of the spalling fracture. More spalling and non-spalling fractures are generated with the propagation of stress waves. Some of these fractures, especially those are close to the tunnel, have the chance to propagate to the surface of the tunnel. Some rock blocks can be clearly seen in the figure that are ejected from the surface of the tunnel.

The contour chart of particle velocity at t = 4 ms is enlarged without plotting fractures for the sake of clarity (Figure 6.18c). Consequently, the rockburst in a tunnel triggered by the dynamic disturbance is modelled in this example. The ejected rock in this simulation is fractured into several pieces. The velocities of ejected rock blocks are in the range of 4 ~ 10 m/s. The total size of the ejected rock is approximately 0.14 m in width and 0.6 m in height.

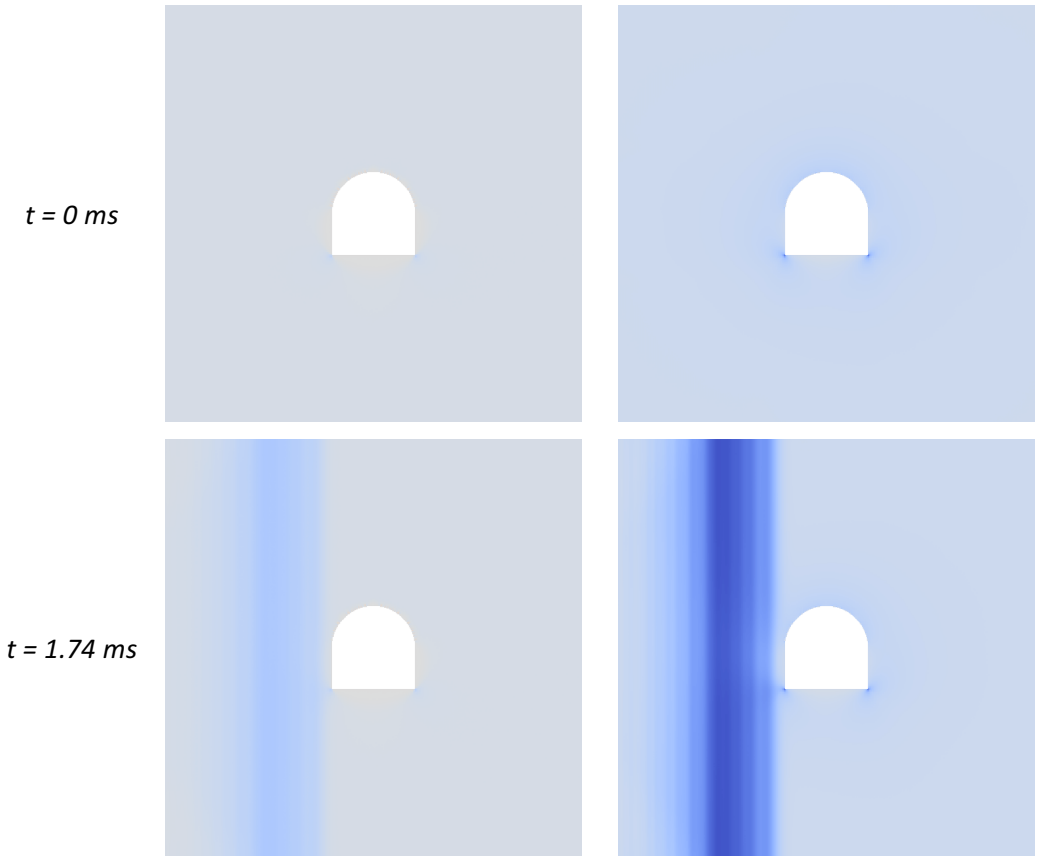

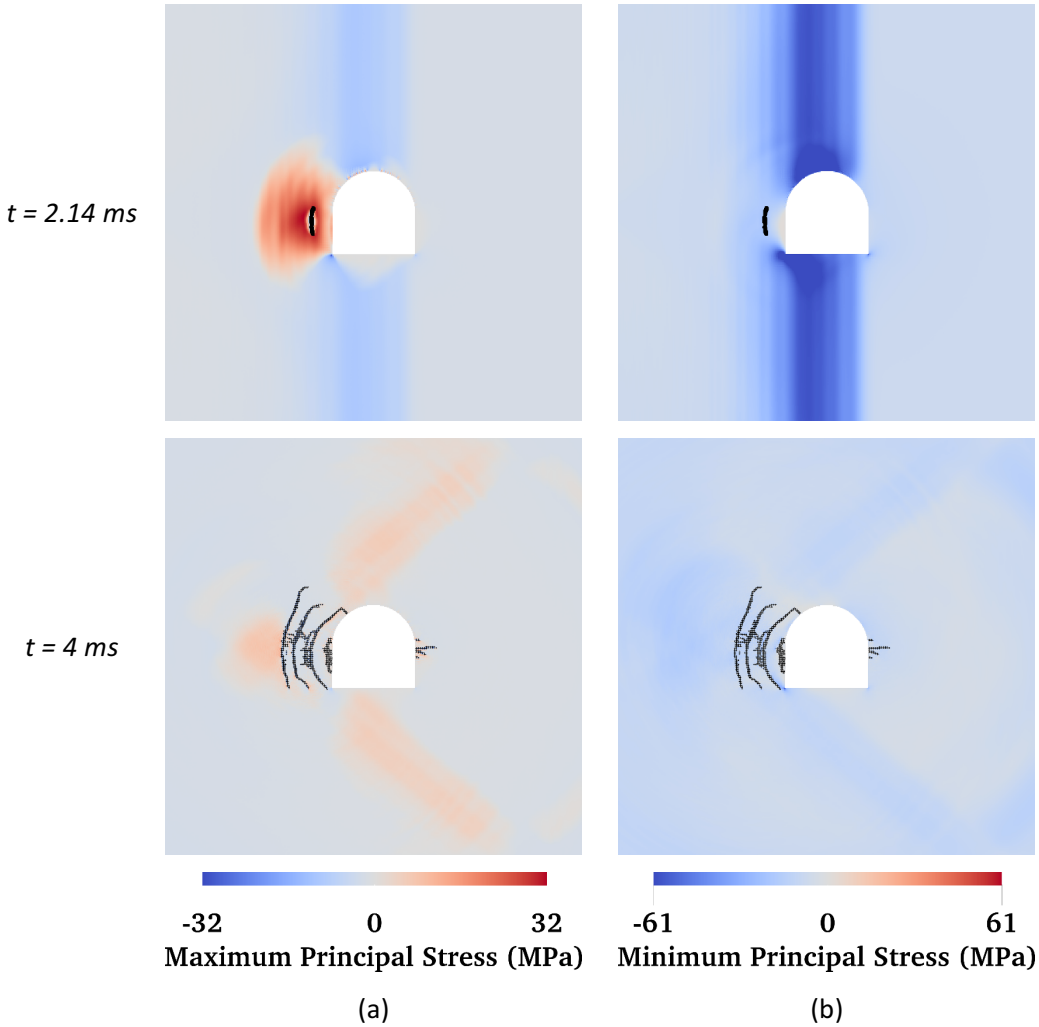

Figure 6.17 The spalling and rockburst process of the tunnel with P_H=10 MPa and P_V=10 MPa: (a) distribution of maximum principal stress; (b) distribution of minimum principal stress

This simulation shows that rockburst is possible to happen in tunnels subjected to in-situ stresses and a dynamic disturbance. The mechanism of the rockburst under this circumstance is the spalling induced by the dynamic disturbance near the surface of the tunnel. The contribution of in-situ stresses is to provide an initial stress field around the tunnel. A compressive stress field helps to offset the reflected tensile stress wave, and therefore has the function to reduce or prevent the spalling/rockburst in tunnel. However, spalling still happens when the peak value of the dynamic disturbance is high enough. Spalling fractures that propagate to the tunnel forms the rockburst with the rock ejection from the surface. Other fractures remaining in the rock mass did not enhance the rockburst but can be a potential hazard to the safety of the tunnel in following use.

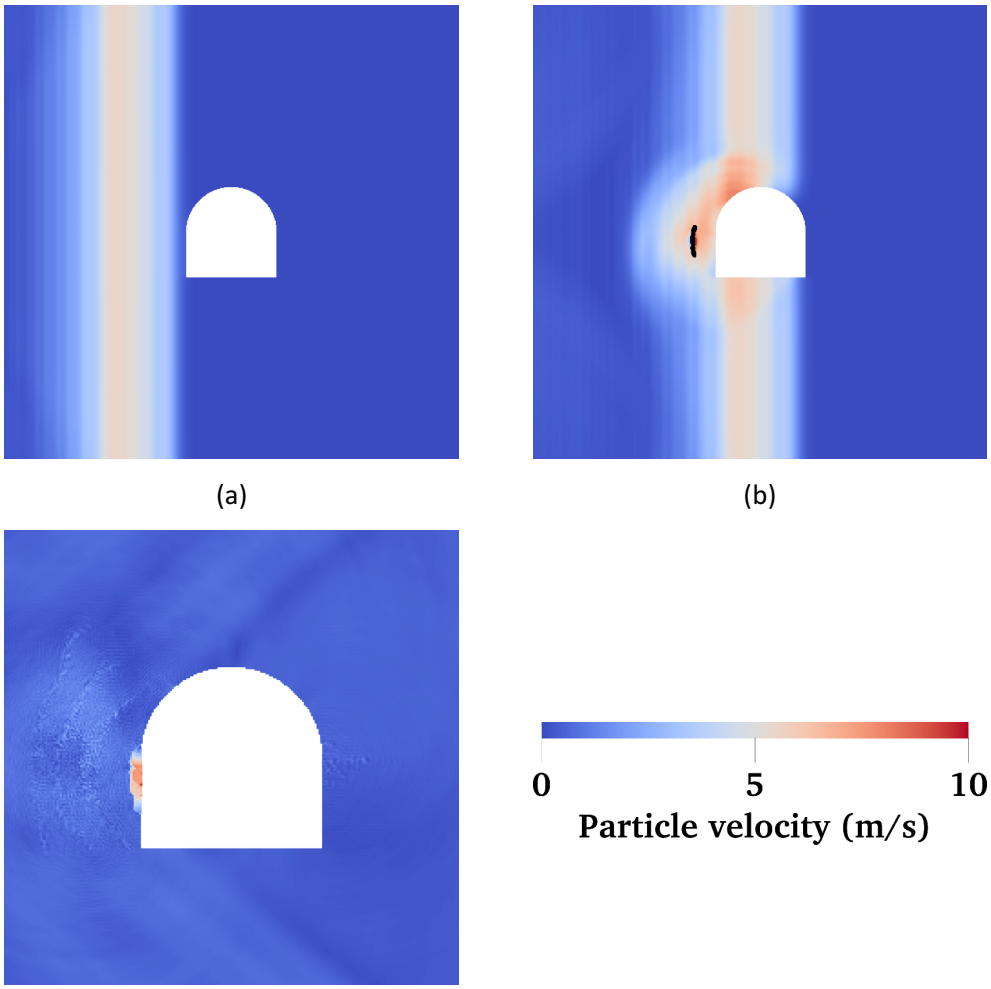

Figure 6.18 The spalling and rockburst process of the tunnel with P_H=10 MPa and P_V=10 MPa, distribution of particle velocity: (a) t = 1.74 ms; (b) t = 2.14 ms; (c) t = 4 ms, enlarged view around the tunnel

6.4.3 Effect of In-situ Stress

The effect of in-situ stresses on the rockburst in tunnels is investigated in this section. The dynamic disturbance to the tunnel is kept the same as that in the previous section. Five cases with different in-situ stresses are considered in total. The horizontal stress and vertical stress for each case is listed in Table 6.2. The term *lateral pressure coefficient* is the ratio of the horizontal stress to the vertical stress.

Table 6.2. The in-situ stresses for different cases

Case	P_H (MPa)	P_V (MPa)	Lateral pressure coefficient
1	20	10	2
2	10	20	0.5
3	20	20	1
4	10	1	10
5	20	2	10

Simulation results of all cases are summarized in Figure 6.19 and Figure 6.20. The distributions of maximum principal stress and minimum principal stress at the initial state, namely subjected to the static in-situ stress only, for each case are presented in Figure 6.19, while the distributions of particle velocity at the time of 4 ms for each case are presented in Figure 6.20. Fractures are explicitly indicated as solid lines.

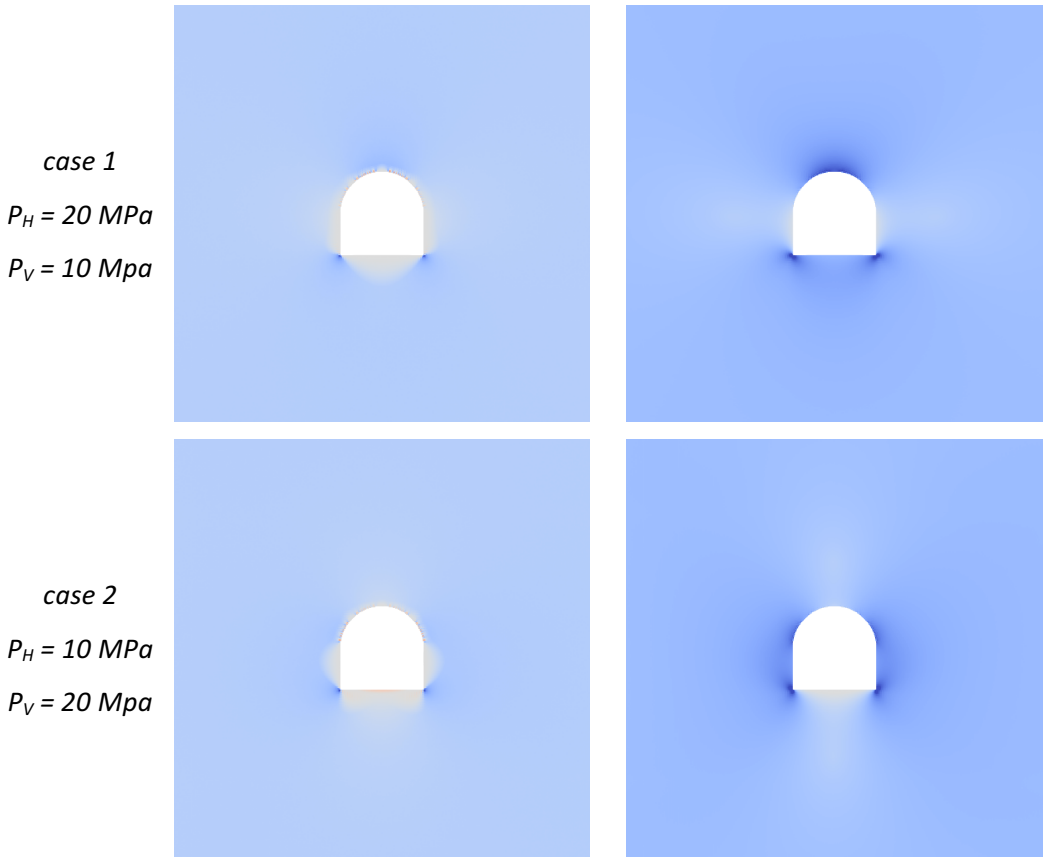

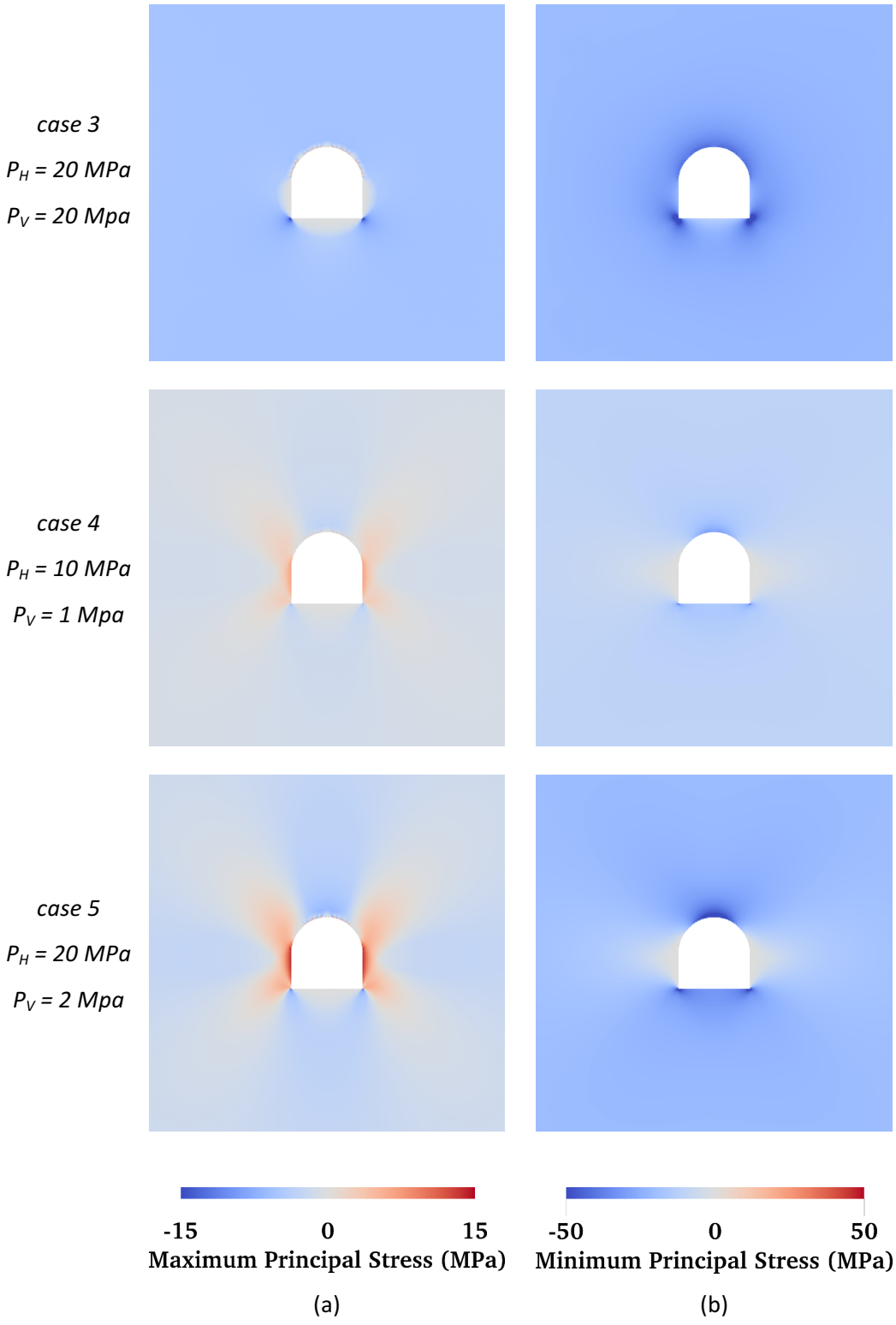

Figure 6.19 Initial states of tunnels subjected to different in-situ stresses: (a) distribution of maximum principal stress; (b) distribution of minimum principal stress

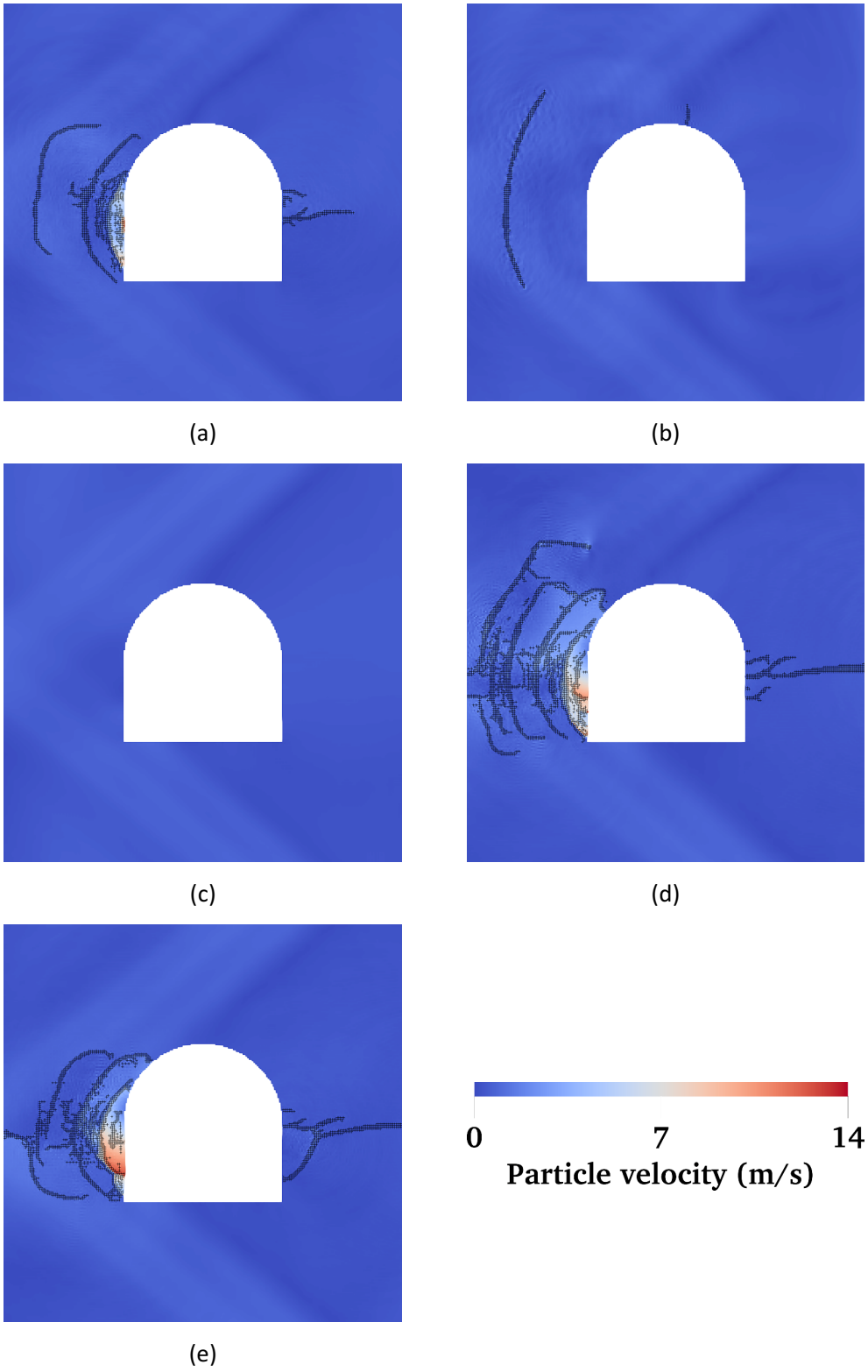

Figure 6.20 The spalling and rockburst of tunnels subjected to different in-situ stresses, enlarged view around the tunnel: (a) case 1, P_H = 20 MPa, P_V = 10 MPa; (b) case 2, P_H = 10 MPa, P_V = 20 MPa; (c) case 3, P_H = 20 MPa, P_V = 20 MPa; (d) case 4, P_H = 10 MPa, P_V = 1 MPa; (e) case 5, P_H = 20 MPa, P_V = 2 MPa

In *case 1*, the horizontal in-situ stress is increased to 20 MPa and the vertical in-situ stress is the same, when comparing with those in the previous section (called *case 0* hereafter). Consequently, the initial compressive stresses at the roof and floor of the tunnel are higher than *case 0*, while the initial compressive stress at the left and right surface of the tunnel is lower. Since the dynamic disturbance is reflected at the left surface of the tunnel, the reflected tensile stress is easier to offset the reduced initial compressive stress in this region. Therefore, spalling fractures are easier to be generated in this case than *case 0*. Simulation result at t = 4 ms indicates that the rockburst in *case 1* is severer than *case 0*, as the ejected rock is bigger in size (1.02 m in height, 0.18 m in width) and higher in flying speed (in the range of 4.5 ~ 11.5 m/s). Spalling fractures that locate far from the tunnel are harder to propagate vertically but tend to propagate toward the tunnel, because the compressive stress is high in the region above the tunnel.

On the other hand, in *case 2*, the horizontal in-situ stress remains at 10 MPa and the vertical in-situ stress is increased to 20 MPa. In contrast to *case 1*, the initial compressive stress at the left surface of the tunnel in *case 2* is higher than that in *case 0*. Therefore, spalling fractures are difficult to be generated and propagated in this case. The fracture pattern at the final stage indicates that there is only one spalling fracture generated and no rockburst is triggered in this case.

Further in *case 3*, when the horizontal and vertical in-situ stresses are both increased to 20 MPa, the initial compressive stresses surrounding the tunnel are even higher than all cases mentioned earlier. As a result, no fracture is generated and the tunnel is safe to the dynamic disturbance in this case.

Above analysis shows that the initial compressive stress at the left surface of the tunnel is mainly determined by the vertical in-situ stress, but also influenced by the horizontal in-situ stress. In general, increasing the vertical in-situ stress, hence decreasing the lateral pressure coefficient, will significantly increase the compressive stress around the left surface of the tunnel and help the tunnel to withstand the dynamic disturbance in horizontal direction. The effect of horizontal in-situ stress is complex. With the increase

of the horizontal in-situ stress and consequently the lateral pressure coefficient, the compressive stress around the left surface of the tunnel will be reduced (*case 0* and *case 1*) or increased (*case 2* and *case 3*) when the horizontal in-situ stress is higher or lower than the vertical in-situ stress respectively. Therefore, the conclusion can be made that the effect of the lateral pressure coefficient on rockburst is not monotonic but related to the relationship between horizontal and vertical in-situ stresses.

Although the lateral pressure coefficient has been greater than 1 in *case 1*, the left surface of the tunnel is still under the state of compression before the dynamic disturbance is applied. In *case 4*, we increase the coefficient to 10 by decreasing the vertical in-situ stress to 1 MPa. Although such a high coefficient has exceeded the typical value range in practice, it helps to reveal the mechanism of rockburst under static in-situ stress and dynamic disturbance and makes the result in this study comparable to the work of Zhu et al. (2010). Simulation results show that the left and right surfaces and surrounding regions are initially under the state of tension instead. The superposition between the initial tensile stress and the reflected tensile stress will weaken the ability of the tunnel to withstand the dynamic disturbance. The fracture pattern of *case 4* indicates a severer rockburst than *case 0*. This result shows that when there is a large difference between the horizontal and vertical in-situ stress, the rockburst can be easily triggered in the direction of the higher in-situ stress.

A constant lateral pressure coefficient of 10 is adopted in *case 5*, but increasing the horizontal and vertical in-situ stress to 20 MPa and 2 MPa respectively. Simulation results show that the initial tensile stress around the left and right surface of the tunnel is increased correspondingly. As a result, the rockburst in *case 5* is severer than that in *case 4*. Although the size of the ejected rock in two cases is almost the same, the maximum velocity of the ejected rock is increased from 11.6 m/s to 14.0 m/s. However, on the other hand, if there is no large difference between the horizontal and vertical in-situ stresses, increasing the value of in-situ stress while keeping a constant lateral pressure coefficient will not lead to a severer rockburst, e.g., *case 0* and *case 3*. In practice, it is common to see the horizontal and vertical in-situ stresses increase proportionally with the increase

of the depth of the tunnel, keeping an almost constant lateral pressure coefficient. This simulation indicates that in deep tunnels, severe rockburst can be easily triggered by dynamic disturbance when there is a large difference between horizontal and vertical in-situ stresses along the direction of the higher one.

Analysis above is made on condition that the dynamic disturbance is imposed and reflected horizontally. In fact, the effect of in-situ stress on rockburst is closely related to the direction of dynamic disturbance. If the dynamic disturbance is reflected at the roof or floor of the tunnel, in-situ stresses that produce high tensile stresses along the vertical direction will lead to severe rockburst.

6.5 Summary

Rock spalling is found to be closely related to strain bursting, the most common type of rockburst. In this chapter, PNMM is applied to study the spalling failure of rock materials and spalling-induced rockburst. The spalling of long rock bars is first studied. Simulation results provide satisfactory prediction for the thickness of the first spall piece and spall strengths at different loading rates. The effect of loading types on the spalling fracture pattern is also studied. Then, plate impact tests with both long and short flyers at both low and high impact velocities are simulated. The simulated failure pattern agrees well with the numerical results by other models in the reference. Last, the validated model is adopted to simulate the rockburst of tunnels under various static in-situ stress conditions, triggered by a same dynamic disturbance. Following conclusions can be drawn from the simulation results:

1) The mechanism of rockburst under this circumstance is the spalling failure near the surface of tunnel induced by the dynamic disturbance. The ejection of rock is formed by spalling fractures that propagate to the surface of tunnel. The function of in-situ stress is to provide an initial stress field around the tunnel. A compressive stress field assists the tunnel in preventing rockburst by offsetting the reflected tensile stress wave, whereas a tensile stress field weakens the ability

of the tunnel to withstand the dynamic disturbance due to its superposition with the reflected tensile stress wave.

2) The initial stress field near the horizontal surface of tunnel is mainly determined by the vertical in-situ stress. When the vertical in-situ stress is much lower than the horizontal in-situ stress, the horizontal surface of tunnel will be under the state of tension. When the vertical in-situ stress is close to or higher than the horizontal in-situ stress, the horizontal surface of tunnel will be under the state of compression. The effect of horizontal in-situ stress on the state of the horizontal surface of tunnel is opposite when it is higher or lower than the vertical in-situ stress. Therefore, the effect of the lateral pressure coefficient on rockburst is not monotonic.

3) The effect of the depth of tunnel on rockburst is related to the lateral pressure coefficient. If the horizontal in-situ stress is much higher/lower than the vertical in-situ stress, increasing the depth of tunnel will also increase the possibility of rockburst in tunnel. However, if the horizontal in-situ stress is close to the vertical in-situ stress, the possibility of rockburst will be decreased by increasing the depth of tunnel. The most dangerous situation for deep tunnels is that there is a large difference between the horizontal and vertical in-situ stresses and the dynamic disturbance comes from the direction of the higher in-situ stress.

Chapter 7 Conclusions

7.1 Summary of Contributions and Findings

This thesis aims to develop a reliable numerical method for rock dynamics, especially for the dynamic fracturing of rock (Chapter 1). After reviewing and comparing the advantages and challenges of existing numerical methods (Chapter 2), a particle-based numerical manifold method (PNMM) is proposed and applied to study the rate-dependent behaviors of rock under various conditions. The developments of PNMM, including its conception, methodology, formulae, implementation, characteristics, and validation, are summarized as follows:

Development of PNMM (Chapter 3 and Chapter 4)

1) PNMM is modified from the numerical manifold method (NMM) and particle manifold method (PMM). Some ideas from the extended finite element method (XFEM) and discrete element method (DEM) are adopted.

2) PNMM is implemented in C++, incorporating some open-source third-party C++ libraries, e.g., the computational geometry algorithms library (CGAL) and Eigen.

3) The dual-layer-cover system is inherited from NMM to form the first level of discretization in PNMM. Manifold elements are generated at this stage. Degrees of freedom and interpolation functions are defined on manifold elements. Particles are introduced as the second level of discretization. A group of particles are generated within each manifold element at this stage. Material parameters, body forces, external loads, and boundary conditions are defined on particles. The global governing equation of PNMM in matrix form is assembled by variables defined on both manifold elements and particles using a particle integration scheme. The mechanical behaviors of particles in a same manifold element are determined by the manifold element, and there are no forces defined between particles. A link is defined between two neighboring particles to represent their continuous status. The JHB strength model is implemented and applied on links

to determine the failure of a link. Failed links simulate the initiation and propagation of fractures. Enrichment are applied on the manifold elements containing a fracture tip. Contact forces are defined on a pair of neighboring particles belong to different blocks/objects.

4) A particle integration scheme is developed for PNMM. The particle integration scheme utilizes existing allocation of particles and requires no further operations. Numerical example shows the proposed integration scheme is suitable for any integrand on both convex and concave integration domains. The integration accuracy is mainly determined by the number of particles, and affected by the size distribution as well as the position of particles, especially when the number of particles is relatively small.

5) An interpolation function enrichment scheme from XFEM has been successfully incorporated into PNMM to improve the accuracy around fracture tips.

6) The Johnson-Holmquist-Beissel (JHB) model is implemented to simulate the rate-dependent behavior of rock in PNMM. Parameters in the model are determined with reference to literature. Numerical examples show that the PNMM coupled with the JHB model can accurately simulate the dynamic response of rock under different loading/strain rates.

7) Calibration examples have been performed to verify the performance of PNMM for both static and dynamic problems. It is also proved that the accuracy of PNMM is primarily influenced by the number of manifold elements, whereas the effect of particle resolution is limited. However, enough number of particles are still necessary to guarantee the accuracy of the particle integration scheme.

8) Comparing with NMM, the proposed method simplifies the contact operation between blocks, improves the flexibility in initiating and determining the propagation path of fractures, and gains the ability to simulate the heterogeneity of rock materials.

9) Comparing with PMM, several aspects have been reclarified and improved in the proposed model, including the adoption of high-order interpolation functions, the

development of a particle integration scheme, an enrichment function around fracture tips, an improved algorithm for the generation of links, the unambiguous failure of links, the incorporation of a rate-dependent strength model, expanded applications in rock dynamics, and improved calculation performance.

Due to its characteristics, PNMM could be easily applied to study the heterogeneity of rock materials, the initiation, coalescence, and propagation of fractures, the detachment and post-failure behavior of rock fragments, the contact between rock blocks, and the rate-dependent behavior of rock, making it a promising tool for modelling the dynamic fracturing of rock. Therefore, in this thesis, PNMM has been applied to study the spalling of rock, the spalling-induced rockburst in tunnels, and rock scratching/cutting. The main conclusions drawn from these applications are summarized as follows:

Rock scratching (Chapter 5)

10) The rock scratching in both ductile and brittle modes of failure could be simulated by PNMM. It is validated that at an intermediate cutting depth, the mode of rock scratching is in the transition from ductile to brittle, the pattern of rock failure and fluctuation of cutting force shows both characteristics of that in ductile and brittle mode.

11) There is a range of cutting depth at which the mode of rock scratching is in the transition from ductile to brittle. The transitional cutting depth range could be estimated by PNMM from the result of MSE.

12) The effect of cutting depth on rock scratching could be divided into three phases. The value of MSE decreases rapidly when the cutting depth is shallow, remains approximately constant when the cutting depth is intermediate, and decreases nonlinearly at an intermediate rate in deep cuts.

13) The effect of cutting speed on rock scratching is significant when the dynamic response of rock is taken into consideration. The cutting force and MSE both increase with the increase of cutting speed. A critical cutting speed exists, above which the increase of cutting force and MSE are accelerated. The value of the

critical cutting speed is believed to be related to the relationship between the dynamic compressive strength of rock and strain rates.

14) The effect of cutter rake angle is significant on cutting force but moderate on MSE. The actual cutting depth is found to be increased with the increase of cutter rake angle, which leads to a significant difference between the cutting force and MSE when the cutter rake angle is great. Besides, there exists a narrow range of cutter rake angle, in which the cutting force and MSE are both found to be constant.

Spalling and rockburst (Chapter 6)

15) The spalling of long rock bars could be successfully simulated by PNMM, since the thickness of the first spall piece is accurately predicted and spall strengths at different loading rates are in a reasonable range. The spalling pattern is related to the type of the wave applied on the bar. When a decreasing or increasing triangular wave was imposed, the second spall fracture would possibly be created on the remaining part of the bar or the first spall piece respectively. Whereas in the case where a symmetrical triangular wave is applied, a spalling zone instead of a single spalling fracture will be generated.

16) The spalling process of the plate impact with a long flyer is similar to that of long bars. In this case, spalling fractures are parallel to the flyer and target, and the number of spalling fractures increases with the increase of the impact velocity. When a short flyer is adopted to impact on the plate, a fracturing zone shorter than the flyer will be formed, and several spalling pieces will be extracted from the target due to the propagation of longitudinal fractures.

17) Rockburst could be triggered by a far-field dynamic disturbance in the tunnel subjected to static in-situ stresses and could be simulated by PNMM. The in-situ stress provides an initial stress field surrounding the tunnel. A compressive stress field assists the tunnel in preventing rockburst, whereas a tensile stress field weakens the ability of the tunnel to withstand the dynamic disturbance. The dynamic disturbance induces spalling fractures near the surface of tunnel. The ejection of rock is formed by spalling fractures that propagate to the surface of tunnel.

18) The initial stress field near the horizontal surface of tunnel is primarily determined by the vertical in-situ stress. When the vertical in-situ stress is much lower than the horizontal one, the horizontal surface of tunnel will be under the state of tension; When the vertical in-situ stress is close to or higher than the horizontal one, the horizontal surface of tunnel will be under the state of compression. The effect of the lateral pressure coefficient on rockburst is not monotonic.

19) The effect of the depth of tunnel on rockburst is related to the lateral pressure coefficient. If the horizontal in-situ stress is much higher/lower than the vertical one, increasing the depth of tunnel will also increase the possibility of rockburst in tunnel; If the horizontal in-situ stress is close to the vertical in-situ stress, the possibility of rockburst will be decreased by increasing the depth of tunnel.

20) When talking about the rockburst in a deep tunnel, the most dangerous situation is that there is a large difference between the horizontal and vertical in-situ stresses and the dynamic disturbance comes from the direction of the higher one.

7.2 Recommendations for Future Work

Based on the development of PNMM and simulation results obtained in this research, following recommendations for future work are outlines:

1) Investigate the heterogeneity of rock materials. The heterogeneity could be defined by either a random distribution of material properties among particles (similar to RFPA) or a meso-scale structure. In the second scenario, the geometry information of aggregates need to be provided first. Then, particles locating in aggregates are assigned with different material parameters. This work could be an important application of PNMM in the future. In the next phase, a PNMM model should be able to be generated from a CT scanning image. The effect of the variety of particle size and particle allocation should also be studied in the scope of this work.

2) Enhance the computational efficiency of PNMM by developing a parallelized version. Both central processing unit (CPU) based and graphics processing unit

(GPU) based technologies are possible to be adopted. The first attempt could be made on solving the global equation.

3) Develop an explicitly coupled method using PNMM and NMM. A major difference between PNMM and NMM is the introduction of particles. It is possible to introduce particles as the second level of discretization in a part of the model, and conducts only the first discretization in the rest portion of the model with less interest, e.g., in far-field, in the domain with small deformation, in the domain where no fracture and contact happens, etc.

4) Extend the PNMM code to three-dimensional cases. Some formulae proposed for three-dimensional PMM in (Sun, 2012) could be borrowed. The extension of the proposed particle integration scheme to three dimensions is straightforward. The three-dimensional PNMM could be applied to the problems that do not obey the plane strain and plane stress assumptions, e.g., the projectile penetration in rock plates.

5) Incorporate thermal and fluid components into PNMM and investigate coupled problems, which have been increasingly important in rock engineering.

6) Based on the results in Chapter 5, the transitional cutting depth range could be thoroughly studied. The effect of the cutting speed, cutter rake angle, and rock properties should be investigated respectively. Experimental tests are better to be conducted as well to validate the simulation results.

7) Based on the results in Chapter 6, rockburst induced by underground excavation, i.e. a near-field dynamic disturbance, could be further investigated. In fact, this type of rockburst is more possibly to take place in practice.

8) The application of PNMM could be extended to the stress wave propagation in jointed rock masses, which is also an important topic in rock dynamics.

References

ABAQUS. 2017. *Computer Software* [Online]. Available: https://www.3ds.com/ [Accessed].

ADACHI, J. I., DETOURNAY, E. & DRESCHER, A. 1996. Determination of rock strength parameters from cutting tests. *2nd North American Rock Mechanics Symposium.* Montreal, Canada: American Rock Mechanics Association.

AI, H. A. & AHRENS, T. J. 2006. Simulation of dynamic response of granite: A numerical approach of shock-induced damage beneath impact craters. *International Journal of Impact Engineering,* 33**,** 1-10.

AKONO, A. T., REIS, P. M. & ULM, F. J. 2011. Scratching as a fracture process: from butter to steel. *Physical Review Letters,* 106**,** 204302.

AKONO, A. T. & ULM, F. J. 2011. Scratch test model for the determination of fracture toughness. *Engineering Fracture Mechanics,* 78**,** 334-342.

ALI, A. 1996. FEM analysis of concrete structures subjected to mode-I and mixed-mode loading conditions. *Computers & structures,* 61**,** 1043-1055.

AN, X. 2010. *Extended numerical manifold method for engineering failure analysis.* Nanyang Technological University, Singapore.

AN, X., NING, Y., MA, G. & HE, L. 2014. Modeling progressive failures in rock slopes with non-persistent joints using the numerical manifold method. *International Journal for Numerical and Analytical Methods in Geomechanics,* 38**,** 679-701.

AN, X. M., LI, L. X., MA, G. W. & ZHANG, H. H. 2011. Prediction of rank deficiency in partition of unity-based methods with plane triangular or quadrilateral meshes. *Computer Methods in Applied Mechanics and Engineering,* 200**,** 665-674.

ANDRADE, J. E., LIM, K. W., AVILA, C. F. & VLAHINIĆ, I. 2012. Granular element method for computational particle mechanics. *Computer Methods in Applied Mechanics and Engineering,* 241-244**,** 262-274.

ANDREEV, K. & HARMUTH, H. 2003. FEM simulation of the thermo-mechanical behaviour and failure of refractories - a case study. *Journal of Materials Processing Technology,* 143-144**,** 72-77.

ANSYS. 2017. *Computer Software* [Online]. Available: http://www.ansys.com/ [Accessed].

BABUŠKA, I. & MELENK, J. M. 1997. The partition of unity method. *International Journal for Numerical Methods in Engineering,* 40**,** 727-758.

BAHAADDINI, M., HAGAN, P. C., MITRA, R. & HEBBLEWHITE, B. K. 2015. Parametric study of smooth joint parameters on the shear behaviour of rock joints. *Rock Mechanics and Rock Engineering,* 48**,** 923-940.

BAILEY, C. & CROSS, M. 1995. A finite volume procedure to solve elastic solid mechanics problems in three dimensions on an unstructured mesh. *International journal for numerical methods in engineering,* 38**,** 1757-1776.

BAO, H. & ZHAO, Z. 2013. Modeling brittle fracture with the nodal-based discontinuous deformation analysis. *International Journal of Computational Methods,* 10**,** 1350040.

BAO, H., ZHAO, Z. & TIAN, Q. 2014. On the Implementation of augmented Lagrangian method in the two-dimensional discontinuous deformation Analysis. *International Journal for Numerical and Analytical Methods in Geomechanics,* 38**,** 551-571.

BEER, G. & POULSEN, B. A. 1994. Efficient numerical modelling of faulted rock using the boundary element method. *International journal of rock mechanics and mining sciences & geomechanics abstracts,* 31**,** 485-506.

BEER, G. & POULSEN, B. A. 1995. Rock joints - BEM computations. *Studies in Applied Mechanics,* 42**,** 343-373.

BELYTSCHKO, T., CHIAPETTA, R. L. & BARTEL, H. D. 1976. Efficient large scale non-linear transient analysis by finite elements. *International Journal for Numerical Methods in Engineering,* 10**,** 579-596.

BELYTSCHKO, T., GRACIE, R. & VENTURA, G. 2009. A review of extended/generalized finite element methods for material modeling. *Modelling and Simulation in Materials Science and Engineering,* 17**,** 043001.

BELYTSCHKO, T., KRONGAUZ, Y., ORGAN, D., FLEMING, M. & KRYSL, P. 1996. Meshless methods: an overview and recent developments. *Computer Methods in Applied Mechanics and Engineering,* 139**,** 3-47.

BOCK, S. & PRUSEK, S. 2015. Numerical study of pressure on dams in a backfilled mining shaft based on PFC3D code. *Computers and Geotechnics,* 66**,** 230-244.

BONORA, N. 1997. A nonlinear CDM model for ductile failure. *Engineering Fracture Mechanics,* 58**,** 11-28.

BOON, C. W., HOULSBY, G. T. & UTILI, S. 2015. Designing tunnel support in jointed rock masses via the DEM. *Rock Mechanics and Rock Engineering,* 48**,** 603-632.

BRESCIANI, L. M., MANES, A., ROMANO, T. A., IAVARONE, P. & GIGLIO, M. 2016. Numerical modelling to reproduce fragmentation of a tungsten heavy alloy projectile impacting a ceramic tile: Adaptive solid mesh to the SPH technique and the cohesive law. *International Journal of Impact Engineering,* 87**,** 3-13.

CAI, J. G. & ZHAO, J. 2000. Effects of multiple parallel fractures on apparent attenuation of stress waves in rock masses. *International Journal of Rock Mechanics and Mining Sciences,* 37**,** 661-682.

CAI, M. 2013. Fracture initiation and propagation in a Brazilian disc with a plane interface: a numerical study. *Rock mechanics and rock engineering,* 46**,** 289-302.

CAI, M., KAISER, P. K. & DUFF, D. J. 2012. Rock support design in burst-prone ground utilizing an interactive design tool. *46th U.S. Rock Mechanics/Geomechanics Symposium.* Chicago, Illinois: American Rock Mechanics Association.

CAI, Y., ZHUANG, X. & ZHU, H. 2013. A generalized and efficient method for finite cover generation in the numerical manifold method. *International Journal of Computational Methods,* 10**,** 1350028.

CAILLABET, Y., FABRIE, P., LANDEREAU, P., NOETINGER, B. & QUINTARD, M. 2000. Implementation of a finite-volume method for the determination of effective parameters in fissured porous media. *Numerical Methods for Partial Differential Equations,* 16**,** 237-263.

CAMACHO, G. T. & ORTIZ, M. 1996. Computational modelling of impact damage in brittle materials. *International Journal of Solids and Structures,* 33**,** 2899-2938.

CARMONA, H. A., WITTEL, F. K. & KUN, F. 2014. From fracture to fragmentation: Discrete element modeling. *The European Physical Journal Special Topics,* 223**,** 2369-2382.

CERROLAZA, M. & GARCIA, R. 1997. Boundary elements and damage mechanics to analyze excavations in rock mass. *Engineering analysis with boundary elements,* 20**,** 1-16.

CHAKRABORTY, S. & SHAW, A. 2013. A pseudo-spring based fracture model for SPH simulation of impact dynamics. *International Journal of Impact Engineering,* 58**,** 84-95.

CHE, D., ZHANG, W. & EHMANN, K. 2016. Chip formation and force responses in linear rock cutting: An experimental study. *Journal of Manufacturing Science and Engineering,* 139**,** 011011.

CHEMENDA, A. I. 2015. Three-dimensional numerical modeling of hydrostatic tests of porous rocks in a triaxial cell. *International Journal of Rock Mechanics and Mining Sciences,* 76**,** 33-43.

CHEN, G., OHNISHI, Y. & ITO, T. 1998. Development of high-order manifold method. *International Journal for Numerical Methods in Engineering,* 43**,** 685-712.

CHEN, H., ZHAO, Z. & SUN, J. 2013. Coupled hydro-mechanical model for fractured rock masses using the discontinuous deformation analysis. *Tunnelling and Underground Space Technology,* 38**,** 506-516.

CHEN, S. G. & ZHAO, J. 1998. A study of UDEC modelling for blast wave propagation in jointed rock masses. *International Journal of Rock Mechanics and Mining Sciences,* 35**,** 93-99.

CHEN, Y. L. & LI, L. X. 2015. An improved numerical manifold method and its application. *Engineering Analysis with Boundary Elements,* 52**,** 120-129.

CHENG, Y. M., ZHANG, Y. H. & CHEN, W. S. 2002. Wilson non-conforming element in numerical manifold method. *Communications in numerical methods in engineering,* 18**,** 877-884.

CHIOU, Y. J., LEE, Y. M. & TSAY, R. J. 2002. Mixed mode fracture propagation by manifold method. *International Journal of Fracture,* 114**,** 327-347.

CHO, N., MARTIN, C. D. & SEGO, D. C. 2007. A clumped particle model for rock. *International Journal of Rock Mechanics and Mining Sciences,* 44**,** 997-1010.

CHO, S. H. & KANEKO, K. 2004. Influence of the applied pressure waveform on the dynamic fracture processes in rock. *International Journal of Rock Mechanics and Mining Sciences,* 41**,** 771-784.

CHO, S. H., OGATA, Y. & KANEKO, K. 2003. Strain-rate dependency of the dynamic tensile strength of rock. *International Journal of Rock Mechanics and Mining Sciences,* 40**,** 763-777.

CLOUGH, R. W. 1960. *The finite element method in plane stress analysis*, American Society of Civil Engineers.

CUI, X., XUE, Z., PEI, Y. & FANG, D. 2011. Preliminary study on ductile fracture of imperfect lattice materials. *International Journal of Solids and Structures,* 48**,** 3453-3461.

DA SILVA, B. G. & EINSTEIN, H. H. 2013. Modeling of crack initiation, propagation and coalescence in rocks. *International Journal of Fracture,* 182**,** 167-186.

DAGRAIN, F., POYOL, E. & RICHARD, T. 2004. Strength logging of geomaterials from scratch tests. *Proceedings of the rock engineering theory and practice.*

DAI, F., WEI, M. D., XU, N. W., MA, Y. & YANG, D. S. 2015. Numerical assessment of the progressive rock fracture mechanism of cracked chevron notched Brazilian disc specimens. *Rock Mechanics and Rock Engineering,* 48**,** 463-479.

DARVE, F. & NICOT, F. 2005. On incremental non-linearity in granular media: phenomenological and multi-scale views (Part I). *International Journal for Numerical and Analytical Methods in Geomechanics,* 29**,** 1387-1409.

DATTOLA, G., DI PRISCO, C., REDAELLI, I. & UTILI, S. 2014. A distinct element method numerical investigation of compaction processes in highly porous cemented granular materials. *International Journal for Numerical and Analytical Methods in Geomechanics,* 38**,** 1101-1130.

DEB, D. & PRAMANIK, R. 2013. Failure process of brittle rock using smoothed particle hydrodynamics. *Journal of Engineering Mechanics,* 139**,** 1551-1565.

DENG, S., LI, H., MA, G., HUANG, H. & LI, X. 2014. Simulation of shale-proppant interaction in hydraulic fracturing by the discrete element method. *International Journal of Rock Mechanics and Mining Sciences,* 70**,** 219-228.

DENG, X. F., CHEN, S. G., ZHU, J. B., ZHOU, Y. X. & ZHAO, Z. Y. 2015. UDEC–AUTODYN hybrid modeling of a large-scale underground explosion test. *Rock Mechanics and Rock Engineering,* 48**,** 737-747.

DENG, X. F., ZHU, J. B., CHEN, S. G. & ZHAO, J. 2012. Some fundamental issues and verification of 3DEC in modeling wave propagation in jointed rock masses. *Rock Mechanics and Rock Engineering,* 45**,** 943-951.

DETOURNAY, E. & DEFOURNY, P. 1992. A phenomenological model for the drilling action of drag bits. *International Journal of Rock Mechanics and Mining Sciences & Geomechanics Abstracts,* 29**,** 13-23.

DíAZ-RUBIO, F. G., PÉREZ, J. R. G. & GÁLVEZ, V. S. 2002. The spalling of long bars as a reliable method of measuring the dynamic tensile strength of ceramics. *International Journal of Impact Engineering,* 27**,** 161-177.

DIEDERICHS, M. S. 2007. The 2003 Canadian Geotechnical Colloquium: Mechanistic interpretation and practical application of damage and spalling prediction criteria for deep tunnelling. *Canadian Geotechnical Journal,* 44**,** 1082-1116.

DING, X., ZHANG, L., ZHU, H. & ZHANG, Q. 2014. Effect of model scale and particle size distribution on PFC3D simulation results. *Rock Mechanics and Rock Engineering,* 47**,** 2139-2156.

DONZÉ, F. V., BOUCHEZ, J. & MAGNIER, S. A. 1997. Modeling fractures in rock blasting. *International Journal of Rock Mechanics and Mining Sciences,* 34**,** 1153-1163.

ELMO, D. & STEAD, D. 2010. An integrated numerical modelling-discrete fracture network approach applied to the characterisation of rock mass strength of naturally fractured pillars. *Rock mechanics and rock engineering,* 43**,** 3-19.

ERZAR, B. & FORQUIN, P. 2011. Experiments and mesoscopic modelling of dynamic testing of concrete. *Mechanics of Materials,* 43**,** 505-527.

FAKHIMI, A. & LANARI, M. 2014. DEM-SPH simulation of rock blasting. *Computers and Geotechnics,* 55**,** 158-164.

FAKHIMI, A. & VILLEGAS, T. 2007. Application of dimensional analysis in calibration of a discrete element model for rock deformation and fracture. *Rock Mechanics and Rock Engineering,* 40**,** 193-211.

FAN, H. & HE, S. 2015. An angle-based method dealing with vertex–vertex contact in the two-dimensional discontinuous deformation analysis (DDA). *Rock Mechanics and Rock Engineering,* 48**,** 2031-2043.

FAN, H., ZHAO, J. & ZHENG, H. 2017. A high-order three-dimensional numerical manifold method enriched with derivative degrees of freedom. *Engineering Analysis with Boundary Elements,* 83**,** 229-241.

FAN, S. C., JIAO, Y. Y. & ZHAO, J. 2004. On modelling of incident boundary for wave propagation in jointed rock masses using discrete element method. *Computers and Geotechnics,* 31**,** 57-66.

FAN, X., KULATILAKE, P. H. S. W. & CHEN, X. 2015. Mechanical behavior of rock-like jointed blocks with multi-non-persistent joints under uniaxial loading: A particle mechanics approach. *Engineering Geology,* 190**,** 17-32.

FANG, Z. Q., HU, G. M., DU, J., FAN, Z. & LIU, J. 2015. A contact detection algorithm for multi-sphere particles by means of two-level-grid-searching in DEM simulations. *International Journal for Numerical Methods in Engineering,* 102**,** 1869-1893.

FENG, Y. T., HAN, K. & OWEN, D. R. J. 2012. Energy-conserving contact interaction models for arbitrarily shaped discrete elements. *Computer Methods in Applied Mechanics and Engineering,* 205–208**,** 169-177.

FERELLEC, J. F. & MCDOWELL, G. 2010. A method to model realistic particle shape and inertia in DEM. *Granular Matter,* 12**,** 459-467.

FLAC. 2017. *Computer software* [Online]. Available: https://www.itascacg.com [Accessed].

FORQUIN, P. & ERZAR, B. 2010. Dynamic fragmentation process in concrete under impact and spalling tests. *International Journal of Fracture,* 163**,** 193-215.

FRANCIONI, M., SALVINI, R., STEAD, D. & LITRICO, S. 2014. A case study integrating remote sensing and distinct element analysis to quarry slope stability assessment in the Monte Altissimo area, Italy. *Engineering Geology,* 183**,** 290-302.

FU, X., SHENG, Q., ZHANG, Y., ZHOU, Y. & DAI, F. 2015. Boundary setting method for the seismic dynamic response analysis of engineering rock mass structures using the discontinuous deformation analysis method. *International Journal for Numerical and Analytical Methods in Geomechanics,* 39**,** 1693-1712.

GALOUEI, M. & FAKHIMI, A. 2015. Size effect, material ductility and shape of fracture process zone in quasi-brittle materials. *Computers and Geotechnics,* 65**,** 126-135.

GARZON, J., O'HARA, P., DUARTE, C. A. & BUTTLAR, W. G. 2014. Improvements of explicit crack surface representation and update within the generalized finite element method with application to three-dimensional crack coalescence. *International Journal for Numerical Methods in Engineering,* 97**,** 231-273.

GEUZAINE, C. & REMACLE, J. F. 2009. Gmsh: A 3-D finite element mesh generator with built-in pre- and post-processing facilities. *International Journal for Numerical Methods in Engineering,* 79**,** 1309-1331.

GHASEMZADEH, H., RAMEZANPOUR, M. A. & BODAGHPOUR, S. 2014. Dynamic high order numerical manifold method based on weighted residual method. *International Journal for Numerical Methods in Engineering,* 100**,** 596-619.

GINGOLD, R. A. & MONAGHAN, J. J. 1977. Smoothed particle hydrodynamics: theory and application to non-spherical stars. *Monthly Notices of the Royal Astronomical Society,* 181**,** 375-389.

GISCHIG, V., EBERHARDT, E., MOORE, J. R. & HUNGR, O. 2015. On the seismic response of deep-seated rock slope instabilities - insights from numerical modelling. *Engineering Geology,* 193**,** 1-18.

GONG, B. & TANG, C. A. 2017. Slope-slide simulation with discontinuous deformation and displacement analysis. *International Journal of Geomechanics,* 17**,** E4016017.

GONG, F. Q. & ZHAO, G. F. 2014. Dynamic indirect tensile strength of sandstone under different loading rates. *Rock Mechanics and Rock Engineering,* 47**,** 2271–2278.

GONG, Q., YIN, L., MA, H. & ZHAO, J. 2016. TBM tunnelling under adverse geological conditions: An overview. *Tunnelling and Underground Space Technology,* 57**,** 4-17.

GONG, Q. M., JIAO, Y. Y. & ZHAO, J. 2006a. Numerical modelling of the effects of joint spacing on rock fragmentation by TBM cutters. *Tunnelling and Underground Space Technology,* 21**,** 46-55.

GONG, Q. M., YIN, L. J., WU, S. Y., ZHAO, J. & TING, Y. 2012. Rock burst and slabbing failure and its influence on TBM excavation at headrace tunnels in Jinping II hydropower station. *Engineering Geology,* 124**,** 98-108.

GONG, Q. M., ZHAO, J. & HEFNY, A. M. 2006b. Numerical simulation of rock fragmentation process induced by two TBM cutters and cutter spacing optimization. *Tunnelling and Underground Space Technology,* 21**,** 263.

GONG, Q. M., ZHAO, J. & JIAO, Y. Y. 2005. Numerical modeling of the effects of joint orientation on rock fragmentation by TBM cutters. *Tunnelling and Underground Space Technology,* 20**,** 183-191.

GRANET, S., FABRIE, P., LEMONNIER, P. & QUINTARD, M. 2001. A two-phase flow simulation of a fractured reservoir using a new fissure element method. *Journal of Petroleum Science and Engineering,* 32**,** 35-52.

GRIFFITH, W. A., BECKER, J., CIONE, K., MILLER, T. & PAN, E. 2014. 3D topographic stress perturbations and implications for ground control in underground coal mines. *International Journal of Rock Mechanics and Mining Sciences,* 70**,** 59-68.

GU, J. & ZHAO, Z. 2009. Considerations of the discontinuous deformation analysis on wave propagation problems. *International journal for numerical and analytical methods in geomechanics,* 33**,** 1449-1465.

GU, R. & OZBAY, U. 2014. Distinct element analysis of unstable shear failure of rock discontinuities in underground mining conditions. *International Journal of Rock Mechanics and Mining Sciences,* 68**,** 44-54.

GUPTA, P. & DUARTE, C. A. 2014. Simulation of non-planar three-dimensional hydraulic fracture propagation. *International Journal for Numerical and Analytical Methods in Geomechanics,* 38**,** 1397-1430.

HAGAN, T. N. 1979. Rock breakage by explosives. *Acta Astronautica,* 6**,** 329-340.

HAHN, M., WALLMERSPERGER, T. & KRÖPLIN, B. H. 2010. Discrete element representation of continua: Proof of concept and determination of the material parameters. *Computational Materials Science,* 50**,** 391-402.

HASANPOUR, R., ROSTAMI, J. & ÜNVER, B. 2014. 3D finite difference model for simulation of double shield TBM tunneling in squeezing grounds. *Tunnelling and Underground Space Technology,* 40**,** 109-126.

HATZOR, Y. H., ARZI, A. A., ZASLAVSKY, Y. & SHAPIRA, A. 2004. Dynamic stability analysis of jointed rock slopes using the DDA method: King Herod's Palace, Masada, Israel. *International Journal of Rock Mechanics and Mining Sciences,* 41**,** 813-832.

HE, L., AN, X. M., MA, G. W. & ZHAO, Z. Y. 2013. Development of three-dimensional numerical manifold method for jointed rock slope stability analysis. *International Journal of Rock Mechanics and Mining Sciences,* 64**,** 22-35.

HE, L., AN, X. M. & ZHAO, Z. Y. 2014. Development of contact algorithm for three-dimensional numerical manifold method. *International Journal for Numerical Methods in Engineering,* 97**,** 423-453.

HE, L. & MA, G. 2010. Development of 3D numerical manifold method. *International Journal of Computational Methods,* 7**,** 107-129.

HE, L. & ZHANG, Q. B. 2015. Numerical investigation of arching mechanism to underground excavation in jointed rock mass. *Tunnelling and Underground Space Technology,* 50**,** 54-67.

HE, M., XIA, H., JIA, X., GONG, W., ZHAO, F. & LIANG, K. 2012. Studies on classification, criteria and control of rockbursts. *Journal of Rock Mechanics and Geotechnical Engineering,* 4**,** 97-114.

HE, X. & XU, C. 2015. Discrete element modelling of rock cutting: from ductile to brittle transition. *International Journal for Numerical and Analytical Methods in Geomechanics,* 39**,** 1331-1351.

HE, X. & XU, C. 2016. Specific Energy as an Index to Identify the Critical Failure Mode Transition Depth in Rock Cutting. *Rock Mechanics and Rock Engineering,* 49**,** 1461-1478.

HE, X., XU, C., PENG, K. & HUANG, G. 2017. On the critical failure mode transition depth for rock cutting with different back rake angles. *Tunnelling and Underground Space Technology,* 63**,** 95-105.

HILLERBORG, A., MODÉER, M. & PETERSSON, P. E. 1976. Analysis of crack formation and crack growth in concrete by means of fracture mechanics and finite elements. *Cement and Concrete Research,* 6**,** 773-781.

HOLEČEK, M. & MORAVEC, F. 2006. Hyperelastic model of a material which microstructure is formed by balls and springs. *International journal of solids and structures,* 43**,** 7393-7406.

HOLMQUIST, T. J. & JOHNSON, G. R. 2005. Characterization and evaluation of silicon carbide for high-velocity impact. *Journal of Applied Physics,* 97**,** 093502.

HOLMQUIST, T. J. & JOHNSON, G. R. 2011. A computational constitutive model for glass subjected to large strains, high strain rates and high pressures. *Journal of Applied Mechanics,* 78**,** 051003.

HOLMQUIST, T. J., JOHNSON, G. R. & COOK, W. H. 1993. A computational constitutive model for concrete subjected to large strains, high strain rates, and high pressures. *In:* M.J., M. & J.E., B. (eds.) *Proceedings of 14th International Symposium on Ballistics.* Quebec, Sweden.

HRENNIKOFF, A. 1941. Solution of problems of elasticity by the framework method. *Journal of applied mechanics,* 8**,** 169-175.

HUANG, H. & DETOURNAY, E. 2008. Intrinsic length scales in tool-rock interaction. *International Journal of Geomechanics,* 8**,** 39-44.

HUANG, H., LECAMPION, B. & DETOURNAY, E. 2013. Discrete element modeling of tool-rock interaction I: rock cutting. *International Journal for Numerical and Analytical Methods in Geomechanics,* 37**,** 1913-1929.

IDELSOHN, S. R. & ONATE, E. 2006. To mesh or not to mesh. That is the question. *Computer Methods in Applied Mechanics and Engineering,* 195**,** 4681-4696.

ISLAM, M. J. 2011. *Response and Failure Mechanics of Structural Member under High Velocity Impact.* National University of Singapore.

JAIME, M. C., ZHOU, Y., LIN, J. S. & GAMWO, I. K. 2015. Finite element modeling of rock cutting and its fragmentation process. *International Journal of Rock Mechanics and Mining Sciences,* 80**,** 137-146.

JIA, P. & ZHU, W. C. 2015. Mechanism of zonal disintegration around deep underground excavations under triaxial stress – Insight from numerical test. *Tunnelling and Underground Space Technology,* 48**,** 1-10.

JIANG, C., ZHAO, G. F. & KHALILI, N. 2017. On crack propagation in brittle material using the distinct lattice spring model. *International Journal of Solids and Structures,* 118-119**,** 41-57.

JIANG, H., WANG, L., LI, L. & GUO, Z. 2014a. Safety evaluation of an ancient masonry seawall structure with modified DDA method. *Computers and Geotechnics,* 55**,** 277-289.

JIANG, M. J., CHEN, H., TAPIAS, M., ARROYO, M. & FANG, R. 2014b. Study of mechanical behavior and strain localization of methane hydrate bearing sediments with different saturations by a new DEM model. *Computers and Geotechnics,* 57**,** 122-138.

JIAO, Y. Y., ZHANG, H. Q., TANG, H. M., ZHANG, X. L., ADOKO, A. C. & TIAN, H. N. 2014. Simulating the process of reservoir-impoundment-induced landslide using the extended DDA method. *Engineering Geology,* 182**,** 37-48.

JIAO, Y. Y., ZHANG, H. Q., ZHANG, X. L., LI, H. B. & JIANG, Q. H. 2015a. A two-dimensional coupled hydromechanical discontinuum model for simulating rock hydraulic fracturing. *International Journal for Numerical and Analytical Methods in Geomechanics,* 39**,** 457-481.

JIAO, Y. Y., ZHANG, X. L., ZHANG, H. Q., LI, H. B., YANG, S. Q. & LI, J. C. 2015b. A coupled thermo-mechanical discontinuum model for simulating rock cracking induced by temperature stresses. *Computers and Geotechnics,* 67**,** 142-149.

JIAO, Y. Y., ZHANG, X. L. & ZHAO, J. 2012. Two-dimensional DDA contact constitutive model for simulating rock fragmentation. *Journal of Engineering Mechanics,* 138**,** 199-209.

JIAO, Y. Y., ZHANG, X. L., ZHAO, J. & LIU, Q. S. 2007. Viscous boundary of DDA for modeling stress wave propagation in jointed rock. *International Journal of Rock Mechanics and Mining Sciences,* 44**,** 1070-1076.

JIAO, Y. Y., ZHAO, J. & GE, X. R. 2004. New formulation and validation of the three-dimensional extension of a static relaxation method. *Advances in Engineering Software,* 35**,** 317-323.

JING, L. 2003. A review of techniques, advances and outstanding issues in numerical modelling for rock mechanics and rock engineering. *International Journal of Rock Mechanics and Mining Sciences,* 40**,** 283-353.

JING, L. & HUDSON, J. A. 2002. Numerical methods in rock mechanics. *International Journal of Rock Mechanics and Mining Sciences,* 39**,** 409-427.

JOHN, F. P., MARK, A. H., RAJU, K. & RONALD, E. W. 2009. A poly-ellipsoid particle for non-spherical discrete element method. *Engineering Computations,* 26**,** 645-657.

JOHNSON, G. R. & HOLMQUIST, T. J. 1992. A computational constitutive model for brittle materials subjected to large strains, high strain rates and high pressures. *In:* MEYERS, M. A., MUIR, L. E. & STAUDHAMMER, K. P. (eds.) *Shock-Wave and High-Strain-Rate Phenomena in Materials.* New York: Marcel Dekker Inc.

JOHNSON, G. R. & HOLMQUIST, T. J. 1994. An improved computational constitutive model for brittle materials. *AIP Conference Proceedings,* 309**,** 981-984.

JOHNSON, G. R., HOLMQUIST, T. J. & BEISSEL, S. R. 2003. Response of aluminum nitride (including a phase change) to large strains, high strain rates, and high pressures. *Journal of Applied Physics,* 94**,** 1639-1646.

KAISER, P. K. 1996. *Canadian Rockburst Support Handbook*, Geomechanics Research Centre.

KAISER, P. K. & MCCREATH, D. R. 1994. Rock mechanics considerations for drilled or bored excavations in hard rock. *Tunnelling and Underground Space Technology,* 9**,** 425-437.

KAMAI, R. & HATZOR, Y. H. 2008. Numerical analysis of block stone displacements in ancient masonry structures: A new method to estimate historic ground motions. *International journal for numerical and analytical methods in geomechanics,* 32**,** 1321-1340.

KANG, Y., LIU, Q., GONG, G. & WANG, H. 2014. Application of a combined support system to the weak floor reinforcement in deep underground coal mine. *International Journal of Rock Mechanics and Mining Sciences,* 71**,** 143-150.

KAZERANI, T. 2013. Effect of micromechanical parameters of microstructure on compressive and tensile failure process of rock. *International Journal of Rock Mechanics and Mining Sciences,* 64**,** 44-55.

KAZERANI, T., YANG, Z. Y. & ZHAO, J. 2012. A discrete element model for predicting shear strength and degradation of rock joint by using compressive and tensile test data. *Rock Mechanics and Rock Engineering,* 45**,** 695-709.

KAZERANI, T. & ZHAO, J. 2010. Micromechanical parameters in bonded particle method for modelling of brittle material failure. *International Journal for Numerical and Analytical Methods in Geomechanics,* 34**,** 1877-1895.

KAZERANI, T. & ZHAO, J. 2014. A microstructure-based model to characterize micromechanical parameters controlling compressive and tensile failure in crystallized rock. *Rock Mechanics and Rock Engineering,* 47**,** 435-452.

KHAZAEI, C., HAZZARD, J. & CHALATURNYK, R. 2015. Damage quantification of intact rocks using acoustic emission energies recorded during uniaxial compression test and discrete element modeling. *Computers and Geotechnics,* 67**,** 94-102.

KLERCK, P. A. 2000. *The Finite Element Modelling of Discrete Fracture in Quasi-brittle Materials.* University of Wales.

KONG, X. & LIU, J. 2002. Dynamic failure numeric simulations of model concrete-faced rock-fill dam. *Soil Dynamics and Earthquake Engineering,* 22**,** 1131-1134.

KOU, S. Q., LINDQVIST, P. A., TANG, C. A. & XU, X. H. 1999. Numerical simulation of the cutting of inhomogeneous rocks. *International Journal of Rock Mechanics and Mining Sciences,* 36**,** 711-717.

KUNA-CISKAL, H. & SKRZYPEK, J. J. 2004. CDM based modelling of damage and fracture mechanisms in concrete under tension and compression. *Engineering Fracture Mechanics,* 71**,** 681-698.

LABORDE, P., POMMIER, J., RENARD, Y. & SALAÜN, M. 2005. High-order extended finite element method for cracked domains. *International Journal for Numerical Methods in Engineering,* 64**,** 354-381.

LAFHAJ, Z. & SHAHROUR, I. 2000. Use of the boundary element method for the analysis of permeability tests in boreholes. *Engineering analysis with boundary elements,* 24**,** 695-698.

LAJTAI, E. Z., DUNCAN, E. J. S. & CARTER, B. J. 1991. The effect of strain rate on rock strength. *Rock Mechanics and Rock Engineering,* 24**,** 99-109.

LAN, M., WAISMAN, H. & HARARI, I. 2013. A High-order extended finite element method for extraction of mixed-mode strain energy release rates in arbitrary crack settings based on Irwin's integral. *International Journal for Numerical Methods in Engineering,* 96**,** 787-812.

LEE, S. J. & HASHASH, Y. M. A. 2015. iDEM: An impulse-based discrete element method for fast granular dynamics. *International Journal for Numerical Methods in Engineering,* 104**,** 79-103.

LEI, W. D., TENG, J., HEFNY, A. M. & ZHAO, J. 2006. Transmission ratio (Tn) in the radian direction normal to joints in 2-D compressional wave propagation in rock masses. *Journal of University of Science and Technology Beijing,* 13**,** 199-206.

LEVY, S., MOLINARI, J. F., VICARI, I. & DAVISON, A. C. 2010. Dynamic fragmentation of a ring: Predictable fragment mass distributions. *Physical Review E,* 82**,** 066105.

LI, J. C., MA, G. W. & ZHAO, J. 2011. Analysis of stochastic seismic wave interaction with a slippery rock fault. *Rock Mechanics and Rock Engineering,* 44**,** 85-92.

LI, S. & LIU, W. K. 2002. Meshfree and particle methods and their applications. *Applied Mechanics Reviews,* 55**,** 1-34.

LI, S., WANG, Z., PING, Y., ZHOU, Y. & ZHANG, L. 2014a. Discrete element analysis of hydro-mechanical behavior of a pilot underground crude oil storage facility in granite in China. *Tunnelling and Underground Space Technology,* 40**,** 75-84.

LI, S. C. & CHENG, Y. M. 2005. Enriched meshless manifold method for two-dimensional crack modeling. *Theoretical and applied fracture mechanics,* 44**,** 234-248.

LI, X., CAO, W., ZHOU, Z. & ZOU, Y. 2014b. Influence of stress path on excavation unloading response. *Tunnelling and Underground Space Technology,* 42**,** 237-246.

LI, X., TAO, M., WU, C., DU, K. & WU, Q. 2017a. Spalling strength of rock under different static pre-confining pressures. *International Journal of Impact Engineering,* 99**,** 69-74.

LI, X., ZHANG, Q. B., HE, L. & ZHAO, J. 2017b. Particle-based numerical manifold method to model dynamic fracture process in rock blasting. *International Journal of Geomechanics,* 17**,** E4016014.

LI, X., ZOU, Y. & ZHOU, Z. 2014c. Numerical simulation of the rock SHPB test with a special shape striker based on the discrete element method. *Rock Mechanics and Rock Engineering,* 47**,** 1693-1709.

LI, X. F., LI, H. B., LIU, Y. Q., ZHOU, Q. C. & XIA, X. 2016. Numerical simulation of rock fragmentation mechanisms subject to wedge penetration for TBMs. *Tunnelling and Underground Space Technology,* 53**,** 96-108.

LI, Y., ZHANG, D., FANG, Q., YU, Q. & XIA, L. 2014d. A physical and numerical investigation of the failure mechanism of weak rocks surrounding tunnels. *Computers and Geotechnics,* 61**,** 292-307.

LIM, K. W. & ANDRADE, J. E. 2014. Granular element method for three-dimensional discrete element calculations. *International Journal for Numerical and Analytical Methods in Geomechanics,* 38**,** 167-188.

LIM, K. W., KRABBENHOFT, K. & ANDRADE, J. E. 2014. A contact dynamics approach to the Granular Element Method. *Computer Methods in Applied Mechanics and Engineering,* 268**,** 557-573.

LIN, C. T., AMADEI, B., JUNG, J. & DWYER, J. 1996. Extensions of discontinuous deformation analysis for jointed rock masses. *International Journal of Rock Mechanics and Mining Sciences & Geomechanics Abstracts,* 33**,** 671-694.

LIN, H., XIONG, W., XIONG, Z. & GONG, F. 2015. Three-dimensional effects in a flattened Brazilian disk test. *International Journal of Rock Mechanics and Mining Sciences,* 74**,** 10-14.

LIN, J. S. 2003. A mesh-based partition of unity method for discontinuity modeling. *Computer Methods in Applied Mechanics and Engineering,* 192**,** 1515-1532.

LIN, S., QI, Y. & SU, H. Formulation of high-order numerical manifold method and fast simplex integration based on special matrix operations. *In:* MACLAUGHLIN, M. M. & SITAR, N., eds. Preceedings of ICADD-7 Seventh International Conference on the Analysis of Discontinuous Deformation, December 2005. 183-190.

LISJAK, A., GARITTE, B., GRASSELLI, G., MÜLLER, H. R. & VIETOR, T. 2015. The excavation of a circular tunnel in a bedded argillaceous rock (Opalinus Clay): Short-term rock mass response and FDEM numerical analysis. *Tunnelling and Underground Space Technology,* 45**,** 227-248.

LISJAK, A. & GRASSELLI, G. 2014. A review of discrete modeling techniques for fracturing processes in discontinuous rock masses. *Journal of Rock Mechanics and Geotechnical Engineering,* 6**,** 301-314.

LISJAK, A., GRASSELLI, G. & VIETOR, T. 2014. Continuum-discontinuum analysis of failure mechanisms around unsupported circular excavations in anisotropic clay shales. *International Journal of Rock Mechanics and Mining Sciences,* 65**,** 96-115.

LISJAK, A., LIU, Q., ZHAO, Q., MAHABADI, O. K. & GRASSELLI, G. 2013. Numerical simulation of acoustic emission in brittle rocks by two-dimensional finite-discrete element analysis. *Geophysical Journal International,* 195**,** 423-443.

LIU, F., JIANG, M. & ZHU, F. 2014a. Discrete element analysis of uplift and lateral capacity of a single pile in methane hydrate bearing sediments. *Computers and Geotechnics,* 62**,** 61-76.

LIU, H. 2004. *Numerical modelling of the rock fragmentation process by mechanical tools.* Lulea University of Technology.

LIU, H. Y., KOU, S. Q., LINDQVIST, P. A. & TANG, C. A. 2002. Numerical simulation of the rock fragmentation process induced by indenters. *International Journal of Rock Mechanics and Mining Sciences,* 39**,** 491-505.

LIU, M. B. & LIU, G. R. 2010. Smoothed particle hydrodynamics (SPH): An overview and recent developments. *Archives of Computational Methods in Engineering,* 17**,** 25-76.

LIU, W. K., JUN, S. & ZHANG, Y. F. 1995. Reproducing kernel particle methods. *International journal for numerical methods in fluids,* 20**,** 1081-1106.

LIU, Y., LI, H., XIAO, K., LI, J., XIA, X. & LIU, B. 2014b. Seismic stability analysis of a layered rock slope. *Computers and Geotechnics,* 55**,** 474-481.

LU, C. Y., TANG, C. L., CHAN, Y. C., HU, J. C. & CHI, C. C. 2014. Forecasting landslide hazard by the 3D discrete element method: A case study of the unstable slope in the Lushan hot spring district, central Taiwan. *Engineering Geology,* 183**,** 14-30.

LU, M. & MCDOWELL, G. R. 2007. The importance of modelling ballast particle shape in the discrete element method. *Granular Matter,* 9**,** 69-80.

LU, Y. B. & LI, Q. M. 2011. About the dynamic uniaxial tensile strength of concrete-like materials. *International Journal of Impact Engineering,* 38**,** 171-180.

LUCY, L. B. 1977. A numerical approach to the testing of the fission hypothesis. *The astronomical journal,* 82**,** 1013-1024.

MA, G., AN, X. & HE, L. 2010. The numerical manifold method: A review. *International Journal of Computational Methods,* 7**,** 1-32.

MA, G. W. & AN, X. M. 2008. Numerical simulation of blasting-induced rock fractures. *International Journal of Rock Mechanics and Mining Sciences,* 45**,** 966-975.

MA, G. W., AN, X. M., ZHANG, H. H. & LI, L. X. 2009. Modeling complex crack problems using the numerical manifold method. *International Journal of Fracture,* 156**,** 21-35.

MA, H., YIN, L. & JI, H. 2011. Numerical study of the effect of confining stress on rock fragmentation by TBM cutters. *International Journal of Rock Mechanics and Mining Sciences,* 48**,** 1021-1033.

MAHABADI, O. K., COTTRELL, B. E. & GRASSELLI, G. 2010. An example of realistic modelling of rock dynamics problems: FEM/DEM simulation of dynamic Brazilian test on Barre granite. *Rock mechanics and rock engineering,* 43**,** 707-716.

MAHABADI, O. K., LISJAK, A., MUNJIZA, A. & GRASSELLI, G. 2012a. Y-Geo: New combined finite-discrete element numerical code for geomechanical applications. *International Journal of Geomechanics,* 12**,** 676-688.

MAHABADI, O. K., RANDALL, N. X., ZONG, Z. & GRASSELLI, G. 2012b. A novel approach for micro-scale characterization and modeling of geomaterials incorporating actual material heterogeneity. *Geophysical Research Letters,* 39**,** L01303.

MASUDA, K., MIZUTANI, H. & YAMADA, I. 1987. Experimental-study of strain-rate dependence and pressure dependence of failure properties of granite. *Journal of Physics of the Earth,* 35**,** 37-66.

MENEZES, P. L., LOVELL, M. R., AVDEEV, I. V. & HIGGS III, C. F. 2014. Studies on the formation of discontinuous rock fragments during cutting operation. *International Journal of Rock Mechanics and Mining Sciences,* 71**,** 131-142.

MIKI, S., SASAKI, T., KOYAMA, T., NISHIYAMA, S. & OHNISHI, Y. O. 2010. Development of coupled discontinuous deformation analysis and numerical manifold method (NMM-DDA). *International Journal of Computational Methods,* 7**,** 131-150.

MILLON, O., RUIZ-RIPOLL, M. L. & HOERTH, T. 2016. Analysis of the behavior of sedimentary rocks under impact loading. *Rock Mechanics and Rock Engineering,* 49**,** 4257-4272.

MITELMAN, A. & ELMO, D. 2016. Analysis of tunnel support design to withstand spalling induced by blasting. *Tunnelling and Underground Space Technology,* 51**,** 354-361.

MOËS, N. & BELYTSCHKO, T. 2002. Extended finite element method for cohesive crack growth. *Engineering Fracture Mechanics,* 69**,** 813-833.

MOËS, N., DOLBOW, J. & BELYTSCHKO, T. 1999. A finite element method for crack growth without remeshing. *International Journal for Numerical Methods in Engineering,* 46**,** 131-150.

MOLINARI, J. F., GAZONAS, G., RAGHUPATHY, R., RUSINEK, A. & ZHOU, F. 2007. The cohesive element approach to dynamic fragmentation: the question of energy convergence. *International Journal for Numerical Methods in Engineering,* 69**,** 484-503.

MOLLON, G. & ZHAO, J. 2014. 3D generation of realistic granular samples based on random fields theory and Fourier shape descriptors. *Computer Methods in Applied Mechanics and Engineering,* 279**,** 46-65.

MONAGHAN, J. J. 2012. Smoothed particle hydrodynamics and its diverse applications. *Annual Review of Fluid Mechanics,* 44**,** 323-346.

MORTAZAVI, A. & KATSABANIS, P. D. 2001. Modelling burden size and strata dip effects on the surface blasting process. *International Journal of Rock Mechanics and Mining Sciences,* 38**,** 481-498.

MUNJIZA, A. 2004. *The combined finite-discrete element method*, John Wiley & Sons.

MUNJIZA, A. & ANDREWS, K. R. F. 1998. NBS contact detection algorithm for bodies of similar size. *International Journal for Numerical Methods in Engineering,* 43**,** 131-149.

MUNJIZA, A., LATHAM, J. P. & ANDREWS, K. R. F. 2000. Detonation gas model for combined finite-discrete element simulation of fracture and fragmentation. *International Journal for Numerical Methods in Engineering,* 49**,** 1495-1520.

NARASIMHAN, T. N. & WITHERSPOON, P. A. 1976. An integrated finite difference method for analyzing fluid flow in porous media. *Water Resources Research,* 12**,** 57-64.

NEMCIK, J., MA, S., AZIZ, N., REN, T. & GENG, X. 2014. Numerical modelling of failure propagation in fully grouted rock bolts subjected to tensile load. *International Journal of Rock Mechanics and Mining Sciences,* 71**,** 293-300.

NGO, N. T., INDRARATNA, B. & RUJIKIATKAMJORN, C. 2014. DEM simulation of the behaviour of geogrid stabilised ballast fouled with coal. *Computers and Geotechnics,* 55**,** 224-231.

NGUYEN, V. P., RABCZUK, T., BORDAS, S. & DUFLOT, M. 2008. Meshless methods: a review and computer implementation aspects. *Mathematics and Computers in Simulation,* 79**,** 763-813.

NIE, W., ZHAO, Z. Y., NING, Y. J. & GUO, W. 2014. Numerical studies on rockbolts mechanism using 2D discontinuous deformation analysis. *Tunnelling and Underground Space Technology,* 41**,** 223-233.

NING, Y., YANG, J., AN, X. & MA, G. 2011a. Modelling rock fracturing and blast-induced rock mass failure via advanced discretisation within the discontinuous deformation analysis framework. *Computers and Geotechnics,* 38**,** 40-49.

NING, Y., YANG, J., MA, G. & CHEN, P. 2011b. Modelling rock blasting considering explosion gas penetration using discontinuous deformation analysis. *Rock Mechanics and Rock Engineering,* 44**,** 483-490.

NING, Y. & ZHAO, Z. 2013. A detailed investigation of block dynamic sliding by the discontinuous deformation analysis. *International Journal for Numerical and Analytical Methods in Geomechanics,* 37**,** 2373-2393.

NING, Y. J., AN, X. M. & MA, G. W. 2011c. Footwall slope stability analysis with the numerical manifold method. *International Journal of Rock Mechanics and Mining Sciences,* 48**,** 964-975.

ORTLEPP, W. D. 2001. The behaviour of tunnels at great depth under large static and dynamic pressures. *Tunnelling and Underground Space Technology,* 16**,** 41-48.

PAN, E., AMADEI, B. & KIM, Y. I. 1998. 2-D BEM analysis of anisotropic half-plane problems - application to rock mechanics. *International Journal of Rock Mechanics and Mining Sciences,* 35**,** 69-74.

PARK, B. & MIN, K.-B. 2015. Bonded-particle discrete element modeling of mechanical behavior of transversely isotropic rock. *International Journal of Rock Mechanics and Mining Sciences,* 76**,** 243-255.

PETERS, M. & HACKL, K. 2005. Numerical aspects of the extended finite element method. *Proceedings in Applied Mathematics and Mechanics,* 5**,** 355-356.

POTYONDY, D. O. & CUNDALL, P. A. 2004. A bonded-particle model for rock. *International Journal of Rock Mechanics and Mining Sciences,* 41**,** 1329-1364.

PRISCO, M. D. & MAZARS, J. 1996. 'Crush-crack': a non-local damage model for concrete. *Mechanics of Cohesive-frictional Materials,* 1**,** 321-347.

PSAKHIE, S. G., SHILKO, E. V., GRIGORIEV, A. S., ASTAFUROV, S. V., DIMAKI, A. V. & SMOLIN, A. Y. 2014. A mathematical model of particle-particle interaction for discrete element based modeling of deformation and fracture of heterogeneous elastic-plastic materials. *Engineering Fracture Mechanics,* 130**,** 96-115.

QU, X. L., FU, G. Y. & MA, G. W. 2014. An explicit time integration scheme of numerical manifold method. *Engineering Analysis with Boundary Elements,* 48**,** 53-62.

RESENDE, R., LAMAS, L., LEMOS, J. & CALÇADA, R. 2014. Stress wave propagation test and numerical modelling of an underground complex. *International Journal of Rock Mechanics and Mining Sciences,* 72**,** 26-36.

RFPA. 2017. *Computer Software* [Online]. Available: http://www.mechsoft.cn/cn/ [Accessed].

RICHARD, T. 1999. *Determination of rock strength from cutting tests.* M.S., University of Minnesota.

RICHARD, T., DAGRAIN, F., POYOL, E. & DETOURNAY, E. 2012. Rock strength determination from scratch tests. *Engineering Geology,* 147**,** 91-100.

RODRIGUEZ, J. M., CARBONELL, J. M., CANTE, J. C. & OLIVER, J. 2017. Continuous chip formation in metal cutting processes using the Particle Finite Element Method (PFEM). *International Journal of Solids and Structures,* 120**,** 81-102.

ROUGIER, E., KNIGHT, E. E., BROOME, S. T., SUSSMAN, A. J. & MUNJIZA, A. 2014. Validation of a three-dimensional Finite-Discrete Element Method using experimental results of the Split Hopkinson Pressure Bar test. *International Journal of Rock Mechanics and Mining Sciences,* 70**,** 101-108.

SARFARAZI, V., GHAZVINIAN, A., SCHUBERT, W., BLUMEL, M. & NEJATI, H. R. 2014. Numerical simulation of the process of fracture of echelon rock joints. *Rock Mechanics and Rock Engineering,* 47**,** 1355-1371.

SASAKI, T., HAGIWARA, I., SASAKI, K., YOSHINAKA, R., OHNISHI, Y. & NISHIYAMA, S. 2004. Earthquake response analysis of rock-fall models by discontinuous deformation analysis. *Proceedings of third Asian rock mechanics symposium, Kyoto***,** 1267-1272.

SCHEI, G., FJÆR, E., DETOURNAY, E., KENTER, C. J., FUH, G. F. & ZAUSA, F. 2000. The scratch test: An attractive technique for determining strength and elastic properties of sedimentary rocks. *SPE Annual Technical Conference and Exhibition.* Texas: Society of Petroleum Engineers.

SCHULER, H., MAYRHOFER, C. & THOMA, K. 2006. Spall experiments for the measurement of the tensile strength and fracture energy of concrete at high strain rates. *International Journal of Impact Engineering,* 32**,** 1635-1650.

SELMIN, V. 1993. The node-centred finite volume approach: bridge between finite differences and finite elements. *Computer Methods in Applied Mechanics and Engineering,* 102**,** 107-138.

SHABANIMASHCOOL, M. & LI, C. C. 2012. Numerical modelling of longwall mining and stability analysis of the gates in a coal mine. *International Journal of Rock Mechanics and Mining Sciences,* 51**,** 24-34.

SHABANIMASHCOOL, M. & LI, C. C. 2013. A numerical study of stress changes in barrier pillars and a border area in a longwall coal mine. *International Journal of Coal Geology,* 106**,** 39-47.

SHI, G.-H. Manifold method of material analysis. Transactions of the Ninth Army Conference on Applied Mathematics and Computing, 1991 Minnesota. University of Minnesota, 51-76.

SHI, G.-H. Modeling rock joints and blocks by manifold method. Rock Mechanics: Proceedings of the 33th US Symposium, 1992 New Mexico. American Rock Mechanics Association, 639-648.

SHI, G.-H. Numerical Manifold Method. *In:* LI, J. C., WANG, C.-Y. & SHENG, J., eds. Preceedings of the First International Conference on Analysis of Discontinuous Deformation (ICADD-1), December 1995 Chungli, Taiwan. 187-222.

SHI, G.-H. Simplex integration for manifold method, FEM, DDA and analytical analysis. Discontinuous deformation analysis (DDA) and simulations of discontinuous media : proceedings of the first International Forum on Discontinuous Deformation Analysis (DDA) and Simulations of Discontinuous Media, , June 12-14, 1996, 1996 Albuquerque, New Mexico, USA. TSI Press, 205-262.

SHI, G.-H. Numerical Manifold Method. *In:* OHNISHI, Y., ed. Preceedings of the Second International Conference on Analysis of Discontinuous Deformation (ICADD-2), July 1997 Kyoto, Japan. 1-35.

SHI, G.-H. & GOODMAN, R. E. 1985. Two dimensional discontinuous deformation analysis. *International Journal for Numerical and Analytical Methods in Geomechanics,* 9**,** 541-556.

SHI, G.-H. & GOODMAN, R. E. 1989. Generalization of two-dimensional discontinuous deformation analysis for forward modelling. *International Journal for Numerical and Analytical Methods in Geomechanics,* 13**,** 359-380.

SHOU, K. J. 2000. A three-dimensional hybrid boundary element method for non-linear analysis of a weak plane near an underground excavation. *Tunnelling and Underground Space Technology,* 15**,** 215-226.

SHYU, K. & SALAMI, M. R. Manifold with four-node isoparametric finite element method. First Working Forum on the Manifold Method of Material Analysis, California, 1995. US Army Corps of Engineers, 165-182.

SIMA, J., JIANG, M. & ZHOU, C. 2014. Numerical simulation of desiccation cracking in a thin clay layer using 3D discrete element modeling. *Computers and Geotechnics,* 56**,** 168-180.

SMEETS, B., ODENTHAL, T., VANMAERCKE, S. & RAMON, H. 2015. Polygon-based contact description for modeling arbitrary polyhedra in the Discrete Element Method. *Computer Methods in Applied Mechanics and Engineering,* 290**,** 277-289.

SMILAUER, V. 2010. *Cohesive Particle Model using the Discrete Element Method on the Yade Platform.* Czech Technical University in Prague.

SONG, G., WAISMAN, H., LAN, M. & HARARI, I. 2015. Extraction of stress intensity factors from Irwin's integral using high-order XFEM on triangular meshes. *International Journal for Numerical Methods in Engineering,* 102**,** 528-550.

STAZI, F. L., BUDYN, E., CHESSA, J. & BELYTSCHKO, T. 2003. An extended finite element method with higher-order elements for curved cracks. *Computational Mechanics,* 31**,** 38-48.

STROUBOULIS, T., ZHANG, L. & BABUSKA, I. 2003. Generalized finite element method using mesh-based handbooks: application to problems in domains with many voids. *Computer Methods in Applied Mechanics and Engineering,* 192**,** 3109-3161.

STROUBOULIS, T., ZHANG, L. & BABUSKA, I. 2007. Assessment of the cost and accuracy of the generalized FEM. *International journal for numerical methods in engineering,* 69**,** 250-283.

SU, H. & XIE, X. Preliminary research on solving large displacement problems by numerical manifold method with fixed mathematical meshes. *In:* MACLAUGHLIN, M. M. & SITAR, N., eds. Preceedings of ICADD-7 Seventh International Conference on the Analysis of Discontinuous Deformation, December 2005. 175-182.

SU, H., XIE, X. & LIANG, Q. Automatic programming for high-order numerical manifold method. *In:* LU, M., ed. Development and Application of Discontinuous Modelling for Rock Engineering, Preceedings of the 6th International Conference on Analysis of Discontinuous Deformation (ICADD-6), October 2003 Trondheim, Norway. 153-157.

SUN, L. 2012. *Particle Manifold Method (PMM) for Multiscale Continuous-Discontinuous Analysis.* Ecole Polytechnique Federale de Lausanne.

SUN, L., ZHAO, G. F. & ZHAO, J. 2013. Particle manifold method (PMM): A new continuum-discontinuum numerical model for geomechanics. *International Journal for Numerical and Analytical Methods in Geomechanics,* 37**,** 1711-1736.

TANG, C. 1997. Numerical simulation of progressive rock failure and associated seismicity. *International Journal of Rock Mechanics and Mining Sciences,* 34**,** 249-261.

TANG, C. A. & KAISER, P. K. 1998. Numerical simulation of cumulative damage and seismic energy release during brittle rock failure-Part I: Fundamentals. *International Journal of Rock Mechanics and Mining Sciences,* 35**,** 113 - 121.

TANG, C. A., THAM, L. G., WANG, S. H., LIU, H. & LI, W. H. 2007. A numerical study of the influence of heterogeneity on the strength characterization of rock under uniaxial tension. *Mechanics of materials,* 39**,** 326-339.

TANG, S. B., HUANG, R. Q., WANG, S. Y., BAO, C. Y. & TANG, C. A. 2017a. Study of the fracture process in heterogeneous materials around boreholes filled with expansion cement. *International Journal of Solids and Structures,* 112**,** 1-15.

TANG, S. B. & TANG, C. A. 2015. Crack propagation and coalescence in quasi-brittle materials at high temperatures. *Engineering Fracture Mechanics,* 134**,** 404-432.

TANG, S. B., TANG, C. A., LIANG, Z. Z., LUO, J. & WANG, Q. 2017b. The development of polygonal fractures due to contraction: A disorder to order transition. *Engineering Fracture Mechanics,* 178**,** 93-108.

TANG, X. H. 2013. *Impulse-based discrete element modelling of rock impact and fragmentation, with applications to block cave mining.* Imperial College London.

TAROKH, A. & FAKHIMI, A. 2014. Discrete element simulation of the effect of particle size on the size of fracture process zone in quasi-brittle materials. *Computers and Geotechnics,* 62**,** 51-60.

TATONE, B. S. A. & GRASSELLI, G. 2015. A calibration procedure for two-dimensional laboratory-scale hybrid finite–discrete element simulations. *International Journal of Rock Mechanics and Mining Sciences,* 75**,** 56-72.

TEDESCO, J. W. & ROSS, C. A. 1998. Strain-rate-dependent constitutive equations for concrete. *Journal of Pressure Vessel Technology,* 120**,** 398-405.

TERADA, K., ASAI, M. & YAMAGISHI, M. 2003. Finite cover method for linear and non-linear analyses of heterogeneous solids. *International Journal for Numerical Methods in Engineering,* 58**,** 1321-1346.

THOENI, K., GIACOMINI, A., LAMBERT, C., SLOAN, S. W. & CARTER, J. P. 2014. A 3D discrete element modelling approach for rockfall analysis with drapery systems. *International Journal of Rock Mechanics and Mining Sciences,* 68**,** 107-119.

TIAN, Q., ZHAO, Z. & BAO, H. 2014. Block fracturing analysis using nodal-based discontinuous deformation analysis with the double minimization procedure. *International Journal for Numerical and Analytical Methods in Geomechanics,* 38**,** 881-902.

TKALICH, D., FOURMEAU, M., KANE, A., LI, C. C. & CAILLETAUD, G. 2016. Experimental and numerical study of Kuru granite under confined compression and indentation. *International Journal of Rock Mechanics and Mining Sciences,* 87**,** 55-68.

TSESARSKY, M. & TALESNICK, M. L. 2007. Mechanical response of a jointed rock beam - numerical study of centrifuge models. *International Journal for Numerical and Analytical Methods in Geomechanics,* 31**,** 977-1006.

VOCIALTA, M., RICHART, N. & MOLINARI, J. F. 2017. 3D dynamic fragmentation with parallel dynamic insertion of cohesive elements. *International Journal for Numerical Methods in Engineering,* 109**,** 1655–1678.

VU-QUOC, L., ZHANG, X. & WALTON, O. R. 2000. A 3-D discrete-element method for dry granular flows of ellipsoidal particles. *Computer Methods in Applied Mechanics and Engineering,* 187**,** 483-528.

VYAZMENSKY, A., STEAD, D., ELMO, D. & MOSS, A. 2010. Numerical analysis of block caving-induced instability in large open pit slopes: a finite element/discrete element approach. *Rock mechanics and rock engineering,* 43**,** 21-39.

WANG, C., TANNANT, D. D. & LILLY, P. A. 2003. Numerical analysis of the stability of heavily jointed rock slopes using PFC2D. *International Journal of Rock Mechanics and Mining Sciences,* 40**,** 415-424.

WANG, G., AL-OSTAZ, A., CHENG, A. H. D. & MANTENA, P. R. 2009. Hybrid lattice particle modeling: Theoretical considerations for a 2D elastic spring network for dynamic fracture simulations. *Computational Materials Science,* 44**,** 1126-1134.

WANG, H., JIANG, Y., ZHAO, Y., ZHU, J. & LIU, S. 2013. Numerical investigation of the dynamic mechanical state of a coal pillar during longwall mining panel extraction. *Rock Mechanics and Rock Engineering,* 46**,** 1211-1221.

WANG, J. & CHAN, D. 2014. Frictional contact algorithms in SPH for the simulation of soil-structure interaction. *International Journal for Numerical and Analytical Methods in Geomechanics,* 38**,** 747-770.

WANG, L. L., YANG, L. M. & ZHOU, F. H. 2007. *Foundations of Stress Waves*, Elsevier.

WANG, S. Y., SLOAN, S. W., HUANG, M. L. & TANG, C. A. 2011a. Numerical study of failure mechanism of serial and parallel rock pillars. *Rock mechanics and rock engineering,* 44**,** 179-198.

WANG, S. Y., SLOAN, S. W., LIU, H. Y. & TANG, C. A. 2011b. Numerical simulation of the rock fragmentation process induced by two drill bits subjected to static and dynamic (impact) loading. *Rock Mechanics and Rock Engineering,* 44**,** 317-332.

WANG, S. Y., SLOAN, S. W., SHENG, D. C. & TANG, C. A. 2012. Numerical analysis of the failure process around a circular opening in rock. *Computers and Geotechnics,* 39**,** 8-16.

WANG, S. Y., SLOAN, S. W., SHENG, D. C., YANG, S. Q. & TANG, C. A. 2014a. Numerical study of failure behaviour of pre-cracked rock specimens under conventional triaxial compression. *International Journal of Solids and Structures,* 51**,** 1132-1148.

WANG, S. Y., SLOAN, S. W. & TANG, C. A. 2014b. Three-dimensional numerical investigations of the failure mechanism of a rock disc with a central or eccentric hole. *Rock Mechanics and Rock Engineering,* 47**,** 2117–2137.

WANG, Y. & TONON, F. 2011. Discrete element modeling of rock fragmentation upon impact in rock fall analysis. *Rock Mechanics and Rock Engineering,* 44**,** 23-35.

WANG, Y. N. 2009. *Three-dimensional rock-fall analysis with impact fragmentation and fly-rock modeling.* The University of Texas at Austin.

WEERHEIJM, J. & VAN DOORMAAL, J. C. A. M. 2007. Tensile failure of concrete at high loading rates: New test data on strength and fracture energy from instrumented spalling tests. *International Journal of Impact Engineering,* 34**,** 609-626.

WELLMANN, C. & WRIGGERS, P. 2012. A two-scale model of granular materials. *Computer Methods in Applied Mechanics and Engineering,* 205–208**,** 46-58.

WENG, L., HUANG, L., TAHERI, A. & LI, X. 2017. Rockburst characteristics and numerical simulation based on a strain energy density index: A case study of a roadway in Linglong gold mine, China. *Tunnelling and Underground Space Technology,* 69**,** 223-232.

WHITTLES, D. N., KINGMAN, S., LOWNDES, I. & JACKSON, K. 2006. Laboratory and numerical investigation into the characteristics of rock fragmentation. *Minerals Engineering,* 19**,** 1418-1429.

WIĄCEK, J. & MOLENDA, M. 2014. Effect of particle size distribution on micro- and macromechanical response of granular packings under compression. *International Journal of Solids and Structures,* 51**,** 4189-4195.

WONG, L. N. Y. & WU, Z. 2014. Application of the numerical manifold method to model progressive failure in rock slopes. *Engineering Fracture Mechanics,* 119**,** 1-20.

WU, J. H. 2010. Seismic landslide simulations in discontinuous deformation analysis. *Computers and Geotechnics,* 37**,** 594-601.

WU, J. H., LIN, J. S. & CHEN, C. S. 2009. Dynamic discrete analysis of an earthquake-induced large-scale landslide. *International Journal of Rock Mechanics and Mining Sciences,* 46**,** 397-407.

WU, J. H., OHNISHI, Y. & NISHIYAMA, S. 2005. A development of the discontinuous deformation analysis for rock fall analysis. *International journal for numerical and analytical methods in geomechanics,* 29**,** 971-988.

WU, R., XU, J. H., LI, C., WANG, Z. L. & QIN, S. 2015. Stress distribution of mine roof with the boundary element method. *Engineering Analysis with Boundary Elements,* 50**,** 39-46.

WU, Z. & FAN, L. 2014. The numerical manifold method for elastic wave propagation in rock with time-dependent absorbing boundary conditions. *Engineering Analysis with Boundary Elements,* 46**,** 41-50.

WU, Z. & WONG, L. N. Y. 2013a. Elastic-plastic cracking analysis for brittle-ductile rocks using manifold method. *International Journal of Fracture,* 180**,** 71-91.

WU, Z. & WONG, L. N. Y. 2013b. Modeling cracking behavior of rock mass containing inclusions using the enriched numerical manifold method. *Engineering Geology,* 162**,** 1-13.

WU, Z. & WONG, L. N. Y. 2014. Extension of numerical manifold method for coupled fluid flow and fracturing problems. *International Journal for Numerical and Analytical Methods in Geomechanics,* 38**,** 1990-2008.

WU, Z., WONG, L. N. Y. & FAN, L. 2013. Dynamic Study on Fracture Problems in Viscoelastic Sedimentary Rocks Using the Numerical Manifold Method. *Rock Mechanics and Rock Engineering,* 46**,** 1415-1427.

WYK, G. V., ELS, D. N. J., AKDOGAN, G., BRADSHAW, S. M. & SACKS, N. 2014. Discrete element simulation of tribological interactions in rock cutting. *International Journal of Rock Mechanics and Mining Sciences,* 65**,** 8-19.

XIAO, N., ZHOU, X. P. & GONG, Q. M. 2017. The modelling of rock breakage process by TBM rolling cutters using 3D FEM-SPH coupled method. *Tunnelling and Underground Space Technology,* 61**,** 90-103.

XU, T., ZHAO, G., ZHU, W., CHEN, C. & YUAN, L. 2016. Mesoscale modeling of spallation failure in fiber-reinforced concrete slab due to impact loading. *International Journal of Geomechanics,* 16**,** B4015001.

YAN, B., REGUEIRO, R. A. & STURE, S. 2010. Three-dimensional ellipsoidal discrete element modeling of granular materials and its coupling with finite element facets. *Engineering Computations,* 27**,** 519-550.

YANG, Q., CAI, F., SU, Z., UGAI, K., XU, L., HUANG, R. & XU, Q. 2014a. Numerical simulation of granular flows in a large flume using Discontinuous Deformation Analysis. *Rock Mechanics and Rock Engineering,* 47**,** 2299-2306.

YANG, S., MA, G., REN, X. & REN, F. 2014b. Cover refinement of numerical manifold method for crack propagation simulation. *Engineering Analysis with Boundary Elements,* 43**,** 37-49.

YANG, S. Q., HUANG, Y. H., JING, H. W. & LIU, X. R. 2014c. Discrete element modelling on fracture coalescence behavior of red sandstone containing two unparallel fissures under uniaxial compression. *Engineering Geology,* 178**,** 28-48.

YANG, Z. J. & CHEN, J. 2005. Finite element modelling of multiple cohesive discrete crack propagation in reinforced concrete beams. *Engineering fracture mechanics,* 72**,** 2280-2297.

YAO, Y., LIU, L. & KEER, L. M. 2015. Pore pressure cohesive zone modeling of hydraulic fracture in quasi-brittle rocks. *Mechanics of Materials,* 83**,** 17-29.

YU, Q. L., RANJITH, P. G., LIU, H. Y., YANG, T. H., TANG, S. B., TANG, C. A. & YANG, S. Q. 2015. A mesostructure-based damage model for thermal cracking analysis and application in granite at elevated temperatures. *Rock Mechanics and Rock Engineering,* 48**,** 2263-2282.

YUAN, F. & PRAKASH, V. 2013. Plate impact experiments to investigate shock-induced inelasticity in Westerly granite. *International Journal of Rock Mechanics and Mining Sciences,* 60**,** 277-287.

ZHANG, H. H., CHEN, Y. L., LI, L. X., AN, X. M. & MA, G. W. 2009. Accuracy comparison of rectangular and triangular mathematical elements in the numerical manifold method. *In:* MA, G. W. & ZHOU, Y. X. (eds.) *9th International Conference On Analysis of Discontinues Deformation: New Developments and Applications.* Singapore.

ZHANG, H. H., LI, L. X., AN, X. M. & MA, G. W. 2010. Numerical analysis of 2-D crack propagation problems using the numerical manifold method. *Engineering Analysis with Boundary Elements,* 34**,** 41-50.

ZHANG, H. H., MA, G. W. & REN, F. 2014a. Implementation of the numerical manifold method for thermo-mechanical fracture of planar solids. *Engineering Analysis with Boundary Elements,* 44**,** 45-54.

ZHANG, K., CAO, P., MENG, J., LI, K. & FAN, W. 2015a. Modeling the progressive failure of jointed rock slope using fracture mechanics and the strength reduction method. *Rock Mechanics and Rock Engineering,* 48**,** 771-785.

ZHANG, Q. 2014. *Mechanical Behaviour of Rock Materials under Dynamic Loading.* Ecole Polytechnique Federale de Lausanne.

ZHANG, Q. B., BRAITHWAITE, C. H. & ZHAO, J. 2017. Hugoniot equation of state of rock materials under shock compression. *Philosophical Transactions of the Royal Society A: Mathematical, Physical and Engineering Sciences,* 375**,** 0169.

ZHANG, Q. B. & ZHAO, J. 2014. A review of dynamic experimental techniques and mechanical behaviour of rock materials. *Rock Mechanics and Rock Engineering,* 47**,** 1411-1478.

ZHANG, W. & GOH, A. T. C. 2015. Numerical study of pillar stresses and interaction effects for twin rock caverns. *International Journal for Numerical and Analytical Methods in Geomechanics,* 39**,** 193-206.

ZHANG, X. P. & WONG, L. N. Y. 2014. Choosing a proper loading rate for bonded-particle model of intact rock. *International Journal of Fracture,* 189**,** 163-179.

ZHANG, Y., WANG, J., XU, Q., CHEN, G., X ZHAO, J., ZHENG, L., HAN, Z. & YU, P. 2015b. DDA validation of the mobility of earthquake-induced landslides. *Engineering Geology,* 194**,** 38-51.

ZHANG, Y., XU, Q., CHEN, G., ZHAO, J. X. & ZHENG, L. 2014b. Extension of discontinuous deformation analysis and application in cohesive-frictional slope analysis. *International Journal of Rock Mechanics and Mining Sciences,* 70**,** 533-545.

ZHANG, Z., YAO, Y. & MAO, X. 2015c. Modeling wave propagation induced fracture in rock with correlated lattice bond cell. *International Journal of Rock Mechanics and Mining Sciences,* 78**,** 262-270.

ZHAO, G. F. 2010. *Development of Micro-Macro Continuum-Discontinuum Coupled Numerical method.* Ecole Polytechnique Federale de Lausanne.

ZHAO, G. F. 2014a. Development of the distinct lattice spring model for large deformation analyses. *International Journal for Numerical and Analytical Methods in Geomechanics,* 38**,** 1078-1100.

ZHAO, G. F. 2014b. Modeling stress wave propagation in rocks by distinct lattice spring model. *Journal of Rock Mechanics and Geotechnical Engineering,* 6**,** 348-355.

ZHAO, G. F. 2015. Modelling 3D jointed rock masses using a lattice spring model. *International Journal of Rock Mechanics and Mining Sciences,* 78**,** 79-90.

ZHAO, G. F. 2017. Developing a four-dimensional lattice spring model for mechanical responses of solids. *Computer Methods in Applied Mechanics and Engineering,* 315**,** 881-895.

ZHAO, G. F., FANG, J. N., SUN, L. & ZHAO, J. 2013a. Parallelization of the distinct lattice spring model. *International Journal for Numerical and Analytical Methods in Geomechanics,* 37**,** 51-74.

ZHAO, G. F. & KHALILI, N. 2012. Graphics processing unit based parallelization of the distinct lattice spring model. *Computers and Geotechnics,* 42**,** 109-117.

ZHAO, G. F., KHALILI, N., FANG, J. N. & ZHAO, J. 2012. A coupled distinct lattice spring model for rock failure under dynamic loads. *Computers and Geotechnics,* 42**,** 1-20.

ZHAO, G. F., RUSSELL, A. R., ZHAO, X. B. & KHALILI, N. 2014a. Strain rate dependency of uniaxial tensile strength in Gosford sandstone by the Distinct Lattice Spring Model with X-ray micro CT. *International Journal of Solids and Structures,* 51**,** 1587-1600.

ZHAO, G. F., ZHAO, X. B. & ZHU, J. B. 2014b. Application of the numerical manifold method for stress wave propagation across rock masses. *International Journal for Numerical and Analytical Methods in Geomechanics,* 38**,** 92-110.

ZHAO, J. & CAI, J. G. 2001. Transmission of elastic P-waves across single fractures with a nonlinear normal deformational behavior. *Rock Mechanics and Rock Engineering,* 34**,** 3-22.

ZHAO, J., CAI, J. G., ZHAO, X. B. & LI, H. B. 2008a. Dynamic model of fracture normal behaviour and application to prediction of stress wave attenuation across fractures. *Rock Mechanics and Rock Engineering,* 41**,** 671-693.

ZHAO, J., ZHAO, X. B. & CAI, J. G. 2006. A further study of P-wave attenuation across parallel fractures with linear deformational behaviour. *International Journal of Rock Mechanics and Mining Sciences,* 43**,** 776-788.

ZHAO, K., BONINI, M., DEBERNARDI, D., JANUTOLO, M., BARLA, G. & CHEN, G. 2015. Computational modelling of the mechanised excavation of deep tunnels in weak rock. *Computers and Geotechnics,* 66**,** 158-171.

ZHAO, S. F. & ZHAO, G. F. 2012. Implementation of a high order lattice spring model for elasticity. *International Journal of Solids and Structures,* 49**,** 2568-2581.

ZHAO, X. B., ZHAO, J., CAI, J. G. & HEFNY, A. M. 2008b. UDEC modelling on wave propagation across fractured rock masses. *Computers and Geotechnics,* 35**,** 97-104.

ZHAO, Y. X., ZHAO, G. F. & JIANG, Y. D. 2013b. Experimental and numerical modelling investigation on fracturing in coal under impact loads. *International Journal of Fracture,* 183**,** 63-80.

ZHENG, H. & LI, X. 2015. Mixed linear complementarity formulation of discontinuous deformation analysis. *International Journal of Rock Mechanics and Mining Sciences,* 75**,** 23-32.

ZHENG, H. & XU, D. D. 2014. New strategies for some issues of numerical manifold method in simulation of crack propagation. *International Journal for Numerical Methods in Engineering,* 97**,** 986-1010.

ZHENG, Q. J., ZHOU, Z. Y. & YU, A. B. 2013. Contact forces between viscoelastic ellipsoidal particles. *Powder Technology,* 248**,** 25-33.

ZHENG, W., ZHUANG, X., TANNANT, D. D., CAI, Y. & NUNOO, S. 2014. Unified continuum/discontinuum modelling framework for slope stability assessment. *Engineering Geology,* 179**,** 90-101.

ZHOU, F. & MOLINARI, J.-F. 2004. Dynamic crack propagation with cohesive elements: a methodology to address mesh dependency. *International Journal for Numerical Methods in Engineering,* 59**,** 1-24.

ZHOU, F., MOLINARI, J.-F. & RAMESH, K. T. 2005. A cohesive model based fragmentation analysis: effects of strain rate and initial defects distribution. *International journal of solids and structures,* 42**,** 5181-5207.

ZHOU, X. P., ZHAO, Y. & QIAN, Q. H. 2015. A novel meshless numerical method for modeling progressive failure processes of slopes. *Engineering Geology,* 192**,** 139-153.

ZHOU, Y. & LIN, J. S. 2013. On the critical failure mode transition depth for rock cutting. *International Journal of Rock Mechanics and Mining Sciences,* 62**,** 131-137.

ZHOU, Y. & LIN, J. S. 2014. Modeling the ductile–brittle failure mode transition in rock cutting. *Engineering Fracture Mechanics,* 127**,** 135-147.

ZHU, J. B., DENG, X. F., ZHAO, X. B. & ZHAO, J. 2013. A numerical study on wave transmission across multiple intersecting joint sets in rock masses with UDEC. *Rock Mechanics and Rock Engineering,* 46**,** 1429-1442.

ZHU, J. B., ZHAO, G. F., ZHAO, X. B. & ZHAO, J. 2011. Validation study of the distinct lattice spring model (DLSM) on P-wave propagation across multiple parallel joints. *Computers and Geotechnics,* 38**,** 298-304.

ZHU, W. C. 2008. Numerical modelling of the effect of rock heterogeneity on dynamic tensile strength. *Rock Mechanics and Rock Engineering,* 41**,** 771-779.

ZHU, W. C., LI, Z. H., ZHU, L. & TANG, C. A. 2010. Numerical simulation on rockburst of underground opening triggered by dynamic disturbance. *Tunnelling and Underground Space Technology,* 25**,** 587-599.

ZHU, W. C., LIU, J., YANG, T. H., SHENG, J. C. & ELSWORTH, D. 2006. Effects of local rock heterogeneities on the hydromechanics of fractured rocks using a digital-image-based technique. *International Journal of Rock Mechanics and Mining Sciences,* 43**,** 1182-1199.

ZHU, W. C., NIU, L. L., LI, S. H. & XU, Z. H. 2015. Dynamic Brazilian test of rock under intermediate strain rate: Pendulum hammer-driven SHPB test and numerical simulation. *Rock Mechanics and Rock Engineering,* 48**,** 1867-1881.

ZHU, W. C. & TANG, C. A. 2006. Numerical simulation of Brazilian disk rock failure under static and dynamic loading. *International Journal of Rock Mechanics and Mining Sciences,* 43**,** 236-252.

ZHU, W. S., CHEN, Y. J., LI, S. C., YIN, F. Q., YU, S. & LI, Y. 2014a. Rock failure and its jointed surrounding rocks: A multi-scale grid meshing method for DDARF. *Tunnelling and Underground Space Technology,* 43**,** 370-376.

ZHU, Z., WANG, C., KANG, J., LI, Y. & WANG, M. 2014b. Study on the mechanism of zonal disintegration around an excavation. *International Journal of Rock Mechanics and Mining Sciences,* 67**,** 88-95.

ZOU, Y. 2016. *Seismic response of rock joints under obliquely incident wave.* Ecole Polytechnique Federale de Lausanne.

Appendix A Algorithm for the Generation of Links

The algorithm for the generation of links in PNMM is given in this appendix. This algorithm is implemented in C++ as a subroutine of PNMM. This algorithm is based on the Munjiza-NBS contact detection algorithm (Munjiza and Andrews, 1998).

```
Loop over all particles
{
    find the maximum radius rmax;
    find the minimum value of the x-coordinate of the centroid xmin;
    find the minimum value of the y-coordinate of the centroid ymin;
    find the maximum value of the x-coordinate of the centroid xmax;
    find the maximum value of the y-coordinate of the centroid ymax;
}

The number of rows nrow = (ymax - ymin) / (2 * rmax);
The number of columns n_col = (xmax - xmin) / (2 * rmax);

Loop over all particles
{
    Locate the particle in the cell (ix, iy);
    place the particle onto the Yiy list;
    mark the list Yiy “new”;
}

Loop over all particles
{
    if the particle belongs to a “new” list Yiy
    {
        mark the list Yiy “old”;
        Loop over all particles in list Yiy
        {
```

```
            place the particle onto the corresponding list XixYiy;
            mark the list XixYiy “new”;
        }
        Loop over all particles in list Yiy-1
        {
            place the particle onto the corresponding list XixYiy-1;
            mark the list XixYiy-1 “new”;
        }
        Loop over all particles in list Yiy
        {
            if the particle i belongs to a “new” list XixYiy
            {
                mark the list XixYiy “old”;
                place particles in list XixYiy, Xix-1Yiy, Xix-1Yiy-1,
                    XixYiy-1, Xix+1Yiy-1 in list neighboring;
                Loop over all particles in list neighboring
                {
                    if the particle is close enough to particle i
                    {
                        generate a link between two particles;
                    }
                }
            }
        }
    }
}
```

References

MUNJIZA, A. & ANDREWS, K. R. F. 1998. NBS contact detection algorithm for bodies of similar size. International Journal for Numerical Methods in Engineering, 43, 131-149.

Appendix B Overview of PNMM Code

An overview of PNMM code is given in this appendix. The class diagram of the PNMM code is illustrated in Figure Appendix B.1a. Particles as the most important component in PNMM is implemented as a class named `Particle_Disk`. A snapshot of the variables and methods in this class is given in Figure Appendix B.1b. Links as another component of PNMM is implemented as the class `Link_DiskToDisk`, whose variables and methods are outlined in Figure Appendix B.1c.

The flowchart and detailed calculation process of PNMM have been given in Section 3.9. Accordingly, the source code of a complete calculation process is presented below. The presented process is for a dynamic case and considers the failure of links. Each task in the calculation procedure is programmed as a method/function with a self-explanatory function name.

```
void ParticleModel::ProcessDynamicFailure(void) {
    //pre-process
    Mesh g_backgroundMesh, g_Model;
    ParticleModel g_ParticleModel;

    g_Model.ReadModelMesh();
    g_backgroundMesh.GenerateBackgroundMesh();
    g_ParticleModel.SetBackground(g_backgroundMesh);
    g_ParticleModel.ManifoldElementsGenerator(g_Model);
    ParticlesGenerator();
    LinksGenerator();
    SeedFilling();
    ManifoldNodesGenerator();
    ManifoldElementsGenerator();
    BlocksGenerator();

    ApplySettings();//apply some constants used in computation
    DefineKinematicBoundary();
    DefineLoadingConditions();
```

```
    //calculation process
    CheckBrokenLinks();
    ApplyFailureParameters();
    GenerateElasticMatrix();
    for (unsigned int istep = 1; istep <= SETTINGS_H::stepNumber;
         ++istep) {
        GenerateElementMatrices();
        GenerateMassMatrices();
        ApplyKinematicBoundary(istep);
        ApplyLoading(istep);
        ApplyDynamicMatrices();
        AssembleStiffness();
        AssembleLoading();
        AssembleDegreeOfFreedom();

        LinearEquationsSolver();

        SetDOFResult();
        CalculateParticleDisplacementsAndUpdateCenters(istep);
        CalculateParticleStrainAndStress();
        CalculateParticlePrincipalStrainAndStress();
        CalculateLinkStrainAndStress();
        CalculateLinkPrincipalStrainAndStress();
        KinematicsIterator();//compute variables in newmark-beta dynamic
                             scheme
        FailureCheck();//apply the JHB criterion
        ParticleManifoldModelRegenerator();

        std::cout << "Time step " << istep << " finishes." << std::endl;
    }

    PostProcess_Print();
}
```

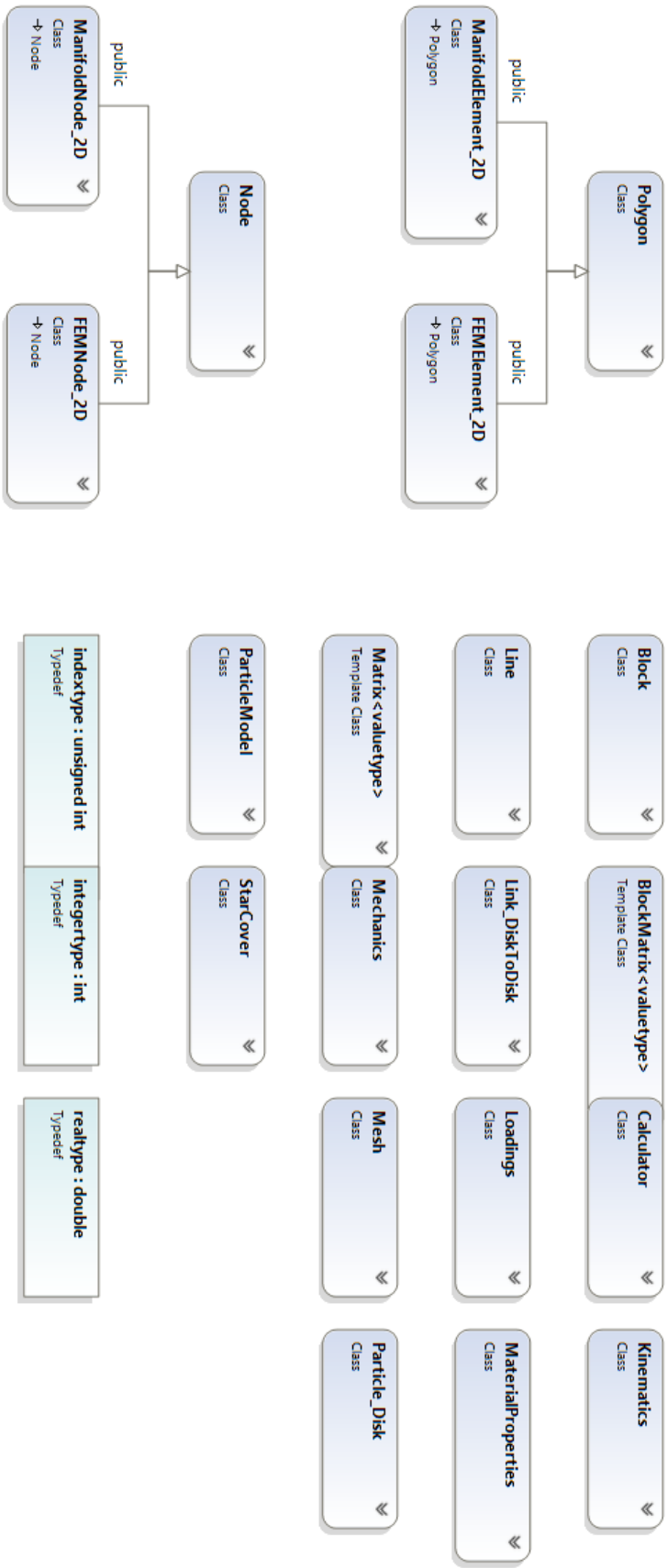
Polygon
Class
ManifoldElement_2D
Class
Polygon
FEMElement_2D
Class
Polygon
public
public
Node
Class
ManifoldNode_2D
Class
Node
FEMNode_2D
Class
Node
public
public
Block
Class
BlockMatrix<valuetype>
Template Class
Calculator
Class
Kinematics
Class
Line
Class
Link_DiskToDisk
Class
Loadings
Class
MaterialProperties
Class
Matrix<valuetype>
Template Class
Mechanics
Class
Mesh
Class
Particle_Disk
Class
ParticleModel
Class
StarCover
Class
indextype : unsigned int
Typedef
integertype : int
Typedef
realtype : double
Typedef

(a)

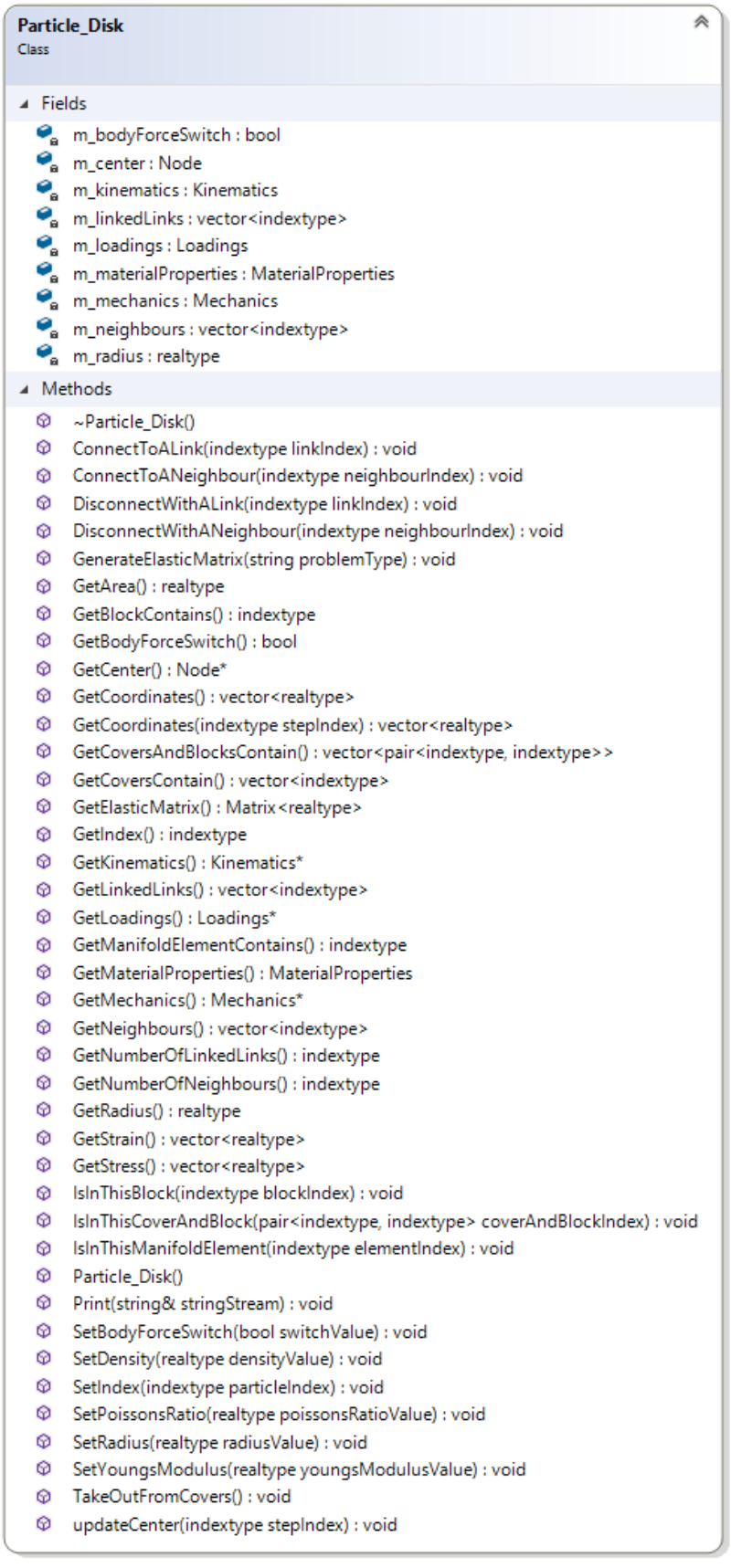
Particle_Disk
Class
Fields
m_bodyForceSwitch : bool
m_center : Node
m_kinematics : Kinematics
m_linkedLinks : vector<indextype>
m_loadings : Loadings
m_materialProperties : MaterialProperties
m_mechanics : Mechanics
m_neighbours : vector<indextype>
m_radius : realtype
Methods
~Particle_Disk()
ConnectToALink(indextype linkIndex) : void
ConnectToANeighbour(indextype neighbourIndex) : void
DisconnectWithALink(indextype linkIndex) : void
DisconnectWithANeighbour(indextype neighbourIndex) : void
GenerateElasticMatrix(string problemType) : void
GetArea() : realtype
GetBlockContains() : indextype
GetBodyForceSwitch() : bool
GetCenter() : Node*
GetCoordinates() : vector<realtype>
GetCoordinates(indextype stepIndex) : vector<realtype>
GetCoversAndBlocksContain() : vector<pair<indextype, indextype>>
GetCoversContain() : vector<indextype>
GetElasticMatrix() : Matrix<realtype>
GetIndex() : indextype
GetKinematics() : Kinematics*
GetLinkedLinks() : vector<indextype>
GetLoadings() : Loadings*
GetManifoldElementContains() : indextype
GetMaterialProperties() : MaterialProperties
GetMechanics() : Mechanics*
GetNeighbours() : vector<indextype>
GetNumberOfLinkedLinks() : indextype
GetNumberOfNeighbours() : indextype
GetRadius() : realtype
GetStrain() : vector<realtype>
GetStress() : vector<realtype>
IsInThisBlock(indextype blockIndex) : void
IsInThisCoverAndBlock(pair<indextype, indextype> coverAndBlockIndex) : void
IsInThisManifoldElement(indextype elementIndex) : void
Particle_Disk()
Print(string& stringStream) : void
SetBodyForceSwitch(bool switchValue) : void
SetDensity(realtype densityValue) : void
SetIndex(indextype particleIndex) : void
SetPoissonsRatio(realtype poissonsRatioValue) : void
SetRadius(realtype radiusValue) : void
SetYoungsModulus(realtype youngsModulusValue) : void
TakeOutFromCovers() : void
updateCenter(indextype stepIndex) : void

(b)

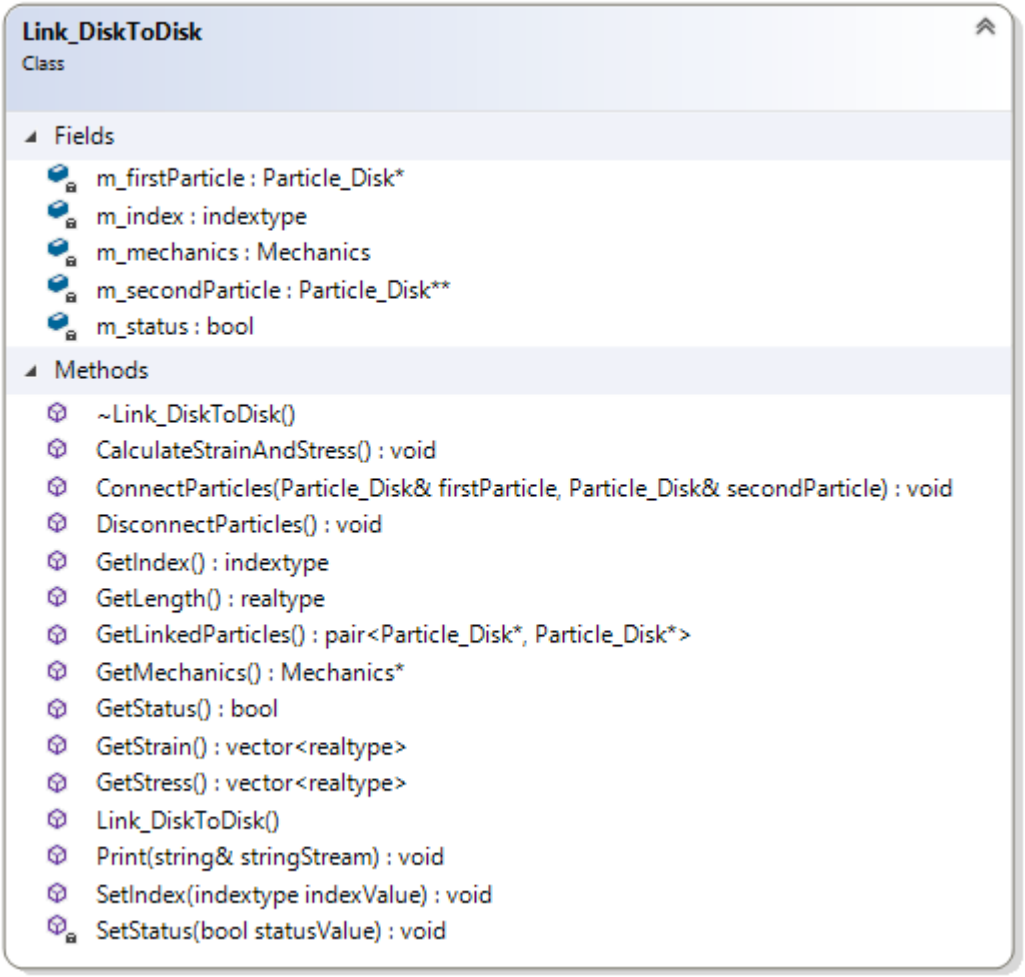

(c)

Figure Appendix B.1 Overview of the PNMM code: (a) the class diagram; (b) a snapshot of the particle class; (c) a snapshot of the link class

Appendix C Source Code of the Seed Filling Method in PNMM

The seed filling method is an image processing operation in computer graphics. It is used for assignment of a special label to the pixels in some region of an image, for example, changing the colour of selected domain. In PNMM, the seed filling method is adopted to generate blocks according to the connectivity between particles, as well as to detect if new manifold elements need to be generated due to the failure of links. The recursive seed filling algorithm is implemented through the `vector` in C++. The method begins with pushing an initial seed into an empty vector, and then repeats the procedure as below:

1) Pop the top element (e.g. a particle) out of the vector;
2) Mark the element which is just popped out;
3) Search for the neighbours of the marked element. If a neighbour has not been marked before, push it into the vector;
4) End if the vector is empty. Otherwise, go back to the first step.

More details of the seed filling method are available in (Sun, 2012). The source code of the seed filling method implemented in PNMM is given below.

```
//This function is to check how many blocks are formed by a group of particles.
  Links between particles have been generated prior to executing this function.
//Two particles sharing a link are a neighbour to each other.
//m_particle: all particles stored in a vector
//Particle_Disk: the class name of particles
//filledSignal: whether the particle has been marked

void StarCover::SeedFilling(void) {
    vector<int> particleIndices;
    for (auto iparticle : m_particles)
        particleIndices.push_back(iparticle->GetIndex());

    vector<bool> filledSignal(m_particles.size(), false);
    vector<Particle_Disk*> seedsQueue;
    auto particlesInBlock = new vector<Particle_Disk*>;
    int blockIndex = 1;
    seedsQueue.push_back(m_particles.front());
```

```
    particlesInBlock->push_back(m_particles.front());
    filledSignal.front() = true;
    m_particles.front()->IsInThisCoverAndBlock(make_pair(this->GetIndex(),
                                               blockIndex));

    while (find(filledSignal.begin(), filledSignal.end(), false) !=
           filledSignal.end()) {
        if (!seedsQueue.empty()) {
            auto currentParticle = seedsQueue.back();
            seedsQueue.pop_back();
            int numberOfNeighbours = currentParticle->GetNumberOfNeighbours();
            for (int ineighbour = 0; ineighbour < numberOfNeighbours;
                 ++ineighbour) {
                for (int iparticle = 0; iparticle < m_particles.size();
                     ++iparticle) {
                    if (m_particles[iparticle]->GetIndex() ==
                        currentParticle->GetNeighbours()[ineighbour] &&
                        filledSignal[iparticle] == false) {
                        seedsQueue.push_back(m_particles[iparticle]);
                        particlesInBlock->push_back(m_particles[iparticle]);
                        filledSignal[iparticle] = true;
                        m_particles[iparticle]->IsInThisCoverAndBlock(make_pair(
                            this->GetIndex(), blockIndex));
                        break;
                    }
                }
            }
        } else {
            m_particlesInBlocks.push_back(*particlesInBlock);
            particlesInBlock->clear();
            auto nextSeed = find(filledSignal.begin(), filledSignal.end(),
                                 false);
            seedsQueue.push_back(*(m_particles.begin() + (nextSeed -
                                 filledSignal.begin())));
            particlesInBlock->push_back(*(m_particles.begin() + (nextSeed -
                                          filledSignal.begin())));
            *nextSeed = true;
            (*(m_particles.begin() + (nextSeed - filledSignal.begin())))
             ->IsInThisCoverAndBlock(make_pair(this->GetIndex(), ++blockIndex));
        }
    }

    if (!particlesInBlock->empty())
        m_particlesInBlocks.push_back(*particlesInBlock);
    delete particlesInBlock;
}
```

Appendix D Matrix and Block Matrix in the Source Code of PNMM

Since the formulation of PNMM is derived in matrix form, as can be seen in Section 3.3.2, frequent operations to matrices in PNMM are conducted. Therefore, in order to abstract the programming flow of the PNMM code, two template classes `Matrix` and `BlockMatrix` are implemented for element matrices and global matrices respectively.

The source code of the template class `Matrix` is given below. Only functions concerning the linear algebra are given in detail.

```
template <typename valuetype>
class Matrix {
    /// \name Constructors and Destructor
public:
    Matrix(void) = default;
    ~Matrix(void) = default;

    /// \name Size Operations
public:
    /// \brief Get the size of the matrix.
    /// \return A pair of integers, the former is the row number while the
                latter is the column number.
    pair<unsigned int, unsigned int> GetSize(void) const;
    /// \brief Check if the matrix is empty.
    /// \return True for empty, and false for non-empty.
    inline bool IsEmpty(void) const;
    /// \brief Check if the matrix is square.
    /// \return True for square, and false for non-square.
    bool IsSquare(void) const;
    /// \brief Check if the matrix is symmetrical.
    /// \return True for empty, and false for non-symmetrical.
    bool IsSymmetrical(void) const;
    /// \brief Check if the matrix is a zero matrix.
    /// \return True for zero, false for non-zero.
    bool IsZero(void) const;

    /// \name Type Operations
```

```
public:
    /// \brief Convert a 1X1 matrix to a basic type.
    /// \return The only element in the matrix.
    inline valuetype ConvertToBasicType(void) const;
    /// \brief Convert a one-dimension matrix to a vector.
    /// \return The converted vector.
    vector<valuetype> ConvertToVector(void) const;

    /// \name Mathematics
public:
    Matrix<valuetype> operator=(const Matrix<valuetype> &anotherMatrix);
    Matrix<valuetype> operator+=(const Matrix<valuetype> &anotherMatrix);
    Matrix<valuetype> operator-=(const Matrix<valuetype> &anotherMatrix);
    Matrix<valuetype> operator*=(valuetype multiplier);
    Matrix<valuetype> operator/=(valuetype divisor);
    Matrix<valuetype> operator*=(const Matrix<valuetype> &anotherMatrix);
    Matrix<valuetype> operator+(const Matrix<valuetype> &anotherMatrix) const;
    Matrix<valuetype> operator-(const Matrix<valuetype> &anotherMatrix) const;
    Matrix<valuetype> operator*(valuetype multiplier) const;
    Matrix<valuetype> operator/(valuetype divisor) const;
    Matrix<valuetype> operator*(const Matrix<valuetype> &anotherMatrix) const;
    bool operator==(const Matrix<valuetype> &anotherMatrix) const;
    bool operator!=(const Matrix<valuetype> &anotherMatrix) const;

    /// \name Linear Algebra
public:
    Matrix<valuetype> Transposition(void) const;///< Get the transpose matrix.
    valuetype Cofactor(unsigned int rowIndex, unsigned int colIndex) const;///<
    Get the cofactor at any given position, mainly used to get the determinant.
    valuetype Determinant(void) const;///< Get the determinant.
    Matrix<valuetype> Adjugate(void) const;///< Get the adjugate matrix.
    Matrix<valuetype> Inverse(void) const;///< Get the inverse matrix.

    /// \name Add and Delete Elements
public:
    inline void PushBackRow(const vector<valuetype> &newRow);
    void PushBackRows(const Matrix<valuetype> &anotherMatrix);
    void PushBackCol(const vector<valuetype> &newCol);
    void PushBackCols(const Matrix<valuetype> &anotherMatrix);
    inline void PopBackRow(void);///< Delete the last row.
    void PopBackCol(void);///< Delete the last column.
    inline void InsertRow(unsigned int rowIndex, const vector<valuetype>
&newRow);
    void InsertCol(unsigned int colIndex, const vector<valuetype> &newCol);
    inline void EraseRow(unsigned int rowIndex);///< Erase the row.
    void EraseCol(unsigned int colIndex);///< Erase the column.
```

```
    /// \name Access Element(s)
public:
    inline vector<vector<valuetype>> GetValues(void) const;
    inline vector<valuetype> GetRow(unsigned int rowIndex) const;
    inline vector<valuetype> &operator()(unsigned int rowIndex);
    vector<valuetype> GetCol(unsigned int colIndex) const;
    vector<valuetype> &operator[](unsigned int colIndex);
    inline valuetype GetElement(unsigned int rowIndex, unsigned int colIndex)
           const;
    inline valuetype &operator()(unsigned int rowIndex, unsigned int colIndex);
    inline vector<valuetype> GetFrontRow(void) const;
    vector<valuetype> GetFrontCol(void) const;
    inline vector<valuetype> GetBackRow(void) const;
    vector<valuetype> GetBackCol(void) const;

    /// \name Memory Management
public:
    void Resize(unsigned int rowSize, unsigned int colSize);
    void Reserve(unsigned int rowSize, unsigned int colSize);
    void ShrinkToFit(void);///< Similar to vector's shrink_to_fit().
    void Clear(void);///< Similar to vector's clear().

    /// \name Printer
public:
    void Print(void) const;///< Print the matrix to screen.

    /// \name Private Members
protected:
    bool CheckSize(void) const;///< Check if the vectors have a same size.

protected:
    vector<vector<valuetype>> values;///< Store elements.
    vector<string> rowLabels;///< Store row labels.
    vector<string> colLabels;///< Store column labels.
};

// Linear Algebra
template<typename valuetype>
Matrix<valuetype> Matrix<valuetype>::Transposition(void) const {
    Matrix<valuetype> result;
    for (unsigned int colIndex = 0; colIndex < this->GetSize().second;
         ++colIndex) {
        vector<valuetype> tempRow;
        for (unsigned int rowIndex = 0; rowIndex < this->GetSize().first;
             ++rowIndex)
```

```
            tempRow.push_back(values[rowIndex][colIndex]);
        result.values.push_back(tempRow);
    }
    return result;
}

template<typename valuetype>
valuetype Matrix<valuetype>::Cofactor(unsigned int rowIndex, unsigned int
    colIndex) const { //the parameters rowIndex and colIndex start from 0
    Matrix<valuetype> tempMatrix(*this);
    auto deletedRow = tempMatrix.values.begin() + rowIndex;
    tempMatrix.values.erase(deletedRow);

    unsigned int rowSize = tempMatrix.GetSize().first;
    for (unsigned int irow = 0; irow < rowSize; ++irow) {
        auto deletedCol = tempMatrix.values[irow].begin() + colIndex;
        tempMatrix.values[irow].erase(deletedCol);
    }
    return tempMatrix.Determinant() * pow(-1, rowIndex + colIndex);
}

template<typename valuetype>
valuetype Matrix<valuetype>::Determinant(void) const {
    if (!this->IsSquare()) {
        cout << "This is not a square matrix." << endl;
        return -1;
    }
    const unsigned int rowIndex = 0;
    valuetype result = 0.;
    if (this->GetSize().first > 1) {
        for (unsigned int colIndex = 0; colIndex < this->GetSize().second;
             ++colIndex) {
            valuetype cofactorValue;
            cofactorValue = this->Cofactor(rowIndex, colIndex);
            result += values[rowIndex][colIndex] * cofactorValue;
        }
        return result;
    }
    return values[0][0];
}

template<typename valuetype>
Matrix<valuetype> Matrix<valuetype>::Adjugate(void) const {
    Matrix<valuetype> result;
    for (unsigned int rowIndex = 0; rowIndex < this->GetSize().first;
         ++rowIndex) {
```

```
        vector<valuetype> tempRow;
        for (unsigned int colIndex = 0; colIndex < this->GetSize().second;
             ++colIndex)
            tempRow.push_back(this->Cofactor(rowIndex, colIndex));
        result.values.push_back(tempRow);
    }
    return result.Transposition();
}

template<typename valuetype>
Matrix<valuetype> Matrix<valuetype>::Inverse(void) const {
    if (this->Determinant() == 0.) {
        cout << "This matrix is singular." << endl;
        return *this;
    }
    return this->Adjugate() / this->Determinant();
}
```

The source code of the template class `BlockMatrix` is given below. The implementation of functions is not presented in detail. But comments are given to explain all the functions.

```
template<typename valuetype>
class BlockMatrix {
public:
    BlockMatrix(void) = default;///< Default constructor.
    ~BlockMatrix(void) = default;///< Default destructor.

public:
    /// \brief Initialize the block matrix with zeros.
    /// \param There are four parameters:
    /// -# The number of blocks in row.
    /// -# The number of blocks in column.
    /// -# The row size of every block.
    /// -# The column size of every block.
    void Initialize(unsigned int rowSize, unsigned int colSize,
                    unsigned int blockRowSize, unsigned int blockColSize);
    /// \brief Similar to vector's clear().
    void Clear(void);
    /// \brief Equals the equivalent matrix to the block matrix.
    /// \warning After modifying the block matrix, this function must be called.
    void RefreshEquivalentMatrix(void);
    /// \brief Equals the block matrix to its equivalent matrix.
    /// \warning After modifying the equivalent matrix, this function must be
                 called.
    void Refresh(void);
```

```
public:
    /// \brief Check if the block matrix is empty.
    inline bool IsEmpty(void) const;
    /// \brief Check if the block matrix is square.
    bool IsSquare(void) const;
    /// \brief Get the size of the block matrix.
    /// \return A pair of integers, the former is the row number while the
                latter is the column number.
    /// \note The returned size indicates the amount of blocks.
    std::pair<unsigned int, unsigned int> GetSize(void) const;
    /// \brief Get the size of the blocks.
    /// \return A pair of integers, the former is the row number while the
                latter is the column number.
    /// \note The returned size indicates the size of every block.
    std::pair<unsigned int, unsigned int> GetBlockSize(void) const;
    /// \brief Get the block at the given position.
    inline Matrix<valuetype>& operator()(unsigned int rowIndex,
                                         unsigned int colIndex);
    /// \brief Get the corresponding normal matrix, elements are not changed.
    Matrix<valuetype>& GetEquivalentMatrix(void);

protected:
    bool CheckSize(void) const;///< Check if the block matrix has a right size.
    bool CheckBlockSize(void) const; ///< Check if every block has a same size.
    bool EquivalentMatrixUpToDate(void) const;///< Check if the equivalent
                            matrix is the same with the block size in value.

protected:
    std::vector<std::vector<Matrix<valuetype>>> matrices;
    Matrix<valuetype> equivalentMatrix;
};
```

Appendix E Solving the Global Equation

The global equation (Eq.15) in PNMM is a system of linear equations represented in the matrix form. It is solved by incorporating a third-party library Eigen (2017) into the source code of PNMM. As a C++ template library developed for linear algebra, Eigen provides a good support for sparse matrices in large size, which meets the demand of PNMM in most cases. Specifically, a conjugate gradient solver for sparse matrices in Eigen is adopted by PNMM. This solver is based on the indirect or iterative version of the conjugate gradient (CG) method (Saad, 2003), whose algorithm will be briefly introduced in this appendix.

Suppose the following system of linear equations is to be solved

$$\mathbf{A} \cdot \mathbf{x} = \mathbf{b} \tag{64}$$

where **A** is a known symmetric, positive definite, and real matrix, **b** is a known vector, and **x** is the vector to be solved.

Starting from an input vector $\mathbf{x}_0$, which can either be an initial solution with guess or simply taken as a vector of 0, we get

$$\begin{cases} \mathbf{r}_0 = \mathbf{b} - \mathbf{A}\mathbf{x}_0 \\ \mathbf{p}_0 = \mathbf{r}_0 \\ k = 0 \end{cases} \tag{65}$$

Then, the iteration starts by calculating following variables in sequence

$$\alpha_k = \frac{\mathbf{r}_k^T \mathbf{r}_k}{\mathbf{p}_k^T \mathbf{A} \mathbf{p}_k} \tag{66}$$

$$\mathbf{x}_{k+1} = \mathbf{x}_k + \alpha_k \mathbf{p}_k \tag{67}$$

$$\mathbf{r}_{k+1} = \mathbf{r}_k - \alpha_k \mathbf{A} \mathbf{p}_k \tag{68}$$

If the value of $\sqrt{\mathbf{r}_{k+1}^T \mathbf{r}_{k+1}}$ is sufficiently small, then the vector $\mathbf{x}_{k+1}$ is the solution to Eq.64. Otherwise, calculate following variables and go back to Eq.66 to repeat the iteration

$$\beta_k = \frac{\mathbf{r}_{k+1}^T \mathbf{r}_{k+1}}{\mathbf{r}_k^T \mathbf{r}_k} \tag{69}$$

$$\mathbf{p}_{k+1} = \mathbf{r}_{k+1} + \beta_k \mathbf{p}_k \tag{70}$$

$$k += 1 \tag{71}$$

A maximum number of times of iteration is given before the calculation. If the solver fails to converge, another preconditioned conjugate gradient (PCG) method will be executed. The PCG method has been implemented as a subroutine in the source code of PNMM. A preconditioner based on the diagonal entries of matrix **A** is adopted. The work flow of PCG method is similar to CG method, by simply replacing equations (65), (66), (69), and (70) with following equations respectively

$$\begin{cases} \mathbf{r}_0 = \mathbf{b} - \mathbf{A}\mathbf{x}_0 \\ \mathbf{p}_0 = \mathbf{M}^{-1}\mathbf{r}_0 \\ k = 0 \end{cases} \tag{65'}$$

$$\alpha_k = \frac{\mathbf{r}_k^T \mathbf{M}^{-1} \mathbf{r}_k}{\mathbf{p}_k^T \mathbf{A} \mathbf{p}_k} \tag{66'}$$

$$\beta_k = \frac{\left(\mathbf{M}^{-1}\mathbf{r}_{k+1}\right)^T \mathbf{r}_{k+1}}{(\mathbf{M}^{-1}\mathbf{r}_k)^T \mathbf{r}_k} \tag{69'}$$

$$\mathbf{p}_{k+1} = \mathbf{M}^{-1}\mathbf{r}_{k+1} + \beta_k \mathbf{p}_k \tag{70'}$$

where **M** is the preconditioner.

These two solvers have been capable of solving all the problems in this thesis. The source code of two solvers are given below as two functions in class `Calculator`. The term `Matrix` is a class template defined in the source code of PNMM. It defines the variable type of matrix and implements useful operations.

```
// The Eigen solver based on CG method
void Calculator::Calculator_Eigen(const Matrix<double> &A, vector<double> &x,
const vector<double> &b) {
    auto sizeOfA = A.GetSize();

    assert(A.IsSquare());
    assert(sizeOfA.first == x.size());
    assert(sizeOfA.first == b.size());

    vector<Eigen::Triplet<double>> nonZeros;
    nonZeros.reserve(sizeOfA.first * sizeOfA.second);
    for (int irow = 0; irow < sizeOfA.first; ++irow) {
        for (int icol = 0; icol < sizeOfA.second; ++icol) {
            if (A.GetElement(irow, icol) != 0.)
                nonZeros.push_back(Eigen::Triplet<double>(irow, icol,
                    A.GetElement(irow, icol)));
        }
    }
    Eigen::SparseMatrix<double> stiffness(sizeOfA.first, sizeOfA.second);
    stiffness.setFromTriplets(nonZeros.begin(), nonZeros.end());

    Eigen::VectorXd loading(b.size());
    for (int i = 0; i < b.size(); ++i)
        loading[i] = b[i];

    Eigen::VectorXd unknown(x.size());

    Eigen::ConjugateGradient<Eigen::SparseMatrix<double>> cgEigenSolver;
    cgEigenSolver.compute(stiffness);
    unknown = cgEigenSolver.solve(loading);

    for (int i = 0; i < unknown.size(); ++i)
        x[i] = unknown[i];
}

//The solver based on PCG method
void Calculator::Calculator_PCG(const Matrix<double> &A, vector<double> &x,
const std::vector<double> &b) {
    auto sizeOfA = A.GetSize();

    assert(A.IsSquare());
    assert(sizeOfA.first == x.size());
    assert(sizeOfA.first == b.size());

    int iterationTimes = 0;
    double rLength;
```

```
    Matrix<double> M;
    vector<double> r, z, p;
    double alpha, beta;

    M.Resize(sizeOfA.first, sizeOfA.second);
    //M is the preconditioner
    for (int irow = 0; irow < sizeOfA.first; ++irow)
        M(irow, irow) = A.GetElement(irow, irow);
    r = b;
    z = (M.Inverse() *
         MATRIX_H::ConvertVectorToVerticalMatrix(r)).ConvertToVector();
    p = z;
    x.clear();
    x.resize(b.size(), 0.);

    do {
        alpha = (MATRIX_H::ConvertVectorToVerticalMatrix(r).Transposition() *
            MATRIX_H::ConvertVectorToVerticalMatrix(z)).ConvertToBasicType() /
            (MATRIX_H::ConvertVectorToVerticalMatrix(p).Transposition() * A *
            MATRIX_H::ConvertVectorToVerticalMatrix(p)).ConvertToBasicType();
        x = (MATRIX_H::ConvertVectorToVerticalMatrix(x) + alpha *
             MATRIX_H::ConvertVectorToVerticalMatrix(p)).ConvertToVector();
        beta = 1.
            / (MATRIX_H::ConvertVectorToVerticalMatrix(z).Transposition() *
               MATRIX_H::ConvertVectorToVerticalMatrix(r)).ConvertToBasicType();
        r = (MATRIX_H::ConvertVectorToVerticalMatrix(r) - alpha * A *
             MATRIX_H::ConvertVectorToVerticalMatrix(p)).ConvertToVector();
        rLength =
            sqrt((MATRIX_H::ConvertVectorToVerticalMatrix(r).Transposition() *
            MATRIX_H::ConvertVectorToVerticalMatrix(r)).ConvertToBasicType());
        z = (M.Inverse() *
             MATRIX_H::ConvertVectorToVerticalMatrix(r)).ConvertToVector();
        beta *= (MATRIX_H::ConvertVectorToVerticalMatrix(z).Transposition() *
            MATRIX_H::ConvertVectorToVerticalMatrix(r)).ConvertToBasicType();
        p = (MATRIX_H::ConvertVectorToVerticalMatrix(z) + beta *
             MATRIX_H::ConvertVectorToVerticalMatrix(p)).ConvertToVector();
    } while (++iterationTimes < GLOBALVARIABLES_H::equationSolverIterationTimes
             && rLength > GLOBALVARIABLES_H::error);
}
```

References

EIGEN. 2017. Available: http://eigen.tuxfamily.org/ [Accessed].

SAAD, Y. 2003. Iterative methods for sparse linear systems, SIAM.

Appendix F Post-process of PNMM

In the post-process of PNMM, simulation results are written by a subroutine of PNMM into a text file, which is later processed by *ParaView* for visualization. ParaView (2017) is an open-source, multi-platform data analysis and visualization application. It supports the import of data in several formats. The interface between PNMM and ParaView is the Visualization Toolkit (VTK) file.

The format of the VTK file should be strictly followed. An example of the VTK file written by PNMM is given below.

# vtk DataFile Version 2.0 An example of rock slope ASCII DATASET UNSTRUCTURED_GRID	■ File Header
POINTS 27659 float 0.073258 5.958376 0.000000 … 1.739018 0.607733 0.000000	■ Particle centroid
CELLS 44401 133203 2 0 322 … 2 24857 7842 CELL_TYPES 44401 3 … 3	■ Link
POINT_DATA 27659 SCALARS radius float 1	■ Particle radius

LOOKUP_TABLE default 0.026360 … 0.017555	
VECTORS displacements float 0.00020562578 -5.3271651e-07 0. … 0.00014568978 -4.5647657e-07 0.	■ Particle results (vector form)
SCALARS X-stress float 1 LOOKUP_TABLE default 4.7480834e+005 … 3.5765755e+005	■ Particle results (scalar form)
CELL_DATA 44401 SCALARS link_status int LOOKUP_TABLE default 1 … 1	■ Link status

References

PARAVIEW. 2017. Available: https://www.paraview.org/ [Accessed].

Curriculum Vitae

Xing LI 李星

Department of Civil Engineering
Monash University, Clayton, VIC 3800, Australia

Date of Birth: 08 Feb 1989
Nationality: China
Email: xing.li@monash.edu; li.xing@outlook.com
URL: https://www.researchgate.net/profile/Xing_Li51

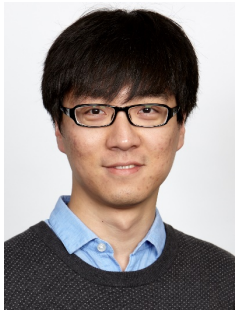

Education

11.2015 – 12.2017 **Doctor of Philosophy in Civil Engineering**
Monash University, Australia
Directors: Prof. Jian Zhao, Dr. Qianbing Zhang

07.2013 – 07.2015 **Doctor of Philosophy in Civil Engineering**
École Polytechnique Fédérale de Lausanne, Switzerland
Directors: Prof. Jian Zhao, Prof. Lyesse Laloui

06.2011 – 06.2013 **Master of Engineering in Mechanics**
Xi'an Jiaotong University, China
Director: Prof. Luxian Li

09.2007 – 2011.06 **Bachelor of Engineering in Mechanics**
Xi'an Jiaotong University, China

Research Projects

05.2013 – 12.2015 **PI, Mechsoft (Dalian) Co. Ltd., China**
Development for the Pre- & Post-processors and User Manual for Particle Manifold Method (PMM)

Development for Heterogeneous Model and Report Generation System for Particle Manifold Method (PMM)

10.2012 – 07.2013 **PI, Academy of Aerospace Solid Propulsion Technology, China**
Fracturing Process of the Propellant-Liner Interface

Advising Students

03.2016 – 10.2016 **Undergraduate Final Year Projects**
Monash University, Australia
A Slope Stability Comparison of Factor of Safety's between the Limit Equilibrium Method and Strength Reduction Method, by Mr. Darcy V. Lier

Numerical Simulation of Rock Blasting with Multiple Blast Holes, by Mr. RoshanKyu P. Karawita

Modelling the Stability of Underground Storage Caverns, by Mr. Yongkun Zhuang

02.2014 – 06.2014 **Teaching Assistant and Exercises Instructor**
École Polytechnique Fédérale de Lausanne, Switzerland
Undergraduate Course: Géométrie

Organising Conferences

- **Organising Committee & Conference Secretariat:** 3rd International Conference on Rock Dynamics and Applications (RocDyn-3), 25 – 29 June 2018, Trondheim, Norway
- **Conference Secretariat:** 6th International Conference on Design and Analysis of Protective Structures (DAPS 2017), 29 November – 01 December 2017, Melbourne, Australia
- **Conference Secretariat:** 3rd International Conference on Tunnel Boring Machines in Difficult Grounds (TBM DiGs 2017), 21 – 22 November, Wuhan, China
- **Conference Secretariat:** 2nd International Conference on Rock Dynamics and Applications (RocDyn-2), 18 – 19 May 2016, Suzhou, China

Publications

Journal papers

- **X. Li**, Q. B. Zhang*, and J. Zhao. A numerical study of spalling and related rockburst under dynamic disturbance using a particle-based numerical manifold method (PNMM). *Tunnelling and Underground Space Technology*. *Accepted*

- **X. Li**, Q. B. Zhang*, and J. Zhao. A numerical study of rock scratch tests using the particle-based numerical manifold method. *Tunnelling and Underground Space Technology*. *Accepted*
- **X. Li**, Q. B. Zhang*, L. He, and J. Zhao. Particle-Based Numerical Manifold Method to Model Dynamic Fracture Process in Rock Blasting. *International Journal of Geomechanics*. 2017, 17(5), E4016014.
- W. Wu*, Y. Zou, **X. Li**, and J. Zhao. An unload-induced direct-shear model for granular gouge friction in rock discontinuities. *Review of Scientific Instruments*. 2014, 85(9), 093902.
- D. Y. Niu*, S. Han, **X. Li**, B. Li, and W. Y. Ren. Mechanical Property of Asphalt Mortar with Additive. *Journal of Traffic and Transportation Engineering*. 2016, 16(3), 8-16. (in Chinese)
- X. F. Li, **X. Li***, H. B. Li, Q. B. Zhang, and J. Zhao. Dynamic tensile behaviours of rocks: the grain scale fracturing characteristics on strength and fragmentation. *International Journal of Impact Engineering*. *Submitted*.
- **X. Li**, Q. B. Zhang, J. C. Li, and J. Zhao. Mesoscopic simulation of the dynamic rock failure using the particle-based numerical manifold method. *Under preparation*.
- H. Z. Xing, **X. Li**, Q. B. Zhang, and J. Zhao. Characterization of dynamic constitutive constants of rock using coupled digital image correlation and finite element inverse method. *Under preparation*.

Conference papers

- **X. Li**, Q. B. Zhang, J. C. Li, and J. Zhao. Modelling spalling-induced rockburst in tunnels using a particle-based numerical manifold method (PNMM). *13th International Conference on Analysis of Discontinuous Deformation (ICADD 13)*, 08 – 10 December 2017, Tianjin, China.
- **X. Li**, Q. B. Zhang, and J. Zhao. A numerical study of spalling under different dynamic loads using a particle-based numerical manifold method (PNMM). *6th International Conference on Design and Analysis of Protective Structures (DAPS 2017)*, 29 November – 01 December 2017, Melbourne, Australia.
- **X. Li**, Q. B. Zhang, and J. Zhao. Numerical Simulation of Rock Dynamic Failure by Particle-Based Numerical Manifold Method. *22nd DYMAT Technical Meeting*, 19 – 21 October 2016, Grenoble, France.
- **X. Li**, Q. B. Zhang, L. He, and J. Zhao. Validation Study of the Particle-based Numerical Manifold Method (PNMM) on Stress Wave Propagation. *2nd International*

Conference on Rock Dynamics and Applications (RocDyn-2), 18 – 19 May 2016, Suzhou, China.

Book Editor

- Charlie C. Li, Zongxian Zhang, and **Xing Li**. Proceedings of the third international conference on rock dynamics and applications (RocDyn-3). CRC Press. *Under preparation*.